Modelling and Numerical Simulation of the multi-scale kinetic electron transport

Roland Duclous

To cite this version:

Roland Duclous. Modelling and Numerical Simulation of the multi-scale kinetic electron transport. Modeling and Simulation. Université Sciences et Technologies - Bordeaux I, 2009. English. NNT : . tel-00472327

HAL Id: tel-00472327
https://theses.hal.science/tel-00472327

Submitted on 10 Apr 2010

`N d’ordre :  3881`

THÈSE

présentée à

L’UNIVERSITÉ BORDEAUX 1

ÉCOLE DOCTORALE DE MATHÉMATIQUES ET INFORMATIQUE

par Roland DUCLOUS

POUR OBTENIR LE GRADE DE

DOCTEUR

SPECIALITÉ : MATHÉMATIQUES APPLIQUÉES ET CALCUL SCIENTIFIQUE

Modélisation et Simulation Numérique multi-échelle du transport cinétique électronique

Soutenue le 24 novembre 2009.

Après avis des Rapporteurs :

M. Axel KLAR, Professeur, Fachbereich Mathematik, T-U Kaiserslautern.
M. Mohammed LEMOU, Directeur de Recherches CNRS, Université Rennes 1.

Devant la commission d’examen formée de :

M. Christophe BERTHON, Professeur, Université de Nantes, Président du jury.
M. Francis FILBET, Professeur, Université Claude Bernard, Lyon 1.
M. Mohammed LEMOU, Directeur de recherche CNRS, Université Rennes 1, Rapporteur.
M. Luc MIEUSSENS, Professeur, Université Bordeaux 1.
M. Pierre CHARRIER, Professeur émérite, Université Bordeaux 1.
M. Martin FRANK, Associate Professor, RWTH Aachen University.
M. Jean-Pierre MORREEUW, Expert Sénior CEA/DAM, invité.
M. Bruno DUBROCA, Expert Sénior CEA/DAM, directeur de thèse.
M. Vladimir TIKHONCHUK, Professeur, Université Bordeaux 1, Directeur de thèse.

0.1 Remerciements

Ce manuscrit tente de résumer des progrès récents (2006-2009) concernant le transport électronique, et réalisés au sein du CELIA pendant cette thèse. Ces résultats ne peuvent se résumer simplement au travail d'une seule personne; ils sont issu d'un travail en commun, au quotidien, au sein du groupe "plasmas chauds". Je tiens ici à remercier les personnes de ce groupe pour ces trois années partagées et pour leur investissement dans ces travaux; en premier lieu Vladimir Tikhonchuk et Bruno Dubroca qui m'ont co-encadrés au CELIA. Ils ont été un véritable soutien avant, pendant et après cette thèse. Leurs qualités humaines, leur disponibilité et leur confiance m'ont été précieuses. J'ai souvent été bluffé par leur raisonnements scientifiques, et ai énormément appris à leur contact. Je profite de cette page pour les saluer et leur adresser un grand "Merci!".

Je me dois aussi de remercier vivement Axel Klar et Mohammed Lemou, bombardés rapporteurs de cette thèse, pour avoir pris le temps de lire et de finaliser ce manuscrit. Parmi les travaux abordés, une des orientations concerne les aspects numériques sur les équations cinétiques, et ont été accomplis grâce à une collaboration fructueuse avec Francis Filbet. Je voudrais le remercier pour son exigence, sa rigueur et sa confiance.
Parallèlement, les travaux concernant l'extension du modèle collisionel aux régimes de l'allumage rapide ont été réalisés sous les bons auspices de Jean-Pierre Morreeuw. C'est une chance que d'avoir pu travailler avec lui, et j'ai pu apprendre beaucoup, à ses côtés, grâce à sa volonté de "transmission" de ses connaissances sur le sujet.
Concernant les développements pour l'allumage par choc, je salue et remercie Guy Schurtz pour l'élaboration du projet KiTSI, dans lequel je me suis investi avec enthousiasme.

Les thématiques développées dans ce manuscrit ont été l'aboutissement d'une formation qui a débuté pour moi à l'école d'ingénieurs Matmeca; ainsi j'apprécie de pouvoir compter sur la présence dans le jury de son fondateur, Pierre Charrier, et de Christophe Berthon, maintenant à l'université de Nantes. J'ai principalement travaillé pendant ces trois années au CELIA dans le groupe "plasmas chauds". Ce groupe est composé de physiciens théoriciens, de mathématiciens et numériciens. Cela a été une expérience enrichissante que de se trouver au croisement de ces différents parcours et je remercie le directeur du CELIA, Philippe Balcou, m'y avoir accueilli. Je voudrais remercier les personnes avec qui j'ai pu partager et apprécier, aussi bien les pauses cafés, les voyages en conférences, que les discussions scientifiques; qui ont bien voulu répondre à mes nombreuses questions avec patience et gentillesse!: Stefan Weber, Emmanuel D'Humières, Xavier Ribeyre, Joao Santos, Anna Levy, Marie Billaud, Pierre-Henri Maire avec le "Château Le Chec". Aussi Yohan Boullet et Capucine Médina pour le fiacre, Jérôme Breil et le périple de Manhattan. Merci aussi à Roland Guichard pour le côté brésilien du bureau B1 et Amelle Zaïr pour son accueil à Londres, Lucia pour partager le capuch' du matin, Jovana pour le café de l'après-midi! Enfin les doctorants de CELIA, et les informatitiens de choc du CELIA Didier Briand et Loïc Baucher, pour leur bonne humeur jamais démentie.

Cette période au CELIA a été rythmée de collaborations avec d'autres équipes. En particulier, j'aimerais remercier chaleureusement les équipes allemandes de Martin Frank, Axel Klar, et Hans-Jörg Kull pour m'avoir accueilli à Kaiserslautern et à Aix-La-Chapelle. Je tiens aussi à remercier Martin Frank pour sa participation au Jury, et lui souhaite bonne chance à Aix-La-Chapelle!

Bein sûr, merci aussi aux équipes anglaises de Tony Bell, Robert Kingham et Roger Evans, pour leur accueil à l'Imperial College et à Oxford, et leur participation au projet KiTSI.

J'aimerais finalement exprimer ma gratitude à Laurence Rouïl, Frédéric Tognet, Gérard Vignoles, Yves Grillon et Pierre Fabrie, pour leur soutien lors de mon passage à Matmeca. Akshara Kaginalkar, Mohit Dalvi pour m'avoir formé au calcul massivement parallèle au C-DAC.

Enfin mes parents, mon frère et ma soeur, Jérôme et Delphine, ma famille et mes amis, pour leur soutien.

Contents

Chapter 1

Introduction

1.1 En français

Intention

Ce manuscrit constitue une contribution à la modélisation et la simulation numérique du transport et du dépôt d'énergie dans les plasmas créés par laser, ayant pour objectif une compréhension détaillée des procédés de compression d'un combustible, à des conditions de température et densité appropriées à l'ignition de réactions de fusion. Cette application, en particulier, sera traitée en prioritée, puisqu'elle constitue la principale motivation de ce travail. Des ouvertures et analogies à d'autres domaines, présentant une physique proche, seront développées ou évoquées. Elles s'étendent à l'électron-thérapie [14], la foudre, les événements énergétiques dans la haute atmosphère [19], la lithographie électronique, la Fusion par Confinement Magnétique (FCM) [15, 16], ou bien l'astrophysique, compte tenu du rôle important des électrons énergétiques dans les ceintures radiatives de Jupiter [2], par exemple. Le point commun à ce panel d'applications tient à la modélisation multi-échelle de la cinétique électronique et de la physique des plasmas.

Contexte et concepts

Parmi les domaines de recherche promis, dans un futur proche, à des implications sociétales importantes, l'interaction laser-plasma balaye un large eventail d'applications, de la production d'energie, au traitement médical des cancers (électron-thérapie, proton-thérapie, hadron-thérapie), à l'astrophysique de laboratoire, voire à la radiographie des objets denses et opaques. La fusion thermonucléaire contrôlée dédiée à la création d'une source abondante d'énergie, est ainsi une voie envisagée. Elle fait l'objet actuellement (2009) d'investissements massifs. Ce procédé vise à la combustion d'un mélange gazeux ou solide de noyaux légers à haute température, jusqu'à atteindre la centaine de millions de degrés Celsius. A cette température le combustible complètement ionisé est sous forme plasma: un ensemble de particules libres chargées, interagissant collectivement sous l'action de forces électromagnétiques [11, 21, 22, 29].

La production d'une large quantité d'énergie par la fusion de noyaux nécessite de vaincre les forces de répulsion Coulombienne. L'utilisation de noyaux de Deutérium et de Tritium (D-T) est actuellement la voie nominale pour atteindre des réactions de fusion avec un minimum d'énergie fournie au système. La section efficace pour la réaction de fusion D-T prédomine en effet sur les sections efficaces des autres principales réactions de fusion (D-^3He, D-Dp, D-Dn, *etc*). La réaction D-T, qui produit des neutrons de 14 MeV, est la suivante

$$D \;+\; T \rightarrow {}^4He \;+\; n(14.1 \text{ MeV}) \;\; (Q = \; 17.6 \text{ MeV}) \, .$$

La section efficace de cette réaction de fusion est de l'ordre d'un barn (1 barn = 10^{-28}m^2), qui est à mettre en perspective des 600 barns de la réaction de fission de l'élément ^{235}U. L'ignition de réactions de fusion est par conséquent beaucoup plus difficile à contrôler, puisqu'elles incorporent une physique bien plus riche et complexe. Par exemple, les sections efficaces de processus concurrents comme l'ionisation et la diffusion Coulombienne de particules chargées sont plus importantes. Dans ce contexte, des conditions drastiques doivent être remplies pour atteindre les densités et temps de confinement requis pour obtenir un gain total d'énergie. Ainsi, le critère de Lawson impose une limite basse sur le produit de la densité ionique n_i avec le temps de confinement τ_e de ce plasma

$$n_i \tau_e > g(T) f(Q) \, ,$$

où $g(T)$ représente la variation du taux de réaction avec la température, f étant une fonction de Q, lui-même le rapport entre la puissance issue des réactions de fusion et la puissance externe, celle fournie au plasma. Pour un plasma D-T de 10 keV, ce critère peut être réécrit

$$n_i \tau_e > 10^{20} m^{-3} s.$$

Le point de fonctionnement $f(Q) = 1$, dit de *break-even*, est désormais presque accessible avec les plus récentes installations expérimentales. Les régimes satisfaisants le critère $f(Q) > 1$ correspondent à des plasmas où les réactions de fusion sont auto-entretenues: il y a alors plus d'énergie générée qu'investie dans le système. Deux voies sont alors explorées, reposant soit sur des plasmas à haute température confinés avec des champs magnétiques de manière quasi-stationnaire: la *Fusion par Confinement Magnétique* (FCM), Fig. 1.2(c), soit sur des plasmas à haute pression et température confinés pendant une échelle de temps courte, de l'ordre de plusieurs nanosecondes seulement. Cette deuxième voie est la *Fusion par Confinement Inertielle* (FCI), Fig. 1.2(a) and 1.2(b).

Le principe de la FCM consiste à confiner un plasma dans un volume macroscopique par des structures de champs magnétique appropriées. La représentation physique sous-jacente choisie décrit le mouvement contraint des particules du plasma, ayant des trajectoires hélicoïdales dans un champ magnétique uniforme, et dérivant avec une vitesse moyenne dans la direction opposée au gradient, dans le cas d'un champ inhomogène. Un confinement transverse du plasma est alors rendu possible, par la création d'une structure avec un champ magnétique minimum sur l'axe. Les tokamaks assurent un confinement longitudinal en proposant une géométrie toroidale pour le réacteur de fusion. D'autres réacteurs similaires sont conçus sur le principes de la FCM: les stellerateurs, spheromak, *etc*. Dans un contexte FCM, le combustible D-T peut être chauffé en injectant des particules de haute énergie, ou bien par le biais d'ondes électromagnétiques de forte puissance.

Les conditions d'opérationelles de la FCI sont atteintes par deux approches possibles, à savoir l'attaque directe et indirecte. Dans le schéma d'attaque directe, une cible est illuminée par un grand nombre de faisceaux laser qui ont pour objet son accélération, suivie de son implosion. Ce processus requiert une très faible tolérance vis-à-vis d'une symétrie d'irradiation idéale. Dans le cadre du schéma d'attaque indirecte, la cible est irradiée par des rayons X, issus de la conversion de l'énergie laser sur une cavité présentant un numéro atomique Z élevé [23], appelée le *holhraum*. Malgré la faible efficacité de conversion, la symétrie de l'irradiation se révèle être meilleure, et peut être optimisée en jouant sur la forme du *holhraum*.

Une catégorie de réacteurs FCI, actuellement étudiée pour l'obtention et le contrôle de réaction de fusion à haut gain, et reposant sur le principe de schéma d'attaque indirecte, est dénomée *Z-pinch*. Ces machines génèrent des décharges électriques de haute intensité, qui permettent la création de plasmas chauds et denses.

Ces réacteurs génèrent des décharges électriques de haute intensité, ce qui permet d'obtenir des plasmas chauds et denses, issus de la stiction magnétique induite par d'importants courants, *via* la force de Lorentz. De tels plasmas sont eux-même la source de rayons X intenses. Les Etats-Unis se sont fortement engagés dans cette voie, et notamment grâce à leur installation SANDIA, montrée Fig. 1.2(b). Celle-ci peut délivrer des courants supérieurs à 1 MA, en 100-200 nanosecondes, grâce à une technologie de puissance pulsée qui permet de comprimer efficacement l'énergie électrique en espace et en temps [25].

En 1996, une percèe dans la puissance délivrée à partir de réseaux de fils en aluminium de type *Z-pinch* (40 TW de puissance de rayon X à partir d'un générateur de 20 TW) [28], a suscité un regain d'intérêt dans la recherche pour les *Z-pinch*: en plaçant le réseau de fil dans une cavité, une source importante de radiation à la température planckienne est créée. Celle-ci peut être utilisée pour des applications de haute densité d'énergie (HEDP), dont les applications FCI [24].

Dans le cadre de la FCI en attaque directe, une réflexion européenne a conduit à proposer une installation reposant sur les techologies de pointe pour les lasers de puissance: HiPER (acronyme de *High Power Laser Energy Research*), qui a pour objectif premier la démonstration de fusion par confinement inertiel à haut taux de répétition, et de sa viabilité économique. L'allumage rapide est, pour l'instant, le schéma nominal retenu. Dans ce schéma, les étapes de compression et d'allumage proprement dit sont décorrélées. Le combustible est tout d'abord compressé à des densités élevés par un *driver* approprié. Le combustible pré-compressé est allumé par un second *driver* ultra-intense. Les spécifications actuelles de HiPER prévoient une configuration de type faisceaux multiples d'énergie 250 kJ, à 3ω, de longueur d'onde $\lambda = 0.35\ \mu m$, supplémentée par des faisceaux nanosecondes, à 2ω, pour l'allumage. Indépendamment, le laser PETAL, actuellement en construction dans la région Aquitaine, est un laser de type PetaWatt, qui doit délivrer un énergie de 3.5 kJ pendant 0.5-10 picosecondes. PETAL est inscrit comme jallon sur la voie de la réalisation du projet HiPER.

Une approche alternative concerne les schémas hybrides de fission-fusion [17]. Leur principe repose sur l'observation suivante: la consommation d'uranium fissile naturel est telle que ces ressources sont supposées manquer d'ici à 40-50 années. La répartition d'isotope, sur terre, montre une forte composante, 99,27 %, pour l'isotope ^{238}U, qui est donc défini comme un isotope *fertile*, vis-à-vis d'une faible composante, 0,72 %, pour l'isotope ^{235}U, qui est dénomé *fissile*, puisque des neutrons d'énergie nulle peuvent déclencher la fission de cet élement. Le shéma hybride fission-fusion offre la possibilité d'une conversion efficace des isotopes fertiles en combustible fissile, grâce à une source de neutrons de fusion à haut flux. Ces neutrons peuvent être utilisés pour plusieurs applications: l'alimentation en neutron pour le combustible fissile, l'introduction de réactions de fission pour produire une puissance additionelle, ou la transmutation de déchets radioactifs à longue vie, comme les éléments de type actinides, *via* l'absorption de neutrons.

Un hybride fission-fusion est un réacteur de type fusion, qui présente des isotopes fertiles dans sa couverture. En l'état actuel de l'art, un tel schéma requiert seulement $f(Q) \sim 2$ pour être économiquement viable, à comparer au seuil de viabilité $f(Q) > 10$ pour un réacteur de fusion. Bien que cette voie hybride ne constitue pas une approche de fusion pure et propre, elle peut néanmoins se révéler intéressante au regard du compromis qu'elle propose, notamment quant à la relative faible puissance laser investie.

Affirmation des directions de recherches

Une problématique théorique majeure en physique de la FCI réside dans le transport cinétique multi-espèce, collectif et collisionel; son couplage avec d'autres processus, comme l'absoption laser -collective et collisionelle-, le transfert radiatif [18], la production de neutrons par les réactions de fusion [13], et la combustion dans le point chaud. La compréhension et la modélisation de ces processus sont cruciales pour proposer et construire des senarii susceptibles de produire des gains en energie élevés, ainsi que pour assister, piloter, et optimiser les futures unités de production FCI à l'aide de simulations intégrées. Un tel programme se situe au-delà des objectifs propres à ce document.

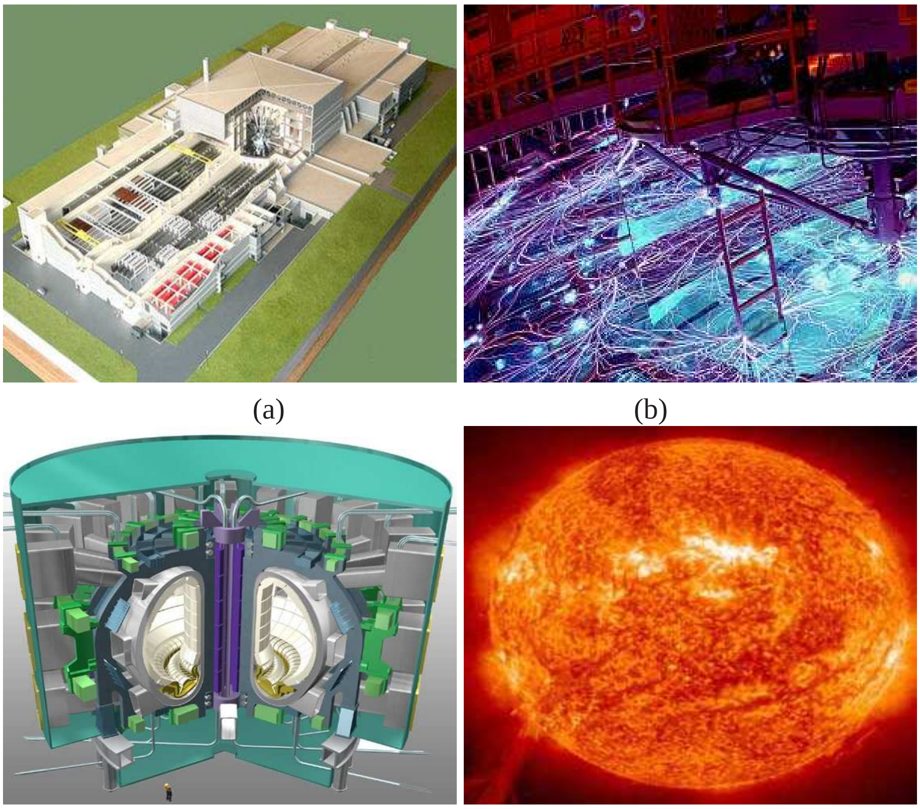

(a) (b)

(c) (d)

Figure 1.1: Illustration d'entités dont le fonctionnement repose sur un principe de fusion par confinement soit inertiel -LMJ Figure (a), Z-pinch Figure (b)-, ou magnétique -ITER Figure (c)-, ou gravitationel -le Soleil Figure (d)-.

L'approche déclinée ici a plutôt pour objet la modélisation, l'étude numérique, et la simulation du transport cinétique électronique collisionnel, dans un schéma FCI, entre la zone d'absorption du laser et la zone du front d'ablation [8]. La physique induite par ces processus met en jeu différents aspects, eux-mêmes considérés comme des points clés à maîtriser pour le transport cinétique en physique de la FCI: un modèle numérique doit pouvoir permettre aussi bien la description de l'interaction laser-plasma dans les régions sous-denses, lorsque les effets collectifs sont dominants, que la description du transport de particules rapides et leur dépôt d'énergie dans la cible extrêmement dense (solide), losque les collisions Coulombiennes à longue distance contribuent largement à la dynamique de transfert dénergie. Nous sommes alors confrontés à un problème présentant des variations importantes vis-à-vis de ses échelles caractéristiques d'espace et de temps. Pour l'allumage par choc [1], les variations importantes de masse surfacique impliquent une variation du libre parcours moyen de collision entre particules, de l'ordre de quatre à cinq ordres de grandeurs. Des barrières au transport, dues aux champs magnétiques forts, de l'ordre du MegaGauss, peuvent entrer en compétition avec les effets collisionels, et ainsi inhiber le transport électronique en infléchissant les trajectoires des électrons, ce qui pourrait conduire à une

modification significative de la sphéricité du front d'ablation de la cible. Une difficulté supplémentaire, liée à l'interaction laser-plasma, réside dans le fort couplage entre les grandeurs caractéristiques dans le plasma. Les différentes échelles se recouvrent, ce qui rend tout traitement séparé d'une seule échelle caractéristique illusoire sans perte de précision.
Pour prendre en compte l'ensemble de ces aspects complexes, nous développons depuis 2006 un code de référence, déterministe, de type Maxwell-Fokker-Planck-Landau, évoluant dans une géométrie plane de l'espace des phases de dimension $2D_{\mathbf{x}} \times 3D_{\mathbf{v}}$. Notre point de départ a été un solveur déterministe de type Poisson-Fokker-Planck-Landau, évoluant dans un espace des phases de dimension $1D_x \times 3D_{\mathbf{v}}$, et issu des travaux de *N. Crouseilles et F. Filbet* [7]. Ils ont, les premiers, intégré d'importants développements, issus de *la communauté française de mathématiques appliquées*, concernant la discrétisation des opérateurs de collision -nous mentionnons pour ce propos les travaux de P. Degond [9], B. Lucquin-Desreux [10], C. Buet [4], F. Filbet [6], et M. Lemou [5]-, et les ont implémentés dans un cadre non homogène, en couplant la discrétisation des collisions à un schéma numérique d'ordre élevé pour l'équation de transport de Vlasov, ouvrant ainsi la voie, à partir de cette approche multi-échelle, à des couplages avec une physique plus variée.

Notre approche, à partir de cette base forte, a consisté à inclure les effets des champs magnétiques, à explorer le régime relativiste, et proposer des modèles réduits qui sont capables de retranscrire notre compréhension du transport électronique pour la FCI. A ce moment-là, ces aspects étaient toujours l'objet de débats, et la manière d'inclure ces effets avec précision dans de tels systèmes raides, multi-échelles, avec un potentiel de Coulomb de longue portée. Ce dernier effet rend la modélisation des collisions non rasantes, entre particules de même espèces, très ardue.
Nous affirmons avoir atteint les objectifs fixés au préalable, et présentons dans ce manuscrit, pour étayer cette affirmation, des simulations numériques précises et robustes, résultant d'analyses numériques appronfondie, de modélisation pour la physique des plasmas, et de calculs scientifiques massivement parallèlles: la version parallèle de ce code s'est révélée être *scalable* sur des milliers de processeurs dédiés (plateforme de Calcul Haute Performance CCRT-CEA platine). Nous nous sommes efforcés de nous tourner, dès que faire se peut, vers des applications physiques pertinentes pour la FCI. Cette approche a été principalement contrainte -en particulier pour les futures comparaisons avec les expériences- par le fait que les ions ont été considérés comme immobiles dans nos équations. S'affranchir de cette hypothèse, en incluant le mouvement des ions, pourrait constituer la base d'un travail à venir.

Structure du manuscrit
Ce travail se situe à l'interface de l'analyse numérique, la physique des plasmas, et les mathématiques appliquées. Ainsi, un cloisenement entre toutes ces activités serait articificiel. Cependant, nous devrons identifier et analyser chacun des processus pertinents pour le transport nonlocal pour la FCI. Par conséquent, pour chacun des processus identifiés, nous présenterons la dérivation de modèles physiques, et développerons une analyse numérique. Ces présentations préluderons aux tests numériques et/ou à des simulations réalistes, représentatives de la physique. Nous complèterons notre présentation, lorsque c'est possible, avec des analogies à d'autres domaines de la physique.
Finalement, nous partageons avec le lecteur notre expérience, et proposerons des perspectives de recherche attractives.

Chapitre 2: Nous proposons ici une brève mise en perspective des processus en jeu en théorie des plasmas, et une revue des modèles de base et des méthodes pour les implémenter, les coupler, et les valider. Dans ce chapitre, *se référant à l'école Russe de physique des plasmas*, nous adoptons une approche critique, en discutant la littérature et introduisant notre travail.

Chapitre 3: Nous nous concentrerons, dans cette partie, sur les aspects collectifs reliés à l'équation de transport électronique libre, dite *free-streaming*, pour la limite non relativiste, ainsi que pour le régime relativiste. Les points clés résident ici dans les développements et analyses numériques des schémas pour le système de Vlasov-Maxwell, et dans la dérivation de schémas numériques appropriés, robustes, d'ordre supérieur à deux. Ainsi, dans le rérime relativiste, nous présentons une technique numérique efficace, non standard, dans laquelle nous proposons d'abandonner la discrétisation d'un résidu relativiste

$$\mathcal{R} \equiv \left[\left(\frac{\partial v_1}{\partial p_2} - \frac{\partial v_2}{\partial p_1}\right) f\right](t, \mathbf{x}, \mathbf{v}) = 0 \ ,$$

en maintenant une discretisation correcte des invariants collisionels. Nous proposons aussi un choix adéquat pour la discrétisation de la vitesse, qui provient de la définition $\mathbf{v} \equiv m_e c^2 \nabla_{\mathbf{p}} \gamma(p)$, pour respecter la conservation de l'énergie discrete pour le système d'équations de Vlasov-Maxwell. Ce choix est directement issu de la discrétisation correcte de

$$\mathbf{0} = \nabla_{\mathbf{p}} \times \left(\nabla_{\mathbf{p}} \gamma(\mathbf{p})\right) \ .$$

Chapitre 4: Dans ce chapitre, nous nous intéressons à des aspects plus spécifiques du transport collectif: le transport multi-espèces, soumis à des discontinuités dans l'espace des phases. Nous nous référons ici au transport cinétique de différentes particules, ayant des charges positives et négatives, et un rapport de masse arbitraire. Cette physique peut s'appliquer, en particulier, aux plasmas electron-ion ou electron-positron. Nous réalisons une analyse de convergence d'un schéma *Volumes Finis* d'ordre élevé, de second ordre, pour le système de Vlasov-Poisson, et démontrons l'efficacité de la méthode pour le traitement des discontinuités, pour un test pertinent, mettant en jeu deux populations avec un rapport de mass intermédiaire

$$1 \leq \frac{m_1}{m_2} \leq 1836 \ .$$

Chapitre 5: Cette partie est dédiée à la modélisation multi-échelle de la physique du transport électronique, avec des termes source de collision, dans un espace des phases $2D_{\mathbf{x}} \times 3D_{\mathbf{v}}$ à géométrie plane. Nous validons cette approche, et démontrons la précision d'un solveur Monte Carlo multigrille pour l'opérateur de collision electron-electron Fokker-Planck-Landau, dans une gamme de régimes étendue, pertinente pour la physique de la FCI. Cette gamme s'étend des régimes collisionels à raréfiés, des régimes non magnétisés aux magnétisés. La méthode multigrille est reconnue comme étant bien adaptée pour l'accélération basé sur les protocoles de type FPGA, et pourrait se révéler interessante pour des d'architectures parallèles et reconfigurables (dites *Reconfigurable Computing Systems in HPC platforms*). Nous présentons une méthode numérique de discrétisation, l'algorithme d'accélération multigrille, ainsi qu'une sélection de tests numériques simples mais représentatifs, qui peuvent servir comme tests de référence pour le transport collisionel avec les modèles réduits présentés dans le chapitre 2.

Chapitre 6: Cette partie est dédiée à des simulations réalistes pour le transport cinétique électronique dans le cadre du schéma d'allumage par choc. Ce schéma est un des candidats officiels, inscrit dans les spécifications du projet européen HiPER, comme schéma nominal d'allumage pour cette future installation à taux de répétition élevé. Une campagne d'étude expérimentale pour l'allumage par choc est actuellement (2009) en cours à l'université de Rochester sur le laser OMEGA. Cette campagne a d'ores et déjà démontré un accroissement significatif du bilan de production de neutrons, à intensité laser fixée, comparé aux schémas classiques d'allumage pour la FCI. Ce schéma est toujours, à ce jour, l'objet de débats. L'étude et le contrôle des aspects cinétiques reliés au transport électronique est un des verrous majeurs, identifié, à traiter pour l'obtention d'un schéma de référence. Le projet de simulation Transport Cinetique Electronique pour l'Allumage par Choc (ayant pour acronyme KiTSI en langue anglaise), à été l'objet d'un besoin spécifique de resources de calcul. En effet, plus de 8 millions d'heures processeurs ont été obtenues *via* l'organisme GENCI, qui gère ces ressources en France depuis 2008. Ce projet est le résultat d'une collaboration avec X. Ribeyre, M. Lafon, G. Schurtz, E. D'Humières, S. Weber du CELIA, les équipes de R. J. Kingham à l'Imperial College, et A. R. Bell au Rutherford Appleton Laboratory et à l'université d'Oxford.

Chapitre 7: Cette partie est dédiée au développement et à la validation d'un modèle de transport électronique réduit en angle, de type $M1$, ainsi qu'au développement d'une méthode numérique HLLC pertinente, associée à ce modèle. La fermeture $M1$ par minimisation entropique pour les électrons [3] peut être dérivée de la manière suivante. Pour fermer le système, nous déterminons une fonction de distribution f_{ME} qui minimise l'entropie des électrons,

$$H(f) = -\int_{S^2} f \log f d\Omega, \tag{1.1}$$

sous la contrainte de reproduire les moments d'ordre les plus bas,

$$\int_{S^2} f_{ME} d\Omega = f_0 \equiv \int_{S^2} f d\Omega \quad \text{and} \quad \int_{S^2} \mathbf{\Omega} f_{ME} d\Omega = \mathbf{f_1} \equiv \int_{S^2} \mathbf{\Omega} f d\Omega\,. \tag{1.2}$$

Cette fermeture est bien adaptée au transport électronique car elle permet des calculs analytiques pour les noyaux de collision, en régime relativiste et non relativiste. A la fois le modèle et la méthode numérique possèdent une limitation de flux appropriée $||\mathbf{f_1}|| \leq f_0$, la positivité $f_{ME} \geq 0$, et les propriétés de conservation adéquates. De plus, nous sommes capables de traiter exactement aussi bien les distributions monoénergétiques, que les fonctions de distribution isotropes. Ces aspects rendent la version multigroupe de ce modèle bien adaptée pour l'interaction laser-plasma relativiste, dans les régimes collisionels et collectifs. Le modèle et les schémas numériques sont testés dans les deux régimes d'intérêt. Une analogie est conduite entre la FCI et le transport électronique pour la radiothérapie. En particulier, nous insistons sur l'importance de la production d'électrons secondaires pour les applications liées à la radiothérapie. Ce processus est étudié en détail dans le chapitre 8 dans un cadre FCI.

Chapitre 8: dans cette partie, nous nous intéressons à l'importance relative des processus impliquant les collisions electron-electron à haute énergie. Nous mettons en évidence l'importance du mécanisme de production d'électrons secondaires à des énergies relativistes. Pour ce faire, nous proposons un modèle multi-échelle, rapide et robuste, qui comporte des termes de Boltzmann relativistes. Ce modèle est destiné à être plus précis et rapide que les modèles existant, et ce de plusieurs ordres de grandeur. *Ce* *modèle peut être considéré comme une simplification de l'équation de Boltzmann, relativiste ou non, de la forme*

$$\frac{\mathrm{d}}{\mathrm{d}t} f(\mathbf{p}) = \int_{\mathbb{R}^3} d^3q \int_{S^2} d\tilde{\boldsymbol{\Omega}}' \, [f(\mathbf{p}')f(\mathbf{q}') - f(\mathbf{p})f(\mathbf{q})] \, \tilde{u} \, \frac{\tilde{W}^2}{W_p W_q} \, Q(\tilde{p}, \tilde{\mu}) \, .$$

En particulier, il généralise et reprend les travaux de L. D. Landau (années 1940), S. T. Beliaev (1956), et A. V. Gurevich (1998), sur les collisions electron-electron, avec un potentiel de Coulomb à longue distance.

$$V_i = \sum_{j \neq i} \frac{q_j}{|r_{ij}|} \, .$$

Une étape importante, dans la dérivation de ce modèle, a été la décomposition de la dépendance du potentiel en $1/r$ à l'aide d'un potentiel de lissage $\mathcal{S}$

$$\frac{1}{r} = \left(\frac{1}{r} - \mathcal{S}(r) \right) + \mathcal{S}(r)$$

Le principal résultat de ce modèle réside dans sa robustesse, grâce à un choix approprié pour la fonction $\mathcal{S}$. Enfin, une attention particulière est portée à la future implémentation numérique de ce modèle. Les applications potentielles concernent le projet européen HiPER pour l'allumage rapide, les domaines de la lithographie électronique, la radiographie des objets opaques et denses, les événements énergétiques dans la haute atmosphère, les plasmas de décharge, ou la créaction de plasmas electron-positron.

Chapitre 9: Conclusions et perspectives à long terme.

1.2 En anglais

Intention
This manuscript provides with a contribution to the kinetic modelling and numerical simulations of the electron energy transport and deposition in laser-produced plasmas, having in view the processes of fuel assembly to temperature and density conditions necessary to ignite fusion reactions. This particular application will be treated in detail, as it is the principal motivation of this work. Some applications to other fields, relying on similar physics, shall be also presented or mentioned. They concern electron radiotherapy [14], lightening discharges, high energy phenomena in the upper atmosphere [19], electron lithography, Magnetic Confinement Fusion (MCF) [15, 16], or astrophysics [2]. We should mention for this latter application, as an example, the observed role of energetic electrons in Jupiter radiation belts [2]. The common point of these fields is that they involve multi-scale modelling of electron kinetics and plasma physics.

Context and concepts
One of the fundamental research area that promises significant societal applications, in a very near future, is the laser-matter interaction. A broad spectrum targeted applications ranks from energy production, medical treatment of cancers (electron radiotherapy, protontherapy, hadrontherapy), laboratory astrophysics, to the radiography of dense and opaque objects. Among them, the thermonuclear fusion is at present (2009) the object of large-scale investments, dedicated to the creation of an abundant energy source. To this aim, the combustion of a gaseous or solid mixture of light nuclei at high temperature, at

around a hundred millions of Celcius degrees, proves to be an efficient mechanism. At these temperatures the fuel is fully ionized becoming a *plasma*, an assembly of high-temperature particles interacting collectively by electromagnetic forces [11, 21, 22, 29]. To produce the fusion of two nuclei, and thereby the production of a large amount of energy, one has to overcome the Coulomb repulsive forces between them. The use of deuterium and tritium (D-T) nuclei is currently the nominal way chosen to achieve fusion with a minimum of energy provided to the system. The cross section of D-T reaction fusion is indeed well above those of the other principal fusion reactions (D-^3He, D-Dp, D-Dn, *etc*). The D-T reaction, producing the 14 MeV neutrons, is the following

$$D \ + \ T \rightarrow {}^4He \ + \ n(14.1 \text{ MeV}) \ \ (Q = \ 17.6 \text{ MeV}) \ .$$

The cross section of this fusion reaction is of the order of a barn (1 barn = 10^{-28}m^2), to be compared with the 600 barns of the fission reaction of the ^{235}U. It is, therefore, much more difficult to control, because it involves a more rich and complex physics. For instance, the cross section of concurrent processes such as ionization and Coulomb scattering of charged particles are much higher. In this context, stringent conditions must be fulfilled to achieve the required density and confinement time of a plasma and to obtain a profitable total energy budget. This is the Lawson criteria, which imposes a lower limit on the product between the ion density n_i and the confinement time τ_e of this plasma

$$n_i\tau_e > g(T)f(Q) \ ,$$

where $g(T)$ accounts for the variation of the reaction rate with the temperature, and f a function of Q, the ratio between the power issued from the fusion reaction and the external power provided to the plasma. For a D-T plasma of 10 keV, this criteria can be rewritten as

$$n_i\tau_e > 10^{20} m^{-3} s.$$

$f(Q) = 1$ denotes the break-even, this operating point is almost satisfied in some of the most recent experimental installation. $f(Q) > 1$ denotes regimes where the plasma is ignited and the fusion reaction is self-sustained: there is then more energy generated than energy put in the system. Two ways are then explored, implying either high temperature plasmas confined with magnetic fields for a quasi-steady operation, the *Magnetic Confinement Fusion* (MCF), Fig. 1.2(c), or high pressure and temperature plasmas confined for short time scale of the order of several nanoseconds only, this latter is the *Inertial Confinement Fusion* (ICF), Fig. 1.2(a) and 1.2(b).

The MCF consists in confining plasma in a certain volume by appropriate magnetic field structures. The underlying idea is that plasma particles have a helical trajectory in a uniform magnetic field, and they are drifting in the direction opposite to the gradient in an inhomogeneous field. Then, a transerval confinement of the plasma is achieved by creating a structure with the minimum of magnetic field on the axis. In devices such as Tokamaks, the longitudinal confinement is achieved by choosing a toroidal geometry for the magnetic fusion reactor. Many other MCF devices are designed: stellarator, reversed field pinch, spheromak, *etc*. In the context of MCF, D-T fuel can be heated by injecting high energy particles or by means of high power electromagnetic waves.

The ICF conditions may be fulfilled by two possible approaches, namely the direct and the indirect drive. In the direct drive, a pellet is illuminated by a large number of laser beams that accelerate it until implosion. This requires a very low tolerance to any departure from perfect irradiation symmetry. In the indirect drive, the pellet is irradiated by X-rays, produced by the conversion of laser energy on a high-Z-lined cavity [23], the hohlraum. Despite a lower energy conversion efficiency, the symmetry of the irradiation proves to be better, and can be optimized playing on the shape of the hohlraum.

One category of devices, that is currently considered to reach and control high gain fusion, and relies on indirect drive ICF, falls into the "Z-pinch" denomination. These machines generate electrical discharges of high intensities, that make it possible to obtain a warm and dense plasma, issued from the magnetic striction induced by the high currents, *via* the Lorentz force. Such plasma is itself a source of intense X-rays. The U.S. program is well-engaged in this direction, with the SANDIA facility, shown in Fig. 1.2(b), that can deliver large currents, above 1 MA, in 100-200 nanoseconds, thanks to a pulsed-power technology that could efficiently compress electrical energy in space and time [25]. In 1996, a breakthrough in X-ray power output from aluminium wire array Z-pinches (40 TW X-ray power from a 20 TW electrical generator) [28] triggered a boom in Z-pinch research: placing the wire array inside a hohlraum creates a high temperature Planckian radiation source that can be used for high energy density physics (HEDP) applications, including ICF research [24].

In the frame of direct drive ICF, a European reflexion has proposed the High Power Laser Energy Research (HiPER) facility, with the primary goal of demonstrating laser driven inertial fusion at high repetition rate, and its economic interest. Fast Ignition is the baseline approach, in which the stages of fuel compression and ignition are separated. The fuel is first compressed to high density by a suitable driver; the precompressed fuel is ignited by a second ultra-intense driver. HiPER is expected to provide 250 kJ in multiple, 3ω (wavelength $\lambda = 0.35\ \mu m$), nanosecond beams for compression and 70 kJ in tens of picoseconds, 2ω beams for ignition. Independently the PETAL laser is a 3.5 kJ, 0.5-10 ps, PetaWatt-class laser, which is under construction in the Aquitaine region, France. It is a fore-runner to the HiPER facility.

An alternative approach involves hybrid fission-fusion schemes [17], it is based on the following observation: the natural fissile uranium is expected to lack to be consumed in about 40-50 years. The isotope repartition, on Earth, is 99.27 % for ^{238}U, which stands as a *fertile* isotope, and only 0.72 % for ^{235}U, which is called *fissile*, since zero-energy neutrons can produce the fission of ^{235}U. Hybrid fission-fusion scheme offers the possibility of efficient conversion of fertile isotopes into fissile fuel, with a high flux source of fusion neutrons. These neutrons may be used for several applications: breeding of fissile fuel, induction of fission reactions to produce additional power, or the transmutation of radioactive wastes, such as actinides elements, *via* neutron absorbtion.

A fusion-fission hybrid is a fusion reactor with fertile isotopes in the blanket. As a fusion reactor needs $f(Q) > 10$ to be economical, the fusion-fission hybrid may be economical with only $f(Q) \sim 2$. Although this way is not a pure and clean fusion approach, it may still be interesting with respect to the relatively low laser power invested.

Research direction statement

A major theoritical issue in ICF physics is the mixed collective and collisional multi-species kinetic transport, and its coupling with other processes, such as laser absorption processes, radiative transfer [18], neutron production by fusion reactions [13], and combustion in the hot spot. The understanding and modelling of these processes are indeed crucial to propose and build reliable senarii likely to pro-

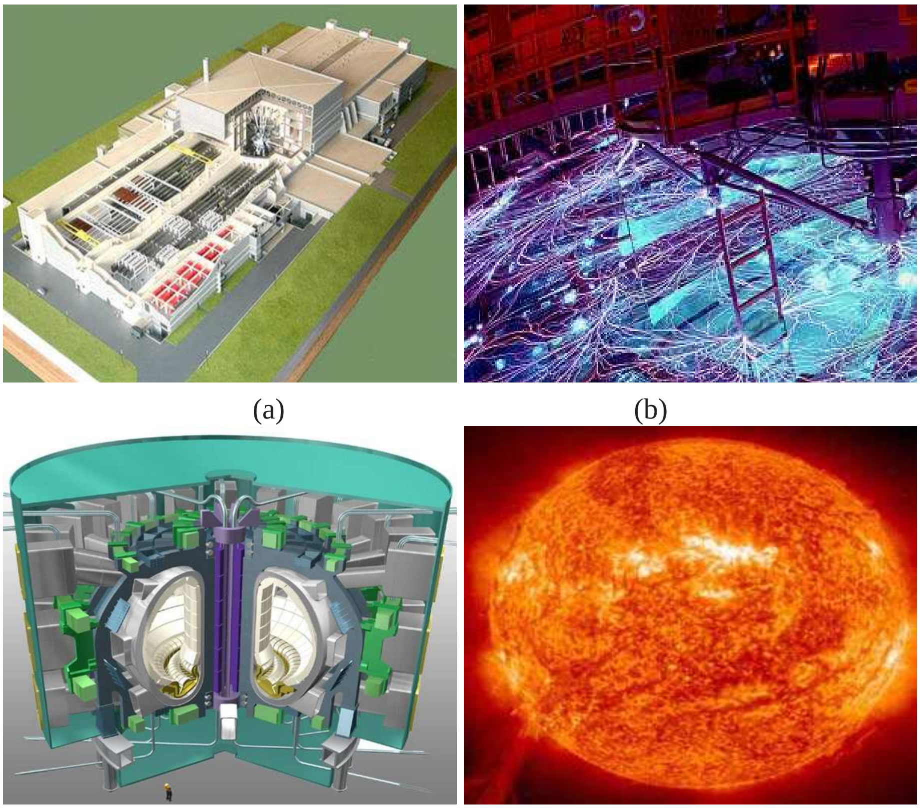

(a) (b)

(c) (d)

Figure 1.2: Various fusion devices relying on either an inertial -LMJ in Figure (a), Z-pinch in Figure (b)-, magnetic -ITER in Figure (c)-, or gravitational -the Sun in Figure (d)- confinement.

duce high energy gains, to assist, pilot, and optimize the future ICF fusion-based power plant units with integrated simulations. Such a comprehensive task is beyond the scope of this document.

The present approach rather focusses on the modelling, numerical study, and simulation of the kinetic electron collisional transport in ICF, between the laser absoption zone and the ablation front [8]. This physics gathers an important variety of features considered as a bottleneck for kinetic transport in ICF physics: a numerical model needs to describe the laser-plasma interaction in the low density region, where the collective effects are dominant, as well as the fast particle transport and energy deposition in the extremely dense (solid) target, where long-range Coulomb collisions contribute greatly to the energy transfer dynamics. We are faced with a problem with a large variation in characteristic length and time scales. In the shock ignition [1], the high areal density variations involves a decrease of about 4-5 orders of magnitude in mean-free-path. Transport barriers due to large magnetic fields, up to MegaGauss order, may compete with collisional effects and inhibit the electron transport while bending the electron trajectories, which may lead to a serious modification of the sphericity of the ablation front of the target. Moreover, a particular feature of this laser-matter interaction is the large interplay between the scales in a plasma. The different scales recover each other, which makes it impossible to isolate the different

mechanisms without a latent loss of accuracy.
To encompass all these complex features, we develop since 2006 a reference deterministic Maxwell-Fokker-Planck-Landau code, in a planar $2D_{\mathbf{x}} \times 3D_{\mathbf{v}}$ phase space geometry. Our starting point was a $1D_x \times 3D_{\mathbf{v}}$ Poisson-Fokker-Planck-Landau deterministic solver from *N. Crouseilles and F. Filbet* [7]. Their work first gathered important developments, issued from the *French school of applied mathematics*, concerning the numerical discretization of collision operators -we should mention here the works from P. Degond [9], B. Lucquin-Desreux [10], C. Buet [4], F. Filbet [6], and M. Lemou [5]-, and cast them in a nonhomogeneous framework, while coupling the discretization of collisions to a high order numerical scheme for the Vlasov transport equation, and opening the path, from this multi-scale approach, to the coupling with additional physics.

Our task, from this strong basis, was to include the effects of magnetic fields, explore the relativistic regime, and propose reduced models that could reproduce our understanding of the electron transport for ICF. At that time, these issues were still under debate, and the answers were not yet known how to include or model these effects accurately with such stiff multi-scale systems, with the long-range Coulomb potential. This latter makes it very difficult to model nongrazing collisions between like particles.
We claim that we have brought some important information, and reached our objectives. We present in this manuscript, to support this claim, accurate and robust numerical simulations, resulting from numerical analysis studies, plasma physics modelling, as well as massively parallel scientific computing: the parallel version of the code has proved to be scalable over thousands of dedicated processors (CCRT-CEA platine High Performance Computing platform). We have tried to turn, as far as possible, to physical appications. This approach was mainly constrained -in particular for future comparisons with experiments- by the fact the ions were considered as fixed in our equations. This could be the object of a forthcoming work.

Structure of the manuscript
This work is at the interface between numerical analysis, plasma physics and applied mathematics. On the one hand, a rough decoupling between all these aspects would then be meaningless. On the other hand, we shall identify and analyse each of the relevant physical processes for ICF nonlocal transport physics. Therefore, for each of the identified process, we first present the derivation of physical models, develop numerical schemes and perform a numerical analysis upon them. Such presentation preludes to numerical tests and/or realistic simulations. We shall complete this presentation, when it is possible, with analogies in other fields of physics.
Finally, we share with the reader our experience and propose research perspectives.

Chapter 2: We provide here with a brief review of the processes at play in the collisional kinetic theory of plasmas, and focus on basic models and methods to implement, couple and validate them. In this chapter, *following the Russian school of plasma physics*, we adopt a critical approach, while discussing the literature and introducing our work.

Chapter 3: We shall focus here on the collective aspect related to the free-streaming electron transport equation, in the nonrelativistic limit, as well as in the relativistic regime. The key points stand in the numerical development and analysis of the scheme for the Vlasov-Maxwell system, and in the selection of a validation procedure and numerical tests. In particular, we show the importance of the derivation of robust numerical schemes, that present higher order than two. Also, in the relativistic regime, we present a non-standard efficient numerical technique, in which we propose to drop the discretization of a relativistic residual

$$\mathcal{R} \equiv \left[\left(\frac{\partial v_1}{\partial p_2} - \frac{\partial v_2}{\partial p_1}\right) f\right](t, \mathbf{x}, \mathbf{v}) = 0 \ ,$$

while maintaining the correct discrete invariants. We also propose a choice for the velocity discretization, that comes from the definition $\mathbf{v} \equiv m_e c^2 \nabla_{\mathbf{p}} \gamma(p)$, in order to satisfy the discrete total energy conservation for the Vlasov-Maxwell system of equations, which is the direct consequence of the correct discretization of

$$\mathbf{0} = \nabla_{\mathbf{p}} \times \left(\nabla_{\mathbf{p}} \gamma(\mathbf{p})\right) \ .$$

Chapter 4: In this chapter, we investigate more specific aspects of the collective transport: the multi-species transport, submitted to phase-space discontinuities. We refer here to the kinetic transport of different species of particles, having positive and negative charges, and an arbitrary mass ratio. Such physics can be applied, in particular, to electron-ion or electron-positron plasmas. We perform a numerical convergence analysis of a high order (second order) Finite Volume scheme for the Vlasov-Poisson system, and show the efficiency of the method for discontinuity handling on a relevant test case, with two populations and with an intermediate mass ratio

$$1 \leq \frac{m_1}{m_2} \leq 1836 \ .$$

Chapter 5: It is devoted to the multi-scale physics of electron transport with collision source terms, in the $2D_{\mathbf{x}} \times 3D_{\mathbf{v}}$ phase space. We validate the accuracy of a fast Monte Carlo multigrid solver for the Fokker-Planck-Landau electron-electron collision operator in a wide range of regimes relevant for ICF physics, ranking from collisional to rarefied, and from unmagnetized to magnetized regimes. The multigrid method is known as being well-suited for FPGA-based acceleration, and could be used efficiently on parallel, reconfigurable hardware architectures (RCS). We present the numerical method, the multigrid acceleration algorithm, and a selection of simple though representative numerical tests, that could serve as reference tests to check the collisional transport with the reduced models presented in Chapter 2.

Chapter 6: It is devoted to realistic simulations for the kinetic electron transport in the frame of the shock ignition scheme. This scheme is an official candidate, in the HiPER European project specifications, for the nominal ignition scheme of this future high repetition rate installation. A shock ignition campaign is currently (2009) tested experimentally on the OMEGA laser at the Rochester University, and has proved to produce an enhanced neutron yield at a given input energy, compared to classical ICF ignition schemes. This scheme is still, at the present date, under debate. The investigation and control of kinetic aspects related to the electron transport is one of the major identified bottleneck for a successful scheme. The proposed Kinetic Electron Transport for Shock Ignition simulation project (with acronym KiTSI) has been the object of a specific need for computational ressources. Indeed, more than 8 million processor hours have been obtained from the GENCI organism, that manages the computational ressources in France since 2008. This project is a joint collaboration with X. Ribeyre, M. Lafon, G.

Schurtz, E. D'Humières, S. Weber from CELIA, the teams of R. J. Kingham at Imperial College, A. R. Bell at the Rutherford Appleton Laboratory and the Oxford University.

Chapter 7: It is devoted to the development and validation of a reduced $M1$ electron transport angular model, together with the development of a relevant HLLC numerical method. The Minimum Entropy $M1$ closure for electrons [3] can be derived in the following way. To close the system we determine a distribution function f_{ME} that minimizes the entropy of the electrons,

$$H(f) = -\int_{S^2} f \log f d\Omega, \tag{1.3}$$

under the constraint that it reproduces the lower order moments,

$$\int_{S^2} f_{ME} d\Omega = f_0 \equiv \int_{S^2} f d\Omega \quad \text{and} \quad \int_{S^2} \mathbf{\Omega} f_{ME} d\Omega = \mathbf{f_1} \equiv \int_{S^2} \mathbf{\Omega} f d\Omega \, . \tag{1.4}$$

This closure is well-suited to electron transport because it allows analytical calculations of the collision kernels, in the relativistic and non-relativistic regimes. Both the model and the numerical method possess the appropriate flux limitation $\|\mathbf{f_1}\| \leq f_0$, positiveness $f_{ME} \geq 0$, and adequate conservation properties. Moreover we are able to treat exactly beams, as well as isotropic distribution functions. These features make the multi-group version of this model be well suited for relativistic laser-plasma interactions, in the collisional and collective regimes. The model and associated numerical schemes are tested in these two regimes. A parallel is drawn between ICF and radiotherapy electron transport. In particular, we insist on the importance of secondary electron production in radiotherapy applications. This process is investigated in detail in the Chapter 8.

Chapter 8: In this chapter, we investigate the relative importance of the processes involving electron-electron collisions at high energy. We bring the evidence of importance of secondary electron production at relativistic energy. To do so, we propose a fast and robust, multi-scale reduced model, with relativistic Boltzmann terms, that is expected to be more accurate than the present models by several orders of magnitude. *This model constitutes a simplification, though very general, of the relativistic, or nonrelativistic, Boltzmann equation*

$$\frac{\mathrm{d}}{\mathrm{d}t} f(\mathbf{p}) = \int_{\mathbb{R}^3} d^3 q \int_{S^2} d\tilde{\mathbf{\Omega}}' \; [f(\mathbf{p}')f(\mathbf{q}') - f(\mathbf{p})f(\mathbf{q})] \; \tilde{u} \, \frac{\tilde{W}^2}{W_p W_q} \, Q(\tilde{p}, \tilde{\mu}) \, .$$

In particular, it generalizes and encompasses the works from L. D. Landau (1940-ies), S. T. Beliaev (1956), and A. V. Gurevich (1998), on electron-electron collisions, with the long-range Coulomb potential

$$V_i = \sum_{j \neq i} \frac{q_j}{|r_{ij}|} \, .$$

One important step, in the derivation of the model, is to decompose the $1/r$ dependence of the potential with a smoothing potential $\mathcal{S}$

$$\frac{1}{r} = \left(\frac{1}{r} - \mathcal{S}(r) \right) + \mathcal{S}(r)$$

The main result of this model lies in its robustness, with a suitable choice for the $\mathcal{S}$ function. Also, a lot of attention is paid on the future numerical implementation of this model. Potential applications reach the HiPER European project for Fast Ignition, the fields of electron lithography, radiography of dense and opaque object, energetic events in the upper atmosphere, discharge plasmas, or creation of electron-positron plasmas.

Chapter 9: Conclusion and long term perspectives.

Bibliography

[1] Betti R., Zhou C. D., Anderson K. S., Perkins L. J., Theobald W. and Solodov A. A., *Shock ignition of thermonuclear Fuel with High Areal Density*, Physical Review Letter, 98, 155001, (2007).

[2] Bolton et al., Ultra-relativistic electrons in Jupiter's radiation belts, *Letters to nature*, Vol. 415, (2002).

[3] Brunner T. A., Holloway J. P., One dimensional Riemann solvers and the maximum entropy closure. J. Quant. Spectrosc. Radiat. Transfer, Volume **69**, pp 543-566, *J. Quant. Spectrosc. Radiat. Transfer*, Paris (2001).

[4] Buet C., Cordier S., *Numerical analysis of conservative and entropy schemes for the Fokker-Planck-Landau equation* , Numer. Anal. 36, 953-97, (1999).

[5] Buet C., Cordier S., Degong P., Lemou M., *Fast algorithm for numerical, conservative and entropy approximation of the Fokker-Planck-Landau equation* , J. Comput. Physics 133 310-322, (1997).

[6] Buet C., Cordier S., Filbet F., *Comparison of numerical scheme for Fokker-Planck-Landau equation* , ESAIM Proc. 10 161-181, (1999).

[7] Crouseilles N., Filbet F., *Numerical approximation of collisional plasmas by high order methods*, Journal of Computational Physics, 201, 546-572, (2004).

[8] Dautray R., Watteau J. P., *La fusion thermonucléaire Inertielle par Laser*, Collection du CEA, série synthèse, Eyrolles, Paris, (1993).

[9] Degond P., Lucquin-Desreux B., *An entropy scheme for the Fokker-Planck collision operator of plasma kinetic theory*, Numer. Math. 68, 239-262 (1994).

[10] Degond P., Lucquin-Desreux B., *The Fokker-Planck asymptotics of the Boltzmann equation in the Coulomb case*, M3AS, 2, 167-182 (1992).

[11] Delcroix J.-L., Bers A., Physique des plasmas, Volume **1**, *Savoirs actuels, InterEditions/CNRS Editions*, Paris (1994).

[12] Delcroix J.-K., Bers A., Physique des plasmas, Volume **2**, *Savoirs actuels, InterEditions / CNRS Editions*, Paris (1994).

[13] Dellacherie S., Contribution à l'analyse et à la simulation numérique des équations cinétiques décrivant un plasma chaud. *PhD thesis from Univ. Denis Diderot Paris VII, CEA BIII*.

[14] Duclous R., Dubroca B. Martin F., Deterministic Partial Differential Equation Model for Dose Calculation in Electron Radiotherapy, *submitted*, (2009).

[15] Eriksson L.-G., Helander P., Andersson F., Anderson D., Lisak M. (2004). *Current Dynamics during Disruptions in Large Tokamaks*, Physical Review Letter, 92, 20.

[16] Eriksson L.-G. and Helander P. (2003). *Simulation of runaway electrons during tokamak disruptions*, Computer Physics communications, 154, 175.

[17] Gerstner, The hybrid returns, Nature, Vol. 460, 2, 2009.

[18] Gonzáles M., Contribution à l'étude numérique de l'hydrodynamique radiative: des expériences de chocs radioatifs aux jets astrophysiques, PhD thesis of Paris-Sud XI Univ, (2006).

[19] Gurevich A. V., Zybin K. P., and Roussel-Dupré R., *Kinetic equation for high energy electrons in gases*, Phys. Lett. , A 237, 240, (1998).

[20] Kruer W. L., The Physics of Laser Plasma Interactions, *Frontiers in Physics*, Volume **73**, Westview Press, Colorado (2003).

[21] Laval G., Physique des Plasmas, edited by Dautray R. and Watteau J.-P., *la fusion thermonucléaire inertielle par laser*, Partie 1, l'interaction laser-matière, Volume **1**, Eyrolles, Paris (1993).

[22] Lifshitz E. M. and Pitaevskii L. P., Physical Kinetics, *Course in theoretical physics*, Volume **10**, Butterworth-Heinemann, Oxford (2006).

[23] Lindl J. D., Inertial Confinement Fusion, *The quest for Ignition and Energy Gain Using Indirect Drive*, ISBN 1-56396-662-X, Springer-Verlag, (1998).

[24] Matzen M. K., *Phys. Plasmas* **4** 1519 (1997).

[25] Melhorn T. A. et al., Recent experimental results on ICF target implosions by Z-pinch radiation sources and their relevance to ICF ignition studies, *Plasma Phys. Control. Fusion* Volume **45**, A325-A334 (2003).

[26] Mora P., Pellat R., Ponderomotive effects and magnetic field generation in radiation plasma interaction, *Physics of Fluids*, Volume **22**, 2408 (1979).

[27] Ribeyre X., Schurtz G., Lafon M., Galera S., and Weber S. , *Shock ignition: an alternative scheme for HiPER* , Plasma Phys. Control. Fusion 51 015013, (2009).

[28] Sanford T. W. L. et al, *Phys. Rev. Lett.* **77** 5063 (1996).

[29] Shkarofsky I. P., Johnston T. W. and Bachynski M. P., *The Particle Kinetics of Plasmas*, Addisson-Wesley Publishing Company, Reading, Massachusetts (1966).

1.3 Appendix: Glossary

In this appendix, we gather several conventions that we use thourough this document.

Table 1.1: Glossary

Quantity	denomination	Units (S.I.)
m_e	electron mass	kg
k_B	Boltzmann constant	$J.K^{-1}$
T_e (without k_B)	electron temperature	K
k_BT_e	electron temperature	J
ϵ_0	vacuum permittivity	$F.m{-}1$
c	speed of light	$m.s^{-1}$
e	positive electron charge	C
$q_e = -e$	signed electron charge	C
n_e	electron density	m^{-3}
γ_p	Lorentz factor for the particle of momentum $\mathbf{p}$	A.U.
n_c	Critical density	m^{-3}
$k\lambda_{ei}$	Effective Knudsen number	A. U.
R_N	Nernst number	A. U.
θ	Scattering angle in the center of mass (CM) frame	A. U.
$\tilde{p}$	Momentum of a particle after collision in the CM frame	A. U.
$\tilde{p}'$	Momentum of a particle before collision in the CM frame	A. U.

Chapter 2

Basic theory & processes relevant for the electron kinetic transport in the plasma physics

The object of the kinetic theory of gases or plasmas is the statistical description of the particles, by means of their distribution function $f(t, \mathbf{x}, \mathbf{v})$ in the phase space of the particules, that contains positions $\mathbf{x}$ and velocities $\mathbf{v}$, or momenta $\mathbf{p}$, the latter set is more adapted in the relativistic regime and for quantum plasmas.

When faced to a more complex physics, one may want to extend this phase space and add extra microscopic variables, accounting for non-translational degrees of freedom of the particules. These refer to the number of components in a mixture, the internal energy, the spin, *etc*. This can be a case for the plasma-assisted combustion, where chemical reactions occur, or for quantum plasmas where the spin must be taken into account.

However, one may rather be interested, and this is generally the case in the context of energy transport and deposition for ICF, in a reduction of such a space. The full numerical treatment of the particle distribution function in this six-dimensional space is traditionally considered too costly to be effective. Several approaches, outlined in Section 2.2.6 and Chapter 7, have been developped to retain only the most important features of this distribution function. Despite of their computational efficiency, the accuracy remain difficult to preserve in regimes of interest for fusion devices, with respect to the numerical noise or a low anisotropy degree that these methods may present. There is a need for a qualification procedure of these simplified methods for particular applications. The present thesis is dedicated to the development of a reference Fokker-Planck-Landau code, that can be considered noise-free and capable to treat high anisotropy degree. We consider it as a step towards a versatile validation tool. On the one hand, an accurate definition of the validity limits of reduced codes can be acheived. On the other hand, clear indications could be provided if and where further modelling improvements are needed.

The need for kinetic modeling for plasma physics becomes a clear issue when confronted with the variety of experimental measurements that display compelling energy and pitch angle-related spatial and/or temporal dispersion, and various types of highly non-Maxwellian features in the distribution functions. Some important aspects of the collisional kinetic theory are first summarized in Section 2.1. Then we give in Section 2.2 an overview of the processes relevant for ICF electron transport issues, that justify a full kinetic description of plasmas far from the statistical equilibrium.

2.1 Collisional kinetic theory of plasmas

A detailed representation, including the movement and interactions of all particules that constitute plasma is out of range of the state-of-the-art simulation capabilities and computational ressources. Moreover, such a treatment carries a huge amount of information that is not necessary to understand and simulate the overall dynamics of the plasma. A semi-microscopic, probabilistic evaluation of the system is sufficient: this approach constitutes the collisional kinetic theory of plasmas.

From the Liouville master equation, a hierarchy of models is constructed. We recall, in the next section, a derivation procedure of this so-called BBGKY (Born-Bogolioubov-Green-Kirkwood-Yvon) hierarchy. Different limits are outlined in Sections 2.1.2 and 2.1.5, respectively the Vlasov and the Boltzmann equations .

2.1.1 Kinetic equation for a single-particle distribution function

Let us consider, at time t, an ensemble of N particles of the same specie, having the positions $\mathbf{x}_{i\in[1,N]}$ and momenta $\mathbf{p}_{i\in[1,N]}$. A N-body joint-probability density is introduced [73]

$$f_N\left(t\ ,\ \mathbf{x}_1,\ \ldots, \mathbf{x}_N\ ,\ \mathbf{p}_1,\ \ldots, \mathbf{p}_N\right)\ ,$$

where $f_N d^3x_1...d^3x_N d^3p_1...d^3p_N$ is the probability for the system to be, at time t, in the elementary $6N{-}D$ volume $d^3x_1...d^3x_N d^3p_1...d^3p_N$., located in the neighbourhood of the point $\mathbf{x}_1,\ \ldots, \mathbf{x}_N\ ,\ \mathbf{p}_1,\ \ldots, \mathbf{p}_N$. In other words, this quantity represents the probability of the particule 1 to be inside the volume d^3x_1 around $\mathbf{x}_1$, with a momemtum whose extremity is around the volume d^3p_1 in the momentum space, around $\mathbf{p}_1$, where in the same time the particule 2 is inside the volume d^3x_2 around $\mathbf{x}_2$, with a momemtum whose extremity is around the volume d^3p_2 around $\mathbf{p}_2$, and so forth until the particle N. The Liouville equation expresses the conservation of this probability density while particles are moving in space and time

$$\frac{\mathrm{d}f_N}{\mathrm{d}t} = \frac{\partial f_N}{\partial t} + \sum_{i=1}^{i=N}\mathbf{v}_i\frac{\partial f_N}{\partial \mathbf{x}_i} + \sum_{i=1}^{i=N}\mathbf{X}_i\frac{\partial f_N}{\partial \mathbf{p}_i} = 0\ , \tag{2.1}$$

where $\mathbf{v}_i = \dfrac{\mathrm{d}\mathbf{x}_i}{\mathrm{d}t}$ and $\mathbf{X}_i = \dfrac{\mathrm{d}\mathbf{p}_i}{\mathrm{d}t}$; $\mathbf{v}_i$ are the velocity of the particle i and the force applied to that particule, respectively.

The N-body distribution function f_N describes the system with a maximum level of refinement. Practically, the computation of such a model is too heavy, and one has to consider a more stringent statistic resolution. To this aim, the reduced s-body joint-probability density is introduced for a sub-system of $s < N$ particles

$$\tilde{f}_s\left(t, \mathbf{x}_1, ..., \mathbf{x}_s\ ,\ \mathbf{p}_1, ..., \mathbf{p}_s\right) \equiv \int f_N\left(t, \mathbf{x}_{s+1}, ..., \mathbf{x}_N, \mathbf{p}_{s+1}, ..., \mathbf{p}_N\right) d^3x_{s+1}...d^3x_N d^3p_{s+1}...d^3p_N\ .$$

This distribution function describes the s-particle state of a group of N particles. As in the general case, $\tilde{f}_s$ is not a symmetric function of its arguments, a symmetric s-body joint-probability density is constructed

$$f_s\left(t\ ,\ \mathbf{x}_1,\ \ldots, \mathbf{x}_s\ ,\ \mathbf{p}_1,\ \ldots, \mathbf{p}_s\right) \equiv \frac{1}{s!}\sum_{P(1,\ldots,s)}\tilde{f}_s\left(t\ ,\ \mathbf{x}_1,\ \ldots, \mathbf{x}_s\ ,\ \mathbf{p}_1,\ \ldots, \mathbf{p}_s\right),$$

where the sum is over the permutations P of particules $1, ..., s$. The normalization is

$$\int f_s\left(t\ ,\ \mathbf{x}_1,\ \ldots, \mathbf{x}_s\ ,\ \mathbf{p}_1,\ \ldots, \mathbf{p}_s\right) d^3x_1...d^3x_s d^3p_1...d^3p_s = 1.$$

It is more appropriate to introduce the s-tuple distribution function $\mathbb{F}_s \equiv \dfrac{N!}{(N-s)!}f_s$, that represents the probable number of s-tuples of identical particules such that one of the particle is in the phase volume $\mathrm{d}^3x_1\mathrm{d}^3p_1$ about the point $(\mathbf{x}_1, \mathbf{p}_1)$, the other one is in the phase volume $\mathrm{d}^3x_2\mathrm{d}^3p_2$ about the point $(\mathbf{x}_2, \mathbf{p}_2)$, and so forth, at a given time. The average kinetic and potential energies of particles, E_K and E_Φ are defined with the $\mathbb{F}_1$ and $\mathbb{F}_2$ functions [73]

$$E_K(t, \mathbf{x}) = \int \mathbb{F}_1(t, \mathbf{x}, \mathbf{p}) mc^2(\gamma_p - 1)\mathrm{d}^3p\ ,$$

$$E_\Phi(t, \mathbf{x}) = \int \mathbb{F}_2(t, \mathbf{x}, \mathbf{x}', \mathbf{p}, \mathbf{p}')\Phi_{12}\left(\mathbf{x}, \mathbf{x}'\right)\mathrm{d}^3p\mathrm{d}^3p'\mathrm{d}^3x'\ ,$$

where $\Phi_{12}(\mathbf{x}, \mathbf{x}')$ is the two-particle interaction potential and $\gamma_p = \sqrt{1 + p^2/(mc)^2}$ is the relativistic Lorentz factor.

The evolution equation for the distribution function $\mathbb{F}_1$, calculated from the Liouville equation (2.1), is the BY_1 equation

$$\frac{\partial \mathbb{F}_1}{\partial t} + \mathbf{x}_1 \frac{\partial \mathbb{F}_1}{\partial \mathbf{v}_1} + \mathbf{X}_1 \frac{\partial \mathbb{F}_1}{\partial \mathbf{p}_1} = -\int \mathbf{X}_{12} \frac{\partial \mathbb{F}_2}{\partial \mathbf{p}_1} \mathrm{d}^3 x_2 \mathrm{d}^3 p_2 \,, \tag{2.2}$$

where $\mathbf{X}_{12}$ represents the force acting on the particule 1 due to the particule 2.
By successive couplings, the equations BY_i, $i \in \mathbb{N}^*$, that relate the functions $\mathbb{F}_i$ and $\mathbb{F}_{i+1}$, can be constructed. The obtained system is refered as the BBGKY system. In [76], it is shown that the BBGKY hierarchy of a plasma with electrostatic interactions inherits a Lie algebra stucture, with Poisson brackets, from the Liouville equation.
From this sytem, different asymptotic regimes can be identified.

2.1.2 Vlasov kinetic equation

A renormalization of the $\mathbb{F}_s$ functions can be performed on the BY_s equations, that defines the distribution function $f(\mathbf{x}, \mathbf{p}) \equiv n_0 \mathbb{F}_1(\mathbf{x}_1, \mathbf{p}_1)$, dropping the subscript 1. With the assumption of $N \gg s$, the dimensionless form of the BY_s equation is derived, that make appear, right in these equations, the parameters [73]

$$\alpha_0 \equiv \frac{\Phi_0}{k_B T} \quad , \quad \mathcal{N}_0 \equiv n_0 r_0^3 \quad , \quad \mathcal{N}_0 \alpha_0 = \frac{\left(n_0 r_0^3\right)^2 \Phi_0}{n_0 r_0^3 k_B T} \simeq \frac{\langle E_\Phi \rangle}{\langle E_K \rangle} \quad ,$$

where Φ_0 is a potential, k_B -the Boltzmann constant, T -the temperature, n_0 -a characteristic number density, and r_0 -a characteristic scale length.

In the limit $\mathcal{N}_0 \alpha_0 \geq 1$, the plasma can be seen as strongly coupled, whereas in the limit $\mathcal{N}_0 \alpha_0 \ll 1$, it is weakly coupled. This partitionning is exploited to reduce the *BBGKY* system, with the help of a set of correlation functions. The correlation function between two particles, C_2, is defined according to the relation

$$f_2 = f_1 f_1 + C_2 \,.$$

By analogy, we can define C_3 such as

$$f_3 = f_1 f_1 f_1 + \sum_{P(1,2,3)} f_1 C_2 + C_3 \,,$$

and so on for the family $\{C_i\}_{i<N}$.

The Vlasov limit is obtained assuming $\Phi_0/(k_B T) \ll 1$, *i.e.* small correlations between particles, and long-range interactions, $n_0 r_0^3 \gg 1$. In this limit, a small parameter ϵ can be defined, with the following renormalization $\alpha \to \epsilon\alpha$ and $\mathcal{N}_0 \to \epsilon \mathcal{N}_0$. The first condition allows to redefine the correlation functions as

$$\begin{aligned} f_2 &= f_1 f_1 + \epsilon C_2 \,, \\ f_3 &= f_1 f_1 f_1 + \epsilon \sum_{P(1,2,3)} f_1 C_2 + \epsilon^2 C_3 \,. \end{aligned}$$

If only the lowest $O(\epsilon)$ terms are kept in the BBGKY system, then the limit is the self-consistent Vlasov equation

$$\left(\frac{\partial}{\partial t} + \frac{\partial}{\partial \mathbf{x}} \cdot \mathbf{v} + \frac{\partial}{\partial \mathbf{p}} \cdot \mathbf{X}\right) f(t, \mathbf{x}, \mathbf{p}) = 0\,, \tag{2.3}$$

which is here written under its conservative form. Its non-conservative form is equivalent, as $\dfrac{\partial}{\partial \mathbf{p}} \cdot \mathbf{X} = 0$. The particle density is defined as $n = \displaystyle\int_{\mathbb{R}^3} f(t, \mathbf{x}, \mathbf{p}) d^3 p$, and the effective temperature as $\dfrac{3}{2} n k_B T = \displaystyle\int_{\mathbb{R}^3} f(t, \mathbf{x}, \mathbf{p}) \frac{p^2}{2m} d^3 p$.

The Vlasov equation (2.3) is not a generic hyperbolic scalar equation, because of its Hamiltonian geometric structure. It satisfies, in particular, an infinite set of conservation laws, the Casimir invariants. This Hamiltonian structure gets lost by any numerical approximation [58], and a major challenge in numerical analysis is to design schemes that preserve at least the low order Casimir invariants. The purpose of high order schemes, as shown in Chapter 3, is to control the dispersive and diffusive artefacts triggered by any "finite dimension" numerical approximation [8].

2.1.3 Self-consistent coupling to the Maxwell equations

The model (2.3) is now applied to charged particles, and completed with a definition of a microscopic electromagnetic force $\mathbf{X}_i + \displaystyle\sum_{j=1}^{j=N} \mathbf{X}_{ij}$, where

$$\mathbf{X}_i = q_i \left(\mathbf{E}^{ext} + \mathbf{v}_i \times \mathbf{B}^{ext}\right)\,,$$

$$\mathbf{X}_{ij} = -\nabla_i \left(\frac{q_i q_j}{4\pi\epsilon_0 r_{ij}}\right)\,,$$

that accounts for the external fields and interactions between the particles. Then it is possible to define the self-consistent electric field as $\mathbf{E}^{sc} = \displaystyle\int_{\mathbb{R}^3} n_2 \mathbf{X}_{12} \mathrm{d}^3 x_2$. Inserting this expression in the BY_1 equation, this leads to a full Lorentz force $\mathbf{X} = q_i \left(\mathbf{E} + \mathbf{v} \times \mathbf{B}\right)$ in the Vlasov equation, where $\mathbf{B} = \mathbf{B}^{sc} + \mathbf{B}^{ext}$, $\mathbf{E} = \mathbf{E}^{sc} + \mathbf{E}^{ext}$, and $\mathbf{B}^{ext}$, $\mathbf{E}^{ext}$ are the external fields.

While considering the Coulomb interaction potential between electrons $\Phi_0 = e^2/(4\pi\epsilon_0 r)$ in a neutralizing fixed ion background, the Vlasov natural regime $\alpha_0 \mathcal{N}_0 = O(1)$, defines a caracteristic length, the Debye length $\lambda_D \equiv \sqrt{\dfrac{\epsilon_0 k_B T_e}{n_0 e^2}}$, that is a distance, where a significant charge separation can occur. The plasma period stands as the characteristic response time of the plasma to any perturbation screened by the Debye length. It is defined as $t_{pe} \equiv 2\pi/\omega_{pe}$, where $\omega_{pe} \equiv v_{th}/\lambda_D$ is the plasma period frequency and $v_{th} \equiv \sqrt{k_B T_e/m_e}$ is the thermal velocity. The condition of plasma neutrality $n_e = Z n_i = n_0$ is the necessary condition for plasma equilibrium in the absence of external forces.

The Lorentz force relates the Vlasov equation with the Maxwell equations

$$\begin{cases} \dfrac{\partial \mathbf{E}}{\partial t} - c^2\,\nabla_{\mathbf{x}} \times \mathbf{B} \;=\; -\dfrac{\mathbf{J}}{\epsilon_0}, \\[2ex] \dfrac{\partial \mathbf{B}}{\partial t} + \nabla_{\mathbf{x}} \times \mathbf{E} \;=\; 0, \end{cases} \tag{2.4}$$

where ϵ_0 represents the permittivity of vacuum, c is the speed of light. The electric current is given by

$$\mathbf{J}(t,\mathbf{x}) \;=\; q_e \int_{\mathbb{R}^3} f_e(t,\mathbf{x},\mathbf{p})\,\mathbf{v}\,d^3p.$$

Moreover, the Maxwell system is supplemented by the Gauss laws

$$\nabla_{\mathbf{x}} \cdot \mathbf{E} \;=\; \frac{\rho}{\epsilon_0}, \quad \nabla_{\mathbf{x}} \cdot \mathbf{B} \;=\; 0, \tag{2.5}$$

where ρ is the charge density:

$$\rho \;=\; q_e\,(n_e - n_o) \;=\; q_e \left(\int_{\mathbb{R}^3} f_e(t,\mathbf{x},\mathbf{p})\,d^3p \;-\; n_0 \right),$$

and n_0/Z is the initial ion density.

2.1.4 Linear analysis of the free-transport system

Waves in a plasma, if it is collisionless, are described with the Vlasov-Maxwell system. These waves give insight on the collective movements within this plasma. They can be caracterized by

- A dispersion law $\omega(\mathbf{k})$, if it is analytically available.
- Its polarisation, *i.e.* the angle $(\mathbf{E},\mathbf{k})$.
- Its energy.

in a plasma, the electromagnetic energy is defined as

$$W_{wave} = W_{vacuum} \frac{\partial(\omega Re[\epsilon(\omega,\mathbf{k})])}{\partial \omega} \,, \tag{2.6}$$

$$W_{vacuum} = \frac{\epsilon_0 E_0^2}{4} \,, \tag{2.7}$$

where ϵ is the dielectric permittivity. This formalism permits the treatment of waves having negative energy. The Poynting vector $\mathbf{S}$ reads

$$\mathbf{S} = W_{vacuum} \frac{\partial(\omega Re[\epsilon(\omega,\mathbf{k})])}{\partial \mathbf{k}} \,, \tag{2.8}$$

$$\mathbf{S} = W_{wave} \mathbf{v_g} \,, \tag{2.9}$$

$$\mathbf{v_g} = \frac{\partial \omega}{\partial \mathbf{k}} \,. \tag{2.10}$$

A criteria for the stability of the plasma can be defined

$$Im(\omega) < 0 \,, \tag{2.11}$$

that guarantees the positivity of the energy.

Instability classifications

The natural response of plasma exposed to a (fast) electron current, is to maintain the charge neutrality. This behaviour induces a configuration where two counterstreaming beams inter-penetrate. This situation can be an origin for various instabilities, that are potential candidates to inhibit/enhance the transport of the incident electron beam, having velocity $\mathbf{V}_b$. The Two-Stream Instability is defined for electrostatic perturbations with a wave vector $\mathbf{k}$ such as $\mathbf{k} \parallel \mathbf{V}_b$ and $\mathbf{k} \parallel \delta\mathbf{E}$, where $\delta\mathbf{E}$ is the created electric field. We shall identify the Weibel instability as an electromagnetic instability for transverse modes, triggered from a distribution function which presents a temperature anisotropy, but satisfies $\dfrac{\partial f_0}{\partial v} > 0$ at each point. This definition matches the definition from Weibel's original paper. On the other hand, the filamentation instability concerns the distribution function whose original shape presents $\dfrac{\partial f_0}{\partial v} < 0$ for a subensemble of points (in between two beam distribution functions, for instance), and may trigger electromagnetic or electrostatic modes, depending on the orientation of the wave vector $\mathbf{k}$ with respect to the beam velocity $\mathbf{V}_b$, in the plane perpendicular to the magnetic field perturbation $\delta\mathbf{B}$. Several confusing and divergent definitions emerge in the literature, and we found a clarification necessary at that point.

Let us assume a homogeneous, spatially infinite, collisionless and unmagnetized plasma, whose dynamics is ruled by the nonrelativistic Vlasov-Maxwell equations. Ions are supposed to form a fixed neutralizing background, while electrons have two components: cold and a beam. Within the linear approximation, the plasma response to the harmonic perturbation of the electric field $\mathbf{E}(\omega, \mathbf{k})$ is described by the tensor of dielectric permittivity , whose tensor elements are

$$\epsilon_{\alpha\beta}(\omega, \mathbf{k}) = \delta_{\alpha\beta}\left(1 - \frac{\omega_{pe}^2}{\omega^2}\right) + \frac{\omega_{pe}^2}{\omega^2}\int_{\mathbb{R}^3} v_\alpha v_\beta \frac{\mathbf{k}\cdot\frac{\partial f_0}{\partial \mathbf{v}}}{\omega - \mathbf{k}\cdot\mathbf{v}} \mathrm{d}^3 v \,.$$

The systematic study of the space-time evolution of an instability, though complex in this Fourier-Laplace space, requires the knowledge of the Green's function of the medium [46]. In one dimension, for the longitudinal perturbation, the Green function reads

$$G(x,t) = \int_L \frac{\mathrm{d}\omega}{2\pi}\int_F \frac{\mathrm{d}k}{2\pi}\frac{\exp(ikx - i\omega t)}{\epsilon(\omega, \mathbf{k})} \,,$$

where $\epsilon(\omega, \mathbf{k}) = 0$ is the dispersion relation of the system, and the Fourier (F) and Laplace (L) contours are chosen such as they satisfy the causality principle and convergence of the integral.

The classification of two-stream instabilities can then be performed with respect to their time-asymptotic behaviour, that can be evaluated with the complex pinch-points (ω_0, k_0), solution of a a system of equations

$$\epsilon(\omega, \mathbf{k}) = 0 \quad , \quad \frac{\partial \epsilon}{\partial k}(\omega, \mathbf{k}) = 0 \,.$$

Finally, the asymptotic behaviour may be deduced:

$$G(x, t \to \infty) \sim \exp(ik_0 x - i\omega_0 t)/t^{1/2} \,.$$

The instability is defined as *absolute* if $\mathrm{Im}(\omega_0) > 0$ [46]. In this case the time-asymptotic behaviour is dominated by the pinch-point with the largest positive $\mathrm{Im}(\omega_0)$. The instability is defined as *convective* if all pinch points satisfy $\mathrm{Im}(\omega_0) < 0$.

Critical comparison of different linear analysis in the relativistic regime

The Vlasov-Maxwell system, describes a variety of multi-scale coupled processes. The first step consists in isolating and analysing each of them. The analytical representative solutions are desirable to validate our numerical schemes.

In a recent publication [14], a linear analysis relying on the dispersion equation of the Vlasov-Maxwell system, valid for any orientation of the wave-vector of the perturbation, provides a detailed picture of the hierarchy of competing modes in the system-parameter space. In particular, the authors are able to treat oblique perturbations, and give insight into the transition that may occur from one mode to another one. However such a method, relying on dispersion relations, is efficient for a limited class of distribution functions that lead to simple singularities in the dispersion equation, in the $(\mathbf{k}, \omega)$ complex plane. This approach, detailed in [15], does not give information in the time evolution of the macroscopic quantities in the linear regime, and is valid only for the limit of large phase velocities $||\mathbf{k}||V/\omega \ll 1$, where V is a characteristic velocity of particules. A set of well-defined eigen-frequencies (modes) is then selected among the variety of possible solutions. Moreover, when back to the physical space, only exponential modes, $\propto \exp(-\omega t)$, are filtered. Non-exponential solutions are much more difficult to find and to characterize. *Although they may bring an important contribution*. Another method is proposed in [87], where a nonlinear eigenvalue problem is solved. This method is worth noticable, because it may potentially address more complex collision terms, such as the Fokker-Planck one, coupled to the Maxwell's equations. Such situations could occur in regimes where the collision frequency becomes comparable to the plasma frequency. However, this technique still smoothes out non-exponential modes that may arise, and does not have the time resolution of the instability in the linear regime.

This deficiency can be illustrated the following way, as explained by B. Wu in [120]: let us consider the non-relativistic Vlasov-Poisson system, with a constant magnetic field $\mathbf{B_0}$. The initial quantities are chosen such as

$$f(t=0,\mathbf{x},\mathbf{p}) = f_0(p) + f_1(t=0,\mathbf{x},\mathbf{p}), \tag{2.12}$$

$$\mathbf{E}(t=0,\mathbf{x}) = \mathbf{E_1}(t=0,\mathbf{x}), \tag{2.13}$$

$$f_1 \ll f_0. \tag{2.14}$$

A Fourier series expansion gives $\forall t > 0$

$$f_1(t,\mathbf{x},\mathbf{p}) = \hat{f}_1(t,\mathbf{p})\cos(\mathbf{k}\cdot\mathbf{x}), \tag{2.15}$$

$$\hat{f}_1(t,\mathbf{p}) = \frac{1}{V}\int_{\mathbb{V}} f_1(t,\mathbf{x},\mathbf{p})e^{-i\mathbf{k}\cdot\mathbf{x}}d^3x. \tag{2.16}$$

Then the linearized equation around the equilibrium state f_0, for the Fourier component $\mathbf{k}$, is

$$i\frac{\partial}{\partial t}\hat{f}_1(t,\mathbf{v}) = \mathcal{K}\hat{f}_1(t,\mathbf{v})\,, \tag{2.17}$$

$$\mathcal{K}\hat{f}_1(t,\mathbf{v}) = \mathbf{k}\cdot\mathbf{v}\hat{f}_1(t,\mathbf{v}) + i\frac{e}{m_e}(\mathbf{v}\times\mathbf{B_0})\cdot\frac{\partial}{\partial\mathbf{v}}\hat{f}_1(t,\mathbf{v}) - \eta(\mathbf{v})\int_{\mathbb{R}^3}\hat{f}_1(t,\mathbf{v})d^3v\,, \tag{2.18}$$

$$\eta(\mathbf{v}) = \frac{\omega_{pe}^2}{k^2}\mathbf{k}\cdot\frac{\partial}{\partial\mathbf{v}}f_0(\mathbf{v})\,. \tag{2.19}$$

The discrete complex eigenvalue and associated eigenfunction couples $(\omega_j, G_j)_{j\in\mathbb{N}} \in \mathbb{C}\times\mathbb{R}$ (we note here that the number of such couples can be infinite), are solution of the eigenvalue problem $\mathcal{K}G_j(\mathbf{v}) = \omega_j G_j(\mathbf{v})$. In particular, the discrete eigenvalues ω_j are solutions of the equations $\epsilon(\omega_j, \mathbf{k}) = 0,\ j \in \mathbb{N}$. Among them, only the real eigenvalues (they appear if $\mathbf{B_0} \neq \mathbf{0}$) have their eigenfunctions that depend on *arbitrary functions* $a_n(v_\perp, v_\|),\ n \in \mathbb{N}$. Therefore the spectrum of the operator $\mathcal{K}$ can be splitted in two parts: the first is continuous and real, the second is discrete and complex. The real eigenvalues are *uncountably infinitely degenerate* [120]. This breaks the relation between eigenfunctions and the usual Laplace resolvent solution where they can be considered as coefficients of $e^{-i\omega t}$. The spectrum obtained for an unstable plasma consists of a continuous straight line through the origin, suplemented with isolated eigenvalues away from this line (thus complex), and associated with unstable solutions of the usual dispersion relation [69].

In the Chapter 3, we illustrate the effects of real eigenvalues on the two-stream instability.

Another particular case where a set of real eigenvalues arise is the relativistic regime, where at least two branch points in the dispersion relation appear when Laplace transform technique is employed to solve the linearized Vlasov-Poisson system.

Finally, we present a method that does not face this problem of non-analiticity (because it does not rely on the ω Fourier space), and thus guarantees the correct time dependence in the linear regime, with a prescribed accuracy. This semi-analytical technique is issued from the work of C. Sartori and G. G. M. Coppa [100]. *The method is here extended to the self-consistent relativistic Vlasov-Maxwell system*, In Appendix 3.11. In the chapter 3, we shall make use of this procedure to validate our numerical schemes. In the paper [22], this method had been employed for external applied fields. An extention of this method with the inclusion of the simple Krook operator [23, 57] is straightforward.

2.1.5 Boltzmann equation

For a collisional plasma, the appropriate limit of the Liouville equation (2.1) is the Boltzmann equation, where the two-particle correlation function is taken into account. The Boltzmann limit can be introduced from the Liouville equation with different perturbation-expansion techniques, relying on diagrams (Prigogine), discrete description of the state of the system (Klimontovitch), or the introduction of truncated distribution function in the Liouville equation (Grad). These procedures can also be used to derive higher-order corrections to the Boltzmann equation, relevant to denser fluids. The rigorous mathematical derivation of the Boltzmann equation has only been investigated for the hard sphere model [116]. A rigorous justification in the case of long-range interactions between particles remains an open mathematical problem [24, 116].

In this section we present the fundamental assumptions that lead to the Boltzmann equation, upon which an heuristic derivation of the Boltzmann equation can be obtained.

- The interactions involving more than two particules are neglected. The gas is assumed to be dilute enough.
- The collisions are assumed to be localized in both space and time, with respect to the characteristic scales of the description.
- The collision is supposed to be elastic, *i.e.* the momentum, number of particles, and the energy are preserved in a collision process. Let $\mathbf{p}'$, $\mathbf{q}'$ stand for the momenta of the particles before the

collision, and $\mathbf{p}$, $\mathbf{q}$ those after collision. Let $\gamma_p \equiv \sqrt{1+\mathbf{p}^2/m_e^2c^2}$ be the Lorentz factor for the particule having momentum $\mathbf{p}$. The elastic conservation laws read

$$\mathbf{p}' + \mathbf{q}' = \mathbf{p} + \mathbf{q} \,,$$

$$\gamma_{p'} + \gamma_{q'} = \gamma_p + \gamma_q \,.$$

- Detailed balance principle: the probability for two particles having momenta $\mathbf{p}'$ and $\mathbf{q}'$ before collision to have the respective momenta $\mathbf{p}$ and $\mathbf{q}$ after the collision event, is the same as the probability for the reverse process.
- Boltzmann "one-sided chaos" assumption: the momenta of two particles which are about to collide are uncorrelated, contrary to the post-collision momenta of the particles.
- Galilean invariance.

With these assumptions, the Boltzmann operator can be derived. We refer to the physics-oriented references [26, 73], and mathematical-oriented references [2, 4, 32, 33, 49, 50, 51, 114], that address issues related to the relativistic Boltzmann equation, or some variants of it.

Its relativistic expression reads

$$\frac{\mathrm{d}}{\mathrm{d}t} f(\mathbf{p}) = \mathcal{Q}_{BO}(f,f) = \int_{\mathbb{R}^3} d^3q \int_{S^2} d\tilde{\mathbf{\Omega}}' \, [f(\mathbf{p}')f(\mathbf{q}') - f(\mathbf{p})f(\mathbf{q})] \, \tilde{u} \, \frac{\tilde{W}^2}{W_p W_q} \, Q(\tilde{p},\tilde{\mu}) \,, \tag{2.20}$$

where the $W_p = m_e c^2 \gamma_p$ is the total energy (including the energy at rest) of the particule with momentum $\mathbf{p}$. The quantities marked with tilde (respectively without tilde) refer to quantities in the center of mass frame (respectively, in the laboratory frame) for a collision event, except for the scattering angle in the center of mass frame, denoted by θ. Here, $\tilde{W}$ is the energy of colliding particles in the center of mass, $\tilde{\mu} = \cos\theta$ is the cosine of the interaction angle. $\tilde{u} = 2\tilde{p}c^2/\tilde{W}$ is the relative velocity. $v_M \equiv \tilde{u}\dfrac{\tilde{W}^2}{W_p W_q}$ is the Møller velocity. Having in view electron-electron Coulomb interactions, we shall consider the screened total relativistic Rutherford cross section Q [68].

A mixed canonical-dissipative expression for the irreversible processes described by the Boltzmann equation can be formulated, using the concept of dissipative bracket, and "suitable Langevin forces" [114].

Finally we present the fundamental properties of solutions of the homogeneous Boltzmann equation (8.6). They satisfy the conservation of mass, momentum and energy

$$\int_{\mathbb{R}^3} \frac{\mathrm{d}f}{\mathrm{d}t}(t,\mathbf{p}) \begin{pmatrix} 1 \\ \mathbf{p} \\ W_p \end{pmatrix} d^3p \;=\; 0, \;\; t \geq 0. \tag{2.21}$$

Moreover, the entropy is decreasing with respect to time

$$\frac{dH}{dt}(t) = \frac{d}{dt}\int_{\mathbb{R}^3} f \, \log f d^3p \;\leq\; 0, \;\; t \geq 0. \tag{2.22}$$

The equilibrium states f_{JS} of the Boltzmann operator (8.6) are the elements of its Kernel:

$$\mathcal{Q}_{BO}(f_{JS}, f_{JS}) = 0 \,.$$

These are the Jüttner-Synge (JS) distribution functions

$$f_{JS}(\mathbf{p}) = \frac{n_{JS}}{4\pi(m_e c)^3\beta_{th}^2\left(K_2\left(\beta_{th}^{-2}\right)\exp\left[\beta_{th}^{-2}\right]\right)}\exp\left[-(\gamma(\mathbf{p})-1)/\beta_{th}^2\right] , \tag{2.23}$$

where K_2 is the modified Bessel function of second order and second kind.
The extension of these equilibrium states from zero to non-zero drift velocity $\mathbf{V_d}$ can be obtained in the same manner, with an entropy maximum principle [74], together with the relativistic definition of the kinetic energy.

$$\begin{aligned} f_{JS}(\mathbf{p}) \quad = \quad & \frac{n_{JS}}{4\pi(m_e c)^3\gamma(\mathbf{V_d})\left[\tilde{\beta}_{th}^2 K_2\left(\tilde{\beta}_{th}^{-2}\right)\exp\left[\beta_{th}^{-2}\right]\right]} \times \\ & \exp\left(-\frac{\gamma(\mathbf{V_d})\left(\gamma(\mathbf{p}) - \frac{\mathbf{V_d}\cdot\mathbf{p}}{m_e c^2}\right) - 1}{\tilde{\beta_{th}}^2}\right) , \end{aligned} \tag{2.24}$$

where $\tilde{\beta}_{th}^2 = \gamma(\mathbf{V_d})\dfrac{k_B T_{JS}}{m_e c^2}$.
The detailed computation of the normalization coefficient is presented in Appendix 2.5. The relativistic Maxwellian probability density function for each component of momentum p_i can be found in Appendix 8.9.

2.1.6 Relativistic Rutherford scattering in a screened potential

For collision of like particles, such as the electron-electron scattering, one cannot distinguish between the electrons after the scattering event, in a probabilistic sense, even if they are affected a spin. This makes the cross sections to be symmetric with respect to interchange between themselves after a scattering, and they can be folded at the angle $\pi/2$.
In the first Born approximation, the non-folded relativistic Rutherford cross section Q [68], including relativistic effects and spin corrections, reads

$$\begin{aligned} Q(\tilde{p},\tilde{\mu}) \quad &= \quad Q_0 A(\tilde{p})\left(\frac{1}{\sin^4(\theta/2)} + \frac{1}{\cos^4(\theta/2)}\right) \\ &+ \quad Q_0 B(\tilde{p})\left(\frac{1}{\sin^2(\theta/2)} + \frac{1}{\cos^2(\theta/2)}\right) + Q_0 C(\tilde{p}) \,, \end{aligned} \tag{2.25}$$

where $Q_0 = (e m_e c)^4/(16\pi\epsilon_0\tilde{p}^2\tilde{W})^2$ and the momentum-dependent functions are

$$A(\tilde{p}) \quad = \quad \left(1 + \frac{2\tilde{p}^2}{m_e^2 c^2}\right)^2 , \tag{2.26}$$

$$B(\tilde{p}) \quad = \quad 1 + \frac{4\tilde{p}^2}{m_e^2 c^2} \,, \tag{2.27}$$

$$C(\tilde{p}) \quad = \quad \frac{2\tilde{p}^4}{m_e^4 c^4} \tag{2.28}$$

In the case of long-range Coulomb interactions, described with the Rutherford cross-section, a screening should be applied that removes the singularity in angle. This screening corresponds to a particular energy exchange (at the Debye length). We shall built, in chapter 8, upon the Boltzmann equation, an intermediate model that take advantage of this correspondance.

2.1.7 The Fokker-Planck-Landau equation: assumptions and limits of the model

Owing to the long-range nature of the Coulomb potential, the assumption of pitch-angle collision is traditionally retained as the dominant interaction mecanism that contributes to the kinetic properties of a plasma. Therefore a simplification of the Bolztmann equation (8.6) in the limit of small angle collisions is desirable. This procedure, in the relativistic regime, leads to the Beliaev-Budker operator [6]. This operator possesses the same conservation properties (mass, momentum and energy), entropy decreasing behaviour, and Jüttner-Synge equilibrium state, respectively equations (2.21), (2.22) and (2.23), as the relativistic Boltzmann equation (8.6).
The non-relativistic form of this operator is far more simple. This is the Fokker-Planck-Landau (FPL) operator, shown in equation (2.29), whose original derivation dates back to Landau [68], in 1936.

$$C_{FPL}(f,f) \;=\; \frac{e^4\,\ln\Lambda}{8\,\pi\,\epsilon_0^2\,m_e^2}\,\nabla_{\mathbf{v}}\cdot\left(\int_{\mathbb{R}^3}\Phi(\mathbf{v}-\mathbf{v}')\,[\,f(\mathbf{v}')\nabla_{\mathbf{v}}f(\mathbf{v})-f(\mathbf{v})\nabla_{\mathbf{v}'}f(\mathbf{v}')]\,\mathbf{dv}'\right). \tag{2.29}$$

Here $\ln\Lambda$ is the Coulomb logarithm [17, 59], defined as an integral over the scattering angles, that contains a Debye screening at small angles, due to the long-range nature of the Coulomb interaction, and $\Phi(\mathbf{u})$ is an operator perpendicular to the relative velocity $\mathbf{u}$

$$\Phi(\mathbf{u}) = \frac{||\mathbf{u}||^2\,\mathrm{Id}\;-\;\mathbf{u}\otimes\mathbf{u}}{||\mathbf{u}||^3}. \tag{2.30}$$

The FPL operator is used to describe binary elastic collisions between electrons. Its algebraic structure is similar to the Boltzmann operator, in that it satisfies the conservation of mass, momentum and energy

$$\int_{\mathbb{R}^3} C_{e,e}(f_e,f_e)(\mathbf{v})\begin{pmatrix}1\\ \mathbf{v}\\ ||\mathbf{v}||^2\end{pmatrix}\mathbf{dv} \;=\; 0,\;\; t\geq 0.$$

Moreover, the entropy is decreasing with respect to time

$$\frac{dH}{dt}(t) = \frac{d}{dt}\int_{\mathbb{R}^3} f_e(\mathbf{v},t)\,\log(f_e(\mathbf{v},t))\mathbf{dv}\;\leq\;0,\;\; t\geq 0.$$

The equilibrium states of the FPL operator, *i.e.* the set of distribution functions in the kernel of $C_{e,e}(f_e,f_e)$, are given by the Maxwellian distribution functions

$$\mathcal{M}_{n_e,\mathbf{u_e},T_e}(\mathbf{v}) \;=\; n_e\left(\frac{m_e}{2\,\pi\,T_e}\right)^{3/2}\exp\left(-m_e\,\frac{||\mathbf{v}-\mathbf{u_e}||^2}{2\,T_e}\right),$$

where n_e is the density, $\mathbf{u_e}$ is the mean velocity and $k_B T_e$ is the temperature, defined as

$$\begin{cases} n_e &= \displaystyle\int_{\mathbb{R}^3} f_e(\mathbf{v})\mathbf{dv}, \\ \mathbf{u_e} &= \displaystyle\frac{1}{n_e}\int_{\mathbb{R}^3} f_e(\mathbf{v})\mathbf{v}\mathbf{dv}, \\ T_e &= \displaystyle\frac{m_e}{3\,n_e}\int_{\mathbb{R}^3} f_e(\mathbf{v})\|\mathbf{v}-\mathbf{u_e}\|^2\mathbf{dv}. \end{cases}$$

A rigorous mathematical derivation of the FPL operator can be obtained (see *e.g.* [3, 34, 35]) as the limit of the Boltzmann operator for a sequence of scattering cross sections, which converge, in an appropriate sense, to a delta function at zero scattering angle. Mathematical stability results on the coupling of the FPL operator with the relativistic Vlasov-Maxwell system is studied by R. Strain and Y. Guo [107]. They are able to construct global in time solutions in a periodic domain, and near relativistic Maxwellian (Jüttner) distribution functions.

However the FPL operator provides with an inadequate description of collisional relaxation caused by Coulomb interactions, whenever the distribution function is far from equilibrium [101]. This is due to the importance of the large angle scattering for Coulomb interactions [54, 101].

In the Chapter 7, we give an illustration, issued from radiotherapy applications, of the importance of large angle scattering for dose deposition in water.
In the Chapter 8, we propose a series of mathematical models, issued from the relativistic Boltzmann equation, to take into account large angle scattering in the case of Coulomb interactions. These models rank from the most general to increasingly simpler and tractable operators.

2.2 Multi-scale methods for modelling electron transport

2.2.1 Outline of physical, numerical, and mathematical challenges

The assumption of scale separation in kinetic ICF electron transport is problem-dependent. There are variety of regimes -from collective to collisional-, with different possible reorderings of characteristic time and spatial scales: the Debye length, electron-ion mean-free-path, Larmor radius, laser wavelength. The treatment of the interactions between small, intermediate, and large scales in kinetic transport equations, motivate the development of models presented in Chapter 7 and 8. Depending on the regime we would like to simulate, different scalings of the kinetic system may be considered, such as those of Appendix 3.9 and 5.5.
These multi-scale aspects can be cast in a more general mathematical framework, where the asymptotical stability and well-posedness properties of transport equations are analysed, with respect to the stiff (singular) coefficients. A well-known method to derive limit models is the Chapman-Enskog expansion [21]. It can be shown, with such a method, that the transport equation, of hyperbolic nature, with parabolic source term, may under certain conditions be reduced to the parabolic limit. This gives rise to an outstanding numerical challenge: *the derivation of numerical schemes valid in the asymptotic limit (AP schemes)*. In the Chapter 3 and 5, we present high order numerical schemes that are designed to

preserve the conservation properties (especially the energy). Except when slope limiters are activated (to ensure the positivity of the solution), these schemes reduce to centered scheme, which is a desirable feature with respect to AP properties. The influence of the choice of slope limiters on the AP limit has been explored in a work from R. G. McClarren and R. B. Lowrie [77]. In the Chapter 5, we validate our scheme, which is not AP in a strict sense, in the limit of low Knudsen number, *i.e.* in the hydrodynamical regime.

Various techniques can be employed to capture multi-scale features, such as sub-mesh models, for turbulence or radiation, homogeneization or correlation methods. A multiscale strategy would consist of a parameterization of outputs to be used in the next level of the hierarchy (suite) of codes in terms of length and timescales. Alternatively, integrated multi-physics, multi-scale simulations make use of the combination of codes within a complete code system, using micro-solvers for regions where micro-resolution is needed, and systems of meso- up to macro-solvers in the other domain areas. In this context, one should apply a step-by-step validation procedure to compare reduced numerical models with exact solutions, microscopic models (see Chapters 3 and 5, Figure 2.1), and experiments, to gain understanding in the couplings of a variety of physical processes.

Various levels of refinements and complexity, and subsequent models, may be required, according to the regime of interest, to describe the multi-scale transport of electrons in ICF plasmas. These models are presented and discussed in the next section.

2.2.2 The classical transport theory

We do not consider here the dynamics due to the Bremsstrahlung heating by the laser light, or mobile ions, and refer to [90, 91] for the related transport theory and systematic treatment.

The Braginskii theory

The classical transport theory, where only regimes close to the hydrodynamical regime are treated, is refered as the Braginskii [16] theory. For the sake of clarty, we present this theory in the non-relativistic regime.
Let us first define the average over velocity of a function $A(\mathbf{v})$

$$< A >= \frac{1}{n_e} \int_{\mathbb{R}^3} A f \mathbf{dv} \quad , \tag{2.31}$$

where $n_e(t,\mathbf{x}) = \int_{\mathbb{R}^3} f(t,\mathbf{x},\mathbf{v})\mathbf{dv}$ is the density of electrons. Following [16, 40], we introduce the macroscopic quantities

$$\begin{cases} \mathbf{j} = q_e n_e \langle \mathbf{v} \rangle , \\ \mathbf{q} = \frac{1}{2} m_e n_e \langle (\mathbf{v}\cdot\mathbf{v})\mathbf{v} \rangle , \\ \mathbf{R} = \int_{\mathbb{R}^3} m_e \mathbf{v} C_{e,i}(f_e)\mathbf{dv}, \end{cases} \tag{2.32}$$

$$\begin{cases} p = n_e T_e = \dfrac{1}{3} m_e n_e \left\langle (\mathbf{v}- < \mathbf{v} >) \cdot (\mathbf{v}- < \mathbf{v} >) \right\rangle, \\[2ex] \mathbf{\Pi} = \dfrac{1}{3} m_e n_e \left\langle (\mathbf{v}- < \mathbf{v} >) \otimes (\mathbf{v}- < \mathbf{v} >) \right\rangle - p\mathbf{I}, \\[2ex] \mathbf{q_{loc}} = \dfrac{1}{2} m_e n_e \left\langle [(\mathbf{v}- < \mathbf{v} >) \cdot (\mathbf{v}- < \mathbf{v} >)] (\mathbf{v}- < \mathbf{v} >) \right\rangle. \end{cases} \tag{2.33}$$

There, $\mathbf{j}$ is the electric current, $\mathbf{q}$ the total heat flow, $\mathbf{R}$ the friction force accounting for the transfer of momentum from ions to electrons in collisions, T_e is the temperature, p is the scalar intrinsic pressure, $\mathbf{\Pi}$ is the stress tensor, $\mathbf{q_{loc}}$ is the intrinsic heat flow and $\mathbf{I}$ the unit diagonal tensor.

Quantities p, $\mathbf{\Pi}$ and $\mathbf{q_{loc}}$ are defined in the local reference frame of the electrons, whereas $\mathbf{j}$, $\mathbf{q}$ and $\mathbf{R}$ are defined relative to the ion center of mass frame. Ions are supposed to be at rest. We have the relation

$$\mathbf{q_{loc}} = \mathbf{q} + \mathbf{j} \cdot (\frac{5}{2} p\mathbf{I} + \mathbf{\Pi})/(n_e e) + \mathbf{j}(\frac{1}{2} m_e n_e < \mathbf{v} >^2)/(n_e e). \tag{2.34}$$

Following the formalism of Braginskii [16] for the transport relations, the transport coefficients in the hydrodynamical regime have been corrected by Epperlein in [40]. These coefficients $\alpha_{\mathbf{ep}}$, $\beta_{\mathbf{ep}}$, $\kappa_{\mathbf{ep}}$, are the electrical resistivity, thermoelectric and thermal conductivity tensors, respectively. The classical derivation procedure to obtain the transport coefficients involves the linearization of the Fokker-Planck-Landau equation, assuming the plasma to be close to the thermal equilibrium. The distribution function is approximated using a truncated Cartesian tensor expansion $f(t, \mathbf{x}, \mathbf{v}) = f^{(0)}(||\mathbf{v}||^2) + \dfrac{\mathbf{v}}{||\mathbf{v}||^2} \cdot \mathbf{f}^{(1)}(t, \mathbf{x}, \mathbf{v})$. Following [40], $\mathbf{\Pi}$ and $m_e n_e < \mathbf{v} >^2$ are neglected. Then considering appropriate velocity moments of $\mathbf{f^{(1)}}$, electric fields and heat fluxes are expressed as a function of thermodynamical variables. The coefficients of proportionality, in the obtained relations, are defined as the transport coefficients.

Several notations can be used, depending on the chosen thermodynamical variables. Adopting the Braginskii notations, we obtain the *transport equations* for the momentum and energy fluxes

$$\begin{cases} \mathbf{R} = \nabla p + e n_e \mathbf{E} - \mathbf{j} \times \mathbf{B} = \dfrac{\alpha_{\mathbf{ep}} \cdot \mathbf{j}}{n_e e} - \beta_{\mathbf{ep}} \cdot \nabla T_e, \\[2ex] \mathbf{q} = -\dfrac{5}{2} \dfrac{\mathbf{j}}{e} T_e - \kappa_{\mathbf{ep}} \cdot \nabla T_e - \beta_{\mathbf{ep}} \cdot \mathbf{j} \dfrac{\mathbf{T_e}}{e}. \end{cases} \tag{2.35}$$

As for the components of these tensors, we make use of the standard notations $||$, $\perp$, and $\wedge$. Directions denoted with $||$ and $\perp$ are respectively parallel and perpendicular to the magnetic field in the plane defined by the corresponding generalized force and magnetic field. Consequently, the parallel and perpendicular components of a vector $\mathbf{u}$ are respectively $u_{||} = \mathbf{b}(\mathbf{u} \cdot \mathbf{b})$ and $u_\perp = \mathbf{b} \times (\mathbf{b} \times \mathbf{u})$, where $\mathbf{b}$ is the unit vector in the direction of the magnetic field. The direction defined by the third direction in a direct orthogonal frame is denoted by $\wedge$. In the system (5.30), the relation between any transport coefficient tensor φ and vector $\mathbf{u}$ is defined by

$$\varphi \cdot \mathbf{u} = \varphi_{||} \mathbf{b}(\mathbf{b} \cdot \mathbf{u}) + \varphi_\perp \mathbf{b} \times (\mathbf{u} \times \mathbf{b}) \pm \varphi_\wedge \mathbf{b} \times \mathbf{u}, \tag{2.36}$$

where the negative sign applies only in the case $\varphi = \alpha_{\mathbf{ep}}$.

Failure of the phenomenological flux limitation

In the Spitzer regime, where no magnetic field occurs in the transport relation (5.30), the flux is given by

$$q^{Spitzer} = -\kappa_{ep}\nabla_x T_e \qquad , \qquad \kappa_{ep} \propto \frac{n_e T_e \tau}{m_e} \qquad ,$$

where τ the mean electron-ion collision time

$$\tau = \frac{3}{4}\frac{16\pi^2\epsilon_0^2\sqrt{m_e}T_e^{3/2}}{\sqrt{2\pi}n_i Z^2 e^4 \ln\Lambda}. \tag{2.37}$$

The flux can then be rewritten as

$$q^{Spitzer} \propto -q_{fs}K_n \ ,$$

where $q_{fs} = m_e n_e v_{th}^3$ is the free-streaming flux. $v_{th} = \sqrt{k_B T_e/m_e}$ is the thermal velocity. The Knudsen number $K_n = \tau v_{th}/\lambda_T$ is a mesure of the thermodynamical non-equilibrium of the system. λ_T is here the electron temperature gradient length. A regime characterized by $K_n \rightarrow 0$ refers to an hydrodynamical descripion, whereas a regime characterized by $K_n \geq 1$ refers to a kinetic description, where the nonlocal phenomena appear. The parameters for ICF imply $K_n \geq 0.1$, while the classical, local approach fails at $K_n \geq 0.01$. This premature failure of the classical diffusion approach in plasma is explained by a specific dependence of the electron mean free path on their energy. In ICF applications the energy is transported by the fastest electrons, which have a much longer mean free path.

To remedy the issue of delocalization , the flux limitation idea comes from the remark that q should not become larger than the free-streaming flux $n_e m_e v_{th}^3$. In fact cross comparison between hydrodynamic and Fokker-Planck simulations [108] showed that the flux should be limited to some fraction f of the free-streaming flux (typically 6%). Also Fokker-Planck simulations revealed that a time and direction dependant limiter f should be phenomenologically “constructed”. A sensitivity study has been conducted in CELIA [67] for hydrodynamical simulations of homothetic targets in the shock ignition scheme [10]. It exhibits a strong dependance with respect to the value chosen for f if the size of the target is reduced (thus overcoming a higher laser irradiation). Also this study has confirmed the sensitivity of the flux limitation on its numerical treatment, whether it is computed at the center or at the interfaces of the meshes [43].

In fact, from a Chapman-Enskog expansion [21] with a small parameter K_n, the equation for the nonlocal heat flux can be written as a diffusion equation

$$\left(1 + \lambda^2(x)\frac{\partial^2}{\partial x^2}\right)q(x) = q^{Spitzer}(x) \tag{2.38}$$

where $\lambda(x)$ is a delocalization (several mean free path) length. This variable accounts for the fact that the heat flux is mostly carried by hot electrons having 3-4 thermal velocity.

2.2.3 Delocalisation, beam deposition, and diffusion models

Several investigations [53, 55] have highlighted situations where the description of thermal smoothing involving the flux limitation technique can be ineffective. Moreover, the correct description of preheat

phenomena, flux inhibition, counterstreaming flux, the inclusion of specific magnetic field related effects (flux inhibition, rotation, Nernst effect) in 2 dimensions, requires more sophisticated nonlocal heat transport models. A series of *ad hoc* models have been derived, relying on delocalization kernels in convolution formulas on the heat flux obtained from the equation (2.38). First models date back to the references [1, 75]. However these models are not well-suited for implementation in multidimensional hydrodynamical codes, due to the use of delocalisation kernels and a large difference in time scales. Indeed, the electron thermal conduction is determined on an electron time scale, and should be included on a ion time step. This requires an implicit treatment over the entire plasma, *i.e* with a dense matrix, which is too costly. In order to overcome this drawback, different models are introduced. A first category of models can be isolated, refered as beam deposition models [78]. They decompose the total volume in a region of high temperature, treated as a source of monoenergetic beams, which scatter and deposit their energy, and a region of lower temperature and a shorter mean free path with respect to the temperature perturbation, where Spitzer theory applies.
Another class of methods, refered as SNB, relies on a reduction of the kinetic equations [103], and an interpretation of the convolution kernels as solutions of nonlocal diffusion equations, similar to the equation (2.38). This model is a valuable candidate for implementation in multidimensional hydrodynamical codes . It permits also to include 2D effects, and an anisotropy of transport coefficients due to the magnetic fields [84], with a hypothesis of weak departure of locality.

Finally, an ongoing subsequent effort is lead for the derivation of models that do not rely on a *ad hoc* interpretation, but on well-defined closure, thus gaining in reliability/predictivity, and permiting the treatment of a wider range of effective Kndusen number $k\lambda_{ei}$, the nonlocality parameter.

A rigorous nonlocal transport model was derived for small amplitude linear perturbations of hydrodynamical variables [12, 18]. This linear transport theory has been developed into a nonlocal nonlinear model, which could be potentially implemented into large scale hydrodynamical codes [5]. The nonlinear model was tested in the configuration of a temperature hot spot with FokkerPlanck simulations [5], with good agreement. A linear model have also been proposed [13] to include the effects of external magnetic fields. The relation between nonlocal and nonstationary effects were explored in [11], in the case of an homogeneous plasma density. This model will be successfully compared to a $2D \times 3V$ Fokker-Planck simulation of a temperature hot spot relaxation in Chapter 5.

2.2.4 Cartesian tensor expansion

The electron distribution function is here decomposed in Cartesian tensors [65]:

$$f(t, \mathbf{x}, \mathbf{p}) = \sum_n f_0(t, \mathbf{x}, \mathbf{p}) + \mathbf{f_1}(t, \mathbf{x}, \mathbf{p}) \cdot \mathbf{v} + \mathbf{f_2}(t, \mathbf{x}, \mathbf{p}) : \mathbf{vv} + ...$$

The closure of the subsequent set of equations relies on a diffusion approximation, using an isotropic pressure tensor, *i.e.* scalar diagonal

$$\mathbf{P} = \frac{1}{3}\mathbf{I}_d f_0 \, , \tag{2.39}$$

This type of method is refered as P_1 models, *e.g* in [52].

2.2.5 Spherical harmonics

The electron distribution function is here represented in momentum space (p, θ, ϕ) by an expansion in spherical harmonics [7, 79]:

$$f(t, \mathbf{x}, \mathbf{p}) = \sum_{n=0}^{n_{max}} \sum_{m=-n}^{n} f_n^m(t, \mathbf{x}, \mathbf{p}) P_n^{|m|}(\cos\theta) e^{(im\phi)} ,$$

where $f_n^{-m} = (f_n^m)^*$ and $P_n^{|m|}(\cos\theta)e^{(im\phi)}$ are the spherical harmonics. The electron distribution can be defined in the ion rest frame, so that electrons with $\mathbf{p} = \mathbf{0}$ move with the ions, locally. The dependance of the coefficients on the magnitude of the momentum means that the distribution function is not constrained to be Maxwellian.

Johnston [63] has shown the equivalence between a Cartesian tensor scalar product expansion and a spherical harmonic expansion. He also demonstrated the correspondance between the order of the spherical harmonic and the order of the tensor transport quantity, for the Boltzmann equation.
The description of electron transport with an anisotropic pressure [112] requires second order terms, whereas the description of energy transport would require third order terms [63].

One strength of such formalism is that it constitutes an efficient platform to include additional physics [94]. Moreover, the spherical harmonic formalism permits an implicit treatment for both the magnetic field and collisions, appart from the explicit core of a given spherical harmonic solver.

However, the spherical harmonic expansion relies on high order harmonic truncation, rather than moment closure. In [58], it is mentioned that moment closures inherit the Lie-Poisson bracket structure from the Vlasov Lie-Poisson structure, while moment truncations do not.

This is a reason why we adopt the denomination KET, an acronym for Kinetic Electron Transport, according to the $|\cdot\rangle$ brackets in Dirac notation, for the deterministic solvers we develop in this document. This denomination permits to distinguish solvers of different mathematical structure.

2.2.6 Reduced angular model

The original derivation of reduced model dates back to mesoscopic modelling of the radiative transfer [30], where the authors introduced a closure of the equation relying on a minimum entropy principle together with an average on the radiation frequency spectrum and propagation direction: this is the so-called $M1$ model [30].
In the case of (fast) electron transport, instead of using the closure from Levermore [71, 30], the closure from Minerbo [80] is more suitable, because it is directional, allows analytical calculation on the collision operators, and makes it possible to obtain a convex set of admissible electron distribution functions. The convexity property is indeed a desirable property, which sets the system in a standard form, that can be treated with standard numerical techniques, such as the HLLC method.

Both radiative or electronic $M1$ closure make use of a tensorial pressure, written as [71]

$$\mathbf{P} = \left(\frac{1-\chi}{2} \mathbf{I}_d + \frac{3\chi - 1}{2} \frac{\mathbf{f_1}}{f_0} \otimes \frac{\mathbf{f_1}}{f_0} \right) f_0 \, ,$$

which differs from the P_1 closure (2.39) in the rarefied (collective) regimes, or for beam treatments. It is similar to the P_1 closure (2.39) in the diffusion (collisional) regime. Here χ is the electron Eddigton factor, which is precised in Chapter 7.

2.2.7 Collisional PIC

The different calculation steps in a *Particle-In-Cell* (PIC) code are the following:

- (1) The resolution of the macroparticle movement from dynamic equations. The electromagnetic fields are interpolated at the macroparticle positions.
- (2) The current are transfered on the spatial grid based on the positions and velocities of the particles. In order to avoid large amplitude statistical fluctuations, the charge of each macroparticle is distributed over a certain volume. This accumulation is done using an algorithm that guarantees by construction that the continuity equation is verified particle by particle. This method can be made compatible (employing Villasenor-Buneman, Esirkepov, or zigzag scheme) with Poisson's equation which solving is difficult to parallelize [115].
- (3) Maxwell's equations are solved on the spatial grid.

High order interpolation, up to 4th order at the present time [99], can be used for steps (1) and (2), to improve the performance of PIC simulations by extending the simulation grid size to the plasma skin length. The latter is much larger than the Debye length of the cold plasma, while the interpolation avoids the numerical heating. This enables also to reduce the computational cost drastically.

The modeling of large plasma density gradients may require variable weighted particles [99]. Keeping the charge-to-mass ratio of the macro-particles constant, the density of real charges that they represent can be changed. In a situation where the plasma density varies from the under-dense region, where the laser pulse is absorbed, to a more than a hundred times over-dense target, it is unpractical to keep the number density per macro-particle constant because choosing a reasonable resolution in the under-dense region means an enormous number of particles in the target. This can be avoided by using variable particle weights.

The expansion of the electron distribution function in spherical harmonics and nonlocal approach apply for relatively long laser pulses (hundreds of ps) and nonrelativistic intensities (below 10^{15}-10^{16} W/cm^2) where the deviation from the local thermal equailibrium is not too large. The ultra-short laser accelerated electrons have an energy spread of a hundred percent from non-relativistic to ultra relativistic energies.They have a beam-like distribution function and their transport has to be treated kinetically. Collisions in the target are an important issue to determine the characteristics of hot electron transport. Fully relativistic binary-collision model is developed [98, 109], that has a desirable feature to preserve the energy in individual collisions, and momentum on the average, which is a great advantage for HEDP simulations in which the numerical heating or energy violation, must be very small to get an accurate laser energy coupling to plasmas. The combined use of weighted particles has significant consequences for the binary collision model, and such model are tested with respect to Monte-Carlo models [82]. We mention here some attemps for the derivation of Asymptotic Preserving Monte Carlo methods [85], in the collisional limit.

For the problem of high energy density physics (HEDP), the transport of fast electrons in solid-density plasmas is the essential question. It is difficult to model high-density plasmas with Particle-in-Cell (PIC) simulations because of the small plasma Debye length, which needs to be resolved to avoid numerical heating of particles, due to the “finite grid instability” [36, 37]. Although impressive improvements have been realized in the recent years, the statistical noise and the low resolution of the electron distribution function by PIC solvers can lead to very stringent constraint in low temperature and high density plasmas. This is why the traditional operating point of PIC codes concerns the source, *i.e.* the zone of absorption of the laser and the generation of electrons that propagate further in plasma. Moreover, the treatment of collisions is often made with *ad hoc* methods, not physically well-formulated.

2.2.8 Langevin approach

In contrast to the methods traditionally designed to incorporate collisions in PIC codes, the Fokker-Planck approach, though computationally costly, relies on a well-formulated physical basis. A possibility remains open to combine the advantages of both theories (low computational cost and well-posedness of the collision process) within a Langevin approach [19, 118, 42]. This approach is a stochastic partial differential equation mathematically equivalent to the Fokker-Planck equation.
The Langevin equation used for the modelling of laser-plasma iteraction has the form

$$\frac{\mathrm{d}\mathbf{p}}{\mathrm{d}t} = \mathbf{A_0} + \underline{\underline{\mathbf{C}}}.\xi + \underline{\underline{\mathbf{C}}}.\eta\,, \tag{2.40}$$

with two scalar stochastic processes ξ and η. Using the Cayley-Hamilton theorem, that defines the root of specific second-rank tensors [48, 66] of this form

$$\left(M\mathbf{I} - N\frac{\mathbf{v}\otimes\mathbf{v}}{v^2}\right)^{1/2} = \sqrt{M}\mathbf{I} - \left(\sqrt{M} \pm \sqrt{M-N}\frac{\mathbf{v}\otimes\mathbf{v}}{v^2}\right)\,, \tag{2.41}$$

where $M > 0$ & $M \geq N$, then the direct acceleration term and the stochastic sources in equation (2.40) have the form,

$$\mathbf{A_0} = \mathbf{A} - \mathcal{N}\left(\underline{\underline{\mathbf{C}}} + \underline{\underline{\mathbf{D}}}\right)\cdot\nabla\cdot\left(\underline{\underline{\mathbf{C}}} + \underline{\underline{\mathbf{D}}}\right)\,, \tag{2.42}$$

$$\underline{\underline{\mathbf{C}}} = \frac{\underline{\underline{\mathbf{B}}}_{+}^{1/2}}{\sqrt{2}}\,, \tag{2.43}$$

$$\underline{\underline{\mathbf{D}}} = \frac{\underline{\underline{\mathbf{B}}}_{-}^{1/2}}{\sqrt{2}} \tag{2.44}$$

where ξ is a Wiener process, chosen such as successive, independent small angle Coulomb scattering leads to a Gaussian distribution. $\mathcal{N}$ is a possible realization of a stochastic integral. The choice for $\mathcal{N}$

depends both on physical and numerical considerations. $\mathbf{A}$ and $\underline{\underline{\mathbf{B}}}$ are the Fokker-Planck coefficients of the FPL operator, under the form

$$\frac{\partial f}{\partial t} = -\nabla_{\mathbf{v}} \cdot \left(\mathbf{A} - \frac{1}{2} \nabla_{\mathbf{v}} \left(\underline{\underline{\mathbf{B}}} f \right) \right) . \tag{2.45}$$

2.2.9 Hybrid approches

Hybrid codes combine a kinetic resolution for the fast, highly anisotropic, electron population with an hydrodynamic fluid description for the bulk electron population. Such codes are able to describe both collective and collisional effects. Hybrid codes rely on the assumption of low beam to plasma density ratio, therefore they cannot simulate the fast electron transport near the critical density, where the full kinetic description is more appropriate. Moreover the thermodynamical equilibrium assumption of the bulk population is not a general statement [104]. However, these methods offer the most realistic approach to date since they encompass the fast particle description and permit integrated simulations. Several problems arise when coupling the populations, such as the cut-off between population in the energy space, which is arbitrary, and depends on the physical assumptions and the boundary conditions. Stability problems associated with the coupling of different methods may also arise, because of the different scales and grid resolutions.

2.2.10 On the choice for a deterministic Eulerian Vlasov-Maxwell solver

A strong motivation for the choice of Eulerian deterministic solvers lies in their robustness properties with respect to density and temperature gradients. Another desirable feature is that they are noise-free. Interestingly, some low-level noise might be introduced (that could be thought as representative of the plasma fluctuations), with or without frequency filters, in initial conditions, for Eulerian deterministic resolution of laser-matter interactions. The objective would then be two-fold. First, an instability could be triggered more fastly, so that the required range of unstable frequencies could be selected within the white noise that is “artificially” introduced. Second, this could be a way to get rid of, or postpone the recurrence effects.

Finally, Eulerian solvers provide with a well-defined frame for coupling with the collision terms, contrary to PIC solvers, where the use of macroparticles render the treatment of collision be *ad hoc*.

The counterparts of these good features are the high computational ressources needed, and the small amount of literature about the accuracy and robustness results with regard to coupling of Vlasov-Maxwell solvers with collision kernels.

A number continuous properties of the model should be reproduced at a discrete level by the numerical schemes, and should guide a design of deterministic Eulerian Vlasov-Maxwell solvers. The coupling with collision brings additional constraints. Gathering of all these properties in a single scheme is out of reach of any existing algorithm, and one should select a numerical method that would be appropriate to the regime of interest. The potential candidate should share most of the following feature:

- Unsplit advection scheme [31, 39]. Avoiding the numerical heating issued from the time splitting technique [105, 102].
- Discrete energy conservation when coupling with Maxwell equations [31].

- Total mass conservation [25, 31, 44].
- Positivity of the particle distribution function [25, 31, 44].
- Ampère-Poisson compatibility *via* the continuity equation [105], we refer to the compatibility between the statistical repartition of particle charges and positions.
- Local reconstruction stencil in space for ease of parallelisation [25, 31, 44].
- High order schemes for accuracy [25, 31, 44], that control the dispersive and diffusive artefacts of the numerical approximation.
- Hamiltonian preserving [20], which is a feature that symplectic methods aim at capturing. The Vlasov equation presents indeed a rich geometric structure related to its Hamiltonian character. In particular, it satisfies an infinite set of conservation laws, that are the Casimir invariants. In [96], a rigourous mathematical proof, relying on the Lie algebra, shows that any discretization of the Vlasov-Poisson system cannot preserve the conservation of all the Casimir invariants.
- High order preservation discrete dispersion relations, in particular the one related to the electromagnetic and plasma waves and the Two-Stream Instability (TSI).
- Capture of the propagation velocities (eigenvalues of the Maxwell equations) of the electromagnetic waves, for laser propagation.
- Avoiding numerical checkerboard instability with the numerical scheme for Maxwell equations [105].
- Avoiding numerical Cherenkov effect in the relativistic regime [9, 61].
- Implicit resolution of the Maxwell equations [31, 9] is desirable since this method is not constrained a stringent CFL condition.
- Avoiding (postponing) recurrence effects [70]. This numerical artefact is a signature of reapparition of some parts of the initial condition in the course of a simulation, where the caracteristic modes return back to their initial state. This phenomenon may damage the solution in the case of a long time evolution of a wave that is not submitted to other dominant process. A way to supress this effect would be to introduce an initial “artificial” low-level white noise, representative of the fluctuation level of the plasma.
- Permiting discontinuities in the phase space [25, 31, 44], in particular, for rarefied plasma flows [42]. This is a challenging numerical issue for Eulerian solvers. The PIC solvers are much more adapted to discontinuous configurations, since they do not face the *vacuum problem*.

The use of particular techniques for Eulerian methods, such as Fourier transformation based methods for the Vlasov-Maxwell system, is finally worth mentionning, since they have cast a new light on the Landau damping or time echo phenomena [45], while reinterpreting them [97]. These problems require a particular well-posed outflow boundary conditions [38, 70] in the velocity space, to avoid filamented and unphysical oscillatory structures, related to numerical recurrence effects.

2.3 Key points for a successful modelling of ICF electron transport

2.3.1 Importance of an accurate collision treatment in ICF plasmas

The scaling laws derived in [7] for the inhibition of fast electron transport by electric field, the non-linear conductivity (breakdown of the Spitzer conductivity) of return currents [104], runaway electrons, magnetic collimation, and magnetic inhibition, show that the electric conductivity plays an important role in the ICF physics. An accurate modelling of the highly collisional slow electrons is, therefore, crucial, even for simulation of fast electron beam (having lower collision probability), propagating in a thermal plasma. This motivates developments in Chapter 8 of a two-scale collision model, involving two kinetic populations (that may share some intermediate energy ranges, and allow runaway particules). This approach can be seen as an extension of the model of A. V. Gurevich [54], where the thermal population was assumed to be a cold population, with infinite number of particles.

How accurate should be the treatment of thermal particules? This question remains open. If a Cartesian tensor expansion technique is employed (see section 2.2.4), some clues are given in the literature [56, 112]. For instance, the capture of the collisional Weibel instability [56] requires that the perturbative expansion in the Knudsen number of the equilibrium distribution function should be pushed to the second order. However, a closure on the $\mathbf{f}^{(3)}$ component is reported to give Weibel growth rates five times larger than when it was applied on the $\mathbf{f}^{(2)}$ component. What do we know about the regime dependence of other instabilities on the convergence of high order terms for cartesian tensor expansion, spherical harmonics, or angular reduced models (These methods will be presented in the sections 2.2.4, 2.2.5 , and 2.2.6, respectively)?

This issue is one of the reasons for development of a reference deterministic Maxwell-Fokker-Planck-Landau code, which can deal with high anisotropy degrees of the distribution function.

2.3.2 Collective transport

The transport of electrons does not only rely on the sum of individual interactions between particules, but also, and this is a characteristic feature of plasmas, on collective effects. They are due, one the one hand, to the long-range Coulomb interaction, and on the other hand to the dynamic of the charge neutralization in the plasma, generation of electric and magnetic fields, and wave propagation.

For instance, the charge separation, created by electrons accelerated in the target, induces an electrostatic field that tend to mantain a charge equilibrium. This field is screened by thermal electrons, and its strength depends on the value of the electric resistivity. Generation of magnetic fields (up to MegaGauss) by the currents of fast and slow electrons have a significant effect on the transport coefficients, collimate a beam a fast paticules or filament it.

2.3.3 Coupling between magnetic field and nonlocal transport

The ICF experiments [106, 111] are confronted to the emergence of strong magnetic fields, spontaneously generated in hydrodynamic flows that lack of the spherical symmetry. These assymetries due to non-uniform laser irradiation -this case will be numerically considered later in Chapter 5-, nonuniformities in the target, or to an instability.

The generic equation for the magnetic field issued from the combination of the Faraday's law with local transport equations can be written [56] as

$$\frac{\partial \mathbf{B}}{\partial t} = \mathcal{S} + \mathcal{V} + \mathcal{D}\,, \tag{2.46}$$

where the right-hand side describes the sources due to the low frequency currents $\mathcal{S}$, convection $\mathcal{V}$ and diffusion $\mathcal{D}$ processes. The major term is generally due to crossed gradients $\nabla T_e \times \nabla n_e$ effect. The anisotropic pressure (rotational part of the stress tensor) and the laser field also contribute to the source terms. An explicit, low-frequency form of the equation (2.46) is [56, 90]

$$\begin{aligned}
\frac{\partial \mathbf{B}}{\partial t} &= \nabla \times \left\{ -\frac{\mathbf{j}\times\mathbf{B}}{n_e e}\left[1 + \frac{1}{\omega_e \tau_e}\left(\alpha^c_{ep,\wedge} - \frac{\beta_{ep,\wedge}\beta_{ep,\perp}}{\kappa^c_{ep,\perp}}\right)\right] + \frac{\nabla P_e}{n_e e} + \frac{\beta_{ep,\parallel}}{e}\nabla_{\parallel} T_e \right.\\
&+ \left(\beta_{ep,\perp} + \frac{\beta_{ep,\wedge}\kappa_{ep,\wedge}}{\kappa_{ep,\perp}}\right)\frac{\nabla_{\perp} T_e}{e} + \frac{\beta_{ep,\wedge}}{e\kappa_{ep,\perp}}\mathbf{q}_e \times \mathbf{b} - \frac{\alpha_{ep,\parallel}}{n_e^2 e^2}\mathbf{j}_{\parallel}\\
&- \left.\left(\frac{\alpha_{ep,\perp}}{n_e^2 e^2} - \frac{\beta^2_{ep,\wedge} T_e}{e^2 \kappa_{ep,\perp}}\right)\mathbf{j}_{\perp}\right\}\,,
\end{aligned} \tag{2.47}$$

where the last two current terms, with $\mathbf{j}_{\parallel}$ and $\mathbf{j}_{\perp}$, can be interpreted and recast under the generic resistive form $\eta\mathbf{j}$, where η is the resistivity. The $\mathbf{j}\times\mathbf{B}$ term can be interpreted in the same manner, as a magnetic resistivity, that collimates an electron current. The Nernst term, proportional to $\mathbf{q}_e \times \mathbf{b}$, advects the magnetic field along with the heat flow. The thermoelectric term $\nabla P_e/n_e e$, contains the well-known, first order cross gradient $\nabla n_e \times \nabla T_e$ source of magnetic field. Finally, the ∇T_e terms account for the friction, issued from the electron-ion collisions, and their coupling with magnetic field generation.

In the low-frequency and local regimes, an analytical decomposition (2.46) is possible [56, 90]. However, for high frequency fields, or in the nonlocal regime where the distribution functions are not Maxwellian, such a general analytical expression is not available. Several cases may still be isolated as remarkable, as they may lead to identified forms of the Ohm's law.

In the situation where a fast beam population propagates through a cold static plasma population, the magnetic field source can be represented [28] as

$$\frac{\partial \mathbf{B}}{\partial t} = \eta \times \nabla \mathbf{j}_b + \nabla \eta \times \mathbf{j}_b\,, \tag{2.48}$$

where η is the resistivity and $\mathbf{j}_b$ the fast beam current. J. R. Davies [28] proposed a simple qualitative interpretation of the equation (7.6.5). The first term on the right-hand side generates a magnetic field that pinches the beam of fast electrons, while the second term pushes fast electrons towards regions of higher resistivity. Such an analytical model can be of use to estimate the growth of a magnetic field collimating a fast electron beam [27], or to estimate the guiding effects of background density modulations, that induce themselves resistivity and magnetic collimation modulations [93]. Target designs have been proposed based on these interpretations [93].

In the situation where the density is constant, the $\nabla T_e \times \nabla n_e$ effects cancel and the high order moments of the distribution function are required to describe the departure from the spherical symmetry that seeds the magnetic field generation [65]. This situation will be reproduced numerically in Chapter 5.

It should be also noted that the magnetic field source could be expressed, under particular plasma conditions, as the curl of off-diagonal terms of the pressure tensor [81]. Independently, a possible source could be the resonant absorption at high laser intensities [113].

A well-known kinetic effect is the *flux inhibition of a nonlocal heat flow by a magnetic field*, where the heat carrying electrons movement is bent preferentially along the magnetic field lines. This effect can be characterized by the Hall parameter $\chi = \omega_c \tau$, which is the product of the cyclotron frequency ω_c and the electron-ion collision frequency τ. A strong Hall parameter reveals the formation of a transport barrier, that reduces the preheat, even could lead to the suppression the heat flow, whereas a low one permits nonlocal features to develop. The competition between a nonlocal heat flow and a strong magnetic field will be illustrated in Chapter 5.

A strong coupling may occur between nonlocal phenomena (that modify the mean velocity of the flow), and the Nernst effect (caracterized by the Nernst velocity, proportional to the heat flow). T. H. Kho and M. G. Haines [64] describe how nonlocality modifies the rate of magnetic field advection. C. Ridgers [92] describes the reemergence of nonlocality due to the cavitation of the magnetic fields by the Nernst effects.

Last but not least, a magnetic fied can emerge from the electromagnetic perturbation of anisotropic distribution functions. In laser-plasma interactions, the development of an anisotropy of the distribution function can be due to temperature gradients [89], or absorption of laser light, *via* the capture of laser photons by plasma electrons (Inverse Bremsstrahlung) [112]. This mechanism for magnetic field generation is relevant for the Weibel instability, and develops at a nanosecond time scale for conditions foreseen for ICF [95].

2.3.4 Fast electrons as energy carriers for ignition and source for electron-positron plasmas

The fast electrons that are generated by laser in low density corona regions are responsible for carrying the energy to the ablation front. Therefore an accurate treatment of the their energy deposition into the thermal plasma is of importance for the ICF target design. A review of fast electron physics in laser plasmas is presented by A. R. Bell in [7], and more recently by F. Pisani in [88]. The mecanisms of generation of fast electrons, as well as their transport in matter, considered as an insulator or a conductor, compressed or not, are summarized in there. The main diagnostics of fast electrons, namely the K^α radiation, is also recalled in this latter reference. Therefore, we shall not reproduce such a comprehensive task, but rather insist on specific but important aspects of the fast electron transport.

At this point we comment on the fact that a simple estimate of the heating rate of the thermal plasma based on the collisional energy deposition of fast electrons may not be relevant for certain relativistic regimes. The heating rate could indeed be different by several orders of magnitude, and the penetration of beam electrons may be underestimated, due to the large angle scattering in the collision processes. We refer to the Chapter 8 for further detailled consideration on this crucial issue.

The fast electrons produced by ultraintense lasers reach energies more than several tens of MeV. These become sources for creating electron-positron pairs *via* their interaction with nuclei, according to two processes [83], the Trident process

$$e^- + Z \rightarrow e^+ + 2e^- + Z \; ,$$

and the Bethe-Heitler process

$$e^- + Z \rightarrow \gamma + e^- + Z \; ,$$

$$\gamma + Z \rightarrow e^+ + e^- + Z \; .$$

The generated electron-positron plasmas might exhibit very different dynamics and regimes from those traditionally encuontered. Such regime could be reached with the Extreme Light Infrastructure (ELI) European project.

2.4 Objectives

2.4.1 Objectives of the present work

High Energy Density Physics (HEDP) is a exciting field where improvements in modelling and numerical analysis can bring a deeper understanding. Having in view applications such as the Inertial Confinement Fusion (ICF) and more generally the laser-matter interactions, the kinetic electronic transport in the conduction zone, from the laser absorption zone to the ablation front of the target, is identified as a bottleneck. It is indeed necessary to treat within the same transport model collective and collisional effects, for both thermal and fast relativistic particles. This stands as a multi-scale problem, which is a challenge for modelling as well as for designing efficient numerical schemes. There is only a small amount of literature where all these scales are present together, considering the coupling of Vlasov-Maxwell solvers with Fokker-Planck-Landau collision kernels, and few results on the accuracy and robustness for numerical schemes are available in this situation. To step forward in this direction, we would like to develop and analyse robust and accurate, high order numerical methods that control the dissipative and dispersive aspects inherent to the discretization of the system.
A a second step, we shall qualify (see figure 2.1) the numerical schemes in a wide range of regimes relevant for the ICF physics. To this aim, we propose and develop an original validation procedure, that addresses the multi-scale and high dimensionality features of the coupled system.
As a third step, we develop numerical tools for the modelling of electron transport under the conditions of a new class of high power / high energy lasers, with intensities that go beyond $10^{20}\mathrm{Wcm}^{-2}$, entering into the relativistic regime. We first extend the schemes to the relativistic regime, then evaluate the relative importance of the different electron-electron collision mecanisms. The role of electron-electron collisions at small impact parameters was indeed not clear before this thesis. In particular, we reconsider the importance of large energy exchanges in the long range Coulomb collision processes, and propose a fast and robust model to identify and accurately capture the regimes where this mechanism could be dominant.

A concomitant aspect of this work will address the developement of an operational simulation tool, written in C++. We bring an evidence of computational affordability for deterministic simulation in the $2D_x \times 3D_v$ space. To reach this objective, we implement MPI parallelisation with domain decomposition in the $2D_x$ subspace, together with fast algorithms, such as the multigrid method, to accelerate the calculations of the collisional terms in the velocity space. Such demonstration will enable a systematic comparison with reduced but faster models. This cross comparison between solvers of different origins ends up with a large-scale, realistic simulation for the kinetic electron transport shock ignition scheme, in collaboration with the teams of Imperial College and Oxford. This latter constitutes our contribution for the HiPER European project.

Finally, we are able to demonstrate the relevance of our approach for problems in other domains of science. We focus on the electron radiotherapy, and prove that a deterministic M1 model is able to reach an attractive accuracy/efficiency compromise over the existing methods (pencil-beam or Monte-Carlo). This method is expected to meet practical applications for real patient treatment. In this application, an accurate dose depostion by the electron beam requires the modelling of secondary electron production, with large energy exchanges during the collision events. We discuss a similarity between the processes at stake for the electron radiotherapy and the Fast Ignition electron transport.

2.4.2 Mid term perspectives

A deeper understanding of nonlocal transport processes in laser-matter interactions at high fluxes would require a systematic comparison with experiments, in the frame of the qualification procedure shown in figure 2.1. Simple though representative experimental configuration could be proposed [47], for instance in the installation LULI2000. Very large discrepancies have been found between experimental and 1D hydrodynamical simulation results (LILAC)[72], for the investigation of Implosion Dynamics in Direct-Drive Inertial Confinement Fusion experiments at OMEGA laser facility. Nonlocal aspects of the implosion, as well as 2D features of the transport should be explored to gain in accuracy between simulation and experiments. To this aim the implementation of the background ion motion would be necessary to reach nanosecond time scale simulations. Such upgrade of the model would allow the exploration of the absorbtion zone of the laser, at the critical density, with a 2D deterministic code including collisions.

Independently, the model for Coulomb collisions we derived in the Chapter 8 exhibits low computational cost, together with accuracy and robustness features. These points are not shared by any other models. We bring, using this model, the evidence of importance of large energy exchange for electron-electron collisions, *via* a first quantitative estimation. The model is most useful to explore, at a reduced computational cost, the effects of large energy exchanges in collisions between like particles, and the associated secondary electron production. The model can be efficiently coupled with electro-magnetic fields and it restitutes most of the properties of the original relativistic Boltmann equation, with the Coulomb cross section. The difficulty for treating this Boltzmann operator lies in the long-range nature, at the limit of integrability, of the Coulomb cross section, and the large difference in scales between the particules. A traditional treatment of such mechanism involves Monte Carlo methods, that are very costly.

The derivation of such a model opens the path for other applications in the near future, ranking from electron-positron pair production at high laser intensity, to the electron lithography or high energetic processes in the upper atmostphere and ionosphere, namely thunderstorms and sprites.

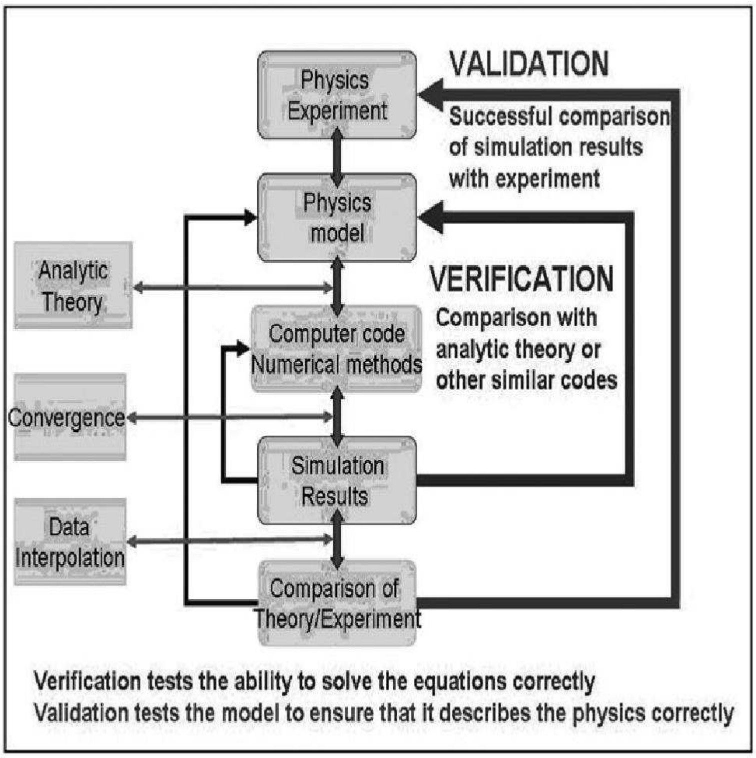

Figure 2.1: *Generic qualification procedure for a simulation code.*

Bibliography

[1] Albritton J. R., Williams E. A., Bernstein I. B., Swartz K. P., , *Phys. Rev. Lett.* 57, 1887 (1986).

[2] Andreasson H., Regularity of the gain term and strong L^1 convergence to equilibrium for the relativistic Boltzmann equation, *SIAM J. Math. Anal.* 27, 5, 1386-1405 (1996).

[3] Arsen'ev A. A., Buryak O. E., On the connexion between a solution of the Boltzmann equation and a solution of the Fokker-Planck-Landau equation, *Math. USSR Sbornik* 69, 465-478, (1991).

[4] Bancel D., Choquet-Bruhat Y., Existence, Uniqueness, and local stability for the Einstein-Maxwell-Boltzmann system, *Comm. Math. Phys.* 33, 83-96, (1971).

[5] Batischev O. V., Bychenkov V. Yu., Detering F., Rozmus W., Sydora R., Capjack C. E., Novikov V. N., *Phys. Plasmas* 9, 2302, (2002).

[6] Beliaev S. T. and Budker G. I., *Dokl. Akad. Nauk SSSR*, 107, 807, (1956) [*Sov. Phys. Dokl.*, 1, 218, (1957)].

[7] Bell A. R., Robinson A. P. L., Sherlock M., Kingham M., Rozmus W., Fast electron transport in laser-produced plasmas and the KALOS code for solution of the Vlasov-Fokker-Planck equation, *Topical review, Plasma Phys. and Control. Fusion*, 48, R37-R57, (2006).

[8] Benedetti C., Londrillo P., Rossi L., Turchetti G. Numerical investigation of Maxwell-Vlasov equations. Part I: Basic physics and algorithms, *Communications in Nonlinear Science and Numerical Simulation*, 13, 204-208, (2008).

[9] Benedetti C., Londrillo P., Rossi L., Turchetti G. Numerical investigation of Maxwell-Vlasov equations. Part II: Preliminary tests and validation, *Communications in Nonlinear Science and Numerical Simulation*, 13, 209-214, (2008).

[10] Betti R., Zhou C. D., Anderson K. S., Perkins L. J., Theobald W. Solodov A. A. Shock Ignition of Thermonuclear Fuel with High Areal Density, *Physical Review Letters*, 98, 155001, (2007).

[11] Brantov A. V., Bychenkov V. Yu., Rozmus W., Relaxation of a Thermal Perturbation in a Collisional Plasma, *Transport Processes, Plasma Physics Reports*, 32, 4, 337-343, (2006).

[12] Brantov A. V., Bychenkov V. Yu., Rozmus W., Tikhonchuk. V. T., *JETP*, 84, 716, (1996).

[13] Brantov A. V., Bychenkov V. Yu., Rozmus W., Capjack C. E., Sydora R. Linear theory of nonlocal transport in a magnetized plasma *Physics of Plasmas*, 10, 12, 4633-4644 (2003).

[14] Bret A., Gremillet L., Bnisti D., Lefbvre E., Exact Relativistic Kinetic Theory of an Electron-Beam-Plasma System: Hierarchy of the Competing Modes in the System-Parameter Space, *Physical Review Letters* 100, 105008, (2008).

[15] Bret A., Firpo M.-C., Deutsch C., *Physical Review E* 70, 046401, (2004).

[16] Braginskii S. I., *Rewiews of plasma physics*, Consultants Bureau, New York, 1965, Vol.1, p.205

[17] Brysk H., Campbell P. M., Hammerling P., *Thermal conduction in laser fusion* Plasma Phys., 17, 473-484, (1975).

[18] Bychenkov V. Yu., Rozmus W., Brantov A. V., Tikhonchuk. V. T., *Phys. Rev. Lett*, 75, 4405, (1995).

[19] Cadjan M. G., Ivanov M. F., Langevin approach to plasma kinetics with Coulomb collisions , *Journal of Plasma Physics*, 61, 89-106 (1999).

[20] Celledoni E., McLachlan R. I., McLarren D. I., Owren R., Quispel G. R., Wright W. M., Energy-preserving Runge-Kutta methods, *Mathematical Modelling and Numerical Analysis*, 43, 645-649, (2009).

[21] Chapman S., Cowling T., The mathematical theory of non-uniform gases, , *Cambridge*, (1952).

[22] Colombo V., Coppa G. G. M., Ravetto P., New approach to the problem of the propagation of electrostatic perturbations in Vlasov plasmas, *Phys. Fluids B*, 4, 12 (1992).

[23] Cottrill L. A. et al., Kinetic and collisional effects on the linear evolution of fast ignition relevant instabilities, *Physics of Plasmas*, 15, 082108 (2008).

[24] Cercigianni C., On the Boltzmann equation with cut-off potentials, *Phys. Fluid* 10, 2097, (1967).

[25] Crouseilles N. , Filbet F., *Numerical approximation of collisional plasmas by high order methods*, Journal of Computational Physics, 201, 546-572, (2004).

[26] DeGroot S., Van Leuween W., Van Weer C., Relativistic kinetic theory, *North-Holland* (1980).

[27] Davies J. R., Bell A. R., Haines M. G., Guerin M., Short-pulse high-intensity laser-generated fast electron transport into thick solid targets , *Physical Review E* 56, 7193, (1997).

[28] Davies J. R., Norreys P. A., *Plasma Phys. Controlled Fusion*, 48, 1181, (2006).

[29] Dodd E. S. *et al.*, *Phys. Rev Lett.*, 88, 125001, (2002).

[30] Dubroca B. and Feugeas J.-L., Entropic Moment Closure Hierarchy for the Radiative Transfer Equation, *C. R. Acad. Sci. Paris Ser. I* , 329, 915-920, (1999).

[31] Duclous R., Dubroca B., Filbet F., Tikhonchuk V., High order resolution of the Maxwell-Fokker-Planck-Landau model intended for ICF application , *Journal Comp. Phys.* 228, 14, 5072-5100, (2009).

[32] Dudyński M. , Ekiel-Jeżewska M. L., On the linearized relativistic Boltzmann equation. I. Existence of solutions, *Comm. Math. Phys.* 115, 4, 607-629, (1988).

[33] Dudyński M. , Ekiel-Jeżewska M. L., Global existence proof for relativistic Boltzmann equation, *J. Statist. Phys.* 66, 3-4, 991-1001, (1992).

[34] Degond P. and Lucquin-Desreux B., The Fokker-Planck asymptotics of the Boltzmann collision operator in the Coulomb case, *M3AS* 2, 3, 167-182, (1992).

[35] Desvillettes L., On asymptotics of the Boltzmann equation when collisions become grazing, *Trans. Th. and Stat. Phys.* 21, 3, 259-276, (1992).

[36] Dieckmann M. E., Bret A. and Shukla P. K., Electron surfing acceleration by midly relativistic beams: wave magnetic field effects , *New Journal of Physics* 10, 013029, (2008).

[37] Dieckmann M. E., Frederiksen J. T., Bret A., Shukla P. K., Evolution of the fastest-growing relativistic mixed mode instability driven by a tenuous plasma beam in one and two dimensions , *Physics of Plasmas* 13, 112110, (2006).

[38] Eliasson B., Outflow boundary conditions for the Fourier transformed three-dimensional Vlasov-Maxwell system, *Journal of Computational Physics* 225 1508-1532, (2007).

[39] Elkina N. V., Büchner J., A new conservative unsplit method for the solution of the Vlasov equation, *Journal of Computational Physics* 213 862-875, (2006).

[40] Epperlein E. M., Haines M. G., Plasma transport coefficients in a magnetic field by direct numerical solution of the Fokker-Planck equation *Phys. Fluids*, 29 (4), (1986).

[41] Epperlein E. M. , Short R. W., A practical nonlocal model for electron transport in laers plasmas *Phys. Fluid B,* 3 (11), (1991).

[42] Fertig M. et al., Hybrid Code Development for the Numerical Simulation of Instationary Magnetoplasmadynamic Thrusters, *High Performance Computing in Science and Engineering '08 Transactions of the High Performance Computing Center, Stuttgart (HLRS),* (2008).

[43] Feugeas J.-L., Nicolai Ph. D., Ribeire X., Schurtz G. P., Tikhonchuk V. T. and Grech M., Modelling of two dimensional effects in hot spot relaxation in laser-produced plasmas, *Physics of Plasmas*, 15, 062701, (2008).

[44] Filbet F., Contribution l'analyse et la simulation numrique de l'quation de Vlasov, *PhD of the Universit Henri Poincar, Nancy*, (2001).

[45] Filbet F., Sonnendrücker E., Comparison of Eulerian Vlsov solvers, *Computer Physics Communications*, 150, 247-266 (2003).

[46] Francis G., Ram A. K., Bers A., Finite temperature effects on the space-time evolution of two-stream instabilities, *Physics of Fluids*, 29, 1, (1986).

[47] Froula et al., Quenching of the Nonlocal Electron Heat Transport by Large External Magnetic Fields in a Laser-Produced Plasma Measured with Imaging Thomson Scattering, *Physical Review Letters*, 98, 135001, (2007).

[48] Gardiner C. W., Handbook of stochastic methods, *Springer Verlag* , Berlin Heidelberg, New York, (1985).

[49] Glassey R. T., The Cauchy problem in kinetic theory, *SIAM*, Philadelphia, PA (1996).

[50] Glassey R. T., Strauss W. A., Asymptotic stability of the relativistic Maxwellian, *Publ. Res. Inst. Math. Sci. Kyo.*, 29, 2, 301-347 (1993).

[51] Glassey R. T., Strauss W. A., Asymptotic stability of the relativistic Maxwellian via fourteen moments, *Transport Theory Statist. Phys.*, 24, 4-5, 657-678 (1995).

[52] Gonzáles M., Contribution à l'étude numérique de l'hydrodynamique radiative: des expériences de chocs radioatifs aux jets astrophysiques, PhD thesis of Paris-Sud XI Univ, (2006).

[53] Gregori G. *et al.*, Effects of Nonlocal Transport on Heat-Wave Propagation, *Physical Review Letters*, 92, 20, (2004).

[54] Gurevich A. V., Zybin K. P., and Roussel-Dupré R., *Kinetic equation for high energy electrons in gases*, Phys. Lett. , A 237, 240, (1998).

[55] Hawreliak J. *et al.*, , *J. Phys. B*, 37, 1541, (2004).

[56] Haines M. G., Magnetic-field generation in laser fusion and hot-electron transport, *Can. J. Phys.*, 64, 912 (1986).

[57] Hao B., Sheng Z.-M., Ren C., Zhang J., Relativistic collisional current-filamentation instability and two-strem instability in dense plasma, *Can. J. Phys.*, 64, 912 (1986).

[58] Holm D. D., Tronci C., Geodesic Vlasov equations and their integrable moment closures, *Journal of geometric mechanics*, 1, 2 (2009).

[59] Huba J. D. *NRL PLASMA FORMULARY*,Beam Physics Branch Plasma Physics Division Naval Research Laboratory Washington, DC 20375.

[60] Humphries S., Charged particule beams, *Wiley Interscience*, New York, (1990).

[61] Jacobs G. B., Hesthaven J. S., High-order nodal discontinuous Galerkin particle-in-cell method on unstructured grids, *J. Comput. Phys.* 214, 96-121, (2006).

[62] Joachain C. J., Quantum collision theory, Amsterdam, 1983.

[63] Johnston T. W., Cartesian Tensor Scalar Product and Spherical Harmonic Expansions in Boltzmann's Equation, *Physical Review*, 120, 4, (1960).

[64] Kho T. H., Haines M. G., , *Phys. Fluids*, 29, 2665 (1986).

[65] Kingham R. J., Bell A. R., *Nonlocal Magnetic-Field Generation in Plasmas without Density Gradients*, Phys. Rew. Letter, 88, 045004, (2002).

[66] Kloeden P. E., Platten E., Numerical Solution of Stochastic Differential Equations, *Springer Verlag*, Berlin, Heidelberg, New York (1992).

[67] Lafon M., *Private communication* (2009).

[68] Landau L. D., Lifschitz E. M., Vol. 4. Quantum Electrodynamics.

[69] Larsson J., Hermitian Structure for the Linearized Vlasov-Poisson and Vlasov-Maxwell Equations, *Physical Review Letters*, 66, 11, (1991).

[70] Le Bourdiec S., Méthodes déterministes de résolution des équations de Vlasov-Maxwell relativistes en vue du calcul de la dynamique des ceintures de Van Allen, *PhD thesis*, (2007).

[71] Levermore C. D., Relating Eddington Factors to Flux Limiters, *J. Quant. Spectrosc. Radiat. Transfer* , 31, 149-160, (1984).

[72] Li et al., Monoenergetic-Proton-Radiography Measurements of Implosion Dynamics in Direct-Drive Inertial-Confinement Fusion, *Physical Review Letter*, 100, 225001 (2008).

[73] Liboff R. L., Kinetic theory. Classical, quantum, and relativistic descriptions, *Prentice-Hall International, Inc*, ISBN: 0-13-516097-9 (1990).

[74] Lifshitz E., Pitayevski L., Course of theoretical physics. Vol. 10. Physical Kinetics, Translated from the Russian by J. B. Sykes and R. N. Franklin. *Pergamon Press, Oxford Elmsford, N.Y.* (1981).

[75] Luciani J. F., Mora P., Virmont J., , *Phys. Rev. Lett.*, 51, 1664 (1983).

[76] Marsden J. E., Weinstein A., Morrison P. J., Hamiltonian structure of the BBGKY hierarchy, *DOE/ET-53088-122*, (1984).

[77] McClarren R. G., Lowrie R. B., The effects of slope limiting on asymptotic-preserving numerical methods for hyperbolic conservation laws, *J. Comput. Phys.*, 227, 23, 9711-9726 (2008).

[78] Manheimer W. M., Colombant D. G., Beam Deposition model for energetic electron transport in inertial fusion: Theory and initial results *Phys. of Plasmas*, 11, 1, (2004).

[79] Matte J.-P., Virmont J., Electron Heat transport down Steep Temperature Gradients *Physical Review Letters*, 49, 26, (1982).

[80] Minerbo G. N., Maximum entropy Eddington factors, *J. Quant. Spectrosc. Radiat. Transfer* , 20, 541-545, (1978).

[81] Mora P., Pellat R., Magnetic field generation in the underdense plasma *Phys. of Fluids*, 22, 12, (1979).

[82] Nanbu K. and Yonemura S., *J. Comput. Phys.* 145, 639, (1998).

[83] Nakashima K., Takabe H., Numerical study of pair creation by ultraintense lasers, *Physics of plasma* 9, 5, (2002).

[84] Nicolaï Ph. D., Feugeas J.-L. A., Schurtz G. P., A practical nonlocal model for heat transport in magnetized laser plasmas *Phys. of Plasmas*, 13, 032701, (2007).

[85] Pareschi L. Russo G., Asymptotic Preserving Monte Carlo Methods for the Boltzmann Equation, *Transport Theory and Statistical Physics*, 29, 415-430 (1998).

[86] Penrose O., , *Phys. Fluids*, 3, 258 (1960).

[87] Pétri J., Kirk, J. G., Numerical solution of the linear dispersion relation in a relativistic pair plasma, *Plasma Phys. Control Fusion*, 49, 297-308, (2007).

[88] Pisani F., Etude expérimentale de la propagation et du dépot d'énergie d'électrons rapides dans une cible solide ou comprimée par choc laser: application à l'allumeur rapide., *PhD thesis of Ecole Polytechnique*, (2000).

[89] Ramani A., Laval G., Heat flux reduction by electromagnetic instabilities, *Physics of Fluids*, 21, 980, (1978).

[90] Ridgers C. P., Magnetic fields and Non-local Transport in Laser Plasmas, *PhD thesis*, (2009).

[91] Ridgers C. P., Thomas A. G. R., Kingham R. J., Robinson A. P. L. Transport in the presence of inverse bremsstrahlung heating and magnetic fields *Physics of Plasmas*, 15, 9, 092311-092311-11 (2008).

[92] Ridgers C. P., Kingham R. J., Thomas A. G. R., Magnetic Cavitation and the Reemergence of Nonlocal Transport in Laser Plasmas *Phys. Rev. Lett.*, 100, 075003 (2008).

[93] Robinson A. P. L., Sherlock M., Magnetic collimation of fast electrons produced by ultraintense laser irradiation by structuring the target composition, *Physics of Plasmas*, 14, 083105, (2007).

[94] Robinson A. P. L., Bell A. R., Kingham R. J., Fast electron transport and ionization in a target irradiated by a high power laser, *Plasma Physics and Controlled Fusion*, 48, 1063, (2006).

[95] Sangam A., Morreeuw J.-P., Tikhonchuk V. T., Anisotropic instability in a laser heated plasma *Physics of Plasmas*, 14, 053111, (2008).

[96] Scovel C., Weinstein A., Finite dimensional Lie-Poisson approximations to Vlasov-Poisson equations *Communications on Pure and Applied Mathematics*, 47, 5, 683-709, (2006).

[97] Sedlàček Z., Nocera L., linear plasma oscillations in the Fourier transformed velocity space *Physics Letters A*, 296, 2-3, 117-124 (2002), and references therein.

[98] Sentoku Y., Kemp A., Numerical methods for particle simulations at extreme densities and temperatures: weighted particles, relativistic collisions and reduced currents, *J. Comput. Phys.* 227, 14, 6846-6861, (2008).

[99] Sentoku Y. *et al.*, *J. Phys. IV France* 133, 425-427, (2006).

[100] Sartori C. et Coppa G. G. M., Analysis of transient and asymptotic behavior in relativistic Landau damping, *Phys. Plasmas* 2 (11), (1995).

[101] Shoub E. C., Failure of the Fokker-Planck approximation to the Boltzmann integral for (1/r) potentials *Phys. Fluids*, 30, 5, (1987).

[102] Schmitz H., Grauer R., Comparison of time splitting and backsubstitution methods for integrating Vlasov's equation with magnetic fields, *Computer Physics Communications* 175, 86-92, (2006).

[103] Schurtz G. P., Nicolaï Ph. D., Busquet M., *Phys. of Plasmas*, 7, 4238, (2000).

[104] Sherlock M., Bell A. R., Kingham R. J., Robinson A. P. L., Bingham R., Non-Spitzer return currents in intense laser-plasma interactions *Physics of Plasmas*, 14, 102708, (2007).

[105] Sircombe N.J., Arber T. D., VALIS: A split-conservative shceme for the relativistic 2D Vlasov-Maxwell system, *Journal of Computational Physics* 228, 4773-4788, (2009).

[106] Stamper J. A., *Phys. Fluids*, 19, 758, (1976).

[107] Strain R. M., Y. Guo, Stability of the relativistic maxwellian in a collisional plasma *Communications in Mathematical Physics*, Volume 251, Number 2, (2004).

[108] Sunhahara A., Delletrez J. A., Stoeckl C. *et al.*, *Phys. Rev. Lett.*, 91, 095003, (2003).

[109] Takizuka T. and Abe H., *J. Comput. Phys.* 25, 205, (1977).

[110] Tatarakis *et al.*, Propagation Instabilities of High-Intensity Laser-Produced Electron Beams, *Physical Review Letter*, 90, 17, (2003).

[111] Thiell G., *Laser Part. Beams*, 16, 253, (1998).

[112] Thomas A. G. R., Kingham R. J., Ridgers C. P. Rapid self magnetization of laser speckles in plasmas by nonlinear anisotropic instability, *New Journal of Physics*, 11, 033001, (2009).

[113] Thomson J. J., Max C. E., Estabrook K. Magnetic Fields Due to Resonance-Absoption of Laser Light, *Physical Review Letters*, 35, 663, (1975).

[114] Turski L. A., Kaufman A. N. Canonical-dissipative formulation of relativistic plasma kinetic theory with self-consistent Maxwell field, *Physics Letters A*, 120, 7, (1987).

[115] Umeda T., Omura Y., Tominaga T., Matsumoto H. A new charge conservation method in electromagnetic particle-in-cell simulations, *Computer Physics Communications*, 156, 73-85, (2003).

[116] Villani C., A review of Mathematical topics in collisional kinetic theory, Handbook of fluid mechanics, *Handbook of Fluid Mechanics*, (2003).

[117] Yokota T., Nakao Y., Johzaki T., Mima K. Two-dimensional relativistic Fokker-Planck model for core plasma heating in fast ignition targets, *Physics of Plasmas*, 13, 022702, (2006).

[118] Weber S., *Private communication*, (2009).

[119] Winske D., Jackson A. E. Partial trapping of a beam in a cold collisional plasma, *Phys. Fluids*, 18, 3, 389-390, (1975).

[120] Wu B. Vlasov equation of plasma in magnetic field, *J. Phys. A: Math. Gen.*, 32, 5835-5844, (1999).

2.5 Appendix: Normalization of the relativistic Maxwellian distribution function with a non-zero drift velocity

The introduction of a macroscopic drift velocity $\mathbf{V_d}$ in the Jüttner-Synge distribution function (2.23) can be performed with respect to the maximum entropy principle [74]

$$f_{JS}(\mathbf{p}) = \text{const} \times \exp\left(-\frac{\gamma(\mathbf{V_d})}{m_e c^2 \tilde{\beta}_{th}^2}\left(m_e c^2 \gamma(\mathbf{p}) - \mathbf{V_d} \cdot \mathbf{p}\right)\right), \tag{2.49}$$

with the parameter $\tilde{\beta}_{th}^2 = \gamma(\mathbf{V_d}) \dfrac{k_B T_{JS}}{m_e c^2}$.

The drift velocity in f_{JS} satisfies a compatibility condition that is satisfied for any value of $\|\mathbf{V_d}\| \leq c$

$$\mathbf{Vd} = \int_{\mathbb{R}^3} \frac{\mathbf{p}}{m_e \gamma(\mathbf{p})} f_{JS}(\mathbf{p})\mathbf{dp} \Bigg/ \int_{\mathbb{R}^3} f_{JS}(\mathbf{p})\mathbf{dp} \,. \tag{2.50}$$

The constant in (2.49) is defined with the normalisation condition

$$n_{JS} = \int_{\mathbb{R}^3} f_{JS}(\mathbf{p})\mathbf{dp}. \tag{2.51}$$

In (2.52)-(2.57), we provide with detailed calculation leading to the normalisation constant of the relation (2.51)

$$\frac{n_{JS}}{\text{const}} = \int_{\mathbb{R}^3} \exp\left(-\frac{\gamma(\mathbf{V_d})}{m_e c^2 \tilde{\beta}_{th}^2}\left(m_e c^2 \gamma(\mathbf{p}) - \mathbf{V_d} \cdot \mathbf{p}\right)\right)\mathbf{dp}. \tag{2.52}$$

Setting $\mu_a = \gamma(\mathbf{V_d})/\tilde{\beta}_{th}^2$, performing the variable change $\bar{\mathbf{p}} = \mathbf{p}/m_e c$, and integrating on the pitch angle variable yields

$$\frac{n_{JS}}{4\pi (m_e c)^3 \text{const}} = \int_0^\infty exp\left(-\mu_a \sqrt{1 + \bar{p}^2}\right)\left[\frac{\sinh\left(\frac{\mu_a \|\mathbf{V_d}\| \bar{p}}{c}\right)}{\frac{\mu_a \|\mathbf{V_d}\| \bar{p}}{c}}\right]\bar{p}^2 d\bar{p}. \tag{2.53}$$

Then we develop the sinh as a difference of exponential functions and set $\bar{p} = \sinh(\Theta)$, $\alpha = \sinh^{-1}\left(\frac{\|\mathbf{V_d}\|}{c}\gamma(\mathbf{V_d})\right)$. It comes

$$\frac{n_{JS}}{4\pi (m_e c)^3 \text{const}} = \pm \frac{c}{4\|\mathbf{V_d}\|\mu_a} \int_0^\infty exp\left(-\frac{\mu_a}{\gamma(\mathbf{V_d})}\cosh\left(\Theta \mp \alpha\right)\right)\sinh(2\Theta) d\Theta. \tag{2.54}$$

Now we perform the variable changes $\zeta = \Theta \mp \alpha$. We obtain

$$\frac{n_{JS}}{4\pi (m_e c)^3 \text{const}} = \pm \frac{c}{4\|\mathbf{V_d}\|\mu_a} \int_0^\infty exp\left(-\frac{\mu_a}{\gamma(\mathbf{V_d})}\cosh\left(\zeta\right)\right)\sinh\left(2(\zeta \pm \alpha)\right) d\zeta. \tag{2.55}$$

Finally, we develop the sinh as products of sinh and cosh and find

$$\frac{n_{JS}}{4\pi (m_e c)^3 \text{const}} = \frac{c \sinh(2\alpha)}{2\|\mathbf{V_d}\|\mu_a} K_2\left(\frac{\mu_a}{\gamma(\mathbf{V_d})}\right). \tag{2.56}$$

The JS distribution function becomes

$$f_{JS}(\mathbf{p}) = \frac{n_{JS}}{4\pi(m_e c)^3\gamma(\mathbf{V_d})\left[\tilde{\beta}_{th}^2 K_2\left(\tilde{\beta}_{th}^{-2}\right)\right]}\exp\left(-\frac{\gamma(\mathbf{V_d})\left(m_e c^2\gamma(\mathbf{p}) - \mathbf{V_d}\cdot\mathbf{p}\right)}{\left[m_e c^2\widetilde{\beta_{th}}^2\right]}\right) .$$

As for numerical considerations, in order to recover a smooth transition between the relativistic and nonrelativistic limits of the distribution function moments, the following form, wich is similar to an exponential scaling on the modified Bessel function, may be more appropriate. If $\mathbf{V_d} = \mathbf{0}$, this gives

$$f_{JS}(\mathbf{p}) = \frac{n_{JS}}{4\pi(m_e c)^3\beta_{th}^2\left(K_2\left(\beta_{th}^{-2}\right)\exp\left[\beta_{th}^{-2}\right]\right)}\exp\left[-(\gamma(\mathbf{p}) - 1)/\beta_{th}^2\right] . \tag{2.57}$$

Chapter 3

High order numerical schemes for the Vlasov-Maxwell model: the collisionless transport

3.1 Introduction

In this chapter, we shall focus on the collective effects, which are a specific feature of plasmas, and ignore the collisional effects. We present the model, its properties, and discuss on numerical schemes for their discrete implementation in a deterministic solver. Finally we present valdiation test quantifying the accuracy and robustness of the methods at low grid resolution.

3.2 The free-streaming kinetic model

3.2.1 The nonrelativistic Vlasov-Maxwell system

Two particle species (ions and electrons) are considered: ions are supposed to be fixed assuming an electron-ion mass ratio $m_e/m_i \ll 1$, whereas the evolution of electrons is described by a distribution function $f_e(t, \mathbf{x}, \mathbf{v})$ where for the more general case $(\mathbf{x}, \mathbf{v}) \in \Omega \times \mathbb{R}^3$, with $\Omega \subset \mathbb{R}^3$. The non-relativistic Vlasov equation, without collision source term is given by

$$\frac{\partial f_e}{\partial t} + \nabla_{\mathbf{x}} \cdot (\mathbf{v}\, f_e) + \frac{q_e}{m_e} \nabla_{\mathbf{v}} \cdot ((\mathbf{E} + \mathbf{v} \times \mathbf{B})\, f_e) = 0\,, \tag{3.1}$$

where $q_e = -e$ is the charge of an electron and m_e is the mass of an electron. The electromagnetic fields $(\mathbf{E}, \mathbf{B})$ are given by the classical Maxwell system

$$\begin{cases} \dfrac{\partial \mathbf{E}}{\partial t} - c^2\, \nabla_{\mathbf{x}} \times \mathbf{B} = -\dfrac{\mathbf{j}}{\epsilon_0}, \\[2ex] \dfrac{\partial \mathbf{B}}{\partial t} + \nabla_{\mathbf{x}} \times \mathbf{E} = 0, \end{cases} \tag{3.2}$$

where ϵ_0 represents the permittivity of vacuum and c is the speed of light. The current density is given by

$$\mathbf{j}(t, \mathbf{x}) = q_e \int_{\mathbb{R}^3} f_e(t, \mathbf{x}, \mathbf{v})\, \mathbf{v}\, d^3v.$$

Moreover, Maxwell system's is supplemented by Gauss law's

$$\nabla_{\mathbf{x}} \cdot \mathbf{E} = \frac{\rho}{\epsilon_0}, \quad \nabla_{\mathbf{x}} \cdot \mathbf{B} = 0, \tag{3.3}$$

where ρ is the charge density:

$$\rho = q_e\,(n_e - n_o) = q_e \left(\int_{\mathbb{R}^3} f_e(t, \mathbf{x}, \mathbf{v})\, d^3v - n_0 \right),$$

and n_0/Z is the initial ion density.

In this model, the Vlasov equation stands for the invariance of the distribution function along the particles trajectories under the effects of electro-magnetic fields $\mathbf{E}$ and $\mathbf{B}$. The Vlasov transport terms, in the left-hand side of equation (8.1), are written in their conservative form, but they can also be written in an equivalent non-conservative form, while the Maxwell equations (3.2)-(3.3) provide with a complete self-consistent description of low-frequency electromagnetic fields. The coupling between both is performed *via* the Lorentz force term $\mathbf{E} + \mathbf{v} \times \mathbf{B}$ in the Vlasov equation, and the current source terms in the Maxwell equations. The Vlasov-Maxwell system (8.1)-(3.2)-(3.3) is strictly equivalent to (8.1)-(3.2) provided the Gauss's laws (3.3) are initially satisfied. This gives a compatibility condition at initial time. In the remainder of the section, we only consider a periodic or infinite space domain. The mass is preserved with respect to time for the Vlasov-Maxwell system, *i.e.* system (8.1)-(3.2) without collision operators

$$\frac{d}{dt} \int_{\mathbb{R}^3 \times \mathbb{R}^3} f_e(t, \mathbf{x}, \mathbf{v}) d^3x\, d^3v \;=\; 0, \;\; t \geq 0. \tag{3.4}$$

The conservation of momentum can be written as

$$\begin{aligned} & \frac{d}{dt} \left(\int_{\mathbb{R}^3} \left[\frac{m_e}{q_e} \mathbf{j}(t, \mathbf{x}) + \epsilon_0 \left(\mathbf{E}(t, \mathbf{x}) \times \mathbf{B}(t, \mathbf{x}) \right) \right] d^3x \right) \\ = \;\; & q_e \int_{\mathbb{R}^3} \mathbf{E}(t, \mathbf{x}) n_e(t, \mathbf{x}) d^3x + \int_{\mathbb{R}^3} \epsilon_0 \mathbf{E}(t, \mathbf{x}) \times \left(\nabla_{\mathbf{x}} \mathbf{E}(t, \mathbf{x}) \right) d^3x \;, \;\; t \geq 0. \end{aligned} \tag{3.5}$$

Moreover, the conservation of energy can be proved for the Vlasov-Maxwell system by multiplying equation (8.1) by $m_e \, \|\mathbf{v}\|^2/2$ and integrating it in the velocity space. We obtain after an integration by parts

$$\frac{1}{2} \frac{d}{dt} \int_{\mathbb{R}^3} \left\{ \epsilon_0 \, \|\mathbf{E}(t, \mathbf{x})\|^2 \; + \; \frac{1}{\mu_0} \|\mathbf{B}(t, \mathbf{x})\|^2 \; + \; \left[\int_{\mathbb{R}^3} m_e \|\mathbf{v}\|^2 \, f_e(t, \mathbf{x}, \mathbf{v}) d^3v \right] \right\} d^3x \;=\; 0, \;\; t \geq 0, \tag{3.6}$$

with $c^2 \, \epsilon_0 \, \mu_0 \;=\; 1$. The Vlasov-Maxwell system also conserves the kinetic entropy

$$\frac{d}{dt} H(t) \;=\; \frac{d}{dt} \int_{\mathbb{R}^3 \times \mathbb{R}^3} f_e(t, \mathbf{x}, \mathbf{v}) \log(f_e(t, \mathbf{x}, \mathbf{v}))\, d^3x\, d^3v \;=\; 0, \;\; t \geq 0. \tag{3.7}$$

3.2.2 The relativistic Vlasov-Maxwell system

In the relativistic regime, we introduce the momemtum $\mathbf{p}$ and associated Lorentz factor $\gamma(\mathbf{p}) = \sqrt{1 + p^2/(m_e c)^2}$. The distribution function $f_e(t, \mathbf{x}, \mathbf{p})$ is solution of the relativistic extension of equation (8.1)

$$\frac{\partial f_e}{\partial t} \; + \; \nabla_{\mathbf{x}} \cdot (\mathbf{v} \, f_e) \; + \; q_e \, \nabla_{\mathbf{p}} \cdot ((\mathbf{E} \; + \; \mathbf{v} \times \mathbf{B}) \, f_e) \;=\; 0 \;, \tag{3.8}$$

coupled to the Maxwell equations

$$\left\{ \begin{aligned} & \frac{\partial \mathbf{E}}{\partial t} \; - \; c^2 \, \nabla_{\mathbf{x}} \times \mathbf{B} \;=\; -\frac{\mathbf{j}}{\epsilon_0}, \\ & \frac{\partial \mathbf{B}}{\partial t} + \nabla_{\mathbf{x}} \times \mathbf{E} \;=\; 0, \\ & \nabla_{\mathbf{x}} \cdot \mathbf{E} \;=\; \frac{\rho}{\epsilon_0}, \quad \nabla_{\mathbf{x}} \cdot \mathbf{B} \;=\; 0, \\ & \mathbf{j}(t, \mathbf{x}) \;=\; q_e \int_{\mathbb{R}^3} f_e(t, \mathbf{x}, \mathbf{p}) \, \mathbf{v} \, d^3p. \end{aligned} \right. \tag{3.9}$$

Local conservation of charge

Multiplying the equation (3.8) by q_e, and integrating over momentum yields

$$\frac{\partial}{\partial t}\int_{\mathbb{R}^3}(q_e f_e)d^3p + \nabla_{\mathbf{x}}\cdot\int_{\mathbb{R}^3}(q_e\mathbf{v}f_e d^3p + q_e\int_{\mathbb{R}^3}\nabla_{\mathbf{p}}\cdot(f_e\,[q_e(\mathbf{E}+\mathbf{v}\wedge\mathbf{B})])\,d^3p = 0\,. \tag{3.10}$$

The distribution function satisfies $f_e \xrightarrow[p\to 0]{} \infty$. Therefore, for all vector field $\mathbf{X}$

$$\int_{\mathbb{R}^3}\nabla_{\mathbf{p}}\cdot(\mathbf{X}f_e)d^3p = 0\,. \tag{3.11}$$

The equation for conservation of the charge reads

$$\frac{\partial}{\partial t}\int_{\mathbb{R}^3}(q_e f_e)d^3p + \nabla_{\mathbf{x}}\cdot\int_{\mathbb{R}^3}(q_e\mathbf{v}f_e)d^3p = 0\,, \tag{3.12}$$

and can be rewritten

$$\frac{\partial}{\partial t}\rho_e + \nabla_{\mathbf{x}}\cdot\mathbf{j} = 0\,. \tag{3.13}$$

Local conservation of energy

The combination of Ampère (3.14) and Faraday equations (3.15)

$$\nabla_{\mathbf{x}}\times\mathbf{B} = \mu_0\mathbf{j} + \frac{1}{c^2}\frac{\partial}{\partial t}\mathbf{E}\,, \tag{3.14}$$

$$\frac{\partial}{\partial t}\mathbf{B} + \nabla_{\mathbf{x}}\times\mathbf{E} = \mathbf{0}\,. \tag{3.15}$$

gives

$$\frac{\partial}{\partial t}\left(\frac{\epsilon_0 E^2}{2} + \frac{B^2}{2\mu_0}\right) + \nabla_{\mathbf{x}}\cdot\mathbf{S} + \mathbf{j}\cdot\mathbf{E} = 0\,, \tag{3.16}$$

where $\mathbf{S} = \dfrac{\mathbf{E}\wedge\mathbf{B}}{\mu_0}$ is the Poynting vector.
The power term created by the work of the electric field $\mathbf{j}\cdot\mathbf{E}$ is obtained by multiplying the Vlasov equation by $m_e c^2\gamma(\mathbf{p})$, and multiplying over momentum

$$\begin{aligned}\int_{\mathbb{R}^3} m_e c^2\gamma(\mathbf{p})\frac{\partial f_e}{\partial t}d^3p \quad &+ \quad \int_{\mathbb{R}^3} m_e c^2\gamma(\mathbf{p})\mathbf{v}\nabla_{\mathbf{x}} f_e d^3p + \mathbf{E}\cdot\int_{\mathbb{R}^3} q_e m_e c^2\gamma(\mathbf{p})\nabla_{\mathbf{p}} f_e d^3p \\ &+ \quad \int q_e m_e c^2\gamma(\mathbf{p})\,(\mathbf{v}\times\mathbf{B})\cdot\nabla_{\mathbf{p}} f_e d^3p = 0\,.\end{aligned} \tag{3.17}$$

Then, using only integration by parts and the properties

$$\mathbf{v} = m_e c^2\nabla_{\mathbf{p}}\gamma(\mathbf{p})\,, \tag{3.18}$$

$$f_e \xrightarrow[p\to 0]{} \infty\,, \tag{3.19}$$

$$\int_{\mathbb{R}^3}\nabla_{\mathbf{p}}\cdot(\mathbf{X}f_e)d^3p = 0 \qquad \forall\,\mathbf{X}\,, \tag{3.20}$$

we obtain

$$\mathbf{j}\cdot\mathbf{E} = \frac{\partial}{\partial t}\int_{\mathbb{R}^3} m_e c^2 \gamma(\mathbf{p}) f_e d^3p + \nabla_{\mathbf{x}}\cdot\int_{\mathbb{R}^3} m_e c^2\gamma(\mathbf{p})\mathbf{v} f_e d^3 p\ . \tag{3.21}$$

Finally, the local energy conservation reads

$$\frac{\partial}{\partial t}\left(\frac{\epsilon_0 E^2}{2} + \frac{B^2}{2\mu_0} + \int_{\mathbb{R}^3} m_e c^2\gamma(\mathbf{p}) f_e d^3p\right) + \nabla_{\mathbf{x}}\cdot\left(\mathbf{S} + \int_{\mathbb{R}^3} m_e c^2\gamma(\mathbf{p})\mathbf{v} f_e d^3p\right) = 0\ . \tag{3.22}$$

Global conservation laws

In the case of a periodic or infinite domain in space, the conservation laws, (3.4), (3.5), (3.6), and (3.7), valid in the nonrelativistic limit, can be extended to the relativistic regime

$$\frac{d}{dt}\int_{\mathbb{R}^3\times\mathbb{R}^3} f_e(t,\mathbf{x},\mathbf{p}) d^3x\, d^3p \ = \ 0,\ \ t\geq 0\ , \tag{3.23}$$

$$\begin{aligned}\frac{d}{dt}&\left(\int_{\mathbb{R}^3}\left[\int_{\mathbb{R}^3}\mathbf{p}\, f_e(t,\mathbf{x},\mathbf{p})d^3p + \epsilon_0\left(\mathbf{E}(t,\mathbf{x})\times\mathbf{B}(t,\mathbf{x})\right)\right]d^3x\right)\\ &= q_e\int_{\mathbb{R}^3}\mathbf{E}(t,\mathbf{x})n_e(t,\mathbf{x})d^3x + \int_{\mathbb{R}^3}\epsilon_0\mathbf{E}(t,\mathbf{x})\times\left(\nabla_{\mathbf{x}}\mathbf{E}(t,\mathbf{x})\right)d^3x\ ,\ \ t\geq 0.\end{aligned} \tag{3.24}$$

$$\begin{aligned}\frac{d}{dt}\quad\int_{\mathbb{R}^3}\ &\left\{\frac{\epsilon_0}{2}\left\|\mathbf{E}(t,\mathbf{x})\right\|^2 \ + \ \frac{1}{2\mu_0}\left\|\mathbf{B}(t,\mathbf{x})\right\|^2 + \right.\\ &\left.\left[\int_{\mathbb{R}^3} m_e c^2\left(\gamma(\mathbf{p})-1\right) f_e(t,\mathbf{x},\mathbf{p})d^3p\right]\right\} d^3x \ = \ 0,\ \ t\geq 0\ ,\end{aligned} \tag{3.25}$$

$$\frac{d}{dt}H(t) \ = \ \frac{d}{dt}\int_{\mathbb{R}^3\times\mathbb{R}^3} f_e(t,\mathbf{x},\mathbf{p})\log(f_e(t,\mathbf{x},\mathbf{p}))\, d^3x\, d^3p \ = \ 0,\ \ t\geq 0\ . \tag{3.26}$$

3.3 Numerical scheme for the nonrelativistic free-streaming transport

We present a finite volume approximation for the Vlasov-Maxwell system (8.1)-(3.2) without collision operators. Indeed, it is crucial to approximate accurately the transport part of the system to assess the collective behavior[1] of the plasma, that occurs typically at a shorter time scale than the collision processes. We introduce a uniform $1D_x$ space discretization $(x_{i+1/2})_{i\in I}$, $I\subset\mathbb{N}$, of the interval $(0, L_1)$, in the direction denoted by the index 1. The associated space variable is denoted by x_1. We define the control volumes $C_{i,\mathbf{j}} = (x_{i-1/2}, x_{i+1/2})\times(\mathbf{v}_{\mathbf{j-1/2}}, \mathbf{v}_{\mathbf{j+1/2}})$, and the size of a control volume in one direction in space Δx and velocity Δv.

---

[1] By collective effects, we denote here the self-consistent interaction of electromagnetic fields and particles. Some collective effects are also considered in the collision processes, which make two particles interact *via* the Coulomb field. The self-consistent electrostatic field then screens the long range Coulomb potential and removes the singularity in the Fokker-Plank-Landau operator.

The velocity variable $\mathbf{v} = {}^t(v_1, v_2, v_3)$ is discretized on the grid $\mathbf{v_j} = \mathbf{j}\,\Delta v = {}^t(v_{j_1}, v_{j_2}, v_{j_3})$ with $\mathbf{j} = {}^t(j_1, j_2, j_3) \in \mathbb{Z}^3$. Moreover we note $\mathbf{v_{j+1/2}} = {}^t(j_1 + 1/2, j_2 + 1/2, j_3 + 1/2)\,\Delta v$. Finally, the time discretization is defined as $t^n = n\Delta t$, with $n \in \mathbb{N}$.

Let $f^n_{i,\mathbf{j}}$ be an average approximation of the distribution function on the control volume $C_{i,\mathbf{j}}$ at time t^n, that is

$$f^n_{i,\mathbf{j}} \simeq \frac{1}{\Delta x\,\Delta v^3} \int_{C_{i,\mathbf{j}}} f(t^n, x, \mathbf{v}) dx\, d^3v.$$

Moreover since the discretization is presented in a simple $1D_x$ space geometry, the electric and magnetic fields have the following structure: $\mathbf{E} = {}^t(E_1(t, x_1)), E_2(t, x_1), 0)$, $\mathbf{B} = {}^t(0, 0, B_3(t, x_1))$. Hence we denote by ${}^t(E^n_{1,i}, E^n_{2,i})$ an approximation of the electric field ${}^t(E_1, E_2)$ whereas $B^n_{3,i}$ represents an approximation of the magnetic field B_3 in the control volume $(x_{i-1/2}, x_{i+1/2})$ at time t^n.

3.3.1 Second order approximation of a one dimensional kinetic equation

For the sake of simplicity, we focus on the discretization of a $1D_x$ kinetic transport equation; the extension to higher dimensions is straightforward on a grid. The generic $1D_x$ scheme is applied in the five phase space directions, without requiring time splitting techniques between transport terms. In this section, the index 1 is dropped both in space and velocity directions, for this simple $1D_x$ geometry.

Let us consider the following equation for $t \geq 0$ and $x \in (0, L)$,

$$\frac{\partial f}{\partial t} + v\frac{\partial f}{\partial x} = 0\,, \tag{3.27}$$

where the velocity $v > 0$ is given. By symmetry it is possible to recover the case when v is negative. In the following we skip the velocity variable dependency of the distribution function. Using a time explicit Euler scheme and integrating the $1D$ Vlasov equation on a control volume $(x_{i-1/2}, x_{i+1/2})$, it yields

$$f^{n+1}_i = f^n_i - \frac{\Delta t}{\Delta x}\left[\mathcal{F}^n_{i+1/2} - \mathcal{F}^n_{i-1/2}\right], \tag{3.28}$$

where $\mathcal{F}^n_{i+1/2}$ represents a conservative approximation of the flux $v\, f(t^n, x_{i+1/2})$ at the interface $x_{i+1/2}$.

The next step consists of the approximation of the fluxes and the reconstruction of the distribution function. With this aim, we approximate the distribution function $f(t^n, x)$ by $f_h(x)$ using a second order accurate approximation of the distribution function on the interval $[x_{i-1/2}, x_{i+1/2})$, with a reconstruction technique by primitive [7]

$$f_h(x) = f^n_i + \epsilon^+_i \frac{(x - x_i)}{\Delta x}(f^n_{i+1} - f^n_i). \tag{3.29}$$

We introduce the limiter

$$\epsilon^+_i = \begin{cases} 0 & \text{if } (f^n_{i+1} - f^n_i)(f^n_i - f^n_{i-1}) < 0, \\ \min\left(1, \dfrac{2\left(\|f^0\|_\infty - f^n_i\right)}{f^n_i - f^n_{i+1}}\right) & \text{if } (f^n_{i+1} - f^n_i) < 0\,, \\ \min\left(1, \dfrac{2\, f^n_i}{f^n_{i+1} - f^n_i}\right) & \text{else,} \end{cases} \tag{3.30}$$

and set $\mathcal{F}^n_{i+1/2} = v\, f_h(x_{i+1/2})$. This type of limiter introduces a particular treatment for extrema. At this price only (dissipation at extrema), we were able to recover correctly the Two-Stream Instabililty tests I and IV, without oscillations destroying the salient features of the distribution function structure. Another choice for the limitation consits in choosing the “Van Leer’s one parameter family of the minmod limiters” [15, 24]

$$\epsilon_i^+(f_{i+1}^n - f_i^n) = \mathrm{minmod}\left(b\frac{(f_{i+1}^n - f_i^n)}{\Delta x}, \frac{(f_{i+1}^n - f_{i-1}^n)}{2\Delta x}, b\frac{(f_i^n - f_{i-1}^n)}{\Delta x}\right), \tag{3.31}$$

where

$$\mathrm{minmod}(x, y, z) \equiv \max(0, \min(x, y, z)) + \min(0, \max(x, y, z)) \ , \quad (x, y, z) \in \mathbb{R},$$

and $1 \leq b \leq 2$. The importance of the choice of limiters will be observed on the Two-Stream Instability test I.

Finally, this reconstruction ensures the conservation of the average and the positivity on $f_h(x)$ [7].

3.3.2 Fourth order transport scheme

We turn now to a higher order approximation (fourth order MUSCL TVD scheme) [25]. This scheme has also been considered in [2], in the frame of VFRoe schemes for the shallow water equations, where the authors proposed an additional limitation. Here we note that an optimized limitation procedure is possible in our case, breaking the similar treatment for both right and left increments, and taking advantage of the structure of the flux in the non-relativistic Vlasov equation: the force term does not depend of the advection variable.

For this MUSCL scheme, we only give here the algorithm for the implementation of this scheme and refer to [2], [25] for the derivation procedure of this scheme.
The high order flux at the interface $x_{i+1/2}$, at time t^n reads

$$\mathcal{F}_{i+1/2}^n = \mathcal{F}\left(f_{i,r}^n, f_{i+1,l}^n\right) = \begin{cases} v f_{i,r}^n & \text{if} \quad v > 0 \ , \\ v f_{i+1,l}^n & \text{if} \quad v < 0 \ . \end{cases}$$

This numerical flux involves the reconstructed states: $f_{i,r}^n = f_i^n + (\Delta f)_i^+$ and $f_{i,l}^n = f_i^n + (\Delta f)_i^-$, where $(\Delta f)_i^\pm$ are the reconstruction increments.
An intermediate state f_i^*, defined by $\frac{1}{3}\left(f_{i,r}^n + f_i^* + f_{i,l}^n\right) = f_i^n$ is introduced. It is shown in [2] that the introduction of this intermediate state preserves, provided the CFL condition is formally divided by three, the positivity of the distribution function. Following [25] and [2], the fourth order MUSCL reconstruction reads

Algorithm of reconstruction.

Compute

$$(\Delta f)_i^- = -\frac{1}{6}\left(2\Delta^* \bar{f}_{i-1/2} + \Delta^* \tilde{f}_{i+1/2}\right),$$

$$(\Delta f)_i^+ = \frac{1}{6}\left(\Delta^* \bar{f}_{i-1/2} + 2\Delta^* \tilde{f}_{i+1/2}\right),$$

where

$$\Delta^* \bar{f}_{i-1/2} = \mathrm{minmod}(\Delta^* f_{i-1/2}, 4\Delta^* f_{i+1/2}),$$

$$\Delta^* \tilde{f}_{i+1/2} = \mathrm{minmod}(\Delta^* f_{i+1/2}, 4\Delta^* f_{i-1/2})$$

and

$$\Delta^* f_{i+1/2} = \Delta f_{i+1/2} - \frac{1}{6}\Delta^3 \bar{f}_{i+1/2},$$

$$\Delta^3 \bar{f}_{i+1/2} = \Delta \bar{f}^a_{i-1/2} - 2\Delta \bar{f}^b_{i+1/2} + \Delta \bar{f}^c_{i+3/2},$$

with

$$\Delta \bar{f}^a_{i-1/2} = \mathrm{minmod}(\Delta f_{i-1/2}, 2\Delta f_{i+1/2}, 2\Delta f_{i+3/2}),$$

$$\Delta \bar{f}^b_{i+1/2} = \mathrm{minmod}(\Delta f_{i+1/2}, 2\Delta f_{i+3/2}, 2\Delta f_{i-1/2}),$$

$$\Delta \bar{f}^c_{i+3/2} = \mathrm{minmod}(\Delta f_{i+3/2}, 2\Delta f_{i-1/2}, 2\Delta f_{i+1/2}),$$

with the notation $\Delta f_{i+1/2} = f_{i+1} - f_i$.

Reminding that the minmod limiter is given by

$$\mathrm{minmod}(x, y) = \begin{cases} 0, & \text{if } xy \leq 0, \\ x & \text{if } |x| \leq |y|, \\ y & \text{else}, \end{cases} \tag{3.32}$$

with $(x, y) \in \mathbb{R}^3$. The limitation proposed in [2] is then applied and allows the positivity of the reconstructed states to be satisfied.

Algorithm for the limitation involving the intermediate state.

Compute $(\Delta f)_i^{\mathrm{lim},\pm}$ such that

$$f_i^n + (\Delta f)_i^{\mathrm{lim},-} \geq 0,$$

$$f_i^n + (\Delta f)_i^{\mathrm{lim},+} \geq 0,$$

and

$$f_i^* = f_i^n - (\Delta f)_i^{\mathrm{lim},-} - (\Delta f)_i^{\mathrm{lim},+} \geq 0.$$

This limitation reads:

$$\begin{cases} (\Delta f)_i^{\mathrm{lim},-} = \theta \max\Big((\Delta f)_i^-, -f_i^n\Big), \\ (\Delta f)_i^{\mathrm{lim},+} = \theta \max\Big((\Delta f)_i^+, -f_i^n\Big), \end{cases}$$

where

$$\theta = \begin{cases} 1, \quad \text{if} \quad \max\Big((\Delta f)_i^-, -f_i^n\Big) + \max\Big((\Delta f)_i^+, -f_i^n\Big) \leq 0\,, \\ \min\left(1, \dfrac{f_i^n}{\max\Big((\Delta f)_i^-, -f_i^n\Big) + \max\Big((\Delta f)_i^+, -f_i^n\Big)}\right) \quad \text{otherwise.} \end{cases}$$

3.3.3 Application to the Vlasov-Maxwell system.

We exactly follow the same idea to design a scheme for the full Vlasov equation in phase space $(\mathbf{x}, \mathbf{v}) \in \Omega \times \mathbb{R}^3$. In addition, a centered formulation for the electromagnetic fields is chosen:

$$\mathbf{E}^{n+1/2} = \frac{1}{2}\Big(\mathbf{E}^{n+1} + \mathbf{E}^n\Big) \quad \text{and} \quad \mathbf{B}^{n+1/2} = \frac{1}{2}\Big(\mathbf{B}^{n+1} + \mathbf{B}^n\Big). \tag{3.33}$$

The discretization of the Maxwell equations (3.2)-(3.3) is performed *via* an implicit θ-scheme, with $\theta = 1/2$, which corresponds to the Crank-Nicholson scheme and thus preserves the total discrete energy. This discretization is presented in a simple $1D_x$ space geometry. The electric field $\mathbf{E} = {}^t(E_1, E_2, 0)$ and the magnetic field $\mathbf{B} = {}^t(0, 0, B_3)$ are collocated on the discrete grid. These fields are solution of the system

$$\begin{cases} \dfrac{E_{1,i}^{n+1} - E_{1,i}^n}{\Delta t} = -\dfrac{J_{1,i}^n}{\epsilon_0}, \\ \dfrac{E_{2,i}^{n+1} - E_{2,i}^n}{\Delta t} + c^2\,\dfrac{B_{3,i+1}^{n+1/2} - B_{3,i-1}^{n+1/2}}{2\Delta x} = -\dfrac{J_{2,i}^n}{\epsilon_0}, \\ \dfrac{B_{3,i}^{n+1} - B_{3,i}^n}{\Delta t} + \dfrac{E_{2,i+1}^{n+1/2} - E_{2,i-1}^{n+1/2}}{2\Delta x} = 0. \end{cases} \tag{3.34}$$

This scheme is well-suited for the situations involving low frequency self-generated electric and magnetic fields, and is design to minimize the numerical dissipation. The design of this scheme is not tuned

to reduce the numerical dispersion associated to the propagation of high frequency, shorte-pulse electromagnetic waves.
The approximation for the current in (3.34) J_1^n and J_2^n has been chosen such as

$$J_{1,i}^n = \sum_{\mathbf{j}\in\mathbb{Z}^3} \Delta v^3\, v_{j_1}\, f_{i,\mathbf{j}}^n \quad \text{and} \quad J_{2,i}^n = \sum_{\mathbf{j}\in\mathbb{Z}^3} \Delta v^3\, v_{j_2}\, f_{i,\mathbf{j}}^n. \tag{3.35}$$

Unfortunately, these expressions do not preserve the total energy when slopes limiters are active in the discrete Vlasov solver, but we will show that they have the important feature to reproduce the discrete Two-Stream dispersion relation.

First, we remind discrete properties concerning positivity, mass and energy conservation [7] of the second order scheme (3.28)-(3.29) coupled with (3.33)-(3.35), considering the magnetic component.

Proposition 1. *Let the initial datum* $(f_{\mathbf{i},\mathbf{j}}^0)_{\mathbf{i},\mathbf{j}\in\mathbb{Z}^3}$ *be nonnegative and assume the following CFL type condition on the time step*

$$\Delta t \le C \min(\Delta x, \Delta v), \tag{3.36}$$

where $C > 0$ *is related to the maximum norm of the electric and magnetic fields and the upper bound of the velocity domain.*

Then the scheme (3.28)-(3.29) coupled with (3.33)-(3.35), when extended to the infinite $3D_{\mathbf{x}} \times 3D_{\mathbf{v}}$ *geometry, gives a nonnegative approximation, preserves total mass and energy when slopes limiters are not active on the transport in the velocity directions*

$$\frac{1}{2}\sum_{\mathbf{i}\in I} \Delta x^3 \left\{ \epsilon_0 \|\mathbf{E}_{\mathbf{i}}^n\|^2 + \frac{1}{\mu_0}\|\mathbf{B}_{\mathbf{i}}^n\|^2 + m_e \left[\sum_{\mathbf{j}\in\mathbb{Z}^3} \Delta v^3 \|\mathbf{v}_{\mathbf{j}}\|^2 f_{\mathbf{i},\mathbf{j}}^n \right] \right\} = C^0 , \; n \in \mathbb{N}.$$

Remark 1. *Both the second order scheme and its fourth order extension preserve the positivity of the distribution function, provided the CFL criteria are satisfied. The positivity is essential to describe correctly the high energy tail of the distribution function, where the particle density is low. In all the tests presented, the time increment is chosen small enough to satisfy this CFL condition, together with the diffusive-type CFL condition that comes from the collision operators. Here we consider centered numerical schemes (if slope limiters are not active), in order to preserve the energy. This is the reason why we considered only schemes having even order.*

In addition to these properties, we justify our choice for the numerical current thanks to a discrete dispersion relation on the two-stream instability. In the rest of the section, we drop the index 1 on the variables x_1, v_1, E_1 and J_1, because the transport is considered $1D_x \times 1D_v$.

Proposition 2. *Consider the second order scheme (3.28)-(3.29) coupled with (3.33)-(3.35), when slope limiters are not active, to approximate the Vlasov-Ampère system*

$$\begin{cases} \dfrac{\partial f}{\partial t} + v\dfrac{\partial f}{\partial x} + \dfrac{q_e}{m_e} E \dfrac{\partial f}{\partial v} = 0, \\[2ex] \dfrac{\partial E}{\partial t} = -\dfrac{J}{\epsilon_0}. \end{cases} \tag{3.37}$$

Then the definition (3.35) for the current J *defines a discrete dispersion relation that converges toward the continuous dispersion relation when* Δv, Δx *and* Δt *tend to* 0.

Proof: The Two-Stream Instability configuration can be fully analyzed with the Vlasov-Ampère system (3.37) extracted from equations (8.1)-(3.3). The dispersion relation for a perturbation $f^{(1)} \propto e^{i(k\,x - \omega\,t)}$ of an initial equilibrium state $f^{(0)}$, with $\|f^{(1)}\| \ll \|f^{(0)}\|$, then reads

$$1 + \frac{q_e^2}{\epsilon_0\, m_e} \int_{\mathbb{R}} \frac{v}{\omega(\omega - k\,v)} \frac{\partial f^{(0)}}{\partial v}\, dv = 0. \tag{3.38}$$

Here the crucial point is the discretization on the velocity part of the phase space, so that we perform a semi-discrete analysis. In the frame of the discretization (3.28)-(3.29) coupled with (3.33)-(3.35), we consider the semi-discrete scheme approximating (3.37)

$$\begin{cases} \dfrac{\partial f}{\partial t} + v\,\dfrac{\partial f}{\partial x} + \dfrac{q_e}{m_e}\, E\, \dfrac{f_{j+1/2} - f_{j+1/2}}{\Delta v} = 0, \\[2ex] \dfrac{\partial E}{\partial t} = -\dfrac{q_e}{\epsilon_0} \displaystyle\sum_{j\in\mathbb{Z}} \Delta v\, v_j\, f_j, \end{cases} \tag{3.39}$$

with

$$f_{j+1/2} = \frac{f_{j+1} + f_j}{2},$$

assuming the slope limiter is not active. Then we perform a discrete linearization around an equilibrium state

$$f_j = f_j^{(0)} + f_j^{(1)},$$

where $\|f^{(1)}\| \ll \|f^{(0)}\|$. Using $f_j^{(1)} \propto e^{i(k\,x - \omega t)}$ in (3.39), it yields

$$\begin{cases} -i\,(\omega - k\,v_j)\, f_j^{(1)} + \dfrac{q_e}{m_e}\, E^{(1)}\, \dfrac{f_{j+1/2}^{(0)} - f_{j-1/2}^{(0)}}{\Delta v} = 0, \\[2ex] -i\,\omega\, E^{(1)} = -\dfrac{q_e}{\epsilon_0} \displaystyle\sum_{j\in\mathbb{Z}} \Delta v\, v_j\, f_j^{(1)}. \end{cases} \tag{3.40}$$

These equations lead to the discrete dispersion relation

$$1 + \frac{q_e^2}{\epsilon_0\, m_e} \sum_{j\in\mathbb{Z}} \frac{v_j}{\omega\,(\omega - k\,v_j)} \left[\frac{f_{j+1/2}^{(0)} - f_{j-1/2}^{(0)}}{\Delta v} \right] \Delta v = 0. \tag{3.41}$$

We recover the continuous dispersion relation (3.38) when passing to the limit $\Delta v \to 0$. Any other choice for the discrete current in (3.40) would introduce an additional error that would substitute to the $O(\Delta v^2)$ accuracy order of the dispersion relation (3.41). For instance, the choice

$$J = \sum_{j\in\mathbb{Z}} \Delta v\, v_j\, f_{j+1/2}$$

would lead to

$$1 + \frac{q_e^2}{\epsilon_0\, m_e} \sum_{j\in\mathbb{Z}} \frac{(v_j - \Delta v)}{\omega\,(\omega - k\,v_j)} \left[\frac{f_{j+1/2}^{(0)} - f_{j-1/2}^{(0)}}{\Delta v} \right] \Delta v = 0, \tag{3.42}$$

which is a “shifted” dispersion relation, with a $O(\Delta v)$ first oder accuracy, compared to the second order accurate relation given by (3.41). □

3.3.4 Boundary conditions

Truncation of the velocity domain.

The discretization in the velocity space imposes a truncation of the infinite velocity domain, and the introduction of boundary conditions. We only need to consider the direction v_1, where the discretized velocity variable is v_{j_1}, with $j_1 \in [-n_{v_1}, n_{v_1}] \subset \mathbb{Z}$, and $2\, n_{v_1} + 1$ is the total number of discretization points. If the second order scheme (respectively the fourth order scheme) is considered, then the boundary conditions are applied on two ghost points (respectively three ghost points). This is due to the extension of the stencil. Considering the second order scheme, the ghost points at the velocity domain are v_{j_1} with $j_1 = \pm n_{v_1}, \pm(n_{v_1} + 1)$. Therefore, at these points, we impose the truncation $f^{n+1}_{j_1} = 0$.

Boundary conditions in the velocity domain.

The treatment of runaway particles, in the frame of the model presented in Chapter 8, would require boundary conditions in the velocity domain, for these runaway particle to be free to escape from the thermal population and enter into the fast popultaion.

Boundary conditions in the space domain.

The boundary conditions for the space directions satisfy also naturally the positivity constraint with our scheme. It is indeed designed with reconstructed numerical fluxes, that maintain the positivity (under the CFL condition) if the distribution function at the previous time step is positive. At a boundary interface, $x_{-1/2}$ at the left boundary, where the numerical flux should be computed, the only requirement is to specify a positive distribution at ghost points to impose the boundary conditions. We explicit here the non-trivial ghost point used by a zero current left boundary (with temperature T_L) condition, in the direction x_1.

$$f^n_{-1,\mathbf{j}} = C_{-1/2}\, \exp\left(-\frac{\|v_{\mathbf{j}}\|^2}{2\, T_L}\right), \tag{3.43}$$

where $C_{-1/2} > 0$ and satisfies

$$\sum_{\mathbf{j}} \mathcal{F}^n_{-1/2,\mathbf{j}} = 0. \tag{3.44}$$

Such a numerical choice for the boundary condition may induce a Knudsen type boundary layer, in the presence of collisions between particles. The collisions tend to stabilize the distribution function at the thermal equilibrium in a few mean-free-path around this hydrodynamical discontinuity. This behaviour is illustrated in Figure (5.1), for the test 1.

3.4 Extension to the relativisitic regime

In the same manner as in the nonrelativistic limit, we introduce a uniform $1D_x$ space discretization $(x_{i+1/2})_{i\in I}$, $I \subset \mathbb{N}$, of the interval $(0, L_1)$, in the direction denoted by the index 1. The associated space variable is denoted by x_1. We define the control volumes $C_{i,\mathbf{j}} = (x_{i-1/2}, x_{i+1/2}) \times (\mathbf{p}_{\mathbf{j-1/2}}, \mathbf{p}_{\mathbf{j+1/2}})$, the size of a control volume in one direction in space Δx and momentum Δp.

The momentum variable $\mathbf{p} = {}^t(p_1, p_2, p_3)$ is discretized on the grid $\mathbf{p_j} = \mathbf{j}\,\Delta p = {}^t(p_{j_1}, p_{j_2}, p_{j_3})$ with $\mathbf{j} = {}^t(j_1, j_2, j_3) \in \mathbb{Z}^3$. Moreover we note $\mathbf{p}_{\mathbf{j+1/2}} = {}^t(j_1 + 1/2, j_2 + 1/2, j_3 + 1/2)\,\Delta p$. Finally, the time discretization is defined as $t^n = n\Delta t$, with $n \in \mathbb{N}$.

Let $f^n_{i,\mathbf{j}}$ be an average approximation of the distribution function on the control volume $C_{i,\mathbf{j}}$ at time t^n, that is

$$f^n_{i,\mathbf{j}} \simeq \frac{1}{\Delta x\,\Delta p^3} \int_{C_{i,\mathbf{j}}} f(t^n, x, \mathbf{p})dx\,d^3p.$$

Proposition 3. *Let us consider the dimensionless (with normalization of appendix 3.9) Vlasov equation* (3.8) *written under its conservative form. Then the relativistic extension of the scheme* (3.28)-(3.29), *together with the numerical scheme for Maxwell* (3.34), *should present the following centered discretization of the velocity variable,*

$$v_{1,\mathbf{j}} = m_e c^2 \frac{\gamma_{j_1+1,j_2,j_3} - \gamma_{j_1-1,j_2,j_3}}{2\Delta p_1}\,, \tag{3.45}$$

$$v_{2,\mathbf{j}} = m_e c^2 \frac{\gamma_{j_1,j_2+1,j_3} - \gamma_{j_1,j_2-1,j_3}}{2\Delta p_2}\,, \tag{3.46}$$

$$v_{3,\mathbf{j}} = m_e c^2 \frac{\gamma_{j_1,j_2,j_3+1} - \gamma_{j_1,j_2,j_3-1}}{2\Delta p_3}\,, \tag{3.47}$$

in order to respect, at the discrete level, the relation

$$\nabla_{\mathbf{p}} \times \left(\nabla_{\mathbf{p}}\gamma(\mathbf{p})\right) = \mathbf{0}\,.$$

This holds true because the discrete centered derivative commute. This relation ensures the equivalence between the conservative and nonconservative forms of the Vlasov equation.
On the one hand, if the discrete current is defined as

$$\mathbf{J}^n_{\mathbf{i}} \equiv \Delta p^3 \sum_{\mathbf{j}\in\mathbb{Z}^3} \mathbf{v_j}\, f^n_{\mathbf{i,j}}\,, \tag{3.48}$$

then the discrete total energy is preserved, when slopes limiters are not active in the momentum advection term $\nabla_{\mathbf{p}}$. On the other hand, let us consider the discrete expression for the current $\mathbf{J}^n_{\mathbf{i}}$ obtained from the discete analogous of the momentum conservation equation (3.5)*. The discrete form of this equation is issued from the direct integration of the relativistic Vlasov solver, with the prescribed definition for the discrete velocity (3.45-3.47), coupled with the discretization of Maxwell equation (3.34). Then the discrete current, defined as*

$$\mathbf{J}^n_{\mathbf{i}} = q_e \sum_{\mathbf{j}\in\mathbb{Z}^3} \left(f_h(x_{\mathbf{i}}, \mathbf{p}_{j_1,j_2+1/2,j_3})v_{1,\mathbf{j}},\ f_h(x_{\mathbf{i}}, \mathbf{p}_{j_1+1/2,j_2,j_3})v_{2,\mathbf{j}}, 0\right)\Delta p^3\,, \tag{3.49}$$

preserves the discrete total momentum.
Finally discrete current definitions (3.48) *and* (3.49) *satisfy the total mass conservation.*

Proof. The exact conservation of the discrete mass, momentum, and energy is proved here in one space dimension and three momentum dimensions, with a field geometry (E_1, E_2, B_3) that is resolved by the discrete Maxwell equation (3.34). We show here that different definitions of the discrete source term currents are possible, depending whether the discrete total momentum or energy is favoured. Given this geometry, only advections in the p_1 and p_2 directions are needed. The generalization to an arbitrary configuration is straightforward.

Let us recall the numerical scheme for the relativistic extension of the scheme (3.28)-(3.29) with velocity (3.45)-(3.47), coupled with the discrete Maxwell equations (3.34). This scheme must be considered first under its conservative form, because of the dependance of the velocity over the momenta, in the relativisitic regime, in order to recover the discrete total mass conservation (this was not the case in the nonrelativistic limit)

$$f^{n+1}_{\mathbf{i},\mathbf{j}} = f^{n}_{\mathbf{i},\mathbf{j}} - \Delta t\left(D_{x_1}\mathcal{F}^{x_1}_{\mathbf{i},\mathbf{j}} + D_{x_2}\mathcal{F}^{x_2}_{\mathbf{i},\mathbf{j}} + D_{p_1}\mathcal{F}^{p_1}_{\mathbf{i},\mathbf{j}} + D_{p_2}\mathcal{F}^{p_2}_{\mathbf{i},\mathbf{j}}\right) , \tag{3.50}$$

where

$$D_{x_1}\mathcal{F}^{x_1}_{\mathbf{i},\mathbf{j}} \equiv v_{1,\mathbf{j}}\frac{f_h(\mathbf{x}_{(i_1+1/2,i_2)}, \mathbf{p}_\mathbf{j}) - f_h(\mathbf{x}_{(i_1-1/2,i_2)}, \mathbf{p}_\mathbf{j})}{\Delta x} ,$$

$$D_{x_2}\mathcal{F}^{x_2}_{\mathbf{i},\mathbf{j}} \equiv v_{2,\mathbf{j}}\frac{f_h(\mathbf{x}_{(i_1,i_2+1/2)}, \mathbf{p}_\mathbf{j}) - f_h(\mathbf{x}_{(i_1,i_2-1/2)}, \mathbf{p}_\mathbf{j})}{\Delta x} ,$$

$$D_{p_1}\mathcal{F}^{p_1}_{\mathbf{i},\mathbf{j}} \equiv \frac{\mathcal{F}^{p_1}_{\mathbf{i},(j_1+1/2,j_2,j_3)} - \mathcal{F}^{p_1}_{\mathbf{i},(j_1-1/2,j_2,j_3)}}{\Delta p_1} ,$$

$$D_{p_2}\mathcal{F}^{p_2}_{\mathbf{i},\mathbf{j}} \equiv \frac{\mathcal{F}^{p_2}_{\mathbf{i},(j_1,j_2+1/2,j_3)} - \mathcal{F}^{p_2}_{\mathbf{i},(j_1,j_2+1/2,j_3)}}{\Delta p_2} ,$$

$$\mathcal{F}^{p_1}_{\mathbf{i},(j_1+1/2,j_2,j_3)} \equiv \left[E^{n+1/2}_{1,\mathbf{i}} + v_{2,(j_1+1/2,j_2,j_3)}B^{n+1/2}_{3,\mathbf{i}}\right] f_h(\mathbf{x}_\mathbf{i}, \mathbf{p}_{(j_1+1/2,j_2,j_3)}) ,$$

$$\mathcal{F}^{p_2}_{\mathbf{i},(j_1,j_2+1/2,j_3)} \equiv \left[E^{n+1/2}_{2,\mathbf{i}} - v_{1,(j_1,j_2+1/2,j_3)}B^{n+1/2}_{3,\mathbf{i}}\right] f_h(\mathbf{x}_\mathbf{i}, \mathbf{p}_{j_1,j_2+1/2,j_3}) ,$$

where f_h is the high order reconstruction of the distribution function. It is independent of the sign of the force term in the advection scheme: there is no upwinding if the limiter are not active. We obtain

$$f_h(\mathbf{x}_\mathbf{i}, \mathbf{p}_{(j_1+1/2,j_2,j_3)}) = \frac{f_{\mathbf{i},(j_1+1,j_2,j_3)} + f_{\mathbf{i},\mathbf{j}}}{2} ,$$

$$f_h(\mathbf{x}_\mathbf{i}, \mathbf{p}_{(j_1,j_2+1/2,j_3)}) = \frac{f_{\mathbf{i},(j_1,j_2+1,j_3)} + f_{\mathbf{i},\mathbf{j}}}{2} .$$

The interface velocities are defined with a mid-point rule

$$v_{2,(j_1+1/2,j_2,j_3)} \equiv \frac{v_{2,(j_1+1,j_2,j_3)} + v_{2,(j_1,j_2,j_3)}}{2} .$$

$$v_{1,(j_1,j_2+1/2,j_3)} \equiv \frac{v_{1,(j_1,j_2+1,j_3)} + v_{1,(j_1,j_2,j_3)}}{2} .$$

With these discretization choices, the conservative scheme can be rewritten as

$$\begin{aligned}
f_{\mathbf{i},\mathbf{j}}^{n+1} &= f_{\mathbf{i},\mathbf{j}}^{n} - \Delta t D_{x_1} \mathcal{F}_{\mathbf{i},\mathbf{j}}^{x_1} - \Delta t D_{x_2} \mathcal{F}_{\mathbf{i},\mathbf{j}}^{x_2} \\
&- \Delta t \left[E_{1,\mathbf{i}}^{n+1/2} + B_{3,\mathbf{i}}^{n+1/2} v_{2,\mathbf{j}} \right] \times \left[\frac{f_h(\mathbf{x_i}, \mathbf{p}_{(j_1+1/2,j_2,j3)}) - f_h(\mathbf{x_i}, \mathbf{p}_{(j_1-1/2,j_2,j3)})}{\Delta p_1} \right] \\
&- \Delta t \left[E_{2,\mathbf{i}}^{n+1/2} - B_{3,\mathbf{i}}^{n+1/2} v_{1,\mathbf{j}} \right] \times \left[\frac{f_h(\mathbf{x_i}, \mathbf{p}_{(j_1,j_2+1/2,j3)}) - f_h(\mathbf{x_i}, \mathbf{p}_{(j_1,j_2-1/2,j3)})}{\Delta p_2} \right] \\
&+ \Delta t \frac{B_{3,\mathbf{i}}^{n+1/2}}{2} \mathcal{R}_{\mathbf{i},\mathbf{j}} \,, \qquad (3.51) \\
\mathcal{R}_{\mathbf{i},\mathbf{j}} &= - f_h(\mathbf{x_i}, \mathbf{p}_{(j_1+1/2,j_2,j3)}) \left[\frac{v_{2,(j_1+1,j_2,j3)} - v_{2,\mathbf{j}}}{\Delta p_1} \right] \\
&+ f_h(\mathbf{x_i}, \mathbf{p}_{(j_1-1/2,j_2,j3)}) \left[\frac{v_{2,(j_1-1,j_2,j3)} - v_{2,\mathbf{j}}}{\Delta p_1} \right] \\
&+ f_h(\mathbf{x_i}, \mathbf{p}_{(j_1,j_2+1/2,j3)}) \left[\frac{v_{1,(j_1,j_2+1,j3)} - v_{1,\mathbf{j}}}{\Delta p_2} \right] \\
&- f_h(\mathbf{x_i}, \mathbf{p}_{(j_1,j_2-1/2,j3)}) \left[\frac{v_{1,(j_1,j_2-1,j3)} - v_{1,\mathbf{j}}}{\Delta p_2} \right] \qquad (3.52)
\end{aligned}$$

The conservative scheme is splitted twofold. On the one hand, the first terms are expressed with an apparent, nonstandard nonconservative discretization, and actually this is not, since the sum of these terms does conserve energy, momenum and mass on its own. In the nonrelativistic limit, these terms are consistent with the nonrelativistic scheme (3.28-3.29). On the other hand, the relativistic residual term $\mathcal{R}_{\mathbf{i},\mathbf{j}}$ is consistent with the continuous quantity $\left[\left(-\frac{\partial v_2}{\partial p_1} + \frac{\partial v_1}{\partial p_2}\right) f\right](\mathbf{x_i}, \mathbf{v_j}) = 0$, and constitues indeed a discretization of zero, that appears only in the relativistic regime. Any error due to the discretization of this zero residual could be enhanced by strong magnetic fields, because of the $B_{3,\mathbf{i}}^{n+1/2}$ factor.

We shall show that the terms in the right-hand side of the equation (3.51) that do not contribute to the relativistic residual $\mathcal{R}_{\mathbf{i},\mathbf{j}}$ are self-consistent with respect to the discrete mass, momentum and energy conservation (Discrete momentum and energy conservations require different definitions for the current, in the nonrelativistic regime as well). Therefore, the relativistic residual should be neglected, as it only brings unavoidable additional errors to the discretization of zero. The scheme still keeps all the relativistic features of the mass, momentum, and energy transport.Its practical implemention, without the relativistic residual, writes

$$\begin{aligned}
f_{\mathbf{i},\mathbf{j}}^{n+1} &= f_{\mathbf{i},\mathbf{j}}^{n} - \Delta t D_{x_1} \mathcal{F}_{\mathbf{i},\mathbf{j}}^{x_1} - \Delta t D_{x_2} \mathcal{F}_{\mathbf{i},\mathbf{j}}^{x_2} \\
&- \Delta t \left[E_{1,\mathbf{i}}^{n+1/2} + B_{3,\mathbf{i}}^{n+1/2} v_{2,\mathbf{j}} \right] \times \left[\frac{f_h(\mathbf{x_i}, \mathbf{p}_{(j_1+1/2,j_2,j3)}) - f_h(\mathbf{x_i}, \mathbf{p}_{(j_1-1/2,j_2,j3)})}{\Delta p_1} \right] \\
&- \Delta t \left[E_{2,\mathbf{i}}^{n+1/2} - B_{3,\mathbf{i}}^{n+1/2} v_{1,\mathbf{j}} \right] \times \left[\frac{f_h(\mathbf{x_i}, \mathbf{p}_{(j_1,j_2+1/2,j3)}) - f_h(\mathbf{x_i}, \mathbf{p}_{(j_1,j_2-1/2,j3)})}{\Delta p_2} \right] \qquad (3.53)
\end{aligned}$$

Let us first investigate the discrete energy conservation. To this aim we do not activate the slope limiters in the advection term $\nabla_{\mathbf{p}}$, and define the discrete current as $\mathbf{J}_{\mathbf{i}}^{n} \equiv \Delta p^3 \sum_{\mathbf{j} \in \mathbb{Z}^3} \mathbf{v_j} f_{\mathbf{i},\mathbf{j}}^{n}$. We then perform integrations by parts, consider that $f_{\mathbf{i},\mathbf{j}}$ goes to zero as $||\mathbf{j}||$ goes to infinity, and use

$$\frac{v_{1,(j_1,j_2+1,j_3)} - v_{1,(j_1,j_2-1,j_3)}}{2\Delta p_1} - \frac{v_{2,(j_1+1,j_2,j_3)} - v_{2,(j_1-1,j_2,j_3)}}{2\Delta p_2} = 0\ ,$$

which is due to the discete numerical choice for the velocity variable. We finally obtain a simple form for the ohmic heating term

$$\Delta^3 p \sum_{\mathbf{j}\in\mathbb{Z}^3} (\gamma_{\mathbf{j}} - 1)\left(D_{p_1}\mathcal{F}^{p_1}_{\mathbf{i},\mathbf{j}} + D_{p_2}\mathcal{F}^{p_2}_{\mathbf{i},\mathbf{j}}\right) = -\mathbf{J}^n_{\mathbf{i}} \cdot \mathbf{E}^{n+1/2}_{\mathbf{i}}\ .$$

The discrete kinetic energy is defined as

$$\epsilon^n_K \equiv \Delta x \Delta^3 p \sum_{(\mathbf{i},\mathbf{j})\in\mathbb{Z}^2\times\mathbb{Z}3} f^n_{\mathbf{i},\mathbf{j}}\left(\gamma_{\mathbf{j}} - 1\right)\ . \tag{3.54}$$

Multiplying this latter expression by $\gamma_{\mathbf{j}}\Delta x\Delta^3 p$,and summing over $(\mathbf{i},\mathbf{j}) \in \mathbb{Z}^2 \times \mathbb{Z}^3$

cancels the space advection terms with discrete integration by parts. The numerical difinitions for the velocities (3.45) (3.46) and the numerical currents are then introduced

$$J^n_{\mathbf{i}} = \Delta^3 p \sum_{\mathbf{j}\in\mathbb{Z}^3} f^n_{\mathbf{i},\mathbf{j}} \mathbf{v}_{\mathbf{j}}\ . \tag{3.55}$$

The cross term $P_{1,2}$ of the pressure tensor $\mathbf{P}$, at the space point denoted by the subscript $\mathbf{i}$, is then introduced

$$P_{1,2,\mathbf{i}} = \Delta^3 p \sum_{\mathbf{j}\in\mathbb{Z}^3} v_{1,\mathbf{j}} v_{2,\mathbf{j}} f^n_{\mathbf{i},\mathbf{j}}\ . \tag{3.56}$$

We finally obtain

$$\begin{aligned}\epsilon^{n+1}_K = \epsilon^n_K &+ \Delta t \Delta x \left[\sum_{i\in\mathbb{Z}} E^{n+1/2}_{1,\mathbf{i}} J^n_{1,\mathbf{i}} + \sum_{i\in\mathbb{Z}} B^{n+1/2}_{3,\mathbf{i}} P^n_{1,2,\mathbf{i}}\right] \\ &+ \Delta t \Delta x \left[\sum_{\mathbf{i}\in\mathbb{Z}^2} E^{n+1/2}_{2,\mathbf{i}} J^n_{2,\mathbf{i}} - \sum_{\mathbf{i}\in\mathbb{Z}^2} B^{n+1/2}_{3,\mathbf{i}} P^n_{1,2,\mathbf{i}}\right]\ .\end{aligned} \tag{3.57}$$

This expression can be simplified, because the magnetic terms issued from $\mathbf{v} \times \mathbf{B}$ cancel.

$$\epsilon^{n+1}_K = \epsilon^n_K + \Delta t \Delta x \sum_{\mathbf{i}\in\mathbb{Z}^2} \mathbf{J}^n_{\mathbf{i}} \cdot \mathbf{E}^{n+1/2}_{\mathbf{i}}\ . \tag{3.58}$$

The power created by the electric field $\Delta x \sum_{\mathbf{i}\in\mathbb{Z}^2} \mathbf{J}^n_{\mathbf{i}} \cdot \mathbf{E}^{n+1/2}_{\mathbf{i}}$ can be expressed using the discrete Ampère and Faraday equations. Multiplying the Ampère equation by $\mathbf{E}^{n+1/2}_{\mathbf{i}}$, and the Faraday equation by $B^{n+1/2}_{3,\mathbf{i}}$, we obtain

$$\mathbf{E}_{\mathbf{i}}^{n+1/2} \cdot \left[\begin{array}{l} \dfrac{E_{1,\mathbf{i}}^{n+1} - E_{1,\mathbf{i}}^{n}}{\Delta t} - \dfrac{B_{3,i_1,i_2+1}^{n+1/2} - B_{3,i_1,i_2-1}^{n+1/2}}{2\Delta x} = -J_{1,\mathbf{i}}^{n} \\ \dfrac{E_{2,\mathbf{i}}^{n+1} - E_{2,\mathbf{i}}^{n}}{\Delta t} + \dfrac{B_{3,i_1+1,i_2}^{n+1/2} - B_{3,i_1-1,i_2}^{n+1/2}}{2\Delta x} = -J_{2,\mathbf{i}}^{n} \end{array} \right], \tag{3.59}$$

$$B_{3,\mathbf{i}}^{n+1/2} \times \left[\frac{B_{3,\mathbf{i}}^{n+1} - B_{3,\mathbf{i}}^{n}}{\Delta t} + \frac{E_{2,(i_1+1,i_2)}^{n+1/2} - E_{2,(i_1-1,i_2)}^{n+1/2}}{2\Delta x} - \frac{E_{1,(i_1,i_2+1)}^{n+1/2} - E_{2,(i_1,i_2-1)}^{n+1/2}}{2\Delta x} = 0 \right] . \tag{3.60}$$

The combination of equations (3.59) and (3.60) give

$$\frac{\left(\mathbf{E}_{\mathbf{i}}^{n+1}\right)^2 - \left(\mathbf{E}_{\mathbf{i}}^{n}\right)^2}{\Delta t} + \frac{\left(B_{3,\mathbf{i}}^{n+1}\right)^2 - \left(B_{3,\mathbf{i}}^{n}\right)^2}{\Delta t} + D_{\mathbf{i}} \cdot \mathbf{S}_{\mathbf{i}}^{n+1/2} = -\mathbf{J}_{\mathbf{i}}^{n} \cdot \mathbf{E}_{\mathbf{i}}^{n+1/2} , \tag{3.61}$$

where $D_{\mathbf{i}}\cdot$ is the discrete centered divergence operator , and **S** the Ponyting vector, whose discrete expression is

$$\mathbf{S}_{\mathbf{i}}^{n+1/2} = (\mathbf{E} \times \mathbf{B})_{\mathbf{i}}^{n+1/2} . \tag{3.62}$$

A summation is then performed over $\mathbf{i} \in \mathbb{Z}^2$, that cancels the Poynting vector contribution by periodicity

$$\sum_{\mathbf{i}\in\mathbb{Z}^2} \left[\frac{\left(\mathbf{E}_{\mathbf{i}}^{n+1}\right)^2 - \left(\mathbf{E}_{\mathbf{i}}^{n}\right)^2}{\Delta t} + \frac{\left(B_{3,\mathbf{i}}^{n+1}\right)^2 - \left(B_{3,\mathbf{i}}^{n}\right)^2}{\Delta t} \right] = - \sum_{\mathbf{i}\in\mathbb{Z}^2} \mathbf{J}_{\mathbf{i}}^{n} \cdot \mathbf{E}_{\mathbf{i}}^{n+1/2} . \tag{3.63}$$

The equations (3.58) et (3.63) are finally combined to obtain the dimensionless discrete energy conservation

$$\frac{\epsilon_K^{n+1} - \epsilon_K^{n}}{\Delta t} + \sum_{\mathbf{i}\in\mathbb{Z}^2} \left[\frac{\left(\mathbf{E}_{\mathbf{i}}^{n+1}\right)^2 - \left(\mathbf{E}_{\mathbf{i}}^{n}\right)^2}{\Delta t} + \frac{\left(B_{3,\mathbf{i}}^{n+1}\right)^2 - \left(B_{3,\mathbf{i}}^{n}\right)^2}{\Delta t} \right] = 0 . \tag{3.64}$$

The proof of the discrete conservation of momentum is straightforward. The discrete analogous of equation (3.24) is obtained from the numerical scheme (3.53)), coupled with the discretization of Maxwell equation (3.34), where the current source term are defined in equation (3.49). The discrete momentum conservation equation then reads

$$\begin{aligned} & \frac{1}{\Delta t} \left(\sum_{\mathbf{i}\in\mathbb{Z}^2} \left[\left(\sum_{\mathbf{j}\in\mathbb{Z}^3} f_{i,\mathbf{j}}^{n+1} \mathbf{p}_{\mathbf{j}} \Delta p^3 + \epsilon_0 \mathbf{E}_{\mathbf{i}}^{n+1} \times \mathbf{B}_{\mathbf{i}}^{n+1} \right) - \left(\sum_{\mathbf{j}\in\mathbb{Z}^3} f_{i,\mathbf{j}}^{n} \mathbf{p}_{\mathbf{j}} \Delta p^3 + \epsilon_0 \mathbf{E}_{\mathbf{i}}^{n} \times \mathbf{B}_{\mathbf{i}}^{n} \right) \right] \Delta x^2 \right) \\ = \; & q_e \sum_{\mathbf{i}\in\mathbb{Z}^2} \left[\mathbf{E}_{\mathbf{i}}^{n} n_{e,\mathbf{i}}^{n} \right] \Delta x^2 + \sum_{\mathbf{i}\in\mathbb{Z}^2} \epsilon_0 \left[\mathbf{E}_{\mathbf{i}}^{n} \times \left(\mathbf{D}_{\mathbf{x},\mathbf{i}}^{c} \times \mathbf{E}_{\mathbf{i}}^{n} \right) \right] \Delta x^2 , \end{aligned} \tag{3.65}$$

where $\mathbf{D}_{\mathbf{x},\mathbf{i}}^{c}$ is the discrete centered gradient operator is space, at the mesh **i**. □

Remark 2. *This proposition holds true in the nonrelativistic limit, however, in this limit, the definitions for momentum and current only differ by a factor* m_e*. Though these are disctinct quantities, that have to be discretized in a different manner.*
Two relevant expressions have been proposed, and are possible candidates for the current discretization. On the one hand (3.48) *preserves the total energy and discrete Two-Stream Instability dispersion relation, on the other hand* (3.49) *preserves the momentum. We shall see that the expression* (3.49) *also preserves exactly the discrete Poisson equation. In the next section, we use an intermediate approach, that makes use of a two step predictor-corrector approach and involves the two possible identified current discretizations.*

3.5 High order time discretization

Time splitting was historically a standard way for the discretization of the multidimensional, scalar Vlasov equation [5]. However, such technique may introduce some loss of synchronous and symmetric advancing of the distribution function in the phase space [10]. In the frame of Semi-Lagrangian scheme, the time splitting technique was rigourously proven to be unstable [12]. This difficulty is reported to be corrected, in [22], by the adoption of multi-dimensional velocity advections, where a modified semi-lagrangian scheme is able to resolve circular particle orbits due to a strong magnetic field, while maintaining the phase and amplitude of the a momentum rotation on a cartesian grid. We should also mention here the back-substitution method [23], that is closely related to the time discretization. This latter method avoids the systematic heating of the plasma by the time splitting technique.

The numerical schemes we propose do not make use of time splitting techniques, except for the resolution for the FPL collision operator for electron-electron collisions, in Chapter 5, since it uses a specific subcycling algorithm for time discretization.

To our knowledge, none of the present numerical methods is able to satisfy, at the discrete level (even formally, far from the extrema of the distribution function), the positivity, exact total energy, and respect of Poisson equation alltogether. In this Chapter, we have proposed positive high order (second and fourth order) MUSCL schemes designed to satisfy these conservation properties, except the exact Poisson equation. However, for long-time simulations or particular configurations, errors due to the non-respect of the Poisson equation may accumulate and this issue may become crucial. We mention here an alternative time discretization technique, adapted from [22], that permits to bridge the gap, *in an exact manner*, between the Poisson and Ampère equations, *via* the continuity equation. Using this approach, we loose the *formal* discrete energy conservation.
While comparing these schemes, we shall therefore evaluate, for some representative configurations, such as the nonlinear relativistic Landau Damping and Two-Stream Instability tests III and IV, the respective importance and need for an exact discrete total energy conservation and/or exact discrete preservation of the continuity equation.

3.5.1 Second order unsplit energy preserving time discretization

In this section, the time discretization is set up such as the energy conservation is favoured over the exact respect of the discrete continuity equation, because of the time centering of the electromagnetic quantities. The drawback of this method is that long-time error accumulations may occur, due to a lack of accuracy in the charge repartition with respect to the particle positions, due to the non respect of the Poisson equation. The second order in time, semi-discretized scheme reads

$$\begin{aligned}
\begin{pmatrix} \mathbf{E}^* \\ \mathbf{B}^* \end{pmatrix} &= \mathcal{M}^{-1}\left(\Delta t/2, \Delta x, \mathbf{j}^n\right)\begin{pmatrix} \mathbf{E}^n \\ \mathbf{B}^n \end{pmatrix}, && (3.66)\\
f^* &= f^n + \frac{\Delta t}{2}\mathcal{V}\left(f^n, \frac{\mathbf{E}^* + \mathbf{E}^n}{2}, \frac{\mathbf{B}^* + \mathbf{B}^n}{2}, \Delta x, \Delta p\right), && (3.67)\\
\begin{pmatrix} \mathbf{E}^{n+1} \\ \mathbf{B}^{n+1} \end{pmatrix} &= \mathcal{M}^{-1}\left(\Delta t, \Delta x, \mathbf{j}^*\right)\begin{pmatrix} \mathbf{E}^n \\ \mathbf{B}^n \end{pmatrix}, && (3.68)\\
f^{n+1} &= f^n + \Delta t\mathcal{V}\left(f^*, \mathbf{E}^{n+1/2}, \mathbf{B}^{n+1/2}, \Delta x, \Delta p\right), && (3.69)
\end{aligned}$$

where the operator $\mathcal{M}^{-1}$ denotes the operator issued from the discretization (3.34), that only depends on the time step and mesh size. For an homegeneous grid and a constant time-stepping, the matrix associated to the operator $\mathcal{M}$ only requires one inversion at initial time. The operator $\mathcal{V}$ denotes the numerical unsplit high order discretization of the advection terms in the Vlasov equation. The discrete currents are the discrete analogous of $\mathbf{j}^n = q_e \int_{\mathbb{R}^3} \mathbf{v} f^n d^3p$, $\mathbf{j}^* = q_e \int_{\mathbb{R}^3} \mathbf{v} f^* d^3p$ in the relativistic regime. In this scheme, all the variables are collocated at the center of the mesh to satisfy the exact total energy conservation, when slope limiters are not active.

3.5.2 Second order unsplit predictor-corrector time discretization: exact respect of the continuity equation

The resolution of the Ampère equation, of hyperbolic nature, instead of Poisson equation, of elliptic nature, is desirable in term of computational time. This solution is explored in [1], for the Pierce-Buneman instabilility (bump-on-tail), for a PPM scheme discretizing the Vlasov equation. The simulation run is reported to be about 2000 plasma periods, while the maximum relative error is 0.15 % between the Ampère and Poisson solutions, which is considered small there. However, this statement is not general and we found some configurations where the exact respect of the Poisson equation is required. We refer to a $1D_x \times 3D_\mathbf{v}$ relativistic interaction where a transverse short-pulse electomagnetic wave propagates in the vacuum and interacts with a slab of plasma [19].

To remedy this issue, the time discretization may be set up such as the respect of the Poisson equation is favoured over the exact total energy conservation, within a predictor-corrector approach

$$
\begin{aligned}
\begin{pmatrix} \mathbf{E}^{*}_{\partial C} \\ \mathbf{B}^{*}_{S} \end{pmatrix} &= \mathcal{M}^{\pm 1}\left(\Delta t/4, \Delta x, \mathbf{j}^{n}_{\partial C}\right)\begin{pmatrix} \mathbf{E}^{n}_{\partial C} \\ \mathbf{B}^{n}_{S} \end{pmatrix}, \qquad (3.70)\\
f^{*} &= f^{n} + \frac{\Delta t}{2}\mathcal{V}\left(f^{n}, \mathbf{E}^{*}_{\partial C}, \mathbf{B}^{*}_{S}, \Delta x, \Delta p\right), \qquad (3.71)\\
\begin{pmatrix} \mathbf{E}^{n+1/2}_{\partial C} \\ \mathbf{B}^{n+1/2}_{S} \end{pmatrix} &= \mathcal{M}^{\pm 1}\left(\Delta t/2, \Delta x, \mathbf{j}^{n+1/4}_{\partial C,\mathcal{V}}\right)\begin{pmatrix} \mathbf{E}^{n}_{\partial C} \\ \mathbf{B}^{n}_{S} \end{pmatrix}, \qquad (3.72)\\
\begin{pmatrix} \mathbf{E}^{*}_{\partial C} \\ \mathbf{B}^{*}_{S} \end{pmatrix} &= \mathcal{M}^{\pm 1}\left(\Delta t/2, \Delta x, \mathbf{j}^{n+1/4}_{\partial C,\mathcal{V}}\right)\begin{pmatrix} \mathbf{E}^{n}_{\partial C} \\ \mathbf{B}^{n}_{S} \end{pmatrix}, \qquad (3.73)\\
f^{n+1} &= f^{n} + \Delta t\mathcal{V}\left(f^{*}, \mathbf{E}^{*}_{\partial C}, \mathbf{B}^{*}_{S}, \Delta x, \Delta p\right), \qquad (3.74)\\
\begin{pmatrix} \mathbf{E}^{n+1}_{\partial C} \\ \mathbf{B}^{n+1}_{S} \end{pmatrix} &= \mathcal{M}^{\pm 1}\left(\Delta t, \Delta x, \mathbf{j}^{n+1/2}_{\partial C,\mathcal{V}}\right)\begin{pmatrix} \mathbf{E}^{n}_{\partial C} \\ \mathbf{B}^{n}_{S} \end{pmatrix}. \qquad (3.75)
\end{aligned}
$$

The subsripts S and ∂C denote the position where the quantity is calculated, either at the vertex or the interfaces of the mesh, respectively. $\mathcal{M}^{\pm 1}$ denotes any operator associated with an implicit or explicit discretization of the Maxwell equations. At the correction step, the currents $\mathbf{j}^{n+1/4}_{\partial C,\mathcal{V}}$ and $\mathbf{j}^{n+1/2}_{\partial C,\mathcal{V}}$ are computed from the high order spatial fluxes $\mathcal{V}$ issued from the Vlasov solver, at the mesh interfaces ∂C. Therefore the electric fields $\mathbf{E}^{n+1/2}_{\partial C}$ and $\mathbf{E}^{n+1}_{\partial C}$ are computed such as they respects exactly the Poisson equation at time $t^{n+1/2}$ and t^{n+1}, respectively.

This scheme makes use of a staggered grid for the current and fields. Though, we have much more freedom in the choice of the Maxwell solver, since we relax the exact energy preservation constraint of the previous scheme. The Maxwell solver can therefore be either Crank-Nicholson [9], caracteristic scheme (directional splitting, for PIC terminology) [16, 21], FDTD high order scheme [4, 8], Mimetic Finite Difference [13], Finite Element or discontinuous Galerkin methods [6, 14]. For instance, the use of staggered grid for the computation of the electric and magnetic fields can be considered [22], such as to avoid the odd-even decoupling between the field, known as the checkerboard instability.

A potential drawback of this method could be the loss of the formal discrete total energy conservation, however, we shall show, at least in the absence of magnetic fields, for the nonlinear relativistic Landau Damping and Two-Stream Instability (Tests III and IV), a similar departure from energy conservation, when compared to the scheme that is energy preserving, presented in Section 3.5.1. In the presence of self-consistent magnetic fields, the design of the Maxwell solver should focus either on the discrete energy preservation, *i.e.* the low dissipation, in the case of low frequency fields generation, or dispersive properties in the case of high frequency propagation of a transverse electromagnetic field, *i.e.* a short-pulse laser propagation.

3.6 Numerical tests

The objectives of this section are multiple. First we want to bring the evidence of efficiency of the high order MUSCL schemes we have proposed. We intend to do so in several simple, but representative configurations, with respect to ICF physics. These would stand as a validation of the numerical schemes in the collective regime. Second, we focus on coarse grid resolutions, having in view large scale simulation that include more physics (collisions, Inverse Bremsstrahlung heating, secondary electron production, *etc*). Therefore we would like to highlight the need for robust and high order schemes in this context. Finally, we shall propose a validation strategy in the linear, collisionless regime, based on the work of C. Sartori and G.M.M. Coppa [20], to describe the transient behavior of the solution to the Vlasov-Maxwell system, in the nonrelativistic and relativistic cases, when the initial data are close to the equilibrium. The need for such an approach is motivated by the presence of the self-consistent magnetic fields and/or within a relativistic description, that can lead to the failure of the dispersion relation approach. This isssue is explained in detailed in the section 2.1.4. Related analytical calculations are given in Appendix 3.10, in the nonrelativistic regime. In Appendix 3.11, we extend this approach to the Vlasov-Maxwell system, with self-consistent fields. Classical validations of kinetic solvers dedicated to plasma physics [7, 17] are based on the calculation of the growth rates (instability), or decrease rates (damping) in the linear regime. We will show the efficiency of this semi-analytical method, that permits an interpretation of the Two-Stream Instability tests I and IV.

The transport schemes are tested, with a low number of dimensions, $1D_x \times 1D_{v,p}$ for the tests I , II, and IV (The computational resources are then very low), or $1D_x \times 3D_{\mathbf{v}}$ for the test II. For this latter test, a parallelisation technique is employed, with a domain decomposition in the space dimension. The simulation is performed with 42 processors to accelerate the calculations, on the CEA-CCRT-platine facility. This facility is a cluster of Novascale 3045 servers, including 932 nodes, each one having 4 Intel Itanium dual core processors, at 1.6 Ghz. Each processor has a memory of 24 Go. The Novascale servers are interconnected by a Voltaire network, with technology Infiniband DDR.
The scaling of appendix 3.8 is used for tests I and II, whereas the scaling of appendix 3.9 is used for tests III and IV. We do not consider the effects of the collisions in these tests.

3.6.1 Test I: the nonlinear nonrelativistic Two-Stream Instability. Comparison between second and fourth order MUSCL schemes

The ICF physics involves a propagation of electron beams in plasma. The plasma response to the beam consists in a return current that goes in the opposite direction to the beam in order to preserve the quasineutrality. This leads to a very unstable configuration favorable to the excitation of plasma waves. We focus here on the instability with a perturbation wavevector parallel to the beam propagation direction, namely the Two-Stream Instability. Of course, this stands as an academic numerical test but it is closely related to the physics of ICF.

This numerical test is a very demanding for numerical schemes of transport, that have to be specially designed (see Proposition 2). In particular, a discrete dispersion relation relative to that problem is developed to justify numerical choices for the second order scheme. For this scheme also, during the limitation procedure, an additional dissipation at extrema is introduced, compared to [7], in order to preserve the solution from spurious oscillations. We will show the sensitivity of the scheme with respect to the chosen limiter, for this particular test case. Moreover, the fourth order scheme is introduced to reduce numerical heating, for simulations intended to deal with the Two-Stream Instability.

We consider the $1D_x \times 1D_v$ Vlasov-Ampère system (3.37) and choose the scaling (3.81), with $\nu = 0$. The initial distribution function and electric field are

$$\begin{cases} f^0(x,v) \;=\; \dfrac{1}{2}\left[(1 + A\,\cos(kx))\mathcal{M}_{1,v_d}(v) \;+\; (1 - A\cos(kx))\mathcal{M}_{1,-v_d}(v)\right], \\[2ex] E^0(x) \;=\; 0, \end{cases}$$

where

$$\mathcal{M}_{1,v_d}(v) = \frac{1}{\sqrt{2\pi}} \exp\left(-\frac{\|v - v_d\|^2}{2}\right)$$

is the Maxwellian distribution function centered around the drift velocity v_d.

In order to compare the numerical dissipation associated to the second and fourth order schemes, we choose a strong perturbation amplitude $A = 0.1$. The perturbation wavelength is $k = 2\pi/L$ and the beam initial mean velocities are $v_d = \pm 4$, $L = 25$ being the size of the periodic space domain. We choose a truncation of the velocity space to be $v_{max} = 12$ and time steps are chosen to be $\Delta t = 1/200$, such as to satisfy the CFL criteria and maintain the positivity of the distribution function.

The objectives of this numerical simulation are, on the one hand, to compare the second order Finite Volume scheme (specially designed to conserve exactly the discrete total energy, except if the slope limiters are active) for different slope limiters and the fourth order MUSCL scheme. On the other hand, we want to explore the effect of a reduced number of grid points on the conservation of the discrete invariants.

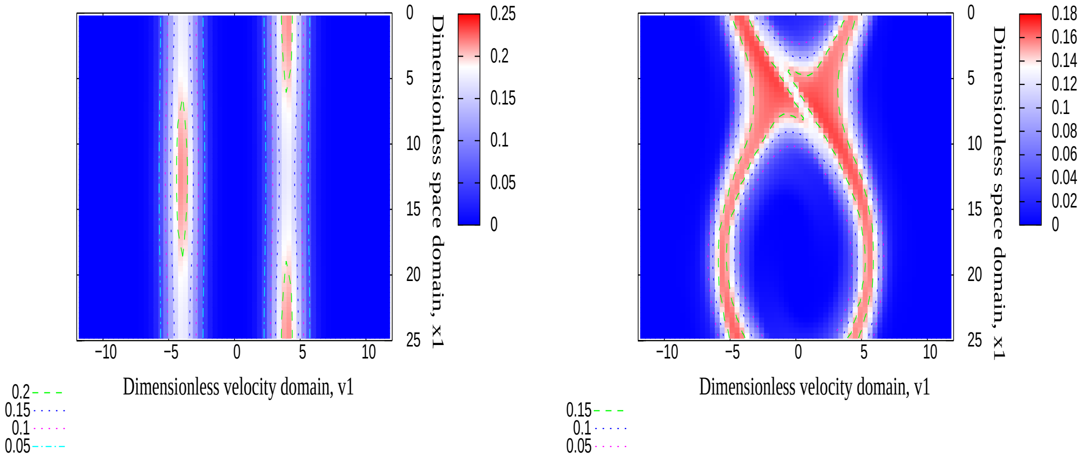

(a) (b)

Figure 3.1: *Beams phase space* (a) *at initial time,* (b) *at* 20 *plasma periods (after saturation), with* 64^2 *grid points.*

In Figure 3.1, two countersteaming beams that are initially well separated in the phase space (a) start to mix together. They finally create a complicated vortex structure, involving wave-particle interactions. This behavior remains quantitatively the same whatever the transport scheme is, second or fourth order. In Figure 3.2, we present the evolution of the electric energy for different schemes and several configurations from 32^2 points to 256^2. We observe that with a reduced number of grid points (smaller than 128 points in velocity), the second order scheme with the slope limiters (3.30), and fourth order scheme, present a different behavior on the total electric energy and total energy. Indeed, for a reduced grid resolutions (32^2 or 64^2 points), the fourth order scheme proves to be better than the second order one. For 32^2 points, plasma oscillations at the plasma frequency in the nonlinear phase are not reproduced with the second order scheme whereas they can be seen with the fourth order scheme (see Figure 3.2). Moreover for this resolution, the transition from the linear phase to the nonlinear phase occurs earlier than it should for the second order scheme. Furthermore, as the grid resolution increases, the accuracy remains better for the fourth order scheme than for the second order one, in the nonlinear phase. The convergence toward curves with 128^2 or 256^2 resolution grid is indeed better. We recall that quantities in Figure 3.2 are plotted with a logarithmic scale, that smoothes out discrepancies between curves. In addition to these results, the respect of total discrete energy conservation proves to be better for the fourth order scheme than for the second order one at a reduced grid resolution, as shown in Figures 3.3 and 3.4.

The use of the slope limiters (3.31) for the second order scheme improves the results. The plasma wave structure can then be captured at reduced grid resolutions, see Figure 3.2 (b) and (c). However, the energy dissipation remains quantitatively the same as the second order scheme with the limiters (3.30), see Figures 3.3 and 3.4. Only in the case of the second order scheme without limiter, could the energy be exactly conserved. The counterpart would be the loss of any exploitable solution (loss of stability).

As this test case requires both a good preservation of invariants and accuracy when nonlinear phenomena occur, we might conclude that the fourth order scheme, with a resolution along each velocity direction greater than 32 cells, is well suited for our physical applications.

Finally, the semi-analytical solution presented in appendix 3.10, allows to interpret the patterns of the electrostatic energy in the linear regime, as represented in Figure 3.2. We show a mean behavior, in the linear regime, that is related to the discrete, imaginary part of the spectrum of the eigenvalue problem associated to the linearized equation (2.17). The corresponding solutions are proportional to $e^{i\omega t}$. The modulations around this mean behavior come from the contribution of the continuous and real part of the spectrum of the eigenvalue problem, that is not reproduced by the classical validation approach relying on dispersion relations.

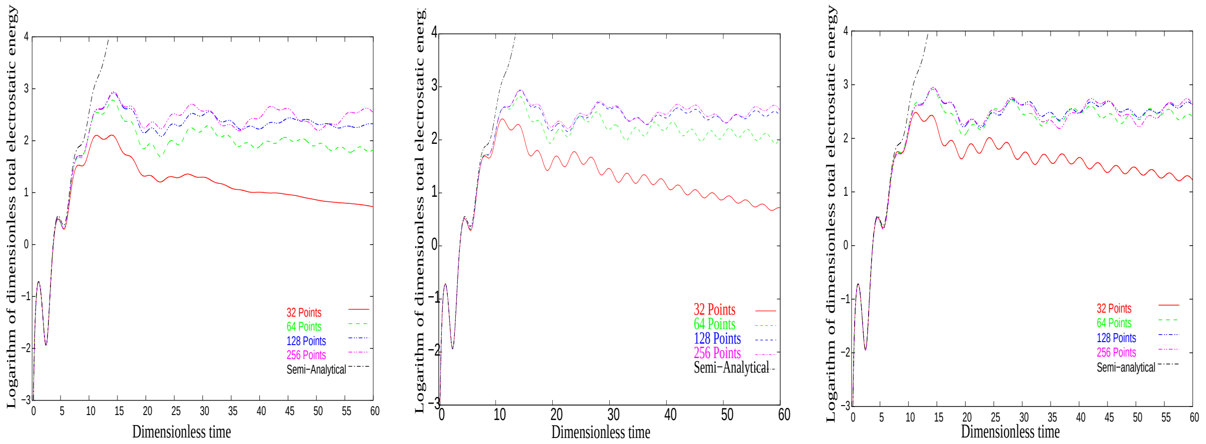

(*a*) (*b*) (*c*)

Figure 3.2: *Evolution of the electrostatic energy for* 32^2, 64^2, 128^2, 256^2 *grid points, and the semi-analytical solution in the linear regime. Results are shown for the second order with* (*a*) *slope limiters* (3.30) *and* (*b*) *slope limiters* (3.31) *with* $b = 2$, *and* (*c*) *fourth order transport scheme.*

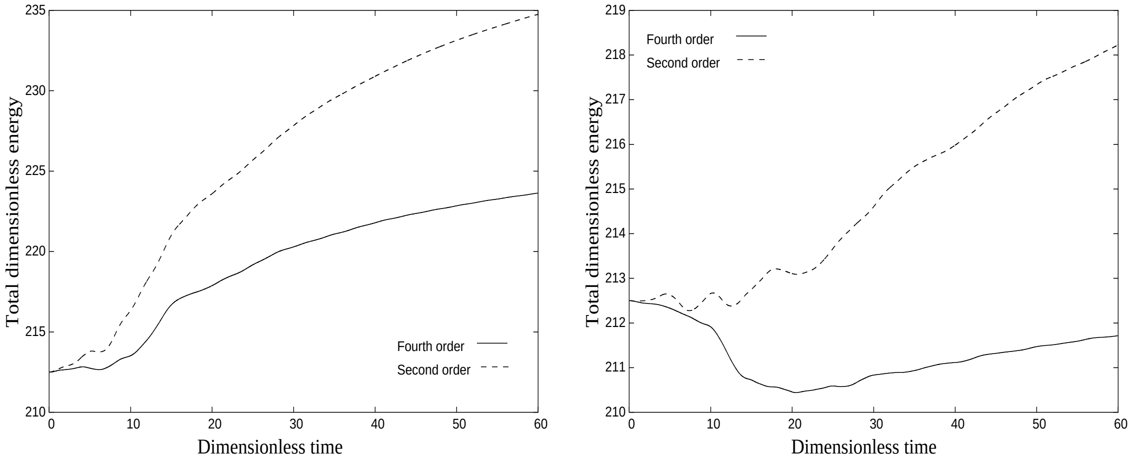

(*a*) (*b*)

Figure 3.3: *Comparison of the energy evolution for the second (with limiter* (3.30)*) and fourth order transport schemes. Results are shown* (*a*) *for* 32^2 (*b*) 64^2 *grid points.*

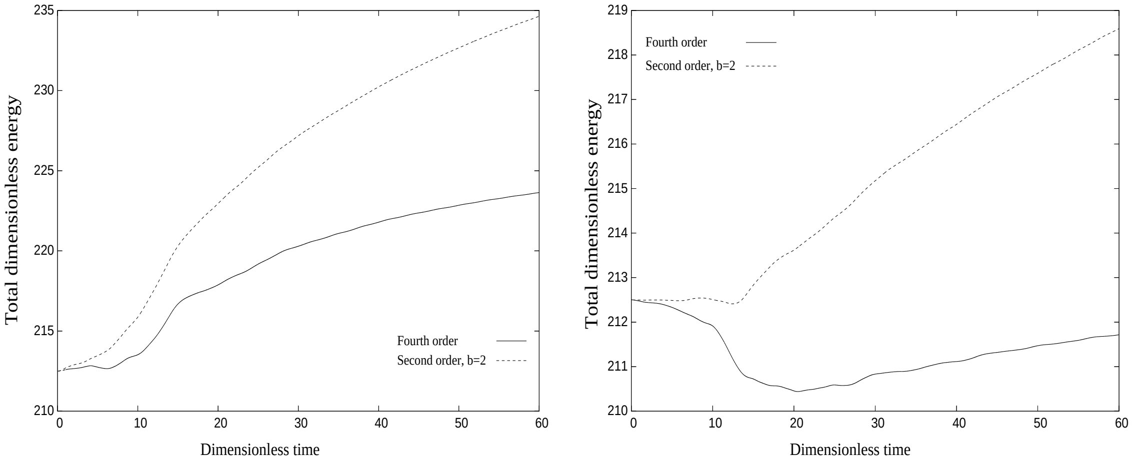

(*a*) (*b*)

Figure 3.4: *Comparison of the energy evolution for the second (with limiter* (3.31), $b = 2$*) and fourth order transport schemes. Results are shown* (*a*) *for* 32^2 (*b*) 64^2 *grid points.*

3.6.2 Test II: $1D_{\mathbf{x}} \times 3D_{\mathbf{v}}$ X-mode plasma waves with self-consistent magnetic field

This numerical test stands as a validation of the schemes in the linear regime, when the Vlasov equation is coupled with the Maxwell system, without the collisions between particles. The second order scheme is used for the transport terms in the x_1, v_1, v_2 and v_3 directions. A particular initial data is chosen (see the derivation in Appendix 3.12) to trigger an X-mode plasma wave at a well-defined frequency ω. This type of wave presents a mixed polarization (longitudinal and transverse with respect to the magnetic field), that propagates in the plane $P_\perp$, perpendicular to the magnetic field direction.

The chosen frequency ω is a solution of the dispersion relation (3.123) of the linearized Vlasov-Maxwell equations, introducing the equilibrium state $f^{(0)}\left(||\mathbf{v}||^2\right)$. The initial data are chosen such that $f^{(0)}$, $\hat{E}_1$, $\hat{E}_2$, and $\hat{B}_3$ only depend on ω, $B^{(0)}$, $k_1 = 2\pi/L_1$ and A; where $\hat{f}_n$, $\hat{B}_3$, $\hat{E}_1$ and $\hat{E}_2$ are the reconstructed (in Appendix 3.12) Fourier transforms of the distribution function and electromagnetic fields. The magnetic field $B^{(0)}$ is the nonperturbed magnitude of the magnetic field, L_1 is the length of the periodic space domain, A is the perturbation amplitude. The initial data can then be constructed with the help of truncated Fourier series

$$\begin{cases} f^{(0)}(x_1,\mathbf{v}) = f^{(0)}(||\mathbf{v}||^2) + \displaystyle\sum_{n=-2}^{2} \hat{f}_n(\mathbf{v}_\perp) e^{ik_1 x_1 + i n\psi}, \quad x_1 \in (0,L_1),\ \mathbf{v} \in \mathbb{R}^3, \\ E_1(t,x_1) = \hat{E}_1\, e^{-i\omega t + ik_1 x_1}, \quad x_1 \in (0,L_1)\,, \\ E_2(t,x_1) = \hat{E}_2 e^{-i\omega t + ik_1 x_1}, \quad x_1 \in (0,L_1)\,, \\ B(t,x_1) = B^{(0)} + \hat{B}_3 e^{-i\omega t + ik_1 x_1}, \quad x_1 \in (0,L_1). \end{cases}$$

We define ψ as the angle in the cylindrical coordinates for the velocity, where the axial direction is the magnetic field direction (See Appendix 3.12).

The scaling is defined by the relations (3.81), with $\nu = 0$. We choose $B^{(0)} = 2$ and a rather strong amplitude perturbation $A = 0.1$ with periodic boundary conditions on the space domain and $\beta = v_{th}/c = 0.05$. Hence, the dispersion relation has been solved for these parameters. One of the solution $\omega \simeq 5.1432$ is choosen in the initial data set.

We considered 126 points along the $1D$ space direction, and 64 points along each velocity direction $\mathbf{v} = {}^t(v_1, v_2, v_3)$. The dimension of the space domain is $L_1 = 25$ whereas the truncation of the velocity space occurs at $v_{max} = 7$ for each velocity direction. Furthermore, the time step is $\Delta t = 1/200$, which ensures the positivity of the distribution function here.

The Fourier spectrum in Figure 3.5 (a) exhibits a well defined frequency $f = 1/T \simeq 1.6375$ (corresponding to a period T) for the total magnetic energy, that corresponds to a frequency $f/2$ for the magnetic field oscillations. We finally find $\omega = 2\pi f/2 \simeq 5.1443$ from the numerical solution, to be compared with the analytical results 5.1432. This proves a good accuracy of the numerical results, while the distribution function is greatly affected by the magnetic field. As an illustration, we show in Figure 3.5 (c) how the magnetic field makes the distribution function rotate in the velocity space perpendicular to the magnetic field axis.

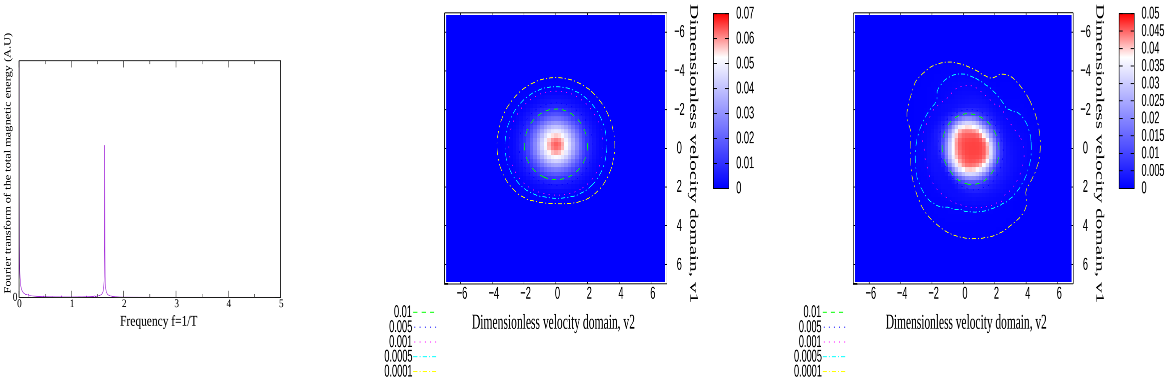

(a) (b) (c)

Figure 3.5: *Discrete Fourier spectrum in frequency (a) of the discrete analogous of the total dimensionless magnetic energy* $\int_0^{L_1} \frac{||B_3||^2}{2} dx_1$. *Projection on the* $v_1 - v_2$ *velocity domain for the distribution function is shown at initial time* $t_n = 0$ *(b) and at* $t_n = 40$ *(c), for a particular point of the space domain,* $x_1 = 0, v_3 = 0$.

3.6.3 Test III: the nonlinear relativistic Landau Damping

This numerical test stands, in the one hand, as a validation the numerical choice we have made to develop the relativitic extension of the kinetic, collisionless, Vlasov solver, as described in Section (3.4). On the other hand, it provides with a comparison between two schemes for time discretization; as described in Section (3.5), one favors discrete total energy preserving, rather than the other one rather projects the solution onto the solutions of the discrete Poisson equation.
The following parameters: time step $\Delta t = 1/500$, simulation time $T = 60$, truncation of the momentum space $p_{max} = 6$, initial temperature $T_e = 0.5^2$ of the maxwelian distribution, length of the space domain $L = \pi$, uniform mesh size $\Delta x = L/64$ in space, uniform mesh size $\Delta p = 2 \times p_{max}/64$ for momentum, and nonlinear perturbation amplitude $A = 0.1$ are chosen for the simulation setup. The initial electric field is homogeneously valued zero. The initial distribution function is under the form prescribed in [20]

$$f(t = 0, x, p_x) \quad = \quad f_0(p_x) + A \frac{\mathrm{d} f_0}{\mathrm{d} p_x}(p_x) cos(k_x x) \, , \tag{3.76}$$

where

$$\begin{aligned} f_0(p_x) &= \exp\left(- \left(\sqrt{(1 + p_x^2)} - 1 \right) / T_e \right) / K \, , \\ K &= \int_{\mathbb{R}} \exp\left(- \left(\sqrt{(1 + p_x^2)} - 1 \right) / T_e \right) \, . \end{aligned}$$

In the Figure (3.6) (b), we show that the departure from the analytic, constant solution, of the discrete total energy, is less than 1%, despite the activation of slope limiters. The choice for the discrete velocity on the momentum grid proves to maintain the numerical heating at a low level, as in the nonrelativistic case.

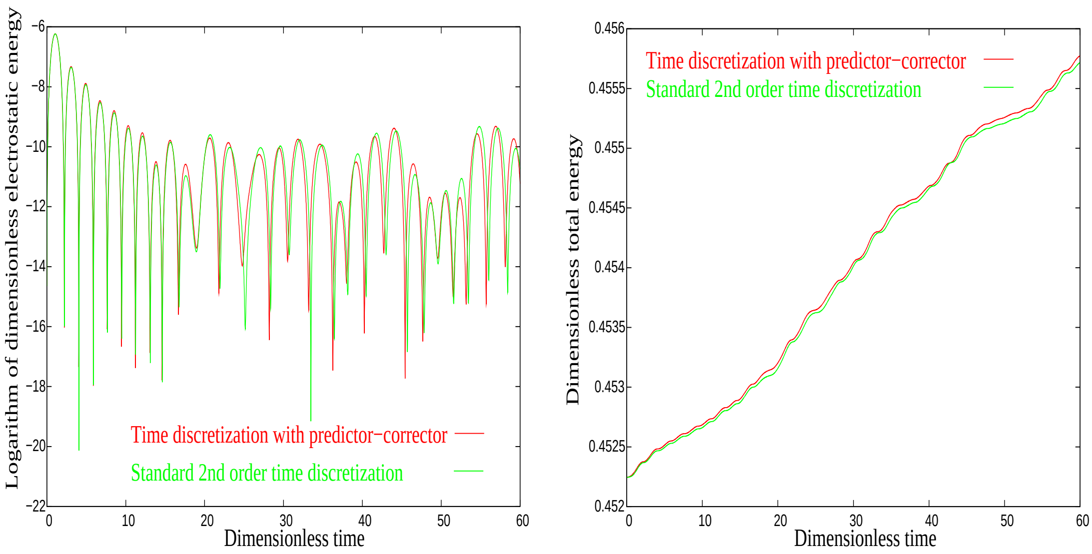

(a) (b)

Figure 3.6: *Nonlinear relativistic Landau damping for a* 64×64 *grid resolution. The evolution of the logarithm of the discrete, dimensionless total electrostatic energy (a) and discrete,dimensionless total energy (b) is shown against time.*

Finally in the Figure (3.6) (a) & (b), the comparison between the two time discretizations, on this Landau damping regime, does not show any improvement of the solution (in terms of total electrostatic field or total energy) due to centered electromagnetic fields on the Vlasov solver. Therefore the Poisson preserving time discretization seems to be competitive here.

3.6.4 Test IV: the nonlinear relativistic Two-Stream Instability

This numerical test continues the Test III of the previous section in the relativistic two-stream instability regime.

The following parameters: time step $\Delta t = 1/500$, simulation time $T = 60$, truncation of the momentum space $p_{max} = 20$, temperature $T_e = 0.5^2$ of the maxwellian distributions, length of the space domain $L = 25$, uniform mesh size $\Delta x = L/32$ in space, uniform mesh size $\Delta p = 2 \times p_{max}/32$ in momentum, nonlinear perturbation amplitude $A = 0.1$, and drift momenta $\pm p_d = \pm 4$ are chosen for the simulation setup. The initial electric field is homogeneously valued zero. The initial distribution function is

$$\begin{aligned} f(t=0,x,p_x) &= \left[f_0(p_x+p_d)(1-A\cos(k_x x)) + f_0(p_x-p_d)(1+A\cos(k_x x)) \right]/2\,, \qquad (3.77)\\ f_0(p_x) &= \exp\left(-\left(\sqrt{(1+p_x^2)}-1\right)/T_e\right)/K\,,\\ K &= \int_{\mathbb{R}} \exp\left(-\left(\sqrt{(1+p_x^2)}-1\right)/T_e\right)\,. \end{aligned}$$

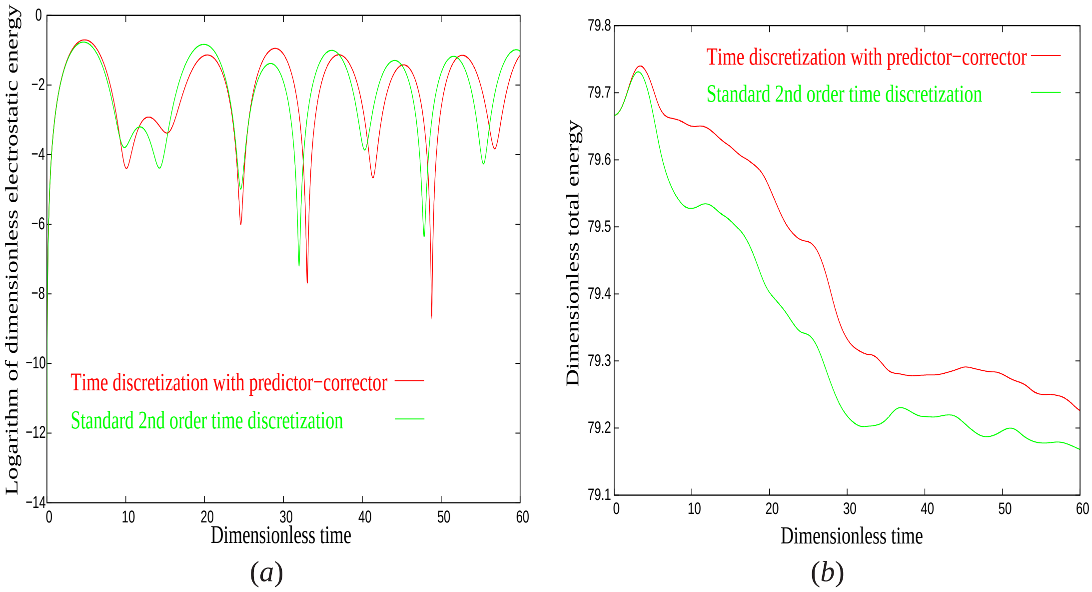

Figure 3.7: *Nonlinear relativistic two-stream instability for a* 32×32 *grid resolution. The evolution of the logarithm of the discrete, dimensionless total electrostatic energy (a) and discrete, dimensionless total energy (b) is shown against time.*

From the Figure (3.7) (a) & (b), and for the same reasons as in the Test III (same low dissipation/heating level, and proximity of the solutions) of the previous section, we again conclude that the choice for the discrete velocity maintains the numerical dissipation at a low level for the relativistic two-stream instability regime. In this regime also, the Poisson preserving time discretization proves to be a competitive numerical design. Indeed, the Poisson equation is not resolved, but it is exactly satisfied at the discrete level, *via* the continuity equation. The computational cost and complexity (especially in $2D_{\mathbf{x}}$) is then lighten while resolving only the Ampère equation, the low energy dissipation is not lost, and additional benefits come from the compliance of the discrete solution with the Poisson equation. This last feature could be relevent in regimes where large density gradients appear or for long time simulations.

3.7 Perspectives

In this section, we would like to mention possible improvements in the approach we present, relying on high order schemes. An endeavour in this direction is desirable, and we have shown in this Chapter the necessity of such schemes. First, the (formal) fourth order scheme, from H. Daiguji, S. Yamamoto, and C. Berthon, that we have presented here, might be optimized, while desyncronizing the limitation, that ensures positivity, on the reconstuction of the right and left states [3].

Second, an attractive perspective, at least for the electromagnetic part of the Maxwell equations in the short pulse regime, could be the usage and improvement upon an *exact*, explicit, third order Discontinuous Galerkin (DG) scheme, from P.-H. Maire [18], whose strength lies in its accurate treatment of extrema [18], in a more efficient manner than the usual limitation procedures. This feature is illustrated in Figure (3.8) for the free linear transport. Another desirable feature of such method is that they present a local stencil, which makes the treatment of boundary conditions much more simpler, and offers the possibility to run 2D simulations with collisions. However, the computational overload coming from the DG scheme, that uses more variables per mesh, could prove to be too stringent in multi-D geometries. To lighten this overload, a GPU acceleration technique can be employed, and has already proven to be efficient [11].

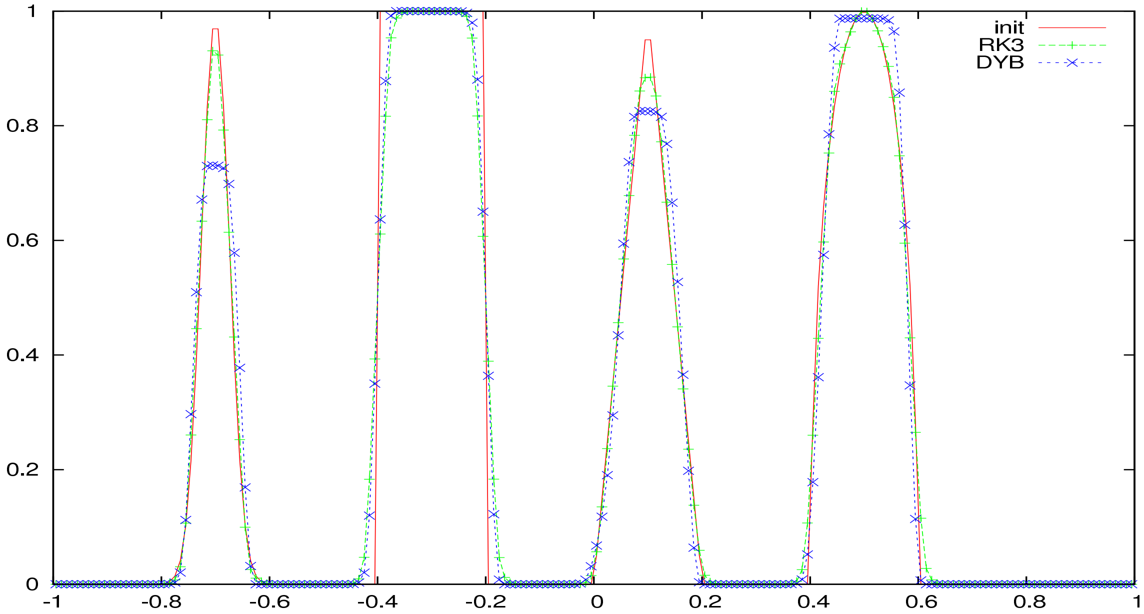

Figure 3.8: *Comparaison of free transport between the formal fourth order scheme issued from Daigugi, Yamamoto, and Berthon (DYB, blue), an exact third order Discontinuous Galerkine scheme from P.-H. Maire [18], with suitable slope limiters (RK3, green). The initial solution is the bold red curve. 200 grid points discretize the [-1,1] computational domain. The CFL condition is* $1/5$*, with 400 time steps until the final time* $t_{end} = 8$*, when the solution of the transport equation (with velocity* $v = 1$*) is represented with green and blue curves.*

Bibliography

[1] Arber T. D., Vann R. G. L., A critical Comparison of Eulerian-Grid-Based vlasov Solvers, *Journal of Computational Physics* 180 339-357, (2002).

[2] Berthon C. and Marche F. *A positive preserving high order VFROE scheme for shallow water equations: a class of relaxation schemes*, SIAM J. Sci. Comput. Vol 30., issue 5, pp. 2587-2612, (2008).

[3] Berthon *Private communication*, (2008).

[4] Bourgeade A. and NKonga B. *Dynamic load balancing Computation of Pulses Propagating in a Nonlinear Medium*, The Journal of Supercomputing, Vol 28., issue 5, pp. 279-294, (2004).

[5] Cheng C. Z., Knorr G., The integration of the Vlasov equation in configuration space, *Journal of Computational Physics* 22 330, (1976).

[6] Cohen G., Ferrieres X., Pernet S., Discontinuous Galerkin methods for Maxwell's equations in the time domain, *C. R. Physique*, 7, 494-500, (2006).

[7] Crouseilles N., Filbet F., *Numerical approximation of collisional plasmas by high order methods*, Journal of Computational Physics, 201, 546-572, (2004).

[8] Deveze T., Contribution à l'analyse, par Différences Finies, des équations de MAXWELL dans le domaine temps , *PhD of Paris 6 University*, (1992).

[9] Duclous R., Dubroca B., Filbet F., Tikhonchuk V., High order resolution of the Maxwell-Fokker-Planck-Landau model intended for ICF application , *Journal Comp. Phys.* 228, 14, 5072-5100, (2009).

[10] Elkina N. V., Büchner J., A new conservative unsplit method for the solution of the Vlasov equation, *Journal of Computational Physics* 213 862-875, (2006).

[11] A. Klökner, T. Warburton, J. Bridge, J. S. Hesthaven, Nodal discontinuous Galerkin methods on graphical processors, *J. Comput. Phys.* 228, 21, (2009).

[12] Huot F., Ghizzo A., Bertrand P., Sonnendrücker E., Coulaud O., Instability of the time splitting scheme for the one-dimensional and relativistic Vlasov- Maxwell system, *J. Comput. Phys.* 185, 512, (2003).

[13] Hyman J. M., Shashkov M., Mimetic Discretization for Maxwell's equations, *J. Comput. Phys.* 151, 2, 881-909, (1999).

[14] Jacobs G. B., Hesthaven J. S., High-order nodal discontinuous Galerkin particle-in-cell method on unstructured grids, *J. Comput. Phys.* 214, 96-121, (2006).

[15] Kurganov A., Tadmor E., *Solution of Two-Dimensional Riemann Problems for Gas Dynamics without Riemann Problem Solvers*, Numerical methods Partial Differential, 218, 584-608, (2002).

[16] Birdsall C. K., Langdon A. B., Plasma Physics via Computer Simulation, *Institute of Physics, London*, (1995).

[17] Le Bourdiec S., de Vuyst F., Jacquet L., *Numerical solution of the Vlasov-Poisson system using generalized Hermite functions*, Computer Physics Communications 175 528-544, (2006).

[18] Rueda Villegas L., Etude de Schémas d'ordres élevés pour la résolution des équations de l'hydrodynamique Lagrangienne, *Master Thesis at CELIA under the direction of P.-H. Maire*, (2009).

[19] Ruhl H. Mulser P., Relativistic Vlasov simulation of intense fs laser pulse-matter interaction, *Phys. Letteres A* 205, 388-392, (1995).

[20] Sartori C. et Coppa G.G M., Analysis of transient and asymptotic behavior in relativistic Landau damping, *Phys. Plasmas* 2 (11), (1995).

[21] Sentoku Y., Kemp A. J., Numerical methods for particle simulations at extreme densities and temperatures: Weighted particles, relativistic collisions and reduced currents, *Journal of Computational Physics* 227, 14, 6846-6861, (2008).

[22] Sircombe N.J., Arber T. D., VALIS: A split-conservative shceme for the relativistic 2D Vlasov-Maxwell system, *Journal of Computational Physics* 228, 4773-4788, (2009).

[23] Schmitz H., Grauer R., Comparison of time splitting and backsubstitution methods for integrating Vlasov's equation with magnetic fields, *Computer Physics Communications* 175, 86-92, (2006).

[24] Van Leer B. *Towards the ultimate conservative difference scheme. V. A second-order sequel to Godunov's method*, J. Comput. Phys., 32, 101-136, (1979).

[25] Yamamoto S., Daiguji H. *High order accurate upwind schemes for solving the compressible Euler and Navier-Stokes equations*, Computers Fluids, 22, 259-270, (1993).

3.8 Appendix: Scaling with a plasma frequency in the nonrelativistic limit

Scaling parameters can be introduced to obtain a dimensionless form of the nonrelativistic Vlasov-Maxwell system (8.1), coupled with Fokker-Planck-Landau collision operators, such as the electron-electron collision operator (2.29). A plasma frequency ω_{pe}, Debye length λ_D, thermal velocity of electrons v_{th}, and cyclotron frequency ω_{ce} can be defined as follows

$$\omega_{pe} = \sqrt{\frac{n_0 e^2}{\epsilon_0 m_e}}, \quad \lambda_D = \sqrt{\frac{\epsilon_0 \kappa_B T_0}{n_0 e^2}}, \quad v_{th} = \sqrt{\frac{\kappa_B T_0}{m_e}}, \quad \omega_{ce} = \frac{eB}{m_e}. \tag{3.78}$$

These parameters enable us to define normalized dimensionless parameters. Normalized time, space and velocity, respectively:

$$\omega_{pe}\, t \to t, \quad \frac{x}{\lambda_D} \to x, \quad \frac{v}{v_{th}} \to v. \tag{3.79}$$

Normalized electric field, magnetic field and distribution function, respectively

$$\frac{e\,E}{m_e\,v_{th}\omega_{pe}} \to E, \qquad \frac{e\,B}{m_e\,\omega_{pe}} = \frac{\omega_{ce}}{\omega_{pe}} \to B, \qquad f_e\,\frac{v_{th}^3}{n_0} \to f_e. \tag{3.80}$$

This leads to the following dimensionless equations

$$\begin{cases} \dfrac{\partial f_e}{\partial t} + \nabla_{\mathbf{x}}\cdot(\mathbf{v} f_e) - \nabla_{\mathbf{v}}\cdot((\mathbf{E}+\mathbf{v}\times\mathbf{B})f_e) = \dfrac{\nu}{Z}\,C_{e,e}(f_e,f_e) + \nu\,C_{e,i}(f_e), \\[2mm] \dfrac{\partial \mathbf{E}}{\partial t} - \dfrac{1}{\beta^2}\nabla_{\mathbf{x}}\times\mathbf{B} = n\,\mathbf{u}, \\[2mm] \dfrac{\partial \mathbf{B}}{\partial t} + \nabla_{\mathbf{x}}\times\mathbf{E} = 0, \\[2mm] \nabla_{\mathbf{x}}\cdot\mathbf{E} = (1-n), \quad \nabla_{\mathbf{x}}\cdot\mathbf{B} = 0, \end{cases} \tag{3.81}$$

where $\beta = v_{th}/c$, ν is the ratio between an electron-ion collision frequency and the plasma frequency

$$\nu = \frac{Z\,n_0\,e^4\ln\Lambda}{8\,\pi\,\epsilon_0^2\,m_e^2\,v_{th}^3\,\omega_{pe}} = \frac{Z\,\ln\Lambda}{8\,\pi\,n_0\,\lambda_D^3} = \frac{\nu_{e,i}}{\omega_{pe}} \quad \text{with} \quad \nu_{e,i} = \frac{Z\,n_0\,e^4\ln\Lambda}{8\,\pi\,\epsilon_0^2\,m_e^2\,v_{th}^3}.$$

The zero and first order moments of the distribution function are

$$\begin{cases} n(t,\mathbf{x}) = \displaystyle\int_{\mathbb{R}^3} f_e(t,\mathbf{x},\mathbf{v})\,\mathbf{dv}, \\[2mm] \mathbf{u}(t,\mathbf{x}) = \dfrac{1}{n(t,\mathbf{x})}\displaystyle\int_{\mathbb{R}^3} f_e(t,\mathbf{x},\mathbf{v})\,\mathbf{v}\,\mathbf{dv} \end{cases}$$

which are normalized respectively by n_0 and v_{th}.

In the system (3.81), one may want to include the effect of collisions as a source term of the Vlasov equation. The dimensionless electron-electron and electron-ion collision operators read

$$\begin{cases} C_{e,e}(f_e,f_e) = \nabla_{\mathbf{v}}\cdot\left(\displaystyle\int_{\mathbb{R}^3}\Phi(\mathbf{v}-\mathbf{v}')\,[f_e(\mathbf{v}')\nabla_{\mathbf{v}}f_e(\mathbf{v}) - f_e(\mathbf{v})\nabla_{\mathbf{v}'}f_e(\mathbf{v}')]\,\mathbf{dv}'\right), \\[2mm] C_{e,i}(f_e) = \nabla_{\mathbf{v}}\cdot[\Phi(\mathbf{v})\nabla_{\mathbf{v}}f_e(\mathbf{v})], \end{cases} \tag{3.82}$$

with Φ given by (5.3).

3.9 Appendix: Scaling with a plasma frequency in the relativistic collisionless regime, with nonrelativistic collisions

There are two basic temporal scales in the kinetic equation (8.1), coupled with Fokker-Planck-Landau collision operators, such as the electron-electron collision operator (2.29). One is related to the collective electron motion and is characterized by the electron plasma frequency, $\omega_{pe} = \sqrt{Zn_0 e^2/\epsilon_0 m_e}$, another is the time of electron collisions characterized by the electron ion collision frequency, ν_{ei}. As it depends on the electron velocity, we have a possibility to choose either the thermal velocity of plasma electrons, $v_{th} = \sqrt{\kappa_B T_0/m_e}$, where κ_B is the Boltzmann constant and T_0 is the characteristic temperature of the bulk plasma electrons, or a characteristic velocity of beam electrons, which is close to c. If we are interested in the beam electrons and on their effect on plasma, it is more appropriate to normalize the electron collision frequency to its value calculated for fast electrons,

$$\nu_{ei} = Z^2 n_0 e^4 \ln\Lambda / 8\pi\epsilon_0^2 m_e^2 c^3. \tag{3.83}$$

Consequently, the electron velocity is normalized by c, the electron momentum by $m_e c$, and the electron distribution function by $Zn_0/m_e^3 c^3$. Then, our small parameter for the future analysis is the ratio of electron collision and plasma frequencies:

$$\nu = \frac{\nu_{ei}}{\omega_{pe}} = \frac{Z^{3/2}\sqrt{n_0}e^3 \ln\Lambda}{8\pi\epsilon_0^{3/2} m_e^{3/2} c^3} \ll 1, \tag{3.84}$$

which is a standard parameter in the ideal theory of plasmas.
If one is interested in the wave-particle interaction processes, it is more appropriate to normalize the time by the electron plasma frequency, $\omega_{pe} t \rightarrow t$, and the space coordinate by the electron inertial length, $x\omega_{pe}/c \rightarrow x$. Then the electric and magnetic fields are normalized by $m_e v_{th}\omega_{pe}/e$ and $m_e\omega_{pe}/e$, correspondingly. This leads to the following dimensionless system of equations:

$$\begin{cases} \dfrac{\partial f_e}{\partial t} + \nabla_{\mathbf{x}} \cdot (\mathbf{v} f_e) - \nabla_{\mathbf{p}} \cdot ((\mathbf{E} + \mathbf{v} \times \mathbf{B}) f_e) = \dfrac{\nu}{Z} C_{ee}(f_e, f_e) + \nu C_{ei}(f_e), \\ \dfrac{\partial \mathbf{E}}{\partial t} - \nabla_{\mathbf{x}} \times \mathbf{B} = -\mathbf{j}, \\ \dfrac{\partial \mathbf{B}}{\partial t} + \nabla_{\mathbf{x}} \times \mathbf{E} = 0, \\ \nabla_{\mathbf{x}} \cdot \mathbf{E} = \rho, \\ \nabla_{\mathbf{x}} \cdot \mathbf{B} = 0, \\ C_{ee}(f_e, f_e) = \nabla_{\mathbf{p}} \cdot \displaystyle\int_{\mathbb{R}^3} \Phi(\mathbf{p} - \mathbf{p}') \left[f_e(\mathbf{p}') \nabla_p f_e(\mathbf{p}) - f_e(\mathbf{p}) \nabla_{\mathbf{p}'} f_e(\mathbf{p}') \right] d\mathbf{p}', \\ C_{e,i}(f_e) = \nabla_{\mathbf{p}} \cdot \left(\Phi(\mathbf{p}) \nabla_{\mathbf{p}} f_e \right). \end{cases} \tag{3.85}$$

3.10 Appendix: semi-analytical solution of an electrostatic configuration in the linear regime

The non-relativistic $1D_x \times 3D_{\mathbf{v}}$Vlasov-Poisson system extracted from the equations (8.1)-(3.3) reads

$$\frac{\partial f}{\partial t} + v_1 \frac{\partial f}{\partial x_1} + \frac{q_e}{m_e} E_1 \frac{\partial f}{\partial v_1} = 0 \, , \tag{3.86}$$

$$\frac{\partial E_1}{\partial x_1} = -\frac{q_e}{\epsilon_0} \left(n_0 - \int_{\mathbb{R}^3} f(t, x_1, \mathbf{v}) d^3 v \right) \, . \tag{3.87}$$

The distribution function f is assumed to be a perturbation around an equilibrium state $f^{(0)}(||\mathbf{v}||)$, $E_1^{(0)} = 0$, $n_0 = \displaystyle\int_{\mathbb{R}^3} f^{(0)}(||\mathbf{v}||) d^3 v$. The system (3.86),(3.87) is linearized around this equilibrium state

$$f(t, x_1, \mathbf{v}) = f^{(0)}(||\mathbf{v}||) + f^{(1)}(t, x_1, \mathbf{v}) \, , \tag{3.88}$$

$$E_1^{(1)}(t, x_1) = E_1^{(0)} + E_1^{(1)}(t, x_1) \, , \tag{3.89}$$

under the hypothesis:

$$||f^{(1)}|| \ll ||f^{(0)}|| \, , \tag{3.90}$$

$$||E_1^{(1)}|| \ll 1 \, . \tag{3.91}$$

The Vlasov-Poisson can then be set under the following form (transport equation along the space directions supplemented by a source term along the v_1 direction), after linearization

$$\begin{cases} \dfrac{\partial f^{(1)}}{\partial t} + v_1 \dfrac{\partial f^{(1)}}{\partial x_1} = -\dfrac{q_e}{m_e} E_1^{(1)} \dfrac{\partial f^{(0)}}{\partial v_1} \, , \\[2ex] \dfrac{\partial E_1^{(1)}}{\partial x_1} = \dfrac{q_e}{\epsilon_0} \displaystyle\int_{\mathbb{R}^3} f^{(1)}(t, x_1, \mathbf{v}) d^3 v \, . \end{cases} \tag{3.92}$$

If $f^{(1)}$ and $E_1^{(1)}$ are periodic and integrable, then their respective normalized Fourier coefficient are well-defined. A Fourier series expansion gives $\forall t > 0$

$$\begin{cases} f^{(1)}(t, x_1, \mathbf{v}) = \hat{f}^{(1)}(t, k_1, \mathbf{v}) cos(k_1 x_1) \, , \\[2ex] \hat{f}^{(1)}(t, k_1, \mathbf{v}) = \dfrac{1}{L_1} \displaystyle\int_0^{L_1} f^{(1)}(t, x_1, \mathbf{v}) e^{-ik_1 x_1} dx_1 \, , \end{cases} \tag{3.93}$$

Where L_1 is the size of the domain. The same reconstruction using Fourier series is used for $E_1^{(1)}$. These coefficients verify the following equations,obtained by Fourier transformation performed on the equations of the system (3.92), for all real k_1

$$\frac{\partial \hat{f}^{(1)}}{\partial t} + i k_1 v_1 \hat{f}^{(1)} = -\frac{q_e}{m_e} \hat{E}_1^{(1)} \frac{\partial f^{(0)}}{\partial v_1} \, , \tag{3.94}$$

$$i k_1 \hat{E}_1 = \frac{q_e}{\epsilon_0} \hat{n}_1 \, . \tag{3.95}$$

Then introducing the notation $\hat{f}^{(1)}(t = 0, k_1, \mathbf{v}) = \hat{f}^{(10)}(k_1, \mathbf{v})$, the equation (3.94) can be written in the integral form

$$\hat{f}^{(1)}(t, k_1, \mathbf{v}) = \hat{f}^{(10)}(k_1, \mathbf{v})e^{-ik_1 v_1 t} - \frac{q_e}{m_e}\int_0^t \hat{E}_1^{(1)}(t', k_1)\frac{\partial f^{(0)}}{\partial v_1}e^{-ik_1 v_1 (t-t')}dt' \ . \tag{3.96}$$

Integrating the equation (3.96) over **v** and injecting in it the relation (3.95), one obtains the following integral equation for the density

$$\hat{n}^{(1)}(t, k_1) = M(t, k_1) + \int_0^t K(t - t', k_1)\hat{n}^{(1)}(t', k_1)dt' \ , \tag{3.97}$$

where

$$K(t, k_1) = \frac{iq_e^2}{k_1 m_e \epsilon_0}\int_{\mathbb{R}^3}\frac{\partial f^{(0)}}{\partial v_1}e^{-ik_1 v_1 t}d^3v \ , \tag{3.98}$$

$$M(t, k_1) = \int_{\mathbb{R}^3}\hat{f}^{(10)}(k_1, \mathbf{v})e^{-ik_1 v_1 t}d^3v \ . \tag{3.99}$$

These kernels can be computed with the desired accuracy, following [20]. The numerical resolution of (3.97) finally reduces to the inversion of a triangular linear system.
Macroscopic quantities such as the density or the heat flux can then be reconstructed using these latter equations.

3.11 Appendix: Semi-analytical solution for an X-mode configuration in the linear regime

In order to illustrate this method, let us now look after the particular X-mode configuration (3.100) of the free transport Vlasov-Maxwell system, that is in the electromagnetic case ($\mathbf{k} \perp \mathbf{E}$). Two momentum components are considered to account for the self-consistent evolution of the magnetic $B_3(t, x_1)$ and electric $E_2(t, x_1)$ fields, in the directions perpendicular to the direction of the perturbation x_1, so as to treat the Weibel and filamentation instabilities. The same semi-analytical procedure can be applied for the Vlasov-Poisson electrostatic case ($\mathbf{k} \parallel \mathbf{E}$), assuming only one component of electric field $E_1(t, x_1)$ [9, 20]. Finally, oblique modes (arbitrary **k**, *i.e.* mixed Weibel, filamentation and two-stream instability) can be treated if the system (3.112)-(3.114) is supplemented with an equation on the current in the x_1 direction, together with the corresponding component of the Ampère equation.

The dimensionless X-mode system reads ,with the scaling described in appendix 3.9,

$$\frac{\partial f}{\partial t} + v_1\frac{\partial f}{\partial x_1} - (v_2 B_3)\frac{\partial f}{\partial p_1} - (E_2 - v_1 B_3)\frac{\partial f}{\partial p_2} = 0, \tag{3.100}$$

$$\frac{\partial E_2}{\partial t} = -\frac{\partial B_3}{\partial x_1} - j_2, \tag{3.101}$$

$$\frac{\partial B_3}{\partial t} = -\frac{\partial E_2}{\partial x_1}. \tag{3.102}$$

The initial quantities are chosen such as

$$f(t=0,x_1,\mathbf{p}) = f_0(p) + f^{(1)}(t=0,x_1,\mathbf{p}), \tag{3.103}$$
$$E_2(t=0,x_1) = E_2^{(1)}(t=0,x_1), \tag{3.104}$$
$$B_3(t=0,x_1) = B_3^{(1)}(t=0,x_1), \tag{3.105}$$
$$f^{(1)} \ll f_0. \tag{3.106}$$

A Fourier series expansion gives $\forall t > 0$

$$f^{(1)}(t,x_1,\mathbf{p}) = \hat{f}^{(1)}(t,k_1,\mathbf{p})\cos(k_1 x_1), \tag{3.107}$$
$$\hat{f}^{(1)}(t,\mathbf{p}) = \frac{1}{L_1}\int_{\mathbb{L}_{\mathbb{x}}} f^{(1)}(t,x_1,\mathbf{p})e^{-ik_1x_1}dx_1. \tag{3.108}$$

The same reconstruction using Fourier series is used for $E_2^{(1)}$ and $B_3^{(1)}$.
Now performing a linearization of (3.100)-(3.102), and applying the Fourier transform (3.108) on the system leads to

$$\frac{\partial \hat{f}^{(1)}}{\partial t} + ik_1 v_1 \hat{f}^{(1)} = v_2 \hat{B}_3^{(1)}\frac{\partial f_0}{\partial p_1} + (\hat{E}_2^{(1)} - v_1\hat{B}_3^{(1)})\frac{\partial f_0}{\partial p_2}, \tag{3.109}$$
$$\frac{\partial \hat{E}_2^{(1)}}{\partial t} = -ik_1\hat{B}_3^{(1)} - \hat{j}_2^{(1)}, \tag{3.110}$$
$$\frac{\partial \hat{B}_3^{(1)}}{\partial t} = -ik_1\hat{E}_2^{(1)}. \tag{3.111}$$

At this point it is worth noticable that we restrict to space Fourier transform, and do not perform Laplace transform, that would face the complex treatment of branch cut in the ω complex plane.
Instead, equation (3.109) is integrated in time. Then it is multiplied by $-v_y$, and finally integrated over momentum

$$\begin{aligned}\hat{j}_2^{(1)}(t) = M_2(t) - &\int_0^t \hat{E}_2^{(1)}(t')K_{2,2}(t-t')dt' \\ &- \int_0^t \hat{B}_3^{(1)}(t')\left(K_{22,1}(t-t') - K_{21,2}(t-t')\right)dt',\end{aligned} \tag{3.112}$$
$$\frac{\partial \hat{E}_2^{(1)}}{\partial t} = -ik_x\hat{B}_3^{(1)} - \hat{j}_2^{(1)}, \tag{3.113}$$
$$\frac{\partial \hat{B}_3^{(1)}}{\partial t} = -ik_1\hat{E}_2^{(1)}, \tag{3.114}$$

where:

$$K_{2,2}(t) = \int_{\mathbb{R}^3} v_2 \frac{\partial f_0}{\partial p_2} e^{-ik_1 v_1 t} d^3 p, \tag{3.115}$$

$$M_2(t) = -\int_{\mathbb{R}^3} v_2 \hat{f}^{(1)}(t=0, \mathbf{p}) e^{-ik_1 v_1 t} d^3 p, \tag{3.116}$$

$$K_{22,1}(t) = \int_{\mathbb{R}^3} v_2^2 \frac{\partial f_0}{\partial p_1} e^{-ik_1 v_1 t} d^3 p, \tag{3.117}$$

$$K_{21,2}(t) = \int_{\mathbb{R}^3} v_2 v_1 \frac{\partial f_0}{\partial p_2} e^{-ik_1 v_1 t} d^3 p. \tag{3.118}$$

The system (3.112)-(3.114) can be simplified following several remarks

- $K_{22,1}(t) - K_{21,2}(t) = 0$: the term $\mathbf{v} \times \mathbf{B}$ has indeed no influence on the energy evolution.
- Using spherical coordinates, $K_{2,2}$ and M_2 can be greatly simplified.

$$K_{2,2}(k_1, t) = -\frac{\pi}{\beta^2} \int_0^\infty \frac{p^4}{\gamma_p^2} f_0(p) I(k_1 x_1 p t / \gamma_p) dp \qquad \forall t > 0 \,, \tag{3.119}$$

$$I(a) = \int_0^\pi \sin^3(\theta) e^{ia\cos(\theta)} d\theta = \frac{4}{a^2}\left(\frac{\sin(a)}{a} - \cos(a)\right) \quad \forall t > 0 \,,\ a \in \mathbb{R} \,, \tag{3.120}$$

$$I(0) = 4/3 \,. \tag{3.121}$$

Then the system (3.112)-(3.114) *can be solved numerically,*
with a simple inversion of a linear system,
at a prescribed accuracy [20].

3.12 Appendix: Initialization for the generation of a single X-mode plasma wave

This test case stands as a validation for the couplings of Vlasov and Maxwell equations. We determine initial conditions that trigger a plasma wave at a given wavelength. To do so, Vlasov-Maxwell equations are linearized, setting $f = f^{(0)} + f^{(1)}$, $E = E^{(1)}$, $B = B^{(0)} + B^{(1)}$ around the equilibrium state $f = f^{(0)}$, $E = 0$, $B = B^{(0)}$. In this appendix, we use the normalization (8.49)-(3.80). We assume periodic boundary conditions. The fluctuations of the total pressure tensor are neglected with respect to those of the magnetic field.

Using the conservation law $\frac{\partial n}{\partial t} + \frac{\partial j_1}{\partial x_1} = 0$, the former hypothesis lead us to solve the system of six equations with six unknown $j_1^{(1)}$, $j_2^{(1)}$, $E_1^{(1)}$, $E_2^{(1)}$, $B_3^{(1)}$ and $n^{(1)}$

$$\left\{\begin{array}{l}\dfrac{\partial j_1^{(1)}}{\partial t}+E_1^{(1)}+B^{(0)}j_2^{(1)}=0\;,\\ \dfrac{\partial j_2^{(1)}}{\partial t}+E_2^{(1)}-B^{(0)}j_1^{(1)}=0\;,\\ \dfrac{\partial n^{(1)}}{\partial t}+\partial_{x_1}j_1^{(1)}=0\;,\\ \dfrac{\partial E_1^{(1)}}{\partial x_1}=-n^{(1)}\;,\\ \dfrac{\partial E_2^{(1)}}{\partial t}=-\dfrac{1}{\beta^2}\dfrac{\partial B_3^{(1)}}{\partial x_1}+j_2^{(1)}\;,\\ \dfrac{\partial B_3^{(1)}}{\partial t}=-\dfrac{\partial E_2^{(1)}}{\partial x_1}\;.\end{array}\right. \tag{3.122}$$

Applying time and space Fourier transform to this system, and identifying Fourier components ($n^{(1)} = \hat{n}\exp(-i\omega t + ik_1x_1)$), the following system is obtain

$$\left\{\begin{array}{l}-i\omega\hat{j}_1+\hat{E}_1+B^{(0)}\hat{j}_2=0\;,\\ -i\omega\hat{j}_2+\hat{E}_2-B^{(0)}\hat{j}_1=0\;,\\ -i\omega\hat{n}+ik_1\hat{j}_1=0\;,\\ ik_1\hat{E}_1=-\hat{n}\;,\\ -i\omega\hat{E}_2=-\dfrac{1}{\beta^2}ik_1\hat{B}_3+\hat{j}_2\;,\\ -i\omega\hat{B}_3=-ik_1\hat{E}_2\;.\end{array}\right.$$

The dispersion equation of this system reads

$$N^2=\frac{k_1^2}{\beta^2\omega^2}=1-\frac{\omega^2-1}{\omega^2(\omega^2-1-\|B^{(0)}\|^2)}\;. \tag{3.123}$$

In this equation, the plasma frequency is $\omega_{pe} = 1$ and the cyclotron frequency is $\omega_c = q_e\|B^{(0)}\|/m$, that is $\|B^0\|$ in this dimensionless case. The perturbation term of the distribution function at initial time can be determined for a particular solution ω of this relation dispersion.
The Fourier transform is applied on the linearized Vlasov equation

$$(-i\omega+ik_1v_1)\hat{f}-\hat{E}_1\frac{\partial f^{(0)}}{\partial v_1}-\hat{E}_2\frac{\partial f^{(0)}}{\partial v_2}-B^{(0)}v_2\frac{\partial\hat{f}}{\partial v_1}+B^{(0)}v_1\frac{\partial\hat{f}}{\partial v_2}\;=\;0\;. \tag{3.124}$$

This equation is expressed in cylindrical coordinates

$$\left\{\begin{array}{l}v_1=v_\perp\cos(\psi)\;,\\ v_2=v_\perp\sin(\psi)\;,\\ v_3=v_{||}\end{array}\right.$$

where

$$\left\{\begin{array}{l}v_\perp=(\|v_1\|^2+\|v_2\|^2)^{1/2}\;,\\ \tan(\psi)=\dfrac{v_2}{v_1}\;.\end{array}\right.$$

Recalling that:

$$\nabla_{\mathbf{v}} f = \frac{\partial f}{\partial v_\perp}\nabla_{\mathbf{v}} v_\perp + \frac{\partial f}{\partial \psi}\nabla_{\mathbf{v}}\psi + \frac{\partial f}{\partial v_{||}}\nabla_{\mathbf{v}} v_{||} \,,$$

$$\begin{cases} \dfrac{\partial v_\perp}{\partial v_1} = \cos(\psi)\,, \\ \dfrac{\partial v_\perp}{\partial v_2} = \sin(\psi)\,, \\ \dfrac{\partial \psi}{\partial v_1} = -\dfrac{1}{v_\perp}\sin(\psi) \\ \dfrac{\partial \psi}{\partial v_2} = \dfrac{1}{v_\perp}\cos(\psi)\,, \end{cases}$$

with $\nabla_{\mathbf{v}} v_\perp = \vec{e}_\perp$, $\nabla_{\mathbf{v}} v_\psi = \vec{e}_\psi$ and $\nabla_{\mathbf{v}} v_{||} = \vec{e}_{||}$, where $\vec{e}$ are vectors in the local basis. Setting $f^{(0)}(||\mathbf{v}||^2) = (2\pi)^{\frac{3}{2}}\exp(-\frac{||\mathbf{v}||^2}{2})$, and writing

$$(\mathbf{v}\wedge\mathbf{B}).\nabla_{\mathbf{v}}\hat{f} = (\nabla_{\mathbf{v}}\hat{f}\wedge\mathbf{v}).\mathbf{B} = -B^{(0)}\frac{\partial f}{\partial \psi},\ \text{with } \mathbf{B} = (0,0,B^{(0)})\,,$$

the kinetic equation (3.124) becomes

$$(-i\omega + ik_1 v_\perp\cos(\psi))\hat{f} + B^{(0)}\frac{\partial \hat{f}}{\partial \psi} + f^{(0)}(||\mathbf{v}||^2)v_\perp(\hat{E}_1\cos(\psi) + \hat{E}_2\sin(\psi)) = 0. \tag{3.125}$$

In order to solve this equation, we decompose the distribution function as a Fourier series

$$\hat{f} = \sum_{n=-\infty}^{+\infty}\hat{f}_n(v_\perp)e^{in\psi}.$$

Then from (3.125),

$$\sum_{n=-\infty}^{+\infty}(-i\omega + ik_1 v_\perp\cos(\psi) + inB^{(0)})\hat{f}_n e^{in\psi} = -f^{(0)}(||\mathbf{v}||^2)v_\perp(\hat{E}_1\cos(\psi) + \hat{E}_2\sin(\psi))\,.$$

Multiplying this equation by $e^{im\psi}$, integrating from 0 to 2π, we obtain

$$\begin{aligned}&\sum_{n=-\infty}^{+\infty}\int_0^{2\pi} e^{im\psi}(-i\omega + ik_1 v_\perp\cos(\psi) + inB^{(0)})\hat{f}_n e^{in\psi}d\psi \\ &= -f^{(0)}(||\mathbf{v}||^2)v_\perp\int_0^{2\pi} e^{im\psi}(\hat{E}_1\cos(\psi) + \hat{E}_2\sin(\psi))d\psi\,.\end{aligned} \tag{3.126}$$

For $m = 0$, terms are different from zero only for $n = -1, 0, 1$. From (3.126) comes

$$k_1 v_\perp\hat{f}_{-1} - 2\omega\hat{f}_0 + k_1 v_\perp\hat{f}_1 = 0\,. \tag{3.127}$$

For $m = -1$,

$$ik_1 v_\perp\hat{f}_0 - 2i(\omega - B^{(0)})\hat{f}_1 + ik_1 v_\perp\hat{f}_2 = -f_0(v^2)v_\perp(\hat{E}_1 - i\hat{E}_2)\,. \tag{3.128}$$

For $m = 1$,

$$ik_1 v_\perp \hat{f}_{-2} - 2i(\omega + B^{(0)})\hat{f}_{-1} + ik_1 v_\perp \hat{f}_0 = -f^{(0)}(||\mathbf{v}||^2)v_\perp(\hat{E}_1 + i\hat{E}_2)\ . \tag{3.129}$$

The case $m = -2$ involves $\hat{f}_3$,

$$ik_1 v_\perp \hat{f}_1 - 2(\omega - 2B^{(0)})\hat{f}_2 + ik_1 v_\perp \hat{f}_3 = 0\ . \tag{3.130}$$

In the same manner the case $m = 2$ involves $\hat{f}_{-3}$,

$$ik_1 v_\perp \hat{f}_{-3} - 2(\omega + 2B^{(0)})\hat{f}_{-2} + ik_1 v_\perp \hat{f}_{-1} = 0\ . \tag{3.131}$$

In order to close the system, the components f_{-3} and f_3 are neglected, and we deduce from (3.127-3.131),

$$\left\{ \begin{array}{rcl} -2(\omega + 2B^{(0)})\hat{f}_{-2} + ik_1 v_\perp \hat{f}_{-1} & = & 0\ , \\ ikv_\perp \hat{f}_{-2} - 2i(\omega + B^{(0)})\hat{f}_{-1} + ik_1 v_\perp \hat{f}_0 & = & -f^{(0)}(||\mathbf{v}||^2)v_\perp(\hat{E}_1 + i\hat{E}_2)\ , \\ kv_\perp \hat{f}_{-1} - 2\omega \hat{f}_0 + k_1 v_\perp \hat{f}_1 & = & 0\ , \\ ik_1 v_\perp \hat{f}_0 - 2i(\omega - B^{(0)})\hat{f}_1 + ik_1 v_\perp \hat{f}_2 & = & -f^{(0)}(||\mathbf{v}||^2)v_\perp(\hat{E}_1 - i\hat{E}_2)\ , \\ ik_1 v_\perp \hat{f}_1 - 2(\omega - 2B^{(0)})\hat{f}_2 & = & 0\ . \end{array} \right.$$

The solution of linearized Vlasov equation can be calculated

$$\left\{ \begin{array}{rcl} f(t,x,v) & = & f^{(0)}(||\mathbf{v}||^2) + \sum_{n=-\infty}^{+\infty} \hat{f}_n(v_\perp)e^{-i\omega t + ik_1 x_1 + in\psi}\ , \\ E_1(t,x) & = & \hat{E}_1 e^{-i\omega t + ik_1 x_1}\ , \\ E_2(t,x) & = & \hat{E}_2 e^{-i\omega t + ik_1 x_1}\ , \\ B(t,x) & = & B^{(0)} + \hat{B}_3 e^{-i\omega t + ik_1 x_1}\ . \end{array} \right.$$

The dispersion relation (3.123) provides with a particular ω. Then we obtain the following results for the construction of the initial solution,

$$f(0,x,v) = f^{(0)}(||\mathbf{v}||^2) + \sum_{n=-2}^{2} \hat{f}_n(v_\perp)e^{ik_1 x + in\psi}$$

With the expressions

$$
\begin{aligned}
\frac{\hat{f}_{-2}}{f^{(0)}(\|\mathbf{v}\|^2)\hat{D}} &= i(-4\,\omega^3\hat{E}_1 - 4\,i\omega^3\hat{E}_2 + 12\,i\omega^2 B^{(0)}\,\hat{E}_2 + 12\,\omega^2 B^{(0)}\,\hat{E}_1 - 8\,\|B^{(0)}\|^2\omega\,\hat{E}_1 \\
&+ {k_1}^2{v_\perp}^2\omega\,\hat{E}_1 + 3\,i{k_1}^2{v_\perp}^2\omega\,\hat{E}_2 - 8\,i\|B^{(0)}\|^2\omega\,\hat{E}_2 - 4\,i{k_1}^2{v_\perp}^2 B^{(0)}\,\hat{E}_2){v_\perp}^2 k_1, \\
\frac{\hat{f}_{-1}}{f^{(0)}(\|\mathbf{v}\|^2)\hat{D}} &= 2\,iv_\perp\,(\hat{E}_1\,{k_1}^2{v_\perp}^2\omega^2 + 4\,iB^{(0)}\,\omega^3\hat{E}_2 - 16\,\|B^{(0)}\|^3\omega\,\hat{E}_1 - 16\,i\|B^{(0)}\|^3\omega\,\hat{E}_2 \\
&+ 3\,i\hat{E}_2\,{k_1}^2{v_\perp}^2\omega^2 - 4\,\hat{E}_1\,\omega^4 - 8\,i\hat{E}_2\,{k_1}^2{v_\perp}^2\|B^{(0)}\|^2 + 2\,{k_1}^2{v_\perp}^2 B^{(0)}\,\omega\,\hat{E}_1 \\
&+ 2\,i{k_1}^2{v_\perp}^2 B^{(0)}\,\omega\,\hat{E}_2 + 16\,\hat{E}_1\,\|B^{(0)}\|^2\omega^2 + 16\,i\hat{E}_2\,\|B^{(0)}\|^2\omega^2 + 4\,B^{(0)}\,\omega^3\hat{E}_1 \\
&- 4\,i\hat{E}_2\,\omega^4), \\
\frac{\hat{f}_{0}}{f^{(0)}(\|\mathbf{v}\|^2)\hat{D}} &= 2\,i{v_\perp}^2 k_1(16\,\|B^{(0)}\|^2\omega\,\hat{E}_1 + {k_1}^2{v_\perp}^2\omega\,\hat{E}_1 - 4\,\omega^3\hat{E}_1 + 4\,i\omega^2 B^{(0)}\,\hat{E}_2 \\
&- 16\,i\|B^{(0)}\|^3\hat{E}_2 + 2\,i{k_1}^2{v_\perp}^2 B^{(0)}\,\hat{E}_2), \\
\frac{\hat{f}_{1}}{f^{(0)}(\|\mathbf{v}\|^2)\hat{D}} &= 2\,i(-2\,B^{(0)} + \omega)v_\perp\,(-4\,i{k_1}^2{v_\perp}^2 B^{(0)}\,\hat{E}_2 + {k_1}^2{v_\perp}^2\omega\,\hat{E}_1 - 3\,i{k_1}^2{v_\perp}^2\omega\,\hat{E}_2 \\
&- 12\,\omega^2 B^{(0)}\,\hat{E}_1 + 12\,i\omega^2 B^{(0)}\,\hat{E}_2 - 4\,\omega^3\hat{E}_1 + 4\,i\omega^3\hat{E}_2 - 8\,\|B^{(0)}\|^2\omega\,\hat{E}_1 \\
&+ 8\,i\|B^{(0)}\|^2\omega\,\hat{E}_2), \\
\frac{\hat{f}_{2}}{f^{(0)}(\|\mathbf{v}\|^2)\hat{D}} &= ik_1{v_\perp}^2(-4\,i{k_1}^2{v_\perp}^2 B^{(0)}\,\hat{E}_2 + {k_1}^2{v_\perp}^2\omega\,\hat{E}_1 - 3\,i{k_1}^2{v_\perp}^2\omega\,\hat{E}_2 - 12\,\omega^2 B^{(0)}\,\hat{E}_1 \\
&+ 12\,i\omega^2 B^{(0)}\,\hat{E}_2 - 4\,\omega^3\hat{E}_1 + 4\,i\omega^3\hat{E}_2 - 8\,\|B^{(0)}\|^2\omega\,\hat{E}_1 + 8\,i\|B^{(0)}\|^2\omega\,\hat{E}_2),
\end{aligned}
$$

where

$$\hat{D} = \omega\,(64\,\|B^{(0)}\|^4 - 16\,{k_1}^2{v_\perp}^2\omega^2 + 16\,\omega^4 + 16\,{k_1}^2{v_\perp}^2\|B^{(0)}\|^2 + 3\,{k_1}^4{v_\perp}^4 - 80\,\|B^{(0)}\|^2\omega^2).$$

$k_1 v_\perp$ being small with respect to $B^{(0)}$ and ω, for this particular application ($v_\perp$ must be considered in the range where the equilibrium distribution function $f^{(0)}(\|\mathbf{v}\|^2) = (2\pi)^{\frac{3}{2}}\exp(-\frac{\|\mathbf{v}\|^2}{2})$ does not vanish. If $B^{(0)} = 2$, $\omega \simeq 5$ and $k = 2\pi/25$, then $kv_\perp \ll B^{(0)}, \omega$), the numerical powers of $k_1 v_\perp$ can be neglected compared to these terms. The solution can be written

$$\begin{aligned}
\frac{\hat{f}_{-2}}{f^{(0)}(\|\mathbf{v}\|^2)\hat{D}} &= i{v_\perp}^2 k_1(-4\,\omega^3\hat{E}_1 - 4\,i\omega^3\hat{E}_2 + 12\,i\omega^2 B^{(0)}\,\hat{E}_2 \\
&+ 12\,\omega^2 B^{(0)}\,\hat{E}_1 - 8\,\|B^{(0)}\|^2\omega\,\hat{E}_1 - 8\,i\|B^{(0)}\|^2\omega\,\hat{E}_2), \\
\frac{\hat{f}_{-1}}{f^{(0)}(\|\mathbf{v}\|^2)\hat{D}} &= 2\,iv_\perp\,(4\,iB^{(0)}\,\omega^3\hat{E}_2 - 16\,\|B^{(0)}\|^3\omega\,\hat{E}_1 - 16\,i\|B^{(0)}\|^3\omega\,\hat{E}_2 - 4\,\hat{E}_1\,\omega^4 \\
&+ 16\,\hat{E}_1\,\|B^{(0)}\|^2\omega^2 + 16\,i\hat{E}_2\,\|B^{(0)}\|^2\omega^2 + 4\,B^{(0)}\,\omega^3\hat{E}_1 - 4\,i\hat{E}_2\,\omega^4), \\
\frac{\hat{f}_0}{f^{(0)}(\|\mathbf{v}\|^2)\hat{D}} &= 2\,i{v_\perp}^2 k_1(16\,\|B^{(0)}\|^2\omega\,\hat{E}_1 + {k_1}^2{v_\perp}^2\omega\,\hat{E}_1 - 4\,\omega^3\hat{E}_1 + 4\,i\omega^2 B^{(0)}\,\hat{E}_2 \\
&- 16\,i\|B^{(0)}\|^3\hat{E}_2), \\
\frac{\hat{f}_1}{f^{(0)}(\|\mathbf{v}\|^2)\hat{D}} &= 2\,iv_\perp\,(\omega - 2\,B^{(0)})(-12\,\omega^2 B^{(0)}\,\hat{E}_1 + 12\,i\omega^2 B^{(0)}\,\hat{E}_2 - 4\,\omega^3\hat{E}_1 + 4\,i\omega^3\hat{E}_2 \\
&- 8\,\|B^{(0)}\|^2\omega\,\hat{E}_1 + 8\,i\|B^{(0)}\|^2\omega\,\hat{E}_2), \\
\frac{\hat{f}_2}{f^{(0)}(\|\mathbf{v}\|^2)\hat{D}} &= ik_1{v_\perp}^2(-12\,\omega^2 B^{(0))}\,\hat{E}_1 + 12\,i\omega^2 B^{(0)}\,\hat{E}_2 - 4\,\omega^3\hat{E}_1 + 4\,i\omega^3\hat{E}_2 \\
&- 8\,\|B^{(0)}\|^2\omega\,\hat{E}_1 + 8\,i\|B^{(0)}\|^2\omega\,\hat{E}_2),
\end{aligned}$$

where

$$\hat{D} = \omega\,(64\,\|B^{(0)}\|^4 + 16\,\omega^4 - 80\,\|B^{(0)}\|^2\omega^2).$$

We choose to initialize the perturbation from the amplitude of the magnetic field:

$$\hat{B}_3 = A \text{ where } A \in [0, 1].$$

Then from the system (3.122) and the dispersion relation (3.123), we deduce the values of $\hat{E}_1$, $\hat{E}_2$ and thus reconstruct the $\hat{f}_i$,

$$\hat{E}_1 = \frac{-i\hat{B}_3\left(\omega^4\beta^2 - \omega^2{k_1}^2 - \omega^2\beta^2 - \|B^{(0)}\|^2\omega^2\beta^2 + \|B^{(0)}\|^2{k_1}^2\right)}{k_1\beta^2 B^{(0)}}, \quad \hat{E}_2 = \frac{\omega\hat{B}_3}{k_1}.$$

Chapter 4

A step towards short-pulse laser multi-species Vlasov simulations & Capture of discontinuities in phase-space: Convergence Analysis of a second order Finite Volume scheme

4.1 Introduction

In this chapter, we shall adress the issu of discontinuous solutions under electrostatic collective effects, and therefore restrict to Vlasov-Poisson systems.

The Vlasov-Poisson system is a model for the motion of a collisionless plasma and describes the evolution of the distribution function of particles, solution of the Vlasov equation, under the effects of free transport and self-consistent electric fields given by the Poisson equation. Here, we consider a dilute electron gas emitted at position $x = 0$ and absorbed at $x = L$. It gives rise to a nonlinear system of equations with boundary conditions. Under an external voltage, the dynamics of such a problem is modeled by the following system [15, 17]

$$\begin{cases} \dfrac{\partial f}{\partial t} + v\dfrac{\partial f}{\partial x} + E(t,x)\dfrac{\partial f}{\partial v} = 0, \quad t \geq 0,\ (x,v) \in Q\,; \\[2ex] -\dfrac{\partial^2 \phi}{\partial x^2}(t,x) = \rho(t,x), \quad E(t,x) = -\dfrac{\partial \phi}{\partial x}(t,x); \quad t \geq 0,\ x \in \Omega\,; \\[2ex] f(0,x,v) = f_0(x,v), \quad (x,v) \in Q\,; \end{cases} \tag{4.1}$$

where $Q := \Omega \times \mathbb{R}$ with $\Omega := (0,L)$. We define the macroscopic charged density $\rho(t,x)$ and the related current density $j(t,x)$ by

$$\rho(t,x) = \int_{-\infty}^{\infty} f(t,x,v)dv, \quad j(t,x) = \int_{-\infty}^{\infty} v f(t,x,v)dv, \quad (t,x) \in \mathbb{R}^+ \times \Omega. \tag{4.2}$$

Here, the boundary conditions for the electron distribution $f(t,x,v) \geq 0$ are given at $x = 0$

$$f(t,0,v) = g(t,v) \geq 0, \quad v > 0; \tag{4.3}$$

and at $x = L$

$$f(t,L,v) = 0, \quad v < 0; \tag{4.4}$$

and external voltages are given at $x = 0$ and $x = L$:

$$\phi(t,0) = 0, \quad \phi(t,L) = -\lambda(t) \leq 0, \quad t \geq 0. \tag{4.5}$$

Mathematical study of such nonlinear boundary value problem was initiated in the pioneering work of C. Greengard and P.-A. Raviart [15], in which stationary solutions are constructed. A higher dimensional generalization was given in [19] and [8]. On the other hand, for the dynamical problem of plane diode (4.1)-(4.5), weak solutions can be constructed as in [7]. Finally, recently Y. Guo *et al.* give a complete existence and uniqueness proof for the present model (4.1)-(4.5) [17] and for the Vlasov-Maxwell system [14].

The aim of this paper is to propose a high order finite volume scheme for the one-dimensional Vlasov-Poisson equation over an interval and to analyze its convergence. In one or two dimension, the numerical resolution of the Vlasov equation is often performed using eulerian methods. These methods are strongly inspired by the discretization of conservation laws in fluid mechanics [4, 23]. They consist in a discretization of the phase space (x, v), which is done by following the characteristic curves at each time step and interpolating the value at the origin of the characteristics by polynomial [12, 13]. This interpolation method works well for simple geometries of the physical space but does not seem to be well suited to more complex geometries. We refer to [13, 1] for a review of the literature on this topic and notice that more recently, J.A Carrillo *et al* [5] propose new schemes based on WENO reconstructions, which are particularly well suited and efficient for the study of discontinuities propagation.

Another type of schemes for the Vlasov equation is the finite volume type method (or flux balance method), where the discrete unknowns are averages of the distribution function on volumes paving the phase space. These unknowns are updated by considering incoming and outgoing fluxes leading to mass conservation. A high order scheme of this type was introduced by J.P. Boris and D.L. Book [4] for transport equations and later F. Filbet *et al.* proposed an improved version of this scheme, called the Positive and Flux Conservative method (PFC) [12, 13], which is not only conservative, but also preserves the positivity and the maximum value of the distribution function. The scheme was implemented up to third order accuracy. Let us also mention related papers where the convergence of a numerical scheme for the Vlasov-Poisson system is investigated. On the one hand, J. Schaeffer [20] proves the convergence of a finite difference scheme for the Vlasov-Poisson-Fokker-Planck system : transport terms are approximated by a characteristic method whereas diffusive term are treated by a classical finite difference operator. On the other hand, N. Besse studies the convergence of semi-lagrangian methods for smooth solutions to the Vlasov-Poisson [2] but it seems difficult to adapt this methodology for discontinuous solutions. Thus, F. Filbet performs a convergence analysis and gets error estimates on a finite volume scheme [10, 11] for weak *BV* solutions allowing discontinuities to occur, but this scheme is only first order and is not enough accurate to get a good approximation of the distribution function. Here, we extend the analysis to second order finite volume schemes and investigate the case where the solution may be discontinuous. More precisely, the purpose of this work is to prove the convergence of a second order finite volume scheme for the dynamic of plane diode model problem in plasma physics, namely, the one-dimensional Vlasov-Poisson system with boundary conditions with respect to the space variable.

We first present a second order upwind finite volume scheme computing the fluxes on the boundary of each cell of the mesh. Thus, from an L^∞ estimate on the velocity moments of f_h, we obtain a bound on the discrete electric field in $W^{1,\infty}$. We next give a weak *BV* inequality which will be useful for the convergence of the approximation to the weak solution to the Vlasov-Poisson system.

4.2 Numerical scheme and main results

In order to compute a numerical approximation of the solution of the Vlasov-Poisson system, let us define a Cartesian mesh of the phase space $\mathcal{M}_h$ consisting of cells, denoted by $C_{i,j}$, $i \in I = \{0, \dots, n_x - 1\}$, where n_x is the number of subcells of $(0, L)$ and $j \in \mathbb{Z}$. The mesh $\mathcal{M}_h$ is given by an increasing sequence $(x_{i-1/2})_{i\in\{0,\dots,n_x\}}$ of the interval $(0, L)$ and by a second increasing sequence $(v_{j-1/2})_{j\in\mathbb{Z}}$ of $\mathbb{R}$ for the velocity space.

Let $\Delta x_i = x_{i+1/2} - x_{i-1/2}$ be the physical space step and $\Delta v_j = v_{j+1/2} - v_{j-1/2}$ be the velocity space step. The parameter h indicates

$$h = \max_{i,j}\{\Delta x_i, \Delta v_j\}.$$

We assume the mesh satisfies the following condition : there exists $\alpha \in (0, 1)$ such that for all $h > 0$ and $(i, j) \in I \times \mathbb{Z}$,

$$\alpha\, h \le \Delta x_i \le h, \quad \text{and} \quad \alpha\, h \le \Delta v_j \le h. \tag{4.6}$$

Finally, we obtain a Cartesian mesh of the phase space constituted of control volumes

$$C_{i,j} = (x_{i-1/2}, x_{i+1/2}) \times (v_{j-1/2}, v_{j+1/2}) \quad \text{for } i \in I \text{ and } j \in \mathbb{Z}.$$

In order to work with a bounded domain, we will truncate at $|v| = v_h$ (v_h sufficiently large which will go to $+\infty$ as $h \to 0$) and we denote by J the following set

$$J := \{j \in \mathbb{Z}, \quad |v_j| \leq v_h\}.$$

Let Δt be the time step and $t^n = n\,\Delta t$ and x_i (resp. v_j) represents the middle of $[x_{i-1/2}, x_{i+1/2}]$ (resp. $[v_{j-1/2}, v_{j+1/2}]$). We set the discrete initial datum as

$$f^0_{i,j} = \frac{1}{\Delta x_i\,\Delta v_j} \int_{C_{i,j}} f_0(x,v)dxdv.$$

For $n \geq 0$, we define a sequence $(f^{n+1}_{i,j})_{i,j}$, which is assumed to approximate the average of the Vlasov equation solution (4.1)-(4.5) on the control volume $C_{i,j}$. It is given by

$$f^{n+1}_{i,j} = f^n_{i,j} - \frac{\Delta t}{\Delta x_i}\left[\mathcal{F}_{i+1/2,j} - \mathcal{F}_{i-1/2,j}\right] - \frac{\Delta t}{\Delta v_j}\left[\mathcal{G}_{i,j+1/2} - \mathcal{G}_{i,j-1/2}\right], \tag{4.7}$$

with

$$\left\{ \begin{array}{lcl} \mathcal{F}_{i+1/2,j} & = & v^+_j\, f^l_{i+1/2,j} - v^-_j\, f^r_{i+1/2,j}, \\ & & \\ \mathcal{G}_{i,j+1/2} & = & E^{n+}_i\, f^l_{i,j+1/2} - E^{n-}_i\, f^r_{i,j+1/2}, \end{array} \right. \tag{4.8}$$

where $f^l_{i+1/2,j}$ and $f^r_{i+1/2,j}$ are second order reconstructions with respect to the space variable $x \in (0,L)$ of the distribution function

$$\left\{ \begin{array}{l} f^l_{i+1/2,j} = f^n_{i,j} + \sigma_{i+1/2,j}\left[f^n_{i+1,j} - f^n_{i,j}\right], \\ \\ f^r_{i+1/2,j} = f^n_{i+1,j} - \sigma_{i+3/2,j}\left[f^n_{i+2,j} - f^n_{i+1,j}\right], \end{array} \right. \tag{4.9}$$

with the slope $\sigma_{i+1/2,j}$ given by the minmod limiter

$$\sigma_{i+1/2,j} = \left\{ \begin{array}{ll} 0, & \text{if } (f^n_{i+1,j} - f^n_{i,j})(f^n_{i,j} - f^n_{i-1,j}) \leq 0, \\ & \\ \dfrac{|f^n_{i,j} - f^n_{i-1,j}|}{|f^n_{i+1,j} - f^n_{i,j}|}\,\dfrac{\Delta x_i}{\Delta x_i + \Delta x_{i-1}} & \text{if } \dfrac{|f^n_{i,j} - f^n_{i-1,j}|}{\Delta x_i + \Delta x_{i-1}} \leq \dfrac{|f^n_{i+1,j} - f^n_{i,j}|}{\Delta x_i + \Delta x_{i+1}}, \\ & \\ \dfrac{\Delta x_i}{\Delta x_i + \Delta x_{i+1}}, & \text{else.} \end{array} \right. \tag{4.10}$$

Also $f^l_{i,j+1/2}$ and $f^r_{i,j+1/2}$ are built using the same type of reconstruction with respect to the velocity space $v \in \mathbb{R}$ for the flux $\mathcal{G}_{i,j+1/2}$

$$\left\{ \begin{array}{l} f^l_{i,j+1/2} = f^n_{i,j} + \sigma_{i,j+1/2,j}\left[f^n_{i,j+1} - f^n_{i,j}\right], \\ \\ f^r_{i+1/2,j} = f^n_{i,j+1} - \sigma_{i,j+3/2}\left[f^n_{i,j+2} - f^n_{i,j+1}\right], \end{array} \right. \tag{4.11}$$

with the slope $\sigma_{i,j+1/2}$ given by the minmod limiter

$$\sigma_{i,j+1/2} = \begin{cases} 0, & \text{if } (f^n_{i,j+1} - f^n_{i,j})\,(f^n_{i,j} - f^n_{i,j-1}) \le 0, \\[2ex] \dfrac{|f^n_{i,j} - f^n_{i,j-1}|}{|f^n_{i,j+1} - f^n_{i,j}|}\,\dfrac{\Delta v_j}{\Delta v_j + \Delta v_{j-1}} & \text{if } \dfrac{|f^n_{i,j} - f^n_{i,j-1}|}{\Delta v_j + \Delta v_{j-1}} \le \dfrac{|f^n_{i,j+1} - f^n_{i,j}|}{\Delta v_{j+1} + \Delta v_j}, \\[2ex] \dfrac{\Delta v_j}{\Delta v_j + \Delta v_{j+1}},, & \text{else.} \end{cases} \tag{4.12}$$

Let us notice that in this paper, we only consider the case of minmod limiters but we can easily apply the present analysis to classical limiters as superbee, etc. These conditions are sufficent to compute some approximations but we add some limiters useful to prove an error estimate result : there exist $K_1, K_2 > 0$ and $\beta \in (1, 2)$ such that

$$\sigma_{i+1/2,j}(f^n_{i,j} - f^n_{i-1,j})^2 \; + \; \sigma_{i,j+1/2}(f^n_{i,j} - f^n_{i,j-1})^2 \;\; \le \;\; K\,h^{\beta}, \qquad \forall (i, j) \in I \times \mathbb{Z}. \tag{4.13}$$

This conditions are used in section 4.3.3 only, for the consistency result.
The value E^n_i is an approximation of the electric field on $[x_{i-1/2}, x_{i+1/2}]$ given below by computing an approximate solution of the Poisson equation. To complete the scheme for the approximation of the Vlasov equation, we impose boundary conditions on x. To do this, we define two approximations $f^n_{-1,j}$ and $f^n_{n_x,j}$ on "virtual cells", given by

$$\begin{cases} f^n_{-1,j} \;=\; g^n_j \;:=\; g(t^n, v_j), & \text{if } v_j > 0, \;\; j \in J, \\[2ex] f^n_{n_x,j} \;=\; 0, & \text{if } v_j < 0, \;\; j \in J, \end{cases} \tag{4.14}$$

and to define slope limiters in the neighborhood of the boundary we also impose zero slope condition, that is, $f_{-2,j} = f_{-1,j}$ and $f_{n_x+1,j} = f_{n_x,j}$. We also set

$$\mathcal{G}_{i,j+1/2} \;=\; 0, \quad \text{for} \quad (i, j) \,\in\, I \times \mathbb{Z} \setminus J.$$

Thus, we are able to define the numerical solution approximating the solution of the Vlasov equation on $Q_T := \Omega_T \times \mathbb{R}$ by

$$f_h(t, x, v) = \begin{cases} f^n_{i,j}, & \text{if } (t, x, v) \in [t^n, t^{n+1}) \times C_{i,j} \text{ and } (i, j) \in I \times J, \\[2ex] 0, & \text{if } |v| > v_h. \end{cases}$$

Computing moments in v of the distribution function f_h, we define the discrete charge and current densities for $(t, x) \in [t^n, t^{n+1}) \times [x_{i-1/2}, x_{i+1/2})$:

$$\begin{aligned} \rho_h(t, x) \quad &= \quad \int_{\mathbb{R}} f_h(t, x, v)dv \;=\; \sum_{j\in\mathbb{Z}} \Delta v_j \, f^n_{i,j} \;=\; \rho^n_i, \\ j_h(t, x) \quad &= \quad \int_{\mathbb{R}} v\, f_h(t, x, v)dv \;=\; \sum_{j\in\mathbb{Z}} \Delta v_j \, v_j \, f^n_{i,j} \;=\; j^n_i. \end{aligned}$$

Now, to complete the scheme we apply a finite volume scheme to the electric field's equation. Let us denote E_i^n an approximation of the electric field in $(x_{i-1/2}, x_{i+1/2})$ given by

$$E_{i+1}^n - E_i^n = \Delta x_i \, \rho_i^n, \quad \text{for} \quad i = 0, \ldots, n_x - 2, \tag{4.15}$$

and is supplemented by the following condition, which comes from the discrete potential

$$\sum_{i=0}^{n_x-1} \Delta x_i \, E_i^n \; = \; \lambda(t^n) - 0 = \lambda(t^n). \tag{4.16}$$

We compute a continuous approximation of the discrete field such that

$$\begin{cases} E_h(t^n, x_i) \; = \; E_i^n, \\ \\ E_h \in Q_1([t^n, t^{n+1}] \times [x_{i-1/2}, x_{i+1/2}]), \end{cases} \tag{4.17}$$

where $Q_1([t^n, t^{n+1}] \times [x_{i-1/2}, x_{i+1/2}])$ represents the space of polynomial of degree one in $[t^n, t^{n+1}] \times [x_{i-1/2}, x_{i+1/2}]$ such that $E_h \in W^{1,\infty}(\Omega_T)$ and $\tilde{E_h}$ is a piecewise constant approximation given by

$$\tilde{E_h}(t, x) \; = \; E_i^n, \quad \text{for} \quad (t, x) \in [t^n, t^{n+1}) \times [x_{i-1/2}, x_{i+1/2}).$$

We introduce the space

$$BV(Q) = \{u \in L^1(Q), \quad TV_Q(u) < \infty\}$$

where

$$TV_Q(u) \; = \; \sup \left\{ \int_Q u(x, v) \, \mathrm{div}_{(x,v)} \varphi(x, v) dx dv, \quad \varphi \in C_c^\infty(\overline{Q}), \quad |\varphi(x, v)| \leq 1, \quad \forall (x, v) \in Q \right\}.$$

We shall now prove the following theorem of convergence for the numerical approximation.

Theoreme 3. *Assume for some $p > 2$, $f_0(x, v)$ and $g(t, v)$ satisfy: for all $T > 0$*

$$TV_Q(f_0) \; + \; \int_0^T \int_{v \geq 0} [1 + v] g(s, v) dv ds + \| |v|^p \, f_0 \|_\infty + \| |v|^p \, g \|_\infty \; < \; \infty. \tag{4.18}$$

Let $\mathcal{M}_h$ be a Cartesian mesh of the phase space and Δt be the time step satisfying the CFL condition : there exists $\xi \in (0, 1)$ such that

$$\frac{3 \, \Delta t}{2} \left(\frac{|v_j|}{\Delta x_i} + \frac{C_\lambda}{\Delta v_j} \right) \leq 1 - \xi \quad \forall (i, j) \in I \times J, \tag{4.19}$$

with

$$C_\lambda = \frac{\|\lambda\|_{L^\infty}}{L} \; + \; 2 \left(\| f^0 \|_{L^1} \; + \; \int_0^T \int_{v \geq 0} v \, g_h(t, v) dv dt \right).$$

We consider the numerical solution given by the scheme (4.7)-(4.12), denoted by $f_h(t, x, v)$, and the discrete self-consistent field $E_h(t, x)$ given by (4.15)-(4.17). Then we have

$$\begin{aligned} f_h(t, x, v) \quad &\rightharpoonup \quad f(t, x, v) \text{ weak-}\star \text{ in } L^\infty(Q_T) \quad \text{as } h \to 0, \\ E_h(t, x) \quad &\to \quad E(t, x) \text{ in } C(\overline{\Omega}_T) \quad \text{as } h \to 0, \end{aligned}$$

where (f, E) *is the unique solution to the Vlasov-Poisson system (4.1)–(4.5), that is for all test functions which belong to*

$$\mathcal{T} := \{\varphi \in C_c^1([0,\infty)\times(0,L)\times\mathbb{R}), \quad \varphi(t,0,v) = \varphi(t,L,-v) = 0, \quad \forall v \leq 0\},$$

we have

$$\int_{Q_T} f(t,x,v)\left[\frac{\partial\varphi}{\partial t} + v\,\frac{\partial\varphi}{\partial x}(t,x,v) + E(t,x)\,\frac{\partial\varphi}{\partial v}(t,x,v)\right]dxdvdt + \int_{\Omega_T} f_0(x,v)\varphi(0,x,v)\,dv\,dx + \int_0^T\int_{v\geq 0} v\,[g(t,v)\varphi(t,0,v)]\,dv\,dt = 0$$

and for the electric field

$$\frac{\partial E}{\partial x} = \rho(t,x), \quad \forall (t,x) \in [0,T]\times\Omega,$$

supplemented with boundary conditions.

4.3 A priori estimates

In this section, we will give some properties satisfied by the numerical approximation as well as by the solution of the continuous problem. We will first prove some properties on the discrete distribution function f_h. From these estimates, we will also give an L^∞ estimate on the electric field E_h. Then, in Proposition 5, we will obtain a uniform bound on $|v|^p\, f_h$ in order to obtain an L^∞ estimate on the moments in velocity of f_h and finally a $W^{1,\infty}$ estimate on the discrete electric field E_h.

4.3.1 Basic estimates

Proposition 4. *Assume that* $f_0(x,v) \geq 0$ *and* $g(t,v) \geq 0$ *satisfy : for all* $T > 0$

$$\int_0^T\int_{v\geq 0}[1+v]g(s,v)dvds + \|f_0\|_{L^\infty} + \|g\|_{L^\infty} + \|f_0\|_{L^1} < +\infty.$$

Let $\mathcal{M}_h$ *be a Cartesian mesh of the phase space and* Δt *be the time step satisfying the CFL condition: there exists* $\xi \in (0,1)$ *such that for all* $k \in \{0,\ldots,n\}$

$$\frac{\Delta t}{\Delta x_i\,\Delta v_j}(\Delta v_j\,|v_j| + \Delta x_i\,|E_i^k|) \leq 1-\xi \quad \forall (i,j) \in I\times J. \tag{4.20}$$

Then, we have

(*i*) *the discrete distribution function at time* t^{n+1} *satisties the following maximum principle*

$$0 \leq f_{i,j}^{n+1} \leq \max(\|f_0\|_{L^\infty}, \|g\|_{L^\infty})\,; \quad \forall (i,j) \in I\times\mathbb{Z}\,; \tag{4.21}$$

(*ii*) *the discrete density function* $\rho_h(t^{n+1})$ *satisfies*

$$0 \leq \sum_{i\in I}\Delta x_i\,\rho_i^{n+1} \leq \|f^0\|_{L^1} + \sum_{k=0}^{n}\sum_{j\in\mathbb{Z}}\Delta t\,\Delta v_j\,v_j^+\,g_j^k\,; \tag{4.22}$$

(iii) *the discrete electric field is bounded*

$$|E_i^{n+1}| \leq \frac{\lambda(t^{n+1})}{L} + 2\left(\|f^0\|_{L^1} + \sum_{k=0}^{n}\sum_{j\in\mathbb{Z}} \Delta t\, \Delta v_j\, v_j^+\, g_j^k\right); \tag{4.23}$$

(iv) *the CFL condition (4.20) at iteration $n+1$ is satisfied.*

Proof: We start from the scheme (4.9)-(4.10) and first introduce the following limiters : for $(i, j) \in I \times J$

$$\begin{aligned} f^l_{i+1/2,j} &= f^n_{i,j} + \sigma_{i+1/2,j}\,[f^n_{i+1,j} - f^n_{i,j}], \\ &= f^n_{i,j} + s_{i+1/2,j}\,[f^n_{i,j} - f^n_{i-1,j}], \end{aligned}$$

with

$$s_{i+1/2,j} = \begin{cases} 0, & \text{if } (f^n_{i+1,j} - f^n_{i,j})(f^n_{i,j} - f^n_{i-1,j}) \leq 0, \\[2ex] \dfrac{|f^n_{i+1,j} - f^n_{i,j}|}{|f^n_{i,j} - f^n_{i-1,j}|}\,\dfrac{\Delta x_i}{\Delta x_i + \Delta x_{i+1}} & \text{if } \dfrac{|f^n_{i+1,j} - f^n_{i,j}|}{\Delta x_i + \Delta x_{i+1}} \leq \dfrac{|f^n_{i,j} - f^n_{i-1,j}|}{\Delta x_i + \Delta x_{i-1}}, \\[2ex] \dfrac{\Delta x_i}{\Delta x_i + \Delta x_{i-1}}, & \text{else} \end{cases} \tag{4.24}$$

and

$$\begin{aligned} f^r_{i+1/2,j} &= f^n_{i+1,j} - \sigma_{i+3/2,j}\,[f^n_{i+2,j} - f^n_{i+1,j}], \\ &= f^n_{i+1,j} - s_{i+3/2,j}\,[f^n_{i+1,j} - f^n_{i,j}]. \end{aligned}$$

Also, $f^l_{i,j+1/2}$ and $f^r_{i,j+1/2}$ can be re-written in a similar way

$$\begin{aligned} f^l_{i,j+1/2} &= f^n_{i,j} + s_{i,j+1/2}\,[f^n_{i,j} - f^n_{i,j-1}], \\ f^r_{i,j+1/2} &= f^n_{i,j+1} - s_{i,j+3/2}\,[f^n_{i,j+1} - f^n_{i,j}], \end{aligned}$$

with

$$s_{i,j+1/2} = \begin{cases} 0, & \text{if } (f^n_{i,j+1} - f^n_{i,j})(f^n_{i,j} - f^n_{i,j-1}) \leq 0, \\[2ex] \dfrac{|f^n_{i,j+1} - f^n_{i,j}|}{|f^n_{i,j} - f^n_{i,j-1}|}\,\dfrac{\Delta v_j}{\Delta v_j + \Delta v_{j+1}}, & \text{if } \dfrac{|f^n_{i,j+1} - f^n_{i,j}|}{\Delta v_j + \Delta v_{j+1}} \leq \dfrac{|f^n_{i,j} - f^n_{i,j-1}|}{\Delta v_j + \Delta v_{j-1}}, \\[2ex] \dfrac{\Delta v_j}{\Delta v_j + \Delta v_{j-1}}, & \text{else,} \end{cases} \tag{4.25}$$

where we observe that $0 \leq s_{i,j+1/2},\ s_{i+1/2,j} < 1$. Using the scheme (4.7)-(4.12), we explicitly write the value of the numerical solution at iteration $n+1$, in terms of the values at time t^n in a better way,

$$\begin{aligned} f_{i,j}^{n+1} \;=\; f_{i,j}^{n} \;&-\; \frac{v_j^+\,\Delta t}{\Delta x_i}\Big[1+s_{i+1/2,j}-\sigma_{i-1/2,j}\Big](f_{i,j}^n-f_{i-1,j}^n)\\ &+\; \frac{v_j^-\,\Delta t}{\Delta x_i}\Big[1-s_{i+3/2,j}+\sigma_{i+1/2,j}\Big](f_{i+1,j}^n-f_{i,j}^n)\\ &-\; \frac{E_i^{n+}\,\Delta t}{\Delta v_j}\Big[1+s_{i,j+1/2}-\sigma_{i,j-1/2}\Big](f_{i,j}^n-f_{i,j-1}^n)\\ &+\; \frac{E_i^{n-}\,\Delta t}{\Delta v_j}\Big[1-s_{i,j+3/2}+\sigma_{i,j+1/2}\Big](f_{i,j+1}^n-f_{i,j}^n). \end{aligned}$$

Under the stability condition (4.20), the discrete distribution function $f_{i,j}^{n+1}$ could be written as a convex combination of $f_{i,j}^n$, $f_{i-1,j}^n$, $f_{i+1,j}^n$, $f_{i,j-1}^n$, $f_{i,j+1}^n$; it yields the nonnegativity of $f_{i,j}^{n+1}$ for all $(i,j)\in I\times\mathbb{Z}$. Thus we get the result

$$0\;\leq\; f_{i,j}^{n+1}\;\leq\;\max\left(\|f_0\|_{L^\infty},\|g\|_{L^\infty}\right).$$

Now, we give an estimate of total mass evolution : for $k\in\{0,\dots,n\}$ we multiply (4.7)-(4.12) by $\Delta x_i\,\Delta v_j$ and sum over $(i,j)\in I\times\mathbb{Z}$. It gives,

$$\begin{aligned} &\sum_{(i,j)\in I\times\mathbb{Z}}\Delta x_i\,\Delta v_j\, f_{i,j}^{k+1} \;+\;\Delta t\sum_{j\in\mathbb{Z}}\Delta v_j\left[v_j^-\,f^r_{-1/2,j}+v_j^+\,f^l_{n_x+1/2,j}\right]\\ =&\sum_{(i,j)\in I\times\mathbb{Z}}\Delta x_i\,\Delta v_j\, f_{i,j}^{k} \;+\;\Delta t\sum_{j\in\mathbb{Z}}\Delta v_j\left[v_j^+\,f^r_{-1/2,j}+v_j^-\,f^l_{n_x+1/2,j}\right]. \end{aligned}$$

Then, using boundary conditions (4.14), it yields

$$\begin{aligned} \sum_{(i,j)\in I\times\mathbb{Z}}\Delta x_i\,\Delta v_j\, f_{i,j}^{k+1} \;&+\;\Delta t\sum_{j\in\mathbb{Z}}\Delta v_j\left[v_j^-\,f^k_{0,j}+v_j^+\,f^k_{n_x-1,j}\right]\\ &=\sum_{(i,j)\in I\times\mathbb{Z}}\Delta x_i\,\Delta v_j\, f_{i,j}^{k} \;+\;\Delta t\sum_{j\in\mathbb{Z}}\Delta v_j\,v_j^+\,g_j^k \end{aligned}$$

and summing over $k\in\{0,\dots,n\}$ we get

$$\begin{aligned} \sum_{(i,j)\in I\times\mathbb{Z}}\Delta x_i\,\Delta v_j\, f_{i,j}^{n+1} \;&+\;\sum_{k=0}^{n}\sum_{j\in\mathbb{Z}}\Delta t\,\Delta v_j\left[v_j^-\,f^k_{0,j}+v_j^+\,f^k_{n_x-1,j}\right]\\ &=\sum_{(i,j)\in I\times\mathbb{Z}}\Delta x_i\,\Delta v_j\, f_{i,j}^{0} \;+\;\sum_{k=0}^{n}\sum_{j\in\mathbb{Z}}\Delta t\,\Delta v_j\,v_j^+\,g_j^k, \end{aligned}$$

which gives the result

$$\sum_{i\in I}\Delta x_i\,\rho_i^{n+1}\;\leq\;\|f^0\|_{L^1}+\sum_{k=0}^{n}\sum_{j\in\mathbb{Z}}\Delta t\,\Delta v_j\,v_j^+\,g_j^k.$$

Now, let us prove that the discrete electric field is bounded at iteration $n+1$. The argument is the same as in the continuous case: using the scheme (4.15)-(4.16), we have $E_0^{n+1}\;=\;C^{n+1}$ and for

$i = \{1, \ldots, n_x - 1\}$

$$\begin{aligned} |E_i^{n+1}| &= \left| C^{n+1} + \sum_{k=0}^{i-1} \Delta x_k \, \rho_k^{n+1} \right|, \\ &\leq C^{n+1} + \|f^0\|_{L^1} + \sum_{k=0}^{n} \sum_{j \in \mathbb{Z}} \Delta t \, \Delta v_j \, v_j^+ \, g_j^k, \end{aligned}$$

where C^{n+1} is such that the relation (4.16) is satisfied at iteration $n+1$, so that

$$C^{n+1} = \frac{\lambda(t^{n+1}) + \sum_{i \in I} \Delta x_i (L - x_{i-1/2}) \, \rho_i^{n+1}}{L},$$

which proves (4.23)

$$|E_i^{n+1}| \leq \frac{\lambda(t^{n+1})}{L} + 2 \left(\|f^0\|_{L^1} + \sum_{k=0}^{n} \sum_{j \in \mathbb{Z}} \Delta t \, \Delta v_j \, v_j^+ \, g_j^k \right).$$

Finally, from this latter bound we check that the CFL condition (4.19) is satistied at time $n+1$. □

4.3.2 Estimates on the electric field

Now, let us give a uniform bound on $|v|^p f_h$ for $p > 2$, which will lead to a uniform bound on the and an estimate on first moments ρ_h and j_h throughout an energy estimate.

Proposition 5. *Assume that for $p > 2$ and for all $(t, x, v) \in Q_T$*

$$|v|^p \, f_0(x, v) \, + \, |v|^p \, g(t, v) \, < \, \infty$$

and $\|\lambda\|_{W^{1,\infty}} < \infty$. Then, there exists $C_T > 0$, ony depending on f_0, g, λ and α, such that

$$0 \leq \max_{i,j} \{ |v_{j-1/2}|^p \, f_{i,j}^n \} \leq C_T. \tag{4.26}$$

Moreover, there exists $C_T > 0$, for all $(n, i) \in \{0, \ldots, N_T\} \times I$,

$$\left| \frac{E_i^{n+1} - E_i^n}{\Delta t} \right| + \left| \frac{E_{i+1}^n - E_i^n}{\Delta x_i} \right| \leq C_T. \tag{4.27}$$

Proof: For $p > 2$, we multiply the scheme (4.7)-(4.12) by $|v_{j-1/2}|^p$ and using the reconstruction proposed in (4.24)-(4.25), we have

$$\begin{aligned}
|v_{j-1/2}|^p\, f_{i,j}^{n+1} &= |v_{j-1/2}|^p\, f_{i,j}^n \\
&- \frac{v_j^+\,\Delta t}{\Delta x_i}\left[1+s_{i+1/2,j}-\sigma_{i-1/2,j}\right](|v_{j-1/2}|^p\, f_{i,j}^n - |v_{j-1/2}|^p\, f_{i-1,j}^n) \\
&+ \frac{v_j^-\,\Delta t}{\Delta x_i}\left[1-s_{i+3/2,j}+\sigma_{i+1/2,j}\right](|v_{j-1/2}|^p\, f_{i+1,j}^n - |v_{j-1/2}|^p\, f_{i,j}^n) \\
&- \frac{E_i^{n+}\,\Delta t}{\Delta v_j}\left[1+s_{i,j+1/2}-\sigma_{i,j-1/2}\right](|v_{j-1/2}|^p\, f_{i,j}^n - |v_{j-3/2}|^p\, f_{i,j-1}^n) \\
&+ \frac{E_i^{n-}\,\Delta t}{\Delta v_j}\left[1-s_{i,j+3/2}+\sigma_{i,j+1/2}\right](|v_{j+1/2}|^p\, f_{i,j+1}^n - |v_{j-1/2}|^p\, f_{i,j}^n). \\
&- \frac{E_i^{n+}\,\Delta t}{\Delta v_j}\left[1+s_{i,j+1/2}-\sigma_{i,j-1/2}\right](|v_{j-3/2}|^p \,-\, |v_{j-1/2}|^p)\, f_{i,j-1}^n \\
&+ \frac{E_i^{n-}\,\Delta t}{\Delta v_j}\left[1-s_{i,j+3/2}+\sigma_{i,j+1/2}\right](|v_{j-1/2}|^p \,-\, |v_{j+1/2}|^p)\, f_{i,j+1}^n.
\end{aligned}$$

Then, using that $\left||v_{j+1/2}|^p - |v_{j-1/2}|^p\right| \;\le\; p\,(1+|v_{j-1/2}|^p)\,\Delta v_j$ and from the CFL condition (4.20), we get

$$\begin{aligned}
\max_{i,j}\{|v_{j-1/2}|^p\, f_{i,j}^{n+1}\} \;&\le\; \max_{i,j}\{|v_{j-1/2}|^p\, f_{i,j}^n\} \\
&+\; \Delta t\,\frac{3\,p\,\|E_h\|_{L^\infty}}{2\,\alpha}\left(\max_{i,j}\{|v_{j-1/2}|^p\, f_{i,j}^n\} \,+\, \|f_h\|_{L^\infty}\right).
\end{aligned}$$

It finally yields using a discrete version of Gronwall's lemma and taking into account boundary conditions

$$\max_{i,j}\{|v_{j-1/2}|^p\, f_{i,j}^n\} \le \left(\max_{i,j}\{|v_{j-1/2}|^p\,[g_j^n \,+\, f_{i,j}^0]\} + \|f_h(0)\|_{L^\infty} + \|g_h\|_{L^\infty}\right)\exp\left(\frac{3\,p\,\|E_h\|_{L^\infty}}{2\,\alpha}\, t^n\right).$$

We remind that in Proposition 6, we have already seen that E_h is bounded in L^∞. On the one hand from the latter estimate, we can prove a uniform upper bound on the discrete density

$$\rho_i^n = \sum_{j\in\mathbb{Z}} \Delta v_j\, f_{i,j}^n \le \|f_h(t^n)\|_{L^\infty} \,+\, \max_{i,j}\{|v_{j-1/2}|^p\, f_{i,j}^n\} \sum_{|v_{j-1/2}|\ge 1} \frac{\Delta v_j}{|v_{j-1/2}|^p} \le C_T.$$

Therefore, from the finite volume scheme for E_i^n we get

$$\left|\frac{E_{i+1}^n - E_i^n}{\Delta x_i}\right| \;=\; \rho_i^n \le C_T.$$

On the other hand, we give a uniform upper bound on the jump

$$\left|\frac{E_i^{n+1} - E_i^n}{\Delta t}\right|.$$

Using the finite volume scheme for E_i^n (4.15)-(4.16) and the scheme for the distribution function $f_{i,j}^n$ (4.7)-(4.12), we get a new formulation

$$\begin{aligned}\frac{E_i^{n+1}-E_i^n}{\Delta t} &= \frac{C^{n+1}-C^n}{\Delta t}+\sum_{k=0}^{i}\frac{\rho_k^{n+1}-\rho_k^n}{\Delta t}\\ &= \frac{C^{n+1}-C^n}{\Delta t} - j_{i+1/2}^n + j_{-1/2}^n,\end{aligned}$$

with

$$j_{i+1/2}^n = \sum_{j\in\mathbb{Z}}\Delta v_j\,[v_j^+ f_{i+1/2,j}^l - v_j^- f_{i+1/2,j}^r],$$

or

$$\frac{E_i^{n+1}-E_i^n}{\Delta t} = \frac{\lambda(t^{n+1})-\lambda(t^n)}{L\,\Delta t} - j_{i+1/2}^n - \frac{1}{L}\sum_{k\in I}\Delta x_k\, j_{k+1/2}^n.$$

It remains to get an upper bound of $j_{i+1/2}^n$, which can be done from (4.26). We have for $h \le 1$

$$\begin{aligned}|j_{i+1/2}^n| &\le \sum_{j\in\mathbb{Z}}\Delta v_j\,[v_j^+ f_{i+1/2,j}^l + v_j^- f_{i+1/2,j}^r],\\ &\le 4\sum_{j\in\mathbb{Z}}\Delta v_j\left(1+|v_{j-1/2}|\right) f_{i,j}^n \le C_T.\end{aligned}$$

Thus under the assumption $\lambda\in W^{1,\infty}(0,T)$, it yields

$$\left|\frac{E_i^{n+1}-E_i^n}{\Delta t}\right| \le C_T.$$

□

4.3.3 Weak *BV* estimate for f_h

The following lemma will be useful to obtain the convergence of (E_h, f_h) to the Vlasov equation solution.

Lemma 4. *Under the stability condition (4.20) on the time step and the condition on the mesh* (4.6), *assume the initial data belong to* $L^1(Q)\cap L^\infty(Q)$. *Consider* $R>0$ *and* $T>0$ *with* $h<R$ *and* $\Delta t<T$. *Let* $j_0, j_1\in\mathbb{Z}$ *and* $N_T\in\mathbb{N}$ *be such that* $-R\in(v_{j_0-1/2}, v_{j_0+1/2})$, $R\in(v_{j_1-1/2}, v_{j_1+1/2})$, *and* $T\in((N_T-1)\Delta t, N_T\,\Delta t)$. *We define*

$$\begin{aligned}EF_{1h} = \Delta t\sum_{n=0}^{N_T}\sum_{i\in I}\sum_{j=j_0}^{j_1}\Delta x_i\,\Delta v_j\Big[&v_j^+\,|f_{i,j}^n - f_{i-1,j}^n| + v_j^-\,|f_{i,j}^n - f_{i+1,j}^n|\\ &+E_i^{n+}\,|f_{i,j}^n - f_{i,j-1}^n| + E_i^{n-}\,|f_{i,j}^n - f_{i,j+1}^n|\Big]\end{aligned} \tag{4.28}$$

and

$$EF_{2h} = \Delta t \sum_{n=0}^{N_T} \sum_{i\in I} \sum_{j=j_0}^{j_1} \Delta x_i \, \Delta v_j \left| f_{i,j}^{n+1} - f_{i,j}^{n} \right|. \tag{4.29}$$

Then, there exists $C > 0$ *depending only on* T, R, f_0, α, ξ *such that*

$$EF_{1h} \;\leq\; C\, h^{1/2} \quad \textit{and} \quad EF_{2h} \;\leq\; C\, \Delta t^{1/2}. \tag{4.30}$$

Proof: Multiplying the scheme (4.7)-(4.12) by $\Delta x_i \, \Delta v_j \, f_{i,j}^n$ and summing over $i \in \{0, \ldots, n_x - 1\}$, $j \in \{j_0, \ldots, j_1\}$, and $n \in \{0, \ldots, N_T\}$, it follows that

$$B_1 \,+\, B_2 \,=\, 0,$$

where

$$B_1 \;=\; \sum_{n,i,j} \Delta x_i \Delta v_j [\, f_{i,j}^{n+1} - f_{i,j}^{n}]\, f_{i,j}^n.$$

$$B_2 \;=\; \Delta t \sum_{n,i,j} \Delta v_j \, [\mathcal{F}_{i+1/2,j} - \mathcal{F}_{i-1/2,j}]\, f_{i,j}^n \;+\; \Delta x_i \, [\mathcal{G}_{i,j+1/2} - \mathcal{G}_{i,j-1/2}]\, f_{i,j}^n$$

Noting that

$$[\, f_{i,j}^{n+1} - f_{i,j}^{n}]\, f_{i,j}^n = -\frac{1}{2}[\, f_{i,j}^{n+1} - f_{i,j}^{n}]^2 - \frac{1}{2}(f_{i,j}^n)^2 + \frac{1}{2}(f_{i,j}^{n+1})^2,$$

then

$$B_1 \;=\; -\frac{1}{2}\sum_{n,i,j} \Delta x_i \Delta v_j [\, f_{i,j}^{n+1} - f_{i,j}^{n}]^2 \;-\; \frac{1}{2}\sum_{i,j} \Delta x_i \Delta v_j (f_{i,j}^0)^2 + \frac{1}{2}\sum_{i,j} \Delta x_i \Delta v_j (f_{i,j}^{N_T+1})^2.$$

By scheme (4.7)-(4.12), we have

$$\begin{aligned}
&\sum_{n,i,j} \Delta x_i \Delta v_j [\, f_{i,j}^{n+1} - f_{i,j}^{n}]^2 \\
&\quad = \sum_{n,i,j} \frac{\Delta t^2}{\Delta x_i \Delta v_j} \Big[\Delta v_j \, v_j^+ \left(1 + s_{i+1/2,j} - \sigma_{i-1/2,j}\right) (f_{i,j}^n - f_{i-1,j}^n) \;+ \\
&\qquad\qquad \Delta v_j \, v_j^- \left(1 - s_{i+3/2,j} + \sigma_{i+1/2,j}\right) (f_{i,j}^n - f_{i+1,j}^n) \;+ \\
&\qquad\qquad \Delta x_i \, E_i^{n+} \left(1 + s_{i,j+1/2} - \sigma_{i,j-1/2}\right) (f_{i,j}^n - f_{i,j-1}^n) \;+ \\
&\qquad\qquad \Delta x_i \, E_i^{n-} \left(1 - s_{i,j+3/2} + \sigma_{i,j+1/2}\right) (f_{i,j}^n - f_{i,j+1}^n) \Big]^2 .
\end{aligned}$$

Using the Cauchy-Schwarz inequality and the stability condition (4.20), there exists $C_0 > 0$, only depending on f_0, such that

$$
\begin{aligned}
B_1 \ \geq\ -\frac{\Delta t}{2}(1-\xi)\sum_{n,i,j}\Big[& \Delta v_j\, v_j^+ \left(1 + s_{i+1/2,j} - \sigma_{i-1/2,j}\right)(f^n_{i,j} - f^n_{i-1,j})^2 \\
& + \Delta v_j\, v_j^- \left(1 - s_{i+3/2,j} + \sigma_{i+1/2,j}\right)(f^n_{i,j} - f^n_{i+1,j})^2 \\
& + \Delta x_i\, E_i^{n+} \left(1 + s_{i,j+1/2} - \sigma_{i,j-1/2}\right)(f^n_{i,j} - f^n_{i,j-1})^2 \\
& + \Delta x_i\, E_i^{n-} \left(1 - s_{i,j+3/2} + \sigma_{i,j+1/2}\right)(f^n_{i,j} - f^n_{i,j+1})^2\Big] - C_0.
\end{aligned}
$$

Now, we study the term B_2, which may be rewritten as $B_2 = B_{21} + B_{22}$ where B_{21} is the contribution of the first order approximation

$$
\begin{aligned}
B_{21} \ =\ & \frac{\Delta t}{2}\sum_{n,i,j}\Big[\Delta v_j\, v_j^+\,[f^n_{i,j} - f^n_{i-1,j}]^2 + \Delta v_j\, v_j^-\,[f^n_{i,j} - f^n_{i+1,j}]^2 + \\
& \qquad \Delta x_i\, E_i^{n+}\,[f^n_{i,j} - f^n_{i,j-1}]^2 + \Delta x_i\, E_i^{n-}\,[f^n_{i,j} - f^n_{i,j+1}]^2\Big] \\
+ \ & \frac{\Delta t}{2}\sum_{n,i}\Big[\Delta x_i\, E_i^{n+}\,[(f^n_{i,j_1})^2 - (f^n_{i,j_0-1})^2] + \Delta x_i\, E_i^{n-}\,[(f^n_{i,j_0})^2 - (f^n_{i,j_1+1})^2]\Big] \\
+ \ & \frac{\Delta t}{2}\sum_{n,j}\Big[\Delta v_j\, v_j^+\,[(f^n_{i_1,j})^2 - (f^n_{i_0-1,j})^2] + \Delta v_j\, v_j^-\,[(f^n_{i_0,,j})^2 - (f^n_{i_1+1,j})^2]\Big]
\end{aligned}
$$

and B_{22} the contribution of the second order term

$$
\begin{aligned}
B_{22} \ =\ \Delta t\sum_{n,i,j} & \Delta v_j\left[v_j^+[s_{i+1/2,j} - \sigma_{i-1/2,j}][f^n_{i,j} - f^n_{i-1,j}] + v_j^-[s_{i+3/2,j} - \sigma_{i+1/2,j}]\,[f^n_{i+1,j} - f^n_{i,j}]\right] f^n_{i,j} + \\
& \Delta x_i\left[E_i^{n+}\,[s_{i,j+1/2} - \sigma_{i,j-1/2}]\,[f^n_{i,j} - f^n_{i,j-1}] + E_i^{n-}\,[s_{i,j+3/2} - \sigma_{i,j+1/2}]\,[f^n_{i,j+1} - f^n_{i,j}]\right] f^n_{i,j}.
\end{aligned}
$$

On the one hand, from the estimates on velocity moments in Proposition 5, we get that there exists a constant $C_1 > 0$, only depending on T and f_0, such that

$$
\begin{aligned}
B_{21} \ \geq\ \frac{\Delta t}{2}\sum_{n,i,j}\Big[& \Delta v_j\, v_j^+\,[f^n_{i,j} - f^n_{i-1,j}]^2 + \Delta v_j\, v_j^-\,[f^n_{i,j} - f^n_{i+1,j}]^2 + \\
& \Delta x_i\, E_i^{n+}\,[f^n_{i,j} - f^n_{i,j-1}]^2 + \Delta x_i\, E_i^{n-}\,[f^n_{i,j} - f^n_{i,j+1}]^2\Big] - C_1.
\end{aligned}
$$

On the other hand, using that

$$
s_{i+1/2,j}(f^n_{i,j} - f^n_{i-1,j}) = \sigma_{i+1/2,j}(f^n_{i+1,j} - f^n_{i,j}),
$$

and

$$
s_{i,j+1/2}(f^n_{i,j} - f^n_{i,j-1}) = \sigma_{i,j+1/2}(f^n_{i,j+1} - f^n_{i,j}),
$$

we prove that there exists a constant C_2, only depending on T and f_0, such that

$$\begin{aligned} B_{22} \;\geq\; & -\Delta t \sum_{n,i,j} \Big[\Delta v_j \left(v_j^+ \, \sigma_{i-1/2,j} \, [f_{i,j}^n - f_{i-1,j}^n]^2 \,+\, v_j^- \, s_{i+3/2,j} \, [f_{i,j}^n - f_{i+1,j}^n]^2 \right) + \\ & \qquad \Delta x_i \left(E_i^{n+} \, \sigma_{i,j-1/2} \, [f_{i,j}^n - f_{i,j-1}^n]^2 \,+\, E_i^{n-} \, s_{i,j+3/2} \, [f_{i,j}^n - f_{i,j+1}^n]^2 \right) \Big] - C_2. \end{aligned}$$

Then, since $B_1 + B_{21} + B_{22} = 0$ the following inequality holds:

$$\begin{aligned} & \frac{\xi \, \Delta t}{2} \sum_{n,i,j} \Big[\Delta v_j \, v_j^+ \, [f_{i,j}^n - f_{i-1,j}^n]^2 + \Delta v_j \, v_j^- \, [f_{i,j}^n - f_{i+1,j}^n]^2 \\ & \qquad + \Delta x_i \, E_i^{n+} \, [f_{i,j}^n - f_{i,j-1}^n]^2 + \Delta x_i \, E_i^{n-} \, [f_{i,j}^n - f_{i,j+1}^n]^2 \Big] \\ \leq \; & \Delta t \sum_{n,i,j} \Delta v_j \, |v_j| \, [s_{i+1/2,j} + \sigma_{i-1/2,j}] \, [f_{i,j}^n - f_{i-1,j}^n]^2 \,+\, \Delta x_i \, |E_i^n| \, [s_{i,j+1/2} + \sigma_{i,j-1/2}] \, [f_{i,j}^n - f_{i,j-1}^n]^2 \\ & + C_0 \,+\, C_1 \,+\, C_2. \end{aligned}$$

Therefore, using hypothesis on the limiters (4.13), there exists a constant $C > 0$, only depending on f_0, T, R and ξ, such that

$$\begin{aligned} & \frac{\Delta t}{2} \sum_{n,i,j} \Big[\Delta v_j \, v_j^+ \, [f_{i,j}^n - f_{i-1,j}^n]^2 + \Delta v_j \, v_j^- \, [f_{i,j}^n - f_{i+1,j}^n]^2 \,+ \\ & \qquad \Delta x_i \, E_i^{n+} \, [f_{i,j}^n - f_{i,j-1}^n]^2 + \Delta x_i \, E_i^{n-} \, [f_{i,j}^n - f_{i,j+1}^n]^2 \Big], \\ \leq \; & \frac{C}{\xi} \left(1 \,+\, K \, h^{\beta-1} \right). \end{aligned}$$

Finally, the previous inequality and the Cauchy–Schwarz inequality lead to

$$\begin{aligned} EF_{1h} \;\leq\; & \Big[\Delta t \sum_{n,i,j} \Delta v_j \, v_j^+ \, [f_{i,j}^n - f_{i-1,j}^n]^2 + \Delta v_j \, v_j^- \, [f_{i,j}^n - f_{i+1,j}^n]^2 \\ & \qquad + \Delta x_i \, E_i^{n+} \, [f_{i,j}^n - f_{i,j-1}^n]^2 + \Delta x_i \, E_i^{n-} \, [f_{i,j}^n - f_{i,j+1}^n]^2 \Big]^{1/2} \\ & \times \Big[\Delta t \sum_{n,i,j} \Delta x_i^2 (\Delta v_j \, |v_j| + \Delta x_i \, |E_i^n|) \Big]^{1/2}, \\ \leq \; & h^{1/2} \left(\frac{C}{\xi} \left(1 \,+\, K \, h^{\beta-1} \right) \right)^{1/2} \Big[2 \, T \, L \, R \, (1 - \xi) \Big]^{1/2}. \end{aligned}$$

Now, we prove the second estimate on EF_{2h}, using the scheme (4.7)-(4.12):

$$\begin{aligned} EF_{2h} &= \Delta t \sum_{n,i,j} \Delta x_i \Delta v_j \left| f_{i,j}^{n+1} - f_{i,j}^{n} \right|, \\ &\leq \Delta t^2 \sum_{n,i,j} \Big[\Delta v_j \, v_j^+ \, |f_{i,j}^n - f_{i-1,j}^n| + \Delta v_j \, v_j^- \, |f_{i,j}^n - f_{i+1,j}^n| \\ &\qquad + \Delta x_i \, E_i^{n+} \, |f_{i,j}^n - f_{i,j-1}^n| + \Delta x_i \, E_i^{n-} \, |f_{i,j}^n - f_{i,j+1}^n| \Big]. \end{aligned}$$

As in the previous case, we use the Cauchy–Schwarz inequality and the stability condition (4.20). We also recall that the discrete electric field is uniformly bounded:

$$EF_{2h} \leq \Delta t^{1/2} \left[2\, T\, L\, R\, (1-\xi)\, \frac{C}{\xi} \left(1 + K\, h^{\beta-1} \right) \right]^{1/2}.$$

□

4.4 Proof of Theorem 3

In a first part, we prove that there are subsequences which converge to a limit (f, E) and in a second step we identify this limit as the unique solution to the Vlasov-Poisson system (4.1)-(4.5).

4.4.1 Compactness of the sequence (f_h, E_h).

We consider a sequence of a mesh of the phase space defined as in the beginning of the paper satisfying the condition (4.6), and we define a time step Δt such that the stability condition (4.20) is true. This sequence is denoted by $(\mathcal{M}_h)_{h>0}$.

For a given mesh, we are able to construct, by the finite volume scheme (4.7)-(4.12), a unique pair (f_h, E_h). Thus, we set

$$A = \left\{ E_h \in W^{1,\infty}(\Omega_T)\,; \quad E_h \text{ given by (4.17) for a mesh } \mathcal{M}_h \right\}.$$

On the one hand, in Proposition 6 and Proposition 5 we have proved there exists a constant independent on the mesh $\mathcal{M}_h$ such that

$$\|E_h\|_{L^\infty} + \left\| \frac{\partial E_h}{\partial t} \right\|_{L^\infty} + \left\| \frac{\partial E_h}{\partial x} \right\|_{L^\infty} \leq C_T.$$

Moreover, from the same estimates, we also have

$$\|E_h - \tilde{E}_h\|_{L^\infty} \leq C_T \; (h + \Delta t)$$

On the other hand, using the fact that the injection from $W^{1,\infty}(\Omega_T)$ to $C^0(\overline{\Omega}_T)$ is compact, there exists a subsequence of $(E_h)_{h>0}$ and a function E belonging to $C^0(\overline{\Omega}_T)$ such that

$$E_h \rightharpoonup E \quad \text{in } L^\infty(\Omega_T) \text{ weak-}\star \quad \text{as} \quad h \to 0,$$

and

$$\begin{aligned} E_h \to E \quad & \text{in } C^0(\overline{\Omega}_T) \text{ strong} \quad \text{as} \quad h \to 0\,; \\ \tilde{E}_h \to E \quad & \text{in } C^0(\overline{\Omega}_T) \text{ strong} \quad \text{as} \quad h \to 0. \end{aligned}$$

Moreover, we also know by Proposition 6 that the discrete distribution function f_h is bounded in $L^\infty(Q_T)$. Therefore, there exists a subsequence and a function $f \in L^\infty(Q_T)$ such that

$$f_h(t,x,v) \rightharpoonup f(t,x,v) \quad \text{in } L^\infty(Q_T) \text{ weak-}\star \quad \text{as} \quad h \to 0.$$

The discrete charge ρ_h is bounded in $L^\infty(\Omega_T)$; then up to the extraction of a subsequence, we also have

$$\rho_h(t,x) \rightharpoonup \rho(t,x) \quad \text{in } L^\infty(\Omega_T) \text{ weak-}\star \quad \text{as} \quad h \to 0.$$

4.4.2 Convergence to the weak solution of the Vlasov equation

Let $\varphi \in \mathrm{C}_c^\infty(Q_T)$, $R > 0$, and $j_0, j_1 \in \mathbb{Z}$ be such that

$$\mathrm{Supp}\Big(\varphi(t,x,.)\Big) \subset [-R,R]$$

and

$$-R \in (v_{j_0-1/2}, v_{j_0+1/2}) \quad \text{and} \quad R \in (v_{j_1-1/2}, v_{j_1+1/2}).$$

Moreover $\varphi(t,0,v) = 0$ for all $v \le 0$ and $\varphi(t,L,v) = 0$ for all $v \ge 0$.

We set $\varphi_{i,j}^n$ such that

$$\varphi_{i,j}^n := \frac{1}{\Delta t\, \Delta x_i\, \Delta v_j} \int_{t^n}^{t^{n+1}} \int_{C_{i,j}} \varphi(t,x,v)dxdvdt$$

and multiply the finite volume scheme (4.7)-(4.12) by $\varphi_{i,j}^n$, sum over $i \in \{0,\dots,n_x-1\}$, $j \in \{j_0,\dots,j_1\}$, and $n \in \{0,\dots,N_T = \frac{T}{\Delta t}\}$,

$$E_1 + E_2 + E_3 = 0,$$

with

$$E_1 = \sum_{n,i,j} (f_{i,j}^{n+1} - f_{i,j}^n)\Delta x_i\, \Delta v_j\, \varphi_{i,j}^n,$$

$$\begin{aligned} E_2 \quad = \quad \sum_{n,i,j} \Big[& \Delta v_j\, v_j^+ \,(f_{i,j}^n - f_{i-1,j}^n) + \Delta v_j\, v_j^- \,(f_{i,j}^n - f_{i+1,j}^n) + \Delta x_i\, E_i^{n+} \,(f_{i,j}^n - f_{i,j-1}^n) \\ & + \Delta x_i\, E_i^{n-} \,(f_{i,j}^n - f_{i,j+1}^n)\Big] \Delta t\, \varphi_{i,j}^n \end{aligned}$$

and

$$\begin{aligned} E_3 \;=\; \sum_{n,i,j}\Big[& \Delta v_j\, v_j^+ \left[s_{i+1/2,j} - \sigma_{i-1/2,j}\right] (f_{i,j}^n - f_{i-1,j}^n) \\ & + \Delta v_j\, v_j^- \left[\sigma_{i+1/2,j} - s_{i+3/2,j}\right] (f_{i,j}^n - f_{i+1,j}^n) \\ & + \Delta x_i\, E_i^{n+} \left[s_{i,j+1/2} - \sigma_{i,j-1/2}\right] (f_{i,j}^n - f_{i,j-1}^n) \\ & + \Delta x_i\, E_i^{n-} \left[\sigma_{i,j+1/2} - s_{i,j+3/2}\right] (f_{i,j}^n - f_{i,j+1}^n)\Big] \Delta t\, \varphi_{i,j}^n. \end{aligned}$$

Moreover, we denote $E_{1,0}$ and $E_{2,0}$ by

$$E_{1,0} = \int_{Q_T} f_h(t,x,v)\frac{\partial \varphi}{\partial t}(t,x,v)dtdxdv \;+\; \int_Q f_0(x,v)\varphi(0,x,v)dxdv$$

and

$$\begin{aligned} E_{2,0} \;=\; & \int_{Q_T} f_h(t,x,v)\left[v\,\frac{\partial \varphi}{\partial x}(t,x,v) \;+\; E_h(t,x)\,\frac{\partial \varphi}{\partial v}(t,x,v)\right] dxdvdt \\ & + \int_0^T \int_{v\geq 0} v\, \left[g_h(t,0,v)\varphi(t,0,v)\right]\, dv\, dt. \end{aligned}$$

In the sequel we will compare E_1 with $E_{1,0}$ and E_2 with $E_{2,0}$ to establish that $E_{1,0} + E_{2,0}$ goes to zero as $h \to 0$. We first treat the terms E_1 and $E_{1,0}$ and remark that $E_{1,0}$ can be rewritten as

$$E_{1,0} = \sum_{n,i,j} f_{i,j}^n \int_{C_{i,j}} \left[\varphi(t^{n+1},x,v) - \varphi(t^n,x,v)\right] dx\, dv \;+\; \int_Q f_0(x,v)\,\varphi(0,x,v)\, dx\, dv.$$

By a discrete integration by parts, it follows that

$$\begin{aligned} E_{1,0} \;=\; & -\sum_{n,i,j}\left(f_{i,j}^{n+1} - f_{i,j}^n\right)\int_{C_{i,j}} \varphi(t^{n+1},x,v)dxdv \\ & - \int_Q \left(f_h(0,x,v) - f_0(x,v)\right)\varphi(0,x,v)dxdv. \end{aligned}$$

Thus,

$$\begin{aligned} |E_1 + E_{1,0}| \;\leq\; & \sum_{n,i,j} |\, f_{i,j}^{n+1} - f_{i,j}^n| \int_{t^n}^{t^{n+1}} \int_{C_{i,j}} \left|\frac{\partial \varphi}{\partial t}(t,x,v)\right| dtdxdv \\ & + \int_Q |\, f_h(0,x,v) - f_0(x,v)|\; |\varphi(0,x,v)| dxdv, \end{aligned}$$

with the discrete initial data defined, for example, by

$$f_h(0,x,v) = \frac{1}{|C_{i,j}|}\int_{C_{i,j}} f_0(x,v)dxdv \quad \forall (x,v) \in C_{i,j}.$$

Using the assumption on the initial data $f_0 \in L^1(Q) \cap L^\infty(Q)$, we then have

$$\lim_{h\to 0} \int_Q |f_h(0,x,v) - f_0(x,v)|\ |\varphi(0,x,v)| dxdv = 0.$$

Moreover, from the inequality on the term EF_{2h} given by (4.30) in Lemma 4, we have

$$\sum_{n,i,j} |f_{i,j}^{n+1} - f_{i,j}^n| \int_{t^n}^{t^{n+1}} \int_{C_{i,j}} \left|\frac{\partial\varphi}{\partial t}(t,x,v)\right| dtdxdv \leq C \|\frac{\partial\varphi}{\partial t}\|_{L^\infty} \Delta t^{1/2}.$$

Then,

$$|E_1 + E_{1,0}| \to 0 \quad \text{ as } h \to 0. \tag{4.31}$$

Now we deal with the terms E_2 and $E_{2,0}$. Therefore, we first introduce the notation

$$\begin{aligned} E_{2,1} \quad = \quad & \sum_{n,i,j}\Bigg[v_j^+ \,(f_{i,j}^n - f_{i-1,j}^n) \int_{t^n}^{t^{n+1}} \int_{v_{j-1/2}}^{v_{j+1/2}} \varphi(t, x_{i-1/2}, v) dvdt \\ & + v_j^- \,(f_{i,j}^n - f_{i+1,j}^n) \int_{t^n}^{t^{n+1}} \int_{v_{j-1/2}}^{v_{j+1/2}} \varphi(t, x_{i+1/2}, v) dvdt \\ & + E_i^{n+} \,(f_{i,j}^n - f_{i,j-1}^n) \int_{t^n}^{t^{n+1}} \int_{x_{i-1/2}}^{x_{i+1/2}} \varphi(t, x, v_{j-1/2}) dxdt \\ & + E_i^{n-} \,(f_{i,j}^n - f_{i,j+1}^n) \int_{t^n}^{t^{n+1}} \int_{x_{i-1/2}}^{x_{i+1/2}} \varphi(t, x, v_{j+1/2}) dxdt \Bigg]. \end{aligned}$$

On the one hand, we compare E_2 and $E_{2,1}$:

$$\begin{aligned} |E_2 - E_{2,1}| \quad = \quad & \Bigg| \sum_{n,i,j}\Bigg[v_j^+ \,(f_{i,j}^n - f_{i-1,j}^n) \left[\frac{1}{\Delta x_i} \int_{t^n}^{t^{n+1}} \int_{C_{i,j}} \varphi(t,x,v) - \varphi(t, x_{i-1/2}, v) dvdt \right] \\ & + v_j^- \,(f_{i,j}^n - f_{i+1,j}^n) \left[\frac{1}{\Delta x_i} \int_{t^n}^{t^{n+1}} \int_{C_{i,j}} \varphi(t,x,v) - \varphi(t, x_{i+1/2}, v) dvdt \right] \\ & + E_i^{n+} \,(f_{i,j}^n - f_{i,j-1}^n) \left[\frac{1}{\Delta v_j} \int_{t^n}^{t^{n+1}} \int_{C_{i,j}} \varphi(t,x,v) - \varphi(t, x, v_{j-1/2}) dxdt \right] \\ & + E_i^{n-} \,(f_{i,j}^n - f_{i,j+1}^n) \left[\frac{1}{\Delta v_j} \int_{t^n}^{t^{n+1}} \int_{C_{i,j}} \varphi(t,x,v) - \varphi(t, x, v_{j-1/2}) dxdt \right] \Bigg] \Bigg|. \end{aligned}$$

Using the inequality on EF_{1h} given by (4.30) in Lemma 4, there exists $c > 0$ depending only on T, R, L, f_0, α, ξ such that the following inequality holds:

$$|E_2 - E_{2,1}| \leq c\, \|\nabla_{(x,v)}\varphi\|_{L^\infty}\ h^{1/2}. \tag{4.32}$$

On the other hand, we estimate $|E_{2,0} + E_{2,1}|$, rewriting the term $E_{2,1}$ and using the boundary conditions, it yields the following (we remind that φ is compactly supported in velocity):

$$\begin{aligned} E_{2,1} &= -\sum_{n,i,j} f_{i,j}^n \int_{t^n}^{t^{n+1}} \int_{C_{i,j}} v_j \frac{\partial\varphi}{\partial x}(t,x,v) + E_i^n \frac{\partial\varphi}{\partial v}(t,x,v) dv dx dt \\ &\quad + \sum_{n,j} v_j^+ g_j^n \int_{t^n}^{t^{n+1}} \int_{v_{j-1/2}}^{v_{j+1/2}} \varphi(t,0,v) dv dt. \end{aligned}$$

Therefore,

$$\begin{aligned} |E_{2,0} + E_{2,1}| &\le \sum_{n,i,j} f_{i,j}^n \left[\int_{t^n}^{t^{n+1}} \int_{C_{i,j}} \left|v - v_j\right| \left|\frac{\partial\varphi}{\partial x}(t,x,v)\right| + \left|E_h(t,x) - E_i^n\right| \left|\frac{\partial\varphi}{\partial v}(t,x,v)\right| dx dv dt \right] \\ &\le \|\nabla\varphi\|_{L^\infty} \sum_{n,i,j} \Delta t\, \Delta x_i\, \Delta v_j\, f_{i,j}^n \left[\Delta v_j + \sup |E_h(t,x) - E_i^n| \right] \end{aligned}$$

and there exists $C > 0$, only depending on $T, R, L, f_0, \alpha, \xi$, such that

$$|E_{2,0} + E_{2,1}| \le C \|\nabla\varphi\|_{L^\infty} h. \tag{4.33}$$

It remains to estimate the last term E_3. Using the definition of $s_{i+1/2,j}$ and $s_{i,j+1/2}$ and performing a discrete integration by part, we get

$$\begin{aligned} E_3 &= \Delta t \sum_{n,i,j} \Delta v_j \left[v_j^+ \sigma_{i-1/2,j} (f_{i,j}^n - f_{i-1,j}^n) - v_j^- \sigma_{i+1/2,j} (f_{i,j}^n - f_{i+1,j}^n) \right] [\varphi_{i-1,j}^n - \varphi_{i,j}^n] + \\ &\qquad \Delta x_i \left[E_i^{n+} \sigma_{i,j-1/2} (f_{i,j}^n - f_{i,j-1}^n) - E_i^{n-} \sigma_{i,j+1/2} (f_{i,j}^n - f_{i,j+1}^n) \right] [\varphi_{i,j-1}^n - \varphi_{i,j}^n]. \end{aligned}$$

However, we know that

$$|\varphi_{i-1,j}^n - \varphi_{i,j}^n| \le \|\frac{\partial\varphi}{\partial x}\|_{L^\infty} \left(\frac{\Delta x_{i-1} + \Delta x_i}{2} \right).$$

and using the estimate on EF_{1H} in Lemma 4, it yields there exists a constant $C > 0$ such that

$$|E_3| \le C \|\nabla_{(x,v)}\varphi\|_{L^\infty} h^{1/2}. \tag{4.34}$$

Finally, recalling that $E_1 + E_2 + E_3 = 0$, we obtain

$$\begin{aligned} \epsilon(\Delta t, h) &= \int_{Q_T} f_h \left(\frac{\partial\varphi}{\partial t} + v \frac{\partial\varphi}{\partial x} + E_h(t,x) \frac{\partial\varphi}{\partial v} \right) dt dx dv + \int_Q f_0(x,v) \varphi(0,x,v) dx dv \\ &= E_{1,0} + E_{2,0} \\ &= E_{1,0} + E_1 + E_{20} + E_{2,1} - E_{2,1} + E_2 + E_3, \end{aligned}$$

and from the previous estimates, we proved there exists a constant C depending only on φ, f_0, L, T, α, ξ such that

$$\begin{aligned} |E_{1,0} + E_1| &\le C (\|f_0 - f_h(0)\|_{L^1} + \Delta t^{1/2}), \\ |E_{2,0} - E_2| &\le C h^{1/2}, \\ |E_{2,0} + E_{2,1}| &\le C h. \\ |E_3| &\le C h^{1/2}. \end{aligned}$$

Then, $\epsilon(\Delta t, h) \to 0$ as $h \to 0$.

As we know

$$f_h(t,x,v) \rightharpoonup f(t,x,v) \text{ in } L^\infty(Q_T) \text{ weak-}\star$$

and

$$E_h(t,x) \to E(t,x) \text{ in } C^0(\overline{\Omega}_T),$$

we have shown that the limit pair (f,E) of a subsequence $(f_h, E_h)_{h>0}$ is a solution of the Vlasov equation (4.1). To conclude, we have to prove that this couple is also a solution of the Poisson equation.

Remark 5. *In practical calculation, we use a large but finite bound M for the velocity space. In this paper, we assume that as $h \to 0$, the support of the velocity space goes to infinity, and the stability condition (4.20) imposes on us that*

$$\exists\, \varepsilon \in (0,1), \quad v_h \simeq \frac{1}{h^\epsilon}, \quad \textit{and} \quad \Delta t \simeq \frac{h^2}{h^{1-\epsilon}+h} \simeq h^{1+\epsilon}.$$

4.4.3 Convergence to the solution of the Poisson equation

We have already proved that there exists a subsequence of $(E_h)_{h>0}$ and $E \in C^0(\overline{\Omega}_T)$ such that E_h converges to E and $\|E_h - \tilde{E}_h\|_{L^\infty}$ goes to zero when h goes to zero. Hence, we know that up to a sub-sequence $\tilde{E}_h$ converges to E. Now let us prove that E is solution to the Poisson equation.

On the one hand, for all test functions which belong to $C_c^1([0,T)\times(0,L))$, we set φ_i^n such that

$$\varphi_i^n := \frac{1}{\Delta t\, \Delta x_i} \int_{t^n}^{t^{n+1}} \int_{x_{i-1/2}}^{x_{i+1/2}} \varphi(t,x)dxdt$$

and multiply the finite volume scheme (4.15) by $\Delta t\, \Delta x_i\, \varphi_i^n$, sum over $i \in \{0,\dots,n_x-1\}$ and $n \in \{0,\dots,N_T = \frac{T}{\Delta t}\}$, it gives $T_1 + T_2 = 0$ with

$$\begin{aligned} T_1 &= \Delta t \sum_{i,n} \Delta x_i\, E_i^n \left(\varphi_i^n - \varphi_{i-1}^n\right) \\ T_2 &= \sum_{i,n} \int_{t^n}^{t^{n+1}} \int_{x_{i-1/2}}^{x_{i+1/2}} \rho_i^n\, \varphi(t,x)dxdt. \end{aligned}$$

We also set $T_{1,0}$ and $T_{2,0}$

$$\begin{aligned} T_{1,0} &= \int_{\Omega_T} \tilde{E}_h(t,x)\, \frac{\partial \varphi}{\partial x}(t,x)\, dxdt \\ T_{2,0} &= \int_{\Omega_T} \rho_h(t,x)\, \varphi(t,x)\, dtdx, \end{aligned}$$

and observe that $T_2 = T_{2,0}$ and

$$\begin{aligned} |T_1 - T_{1,0}| &= \left| \sum_{i,n} \Delta x_i\, E_i^n \int_{t^n}^{t^{n+1}} \left[\varphi_i^n - \varphi(t, x_{i+1/2}) - \varphi_{i-1}^n + \varphi(t, x_{i+1/2})\right] dt \right| \\ &\le C_T \, \|\frac{\partial \varphi}{\partial x}\|_{L^\infty}\, h. \end{aligned}$$

The weak formulation infers that the solution of the Vlasov-Poisson system belongs to $C^0([0,T[;\mathcal{D}')$, but observing the electric field E is bounded in $W^{1,\infty}(\Omega_T)$ and the initial data are continuous, we see that the distribution function f is also continuous in (x,v). Let us recall that under our hypothesis, the solution of the Vlasov-Poisson system (4.1)-(4.5) is unique; then any subsequence that we considered converges to the same limit and the sequence $(f_h, E_h)_{h>0}$ converges to the unique solution.

4.5 Numerical Simulations

In this section, we consider the two component Vlasov-Poisson system. Let f_α be the distribution function of species $\alpha \in \{e,i\}$; it satisfies the Vlasov equation

$$\frac{\partial f_\alpha}{\partial t} + v\frac{\partial f_\alpha}{\partial x} + \frac{q_\alpha}{m_\alpha} E(t,x)\frac{\partial f_\alpha}{\partial v} = 0 \tag{4.35}$$

coupled with the Poisson equation

$$E(t,x) = -\nabla_x \phi(t,x), \quad -\frac{\partial^2 \phi}{\partial x^2}(t,x) = \frac{\rho}{\epsilon_0}, \tag{4.36}$$

where

$$\rho(t,x) = \sum_{\alpha\in\{i,e\}} \rho_\alpha$$

and

$$\rho_\alpha = q_\alpha \int_{\mathbb{R}} f_\alpha(t,x,v)\,dv, \quad \alpha \in \{e,i\}.$$

In the previous analysis we presented for clarity reasons the single component Vlasov-Poisson system, but the result remains true for the multi-component case. We assume here that $q_e = -q_i = 1$ and $\epsilon_0 = 1$ and $m_e/m_i = 0.001$, which means that ions are more heavy than electrons. We perform numerical simulations for this model with a zero initial datum $f_0 = 0$, $\lambda(t) = 1$ and

$$g(t,v) = \frac{1}{\sqrt{2\pi}} \exp(-v^2/2).$$

In order to improve time discretization accuracy, the procedure is achieved by a second order Runge-Kutta scheme. We performed numerical simulations for different meshes and only report the results of a simulation using a number of cells $n_x = 128$ in the x-direction, and $n_v = 128$ in the v-direction with $v_{max} = 6$, and the time step $\Delta t = 0.01$ for the conservative finite volume scheme. For these configurations, numerical results are no more sensitive to the mesh and are comparable in term of accuracy. The evolution obtained by the finite volume scheme clearly appears to give a good approximation with 128×128 points. Here, nonlinear effects are so important that it is necessary to control spurious oscillation; the second order scheme is conservative and also preseves positivity of the numerical solution. Moreover, the use of slope correctors in the finite volume scheme allows to damp spurious osccillations. For the distribution function in the (x,v) space, some filaments become smaller than the phase space grid size. Nevertheless, this smooth approximation seems to give a good description of macroscopic values (physics quantities obtained by the integration of moments of the distribution function with respect to v). Indeed, the evolution of the electric energy is still accurate using the second order accuracy.

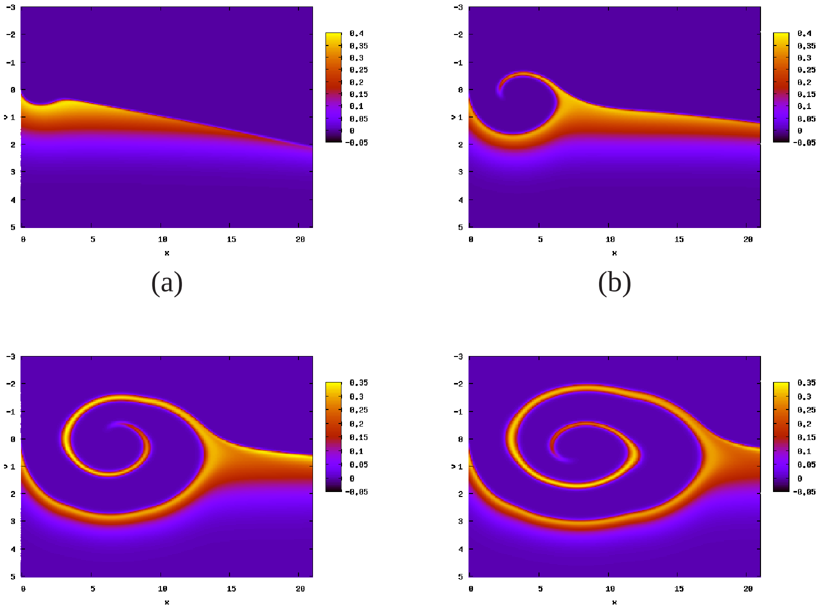

(a) (b)

(c) (d)

Figure 4.1: *Formation of a phase space vortex : the distribution function* $f_h(t, x, v)$ *at time* $t = 12, 24, 36$ *and* 42 *obtained with the second order finite volume scheme with* 128×128 *points.*

The processes that are at stake here are highly nonlinear and present discontinuities in phase space. They consist in the excitation of a plasma wave by injected electrons. As the beam progresses in plasma, the amplitude of the plasma wave grows and more electrons are trapped in this wave as shown in figure (4.1). At the same time, the plasma electron are ejected through the right side of the simulation box to neutralize the injected charge with electron beam. The modulations of electron density are the result of large plasma frequency oscillations.

Bibliography

[1] T.D. Arber and R.G.L. Vann, *A critical comparison of Eulerian-grid-based Vlasov solvers*, J. Comput. Physics, **180**, (2002) pp. 339–357.

[2] N. Besse, *Convergence of a semi-Lagrangian scheme for the one-dimensional Vlasov-Poisson system* SIAM J. Numer. Anal. **42** (2004) pp. 350–382.

[3] N. Besse and M. Mehrenberger, *Convergence of classes of high-order semi-Lagrangian schemes for the Vlasov-Poisson system*, Math. Comp. **77** (2008), pp. 93–123

[4] J. P. Boris and D. L. Book, *Solution of continuity equations by the method of flux-corrected transport*, J. Comput. Phys. **20** (1976) pp. 397–431.

[5] J. A. Carrillo and F. Vecil, *Nonoscillatory interpolation methods applied to Vlasov-based models*, SIAM J. Sci. Comput. **29** (2007) pp. 1179–1206.

C. Z. Cheng and G. Knorr, *The integration of the Vlasov equation in configuration space*, J. Comput. Phys., **22** (1976) pp. 330–351.

[6] C. Z. Cheng and G. Knorr, *The integration of the Vlasov equation in configuration space*, J. Comput. Phys., **22** (1976) pp. 330–351.

[7] J. Cooper and A.J. Klimas, *Boundary value problems for the Vlasov-Maxwell equation in one dimension*, J. Math. Anal. Appl. **75** (1980) pp. 306–329.

[8] P. Degond, P.-A. Raviart, *An asymptotic analysis of the Vlasov-Poisson system: the Child-Langmuir law*, Asymptotic Anal. **4** (1991) pp. 187–214.

[9] R. J. DiPerna and P. L. Lions, *Solutions globales d'équations du type Vlasov-Poisson,* C. R. Acad. Sci. Paris Série I Math., **307** (1988) pp. 306–329.

[10] F. Filbet, *Convergence d'un schéma de type volumes finis pour le système de Vlasov-Poisson*, CRAS Paris **330**, série I Mathématique pp. 979–984 (2000).

[11] F. Filbet, *Convergence of a finite volume scheme for the Vlasov-Poisson system,* SIAM J. Numer. Anal. **39** (2001) pp. 1146–1169.

[12] F. Filbet, E. Sonnendrücker and P. Bertrand, *Conservative Numerical schemes for the Vlasov equation*, J. Comput. Phys. **172** (2001) pp. 166–187.

[13] F. Filbet and E. Sonnendrücker, *Comparison of Eulerian Vlasov Solvers, Computer Physics Communications* **150** (2003) pp. 247–266.

[14] F. Filbet, Y. Guo and C.-W. Shu, *Analysis of the Reduced Vlasov-Maxwell Model with Boundary Conditions*, Quarterly Applied Math., **63** (2005) pp. 691–714.

[15] C. Greengard, P.-A. Raviart, *A boundary-value problem for the stationary Vlasov-Poisson equation : the plane diode*, Comm. Pure. Appl. Math. **43** (1990) pp. 472–507.

[16] Y. Guo, *Global weak solutions of the Vlasov-Maxwell system with boundary conditions*, Comm. Math. Phys. **154** (1993) pp. 254–263.

[17] Y. Guo, C.W Shu and T. Zhou, *The Dynamics of a Plane Diode*, SIAM J. Math. Anal. **35** (2004) pp. 1617–1635.

[18] A. J. Klimas and W. M. Farrell, *A splitting algorithm for Vlasov simulation with filamentation filtration*, J. Comput. Phys. **110** (1994) pp. 150–163.

[19] F. Poupaud, *Boundary value problems for the stationary Vlasov-Maxwell system*, Forum Math. **4** (1992) pp. 499–527.

[20] J. Schaeffer, *Convergence of a difference scheme for the Vlasov–Poisson–Fokker–Planck system in one dimension,* SIAM J. Numer. Anal. **35** (1997) pp. 1149–1175.

[21] M. Shoucri and G. Knorr, *Numerical integration of the Vlasov equation*, J. Comput. Phys. **14** (1974) pp. 84–92.

[22] Y. Zheng and A. Majda, *Existence of global weak solutions to one-component Vlasov-Poisson and Fokker-Planck-Poisson systems in one space dimension with measures as initial data,* Comm. Pure Appl. Math. **47** (1994) pp. 1365–1401.

[23] T. Nakamura and T. Yabe, *Cubic interpolated propagation scheme for solving the hyper-dimensional Vlasov-Poisson equation in phase space*, Comput. Phys. Communications **120** (1999) pp. 122–154.

Chapter 5

High order numerical coupling with the Fokker-Planck-Landau collision model: the collisional multi-scale transport

5.1 Introduction

In this chapter, we step towards a reference numerical solution, able to capture both (self-consistently magnetized) collective and collisional effects and couple them, with high anisotropy degree. We present relevent tests for validation of the coupling between the diferent components, in order to show the robustness of the method and to quantify the accuracy.

5.2 Approximation of the collision operators

5.2.1 The nonrelativistic FPL model for the collisions

In this section, we focus on the approximation of collision operators. Since the space variable is a parameter, we only consider the space homogeneous equation,

$$\begin{cases} \dfrac{\mathrm{d}f}{\mathrm{d}t} = C_{e,e}(f,f) + C_{e,i}(f), \\[2ex] f(0,\mathbf{v}) = f^{(0)}(\mathbf{v}), \end{cases}$$

The FPL operator $C_{e,e}(f_e, f_e)$ stands for the electron-electron collision operator

$$C_{e,e}(f_e, f_e) = \frac{e^4 \ln\Lambda}{8\,\pi\,\epsilon_0^2\, m_e^2} \nabla_{\mathbf{v}} \cdot \left(\int_{\mathbb{R}^3} \Phi(\mathbf{v}-\mathbf{v}')\left[f_e(\mathbf{v}')\nabla_{\mathbf{v}} f_e(\mathbf{v}) - f_e(\mathbf{v})\nabla_{\mathbf{v}'} f_e(\mathbf{v}')\right] \mathbf{dv}' \right), \tag{5.1}$$

whereas $C_{e,i}(f_e)$ is the electron-ion collision operator

$$C_{e,i}(f_e) = \frac{Z\, n_0\, e^4 \ln\Lambda}{8\,\pi\,\epsilon_0^2\, m_e^2} \nabla_{\mathbf{v}} \cdot \left[\Phi(\mathbf{v})\nabla_{\mathbf{v}} f_e(\mathbf{v})\right]. \tag{5.2}$$

where $\ln\Lambda$ is the Coulomb logarithm, which is supposed to be constant over the domain and $\Phi(\mathbf{u})$ is an operator acting on the relative velocity $\mathbf{u}$

$$\Phi(\mathbf{u}) = \frac{||\mathbf{u}||^2\,\mathrm{Id} - \mathbf{u}\otimes\mathbf{u}}{||\mathbf{u}||^3}. \tag{5.3}$$

The FPL operator is used to describe elastic, binary collisions between charged particles, with the long-range Coulomb interaction potential. Classical but important properties of the operators (5.1) and (5.2), are briefly recalled. For detailed proofs, we refer to [11, 12]. As we assume ions to be fixed, the FPL operator can then be simplified for electron-ion collisions [11], and reduced to the Lorentz approximation. We refer to [2] for a physical derivation.

5.2.2 Properties of the nonrelativistic FPL collision operators

The FPL operator is used to describe binary elastic collisions between electrons. Its algebraic structure is similar to the Boltzmann operator, in that it satisfies the conservation of mass, momentum and energy

$$\int_{\mathbb{R}^3} C_{e,e}(f_e, f_e)(\mathbf{v}) \begin{pmatrix} 1 \\ \mathbf{v} \\ ||\mathbf{v}||^2 \end{pmatrix} \mathbf{dv} = 0, \; t \geq 0.$$

Moreover, the entropy is decreasing with respect to time

$$\frac{dH}{dt}(t) = \frac{d}{dt}\int_{\mathbb{R}^3} f_e(\mathbf{v},t)\,\log(f_e(\mathbf{v},t))\mathbf{dv} \,\leq\, 0,\;\; t \geq 0.$$

The equilibrium states of the FPL operator, *i.e.* the set of distribution functions in the kernel of $C_{e,e}(f_e, f_e)$, are given by the Maxwellian distribution functions

$$\mathcal{M}_{n_e,\mathbf{u_e},T_e}(\mathbf{v}) \;=\; n_e\left(\frac{m_e}{2\,\pi\,T_e}\right)^{3/2} \exp\left(-m_e\,\frac{||\mathbf{v}-\mathbf{u_e}||^2}{2\,T_e}\right),$$

where n_e is the density, $\mathbf{u_e}$ is the mean velocity and T_e is the temperature, defined as

$$\left\{\begin{array}{lcl} n_e &=& \displaystyle\int_{\mathbb{R}^3} f_e(\mathbf{v})\mathbf{dv}, \\[2ex] \mathbf{u_e} &=& \displaystyle\frac{1}{n_e}\int_{\mathbb{R}^3} f_e(\mathbf{v})\mathbf{v}\mathbf{dv}, \\[2ex] T_e &=& \displaystyle\frac{m_e}{3\,n_e}\int_{\mathbb{R}^3} f_e(\mathbf{v})||\mathbf{v}-\mathbf{u_e}||^2\mathbf{dv}. \end{array}\right.$$

On the other hand, the operator (5.2), modelling collisions between electrons and ions, is a Lorentz operator. It satisfies the conservation of mass and energy

$$\int_{\mathbb{R}^3} C_{e,i}(f_e)(\mathbf{v})\begin{pmatrix} 1 \\ ||\mathbf{v}-\mathbf{u_e}||^2 \end{pmatrix}\mathbf{dv} \;=\; 0.$$

Moreover, the equilibrium states for this operator are given by the set of isotropic functions:

$$\mathrm{Ker}\,(C_{e,i}) \;=\; \left\{\, f_e \in L^1\left((1+||\mathbf{v}||^2)\mathbf{dv}\right),\quad f_e(\mathbf{v}) \;=\; \phi(z),\;\; z \;=\; ||\mathbf{v}-\mathbf{u_e}||^2 \,\right\}.$$

Finally, each convex function ψ of f_e is an entropy for $C_{e,i}(f_e)$,

$$\frac{d}{dt}\int_{\mathbb{R}^3} \psi(f_e)\,\mathbf{dv} \,\leq\, 0,\;\; t \geq 0.$$

In addition to these properties, we present a symmetry property. This property may have some importance, in particular in presence of self-consistent magnetic fields. Indeed, any break of symmetry due to an inadequate discretization method could lead to generation of artificial magnetic fields, *via* current source terms.

Proposition 6. *If f_e has the following symmetry property with respect to the direction k at time t_0*

$$f_e(t_0,\mathbf{v}) \;=\; f_e(t_0,\mathbf{v}^k), \tag{5.4}$$

with components for

$$\mathbf{v}_i^k \;=\; \left\{\begin{array}{ll} +\mathbf{v}_i & \text{if } i \neq k, \\ -\mathbf{v}_i & \text{if } i = k. \end{array}\right.$$

Then, this symmetry property is preserved with respect to time.

5.2.3 Discrete Lorentz operator

We consider $f_{\mathbf{j}}$ an approximation of the distribution function $f(\mathbf{v_j})$ and introduce the operator **D**, which denotes a discrete form of the usual gradient operator $\nabla_{\mathbf{v}}$ whereas $\mathbf{D}^*$ represents its formal adjoint, which represents an approximation of $-\nabla_{\mathbf{v}}\cdot$. Therefore, for any test sequence $(\psi_{\mathbf{j}})_{\mathbf{j}\in\mathbb{Z}^3}$, we set $(\mathbf{D}\psi_{\mathbf{j}})_{\mathbf{j}\in\mathbb{Z}^3}$ as a sequence of vectors of $\mathbb{R}^3$

$$\mathbf{D}\psi_{\mathbf{j}} \;=\; {}^t(D_1\psi_{\mathbf{j}}, D_2\psi_{\mathbf{j}}, D_3\psi_{\mathbf{j}}) \in \mathbb{R}^3,$$

where D_s is an approximation of the partial derivative $\frac{\partial}{\partial v_s}$ with $s \in \{1,2,3\}$. In order to preserve the property of decreasing entropy at the discrete level, we use the log weak formulation of the Lorentz operator (6.19) [13]

$$\int_{\mathbb{R}^3} C_{e,i}(f)(\mathbf{v})\,\psi(\mathbf{v})\,\mathbf{dv} \;=\; -\int_{\mathbb{R}^3} \Phi(\mathbf{v})\, f(\mathbf{v})\,\nabla_{\mathbf{v}}\log(f(\mathbf{v}))\cdot\nabla_{\mathbf{v}}\psi(\mathbf{v})\,\mathbf{dv},$$

where Φ is given by (5.3) and ψ is a smooth test function. Then, using the notations previously introduced, the discrete operator $C^{\Delta v}_{e,i}(f)$ is given by

$$C^{\Delta v}_{e,i}(f)(\mathbf{v_j}) \;=\; -\mathbf{D}^*\left[\frac{1}{\|\mathbf{v_j}\|^3}\,S(\tilde{\mathbf{v}}_{\mathbf{j}})\,f_{\mathbf{j}}\,\mathbf{D}(\log(f_{\mathbf{j}}))\right], \tag{5.5}$$

where $S(\tilde{\mathbf{v}}_{\mathbf{j}})$ is the following matrix

$$S(\tilde{\mathbf{v}}_{\mathbf{j}}) \;=\; \|\tilde{\mathbf{v}}_{\mathbf{j}}\|^2\,\mathrm{Id} \;-\; \tilde{\mathbf{v}}_{\mathbf{j}}\otimes\tilde{\mathbf{v}}_{\mathbf{j}}.$$

Now, $\tilde{\mathbf{v}}_{\mathbf{j}}$ has to satisfy the discrete conservation of energy

$$\frac{D_1(\|\mathbf{v_j}\|^2)}{\tilde{\mathbf{v}}_{j_1}} \;=\; \frac{D_2(\|\mathbf{v_j}\|^2)}{\tilde{\mathbf{v}}_{j_2}} \;=\; \frac{D_3(\|\mathbf{v_j}\|^2)}{\tilde{\mathbf{v}}_{j_3}}. \tag{5.6}$$

Then, we consider the 8 uncentered operators $\mathbf{D}^\epsilon$, with the formalism:

$$\mathbf{D}^\epsilon \;=\; {}^t(D_1^{\epsilon_1}, D_2^{\epsilon_2}, D_3^{\epsilon_3}),$$

with $\epsilon = {}^t(\epsilon_1,\epsilon_2,\epsilon_3)$, and $\epsilon_i \in \{+1,-1\}$ for $i \in \{1,2,3\}$. More precisely, the operator D^{ϵ_i} is the forward uncentered discrete operator if $\epsilon_i = +1$ and the backward uncentered discrete operator if $\epsilon_i = -1$:

$$\mathbf{D}^\epsilon\mathbf{\Psi_j} = \frac{1}{\Delta v}\begin{pmatrix} \epsilon_1[\Psi_{j_1+\epsilon_1} - \Psi_{j_1}] \\ \epsilon_2[\Psi_{j_2+\epsilon_2} - \Psi_{j_2}] \\ \epsilon_3[\Psi_{j_3+\epsilon_3} - \Psi_{j_3}] \end{pmatrix} \tag{5.7}$$

This 8 operators respectively match to 8 expressions of $\tilde{\mathbf{v}}^\epsilon_{\mathbf{j}}$, following (5.6)

$$\tilde{\mathbf{v}}^\epsilon_{\mathbf{j}} \;=\; \frac{1}{2}\left(\mathbf{v_j} \;+\; \mathbf{v}_{\mathbf{j}+\epsilon}\right).$$

This choice has been made to avoid the use of the centered discrete operator that conserves non physical quantities. On the other hand, the uncentered operators, taken separately, introduce some artificial asymmetry in the distribution function leading to a loss of accuracy when coupling to Maxwell equations.

To overcome these difficulties, following the idea of [8], we introduce a symmetrization of the discrete operator based on the averaging over the eight uncentered discretizations:

$$
\begin{aligned}
C^{\Delta v}_{e,i}(f)(\mathbf{v_j}) &= \frac{1}{8}\sum_{\epsilon} C^{\epsilon}_{e,i}(f) \\
C^{\epsilon}_{e,i}(f) &= -\mathbf{D}^{*,\epsilon}\left[\frac{1}{||\mathbf{v_j}||^3} S(\tilde{\mathbf{v}}^{\epsilon}_{\mathbf{j}})\, f_{\mathbf{j}}\, \mathbf{D}^{\epsilon}(\log(f_{\mathbf{j}}))\right].
\end{aligned}
$$

This final expression presents the desirable properties: the mass and energy conservation, the entropy decreasing behavior, the positivity preservation of the distribution function in a finite time sequence. The proofs are not detailed here but can be deduced easily from those presented in [11]. Also, it introduces an additional discrete symmetry property, compared to the operator presented in [11]. Indeed, we obtain the operator as an average over the full set of the uncentered operators. The motivation of this averaging comes from the isotropization effect of the Lorentz operator: it diffuses in angle. This averaging leads to a discrete analogous of the symmetry property presented in Proposition 6. This symmetry concerns the directions that are aligned with the grid. The symmetries along directions that are not aligned with the grid are preserved with marginal errors.

Proposition 7. *Under the condition (5.6) on* $\tilde{\mathbf{v}}_{\mathbf{j}}$*, the discretization (5.8) to the Lorentz operator (5.2) satisfies the following properties,*

- *it preserves the mass and energy,*
- *it decreases the discrete entropy*

$$
H(t) = \Delta v^3 \sum_{\mathbf{j}\in\mathbb{Z}^3} f_{\mathbf{j}}(t)\, \log(f_{\mathbf{j}}(t)),
$$

- *there exists a time-sequence* Δt_n *such that the scheme*

$$
f^{n+1}_{\mathbf{j}} = f^{n}_{\mathbf{j}} + \Delta t\, C^{\Delta v}_{e,i}(f)(\mathbf{v_j}),
$$

  defines a positive solution at any time i.e. $\sum_n \Delta t_n = +\infty$.

Furthermore, if $f_{\mathbf{j}}$ *is symmetric with respect to* 0 *in the direction* j_k *at time* t^n*, then this property is preserved at time* t^{n+1}*,*

$$
\sum_{\mathbf{j}\in\mathbb{Z}^3} C^{\Delta v}_{e,i}(f)(\mathbf{v_j}) v_{j_k} \Delta v^3 = 0. \tag{5.8}
$$

Proof: The proofs of all the properties but the last one can be found in [11]. We prove the last property and rewrite the operator (5.8) in a different manner, assuming we have a symmetry along the velocity direction v_{j_k}

$$
C^{\Delta v}_{e,i}(f)(\mathbf{v_j}) = \frac{1}{8}\sum_{\epsilon} C^{\epsilon}_{e,i}(f)(\mathbf{v_j}) = \frac{1}{8}\sum_{\epsilon}\left[\frac{1}{3}\sum_{k=1}^{3}\frac{1}{2}\left(C^{\epsilon^{+,(k)}}_{e,i}(\mathbf{v_j}) + C^{\epsilon^{-,(k)}}_{e,i}(\mathbf{v_j})\right)\right], \tag{5.9}
$$

where the notation $\epsilon^{\pm,(k)}$ refers to

$$\begin{cases} \epsilon_i^{\pm,(k)} = \pm 1 & \text{if } i = k, \\ \epsilon_i^{\pm,(k)} = \epsilon_i & \text{if } i \neq k. \end{cases} \tag{5.10}$$

We are interested in the cancellation of the operator $\sum\limits_{\mathbf{j}\in\mathbb{Z}^3} C_{e,i}^{\Delta v}(f)(\mathbf{v_j})v_{j_k}$. This is equivalent to the cancellation of

$$\begin{aligned} Q^{(k)} \quad &:= \quad \sum_{\mathbf{j}\in\mathbb{Z}^3} \left(C_{e,i}^{\epsilon^{+,(k)}}(\mathbf{v_j}) + C_{e,i}^{\epsilon^{-,(k)}}(\mathbf{v_j}) \right) v_{j_k} \\ &= \quad \sum_{\mathbf{j}\in\mathbb{Z}^3} \frac{1}{||\mathbf{v_j}||^3} f_{\mathbf{j}} \left[S(\tilde{\mathbf{v}}_{\mathbf{j}}^{\epsilon^{+,(k)}}) \mathbf{D}^{\epsilon^{+,(k)}} \log(f_{\mathbf{j}}) \right] \cdot \mathbf{D}^{\epsilon^{+,(k)}} v_{j_k} \\ &+ \quad \sum_{\mathbf{j}\in\mathbb{Z}^3} \frac{1}{||\mathbf{v_j}||^3} f_{\mathbf{j}} \left[S(\tilde{\mathbf{v}}_{\mathbf{j}}^{\epsilon^{-,(k)}}) \mathbf{D}^{\epsilon^{-,(k)}} \log(f_{\mathbf{j}}) \right] \cdot \mathbf{D}^{\epsilon^{-,(k)}} v_{j_k}. \end{aligned}$$

Then, since $\mathbf{D}^{\epsilon^{+,(k)}} v_{j_k} = \mathbf{D}^{\epsilon^{-,(k)}} v_{j_k} = \mathbf{e_k}$, it yields

$$\begin{aligned} Q^{(k)} \quad &= \quad \sum_{\mathbf{j}\in\mathbb{Z}^3} \frac{1}{||\mathbf{v_j}||^3} f_{\mathbf{j}} \left(\sum_{i\neq k} \left(\tilde{v}_{j_i}^{\epsilon_i^{+,(k)}} \right)^2 \right) D^{\epsilon_k^{+,(k)}}(\log(f_{\mathbf{j}})) \\ &- \quad \sum_{\mathbf{j}\in\mathbb{Z}^3} \frac{1}{||\mathbf{v_j}||^3} f_{\mathbf{j}} \tilde{v}_{j_k}^{\epsilon_k^{+,(k)}} \left(\sum_{i\neq k} \tilde{v}_{j_i}^{\epsilon_i^{+,(k)}} D^{\epsilon_i^{+,(k)}}(\log f_{\mathbf{j}}) \right) \\ &- \quad \sum_{\mathbf{j}\in\mathbb{Z}^3} \frac{1}{||\mathbf{v_j}||^3} f_{\mathbf{j}} \left(\sum_{i\neq k} \left(\tilde{v}_{j_i}^{\epsilon_i^{-,(k)}} \right)^2 \right) D^{\epsilon_k^{-,(k)}}(\log(f_{\mathbf{j}})) \\ &- \quad \sum_{\mathbf{j}\in\mathbb{Z}^3} \frac{1}{||\mathbf{v_j}||^3} f_{\mathbf{j}} \tilde{v}_{j_k}^{\epsilon_k^{-,(k)}} \left(\sum_{i\neq k} \tilde{v}_{j_i}^{\epsilon_i^{-,(k)}} D^{\epsilon_i^{-,(k)}}(\log f_{\mathbf{j}}) \right). \end{aligned}$$

Then using definition (5.10) and the symmetry of $f_{\mathbf{j}}^n$ with respect to 0 in the velocity direction v_{j_k}, we obtain $Q^{(k)} = 0$. Then multiplying (5.9) by v_{j_k} and integrating in the full velocity space gives the relation (5.8). This relation implies that $f_{\mathbf{j}}^{n+1}$ is symmetric with respect to 0 in the direction v_{j_k}. □

5.2.4 Discrete Landau operator

With a standard splitting algorithm, we may restrict to the homogeneous FPL operator in (6.19), in the $3D_{\mathbf{v}}$ velocity space. Its discretization based on the entropy conservative discretization introduced in [13], where a discrete weak log form of the FPL operator is used. This discretization yields

$$\begin{cases} \dfrac{d f_{\mathbf{j}}(t)}{dt} = (\mathbf{D}^* \rho(t))_{\mathbf{j}} \qquad \mathbf{j} \in \mathbb{Z}^3, \\ \\ \rho(t) = \Delta v^3 \displaystyle\sum_{\mathbf{m}\in\mathbb{Z}^3} f_{\mathbf{j}}(t) f_{\mathbf{m}}(t) \Phi(\mathbf{v_j} - \mathbf{v_m}) \left(\mathbf{D}(\log(f(t))_{\mathbf{j}} - \mathbf{D}(\log f(t))_{\mathbf{m}} \right), \end{cases} \tag{5.11}$$

where $\mathbf{D}$ stands for a downwind or upwind finite discrete operator approximating the usual gradient operator $\nabla_{\mathbf{v}}$. This uncentered approximation ensures that the only equilibrium states are the discrete Maxwellian, and satisfies the discrete conservation of mass, momentum, and energy. The dirct use of the centered discrete operator Q_c would have lead to non physical conserved quantities. The discretization of the FPL operator is then obtained as the average $\frac{1}{8}\sum_{\epsilon\in\{-1,1\}^3} Q^{\epsilon}$, over the eight possible uncentered operators Q^{ϵ}, $\epsilon \in \{-1,1\}^3$, in order to recover the symmetry of the problem. In [9], the scheme is rewritten, for any test sequence ψ, as the sum of two contribution from the operators Q_c and Q^{Δ}, since

$$\sum_{\mathbf{j}\in\mathbb{Z}^3}\left(\left[\frac{1}{8}\sum_{\epsilon\in\{-1,1\}^3} Q^{\epsilon}_{\mathbf{j}}\right] - Q_{c,\mathbf{j}} - \frac{\Delta v^2}{4} Q^{\Delta}_{\mathbf{j}}\right)\psi_{\mathbf{j}} = 0\,,$$

where Q^{Δ} is defines by the duality relation

$$\begin{aligned}\sum_{\mathbf{j}\in\mathbb{Z}^3} Q^{\Delta}_{\mathbf{j}}\Phi_{\mathbf{j}} &= -\frac{1}{2}\sum_{(\mathbf{j},\mathbf{m})\in\mathbb{Z}^3\times\mathbb{Z}^3} f_{\mathbf{j}}(t) f_{\mathbf{m}}(t)\left(\Delta\Psi_{\mathbf{j}} - \Delta\Psi_{\mathbf{m}}\right)^T \\ &\times\ \Phi^{\Delta}\left(\mathbf{v}_{\mathbf{j}} - \mathbf{v}_{\mathbf{m}}\right)\left(\Delta(\ln f)_{\mathbf{j}} - \Delta(\ln f)_{\mathbf{m}}\right)\Delta v^3\,, \qquad (5.12)\\ \Phi^{\Delta}\left(\mathbf{v}_{\mathbf{j}} - \mathbf{v}_{\mathbf{m}}\right) &= \frac{1}{v^3}\mathrm{Diag}\left(v^2 - v_{j_1}^2, v^2 - v_{j_2}^2, v^2 - v_{j_3}^2\right)\,. \qquad (5.13)\end{aligned}$$

The viscosity term Q^{Δ} presents a Δv^2 factor, which kills spurious oscillations. The computational cost of Q^{Δ} can be reduced, repacing the sum over $(\mathbf{j},\mathbf{m}) \in \mathbb{Z}^3 \times \mathbb{Z}^3$, by a sum over $(\mathbf{j},\mathbf{m}) \in \mathbb{Z}^3 \times \mathbb{Z}^3$ with $\|\mathbf{j} - \mathbf{m}\| \leq \sqrt{2}$. This reduction does not affect the conservation properties and does not generate any spurious collisional invariants.

This discrete approximation preserves positivity, mass, momentum, energy, and ensures that the entropy is decreasing. Moreover, the discrete equilibrium states are the discrete Maxwellian. We refer to [13] for the proofs and to [11] for numerical tests cases illustrating these properties in the homogeneous case.

We refer to [9] and [10] for the details of the implementation on the FPL operator.

5.2.5 The multigrid formulation

The computational cost of a direct approximation of (5.11) remains too high. Therefore, a multigrid formulation of the FPL operator is employed [9, 22], inspired from [20]. The multigrid description follows [22].

We first set

$$\begin{aligned} H(\mathbf{v},\mathbf{w}) &= f(\mathbf{v})f(\mathbf{w})v^2 S(\mathbf{v})\left[\nabla_{\mathbf{v}}(\log f) - \nabla_{\mathbf{w}}(\log f)\right]\,, \qquad (5.14)\\ S(\mathbf{v}) &= \mathbf{I_3} - \frac{\mathbf{v}\otimes\mathbf{v}}{v^2}\,, \qquad (5.15)\\ q(f,f)(\mathbf{v}) &= \int_{\mathbb{R}^3}\|\mathbf{v}-\mathbf{w}\|^{-3} H(\mathbf{v},\mathbf{w})\,d^3w\,. \qquad (5.16)\end{aligned}$$

The continuous FPL operator, in(6.19), writes

$$Q(f,f)(\mathbf{v}) = \nabla\cdot q(f,f)(\mathbf{v}) \qquad (5.17)$$

Let us now consider successive refinement layers of regular bounded domains of the velocity space. The initial level consists in considering a regular cube $\mathbf{C}_0$, with edges of length 1, as a domain for integration. Given a refinement level $k \in \mathbb{N}$, with an associated mapping of cubes, having same edge length $1/2^k$, in the $3D_\mathbf{v}$ velocity space, we denote by $\mathbf{C}_k(\mathbf{v})$ the unique cube that belongs to that mapping and contains the velocity $\mathbf{v}$. The cube(s) $\mathbf{C}_k(\mathbf{v}_0)$ and $\mathbf{C}_k(\mathbf{w}_0)$ are said to be well-separated if $||\mathbf{v}_0 - \mathbf{w}_0|| \geq 1/2^{k-1}$. The chosen numerical resolution, that can be either multipole [22] or monte carlo [9], is then performed between well-separated cubes. A refinement to the higher level is performed to compute the remaining not well-separated terms. This distinction between well-separted (ws) and not well-separated cubes (nws) is well-suited to the long-range nature of the Coulomb cross section.

This process is repeated until the higher specified desciption level.
We start at the lowest level, from the truncated analogous of the expression (5.16)

$$q^{(0)}(f,f)(\mathbf{v}) \quad = \quad \int_{\mathbf{C}_0} ||\mathbf{v}-\mathbf{w}||^{-3} H(\mathbf{v},\mathbf{w}) d^3 w \,. \tag{5.18}$$

The first step of the multigrid algorithm consists in splitting the “father cube” $\mathbf{C}_0$ into eight regular “chidren cubes”, having same sizes, and denoted by $\mathbf{C}_1^\mathbf{r}$. Their center coordinates are

$$\mathbf{O}_1^\mathbf{r} = \left(\frac{1}{2^2}+\frac{r_1}{2}, \frac{1}{2^2}+\frac{r_2}{2}, \frac{1}{2^2}+\frac{r_3}{2}\right) ,$$

where $\mathbf{r} = (r_1, r_2, r_3) \in \{0,1\}^3$.
We obtain the following decomposition of $q^{(0)}$

$$q^{(0)}(f,f)(\mathbf{v}) \quad = \quad \sum_{(\mathbf{r},\mathbf{r}')\in\{0,1\}^3\times\{0,1\}^3} \int_{\mathbf{C}_1^\mathbf{r}\times\mathbf{C}_1^{\mathbf{r}'}} ||\mathbf{v}-\mathbf{w}||^{-3} H(\mathbf{v},\mathbf{w}) d^3 w \,, \tag{5.19}$$

where each cube of this mapping is not well-separated from the other ones. A direct refinement is then applied at this first step, without any numerical computation.
As for the higher steps $k \geq 2$, the contribution of the interactions between cubes of same level k can be splitted in well-separated (ws) and not well separated (nws) cubes. The cube $\mathbf{C}_k^r$ is located according to its center position

$$\mathbf{O}_k^\mathbf{r} = \left(\frac{1}{2^{k+1}}+\frac{r_1}{2^k}, \frac{1}{2^{k+1}}+\frac{r_2}{2^k}, \frac{1}{2^{k+1}}+\frac{r_3}{2^k}\right) ,$$

where $\mathbf{r} = (r_1, r_2, r_3) \in \{0,1,...,2^k-1\}^3$.

$$q^{(k)}(f,f)(\mathbf{v}) \quad = \quad q_{ws}^{(k)}(f,f)(\mathbf{v}) + q_{nws}^{(k)}(f,f)(\mathbf{v}) \,, k \geq 2 \tag{5.20}$$

$$q_{ws}^{(k)}(f,f)(\mathbf{v}) \quad = \quad \sum_{\mathbf{r}/\left(C_k^\mathbf{r}\ ws\ C_k(\mathbf{v})\right)} \int_{\mathbf{C}_k^\mathbf{r}} ||\mathbf{v}-\mathbf{w}||^{-3} H(\mathbf{v},\mathbf{w}) d^3 w \,, \tag{5.21}$$

$$q_{nws}^{(k)}(f,f)(\mathbf{v}) \quad = \quad \sum_{\mathbf{r}/\left(C_k^\mathbf{r}\ nws\ C_k(\mathbf{v})\right)} \int_{\mathbf{C}_k^\mathbf{r}} ||\mathbf{v}-\mathbf{w}||^{-3} H(\mathbf{v},\mathbf{w}) d^3 w \,. \tag{5.22}$$

The process is repeated until the finest level n_f , where both well-separated and not well-separated interactions between cubes are computed. Therefore, we come to the expression

$$q(f, f)(\mathbf{v}) = q_{nws}^{(n_f)}(f, f)(\mathbf{v}) + \sum_{k=2}^{n_f} q_{ws}^{(k)}(f, f)(\mathbf{v}) \,, \tag{5.23}$$

that is to be approximated umerically. To this aim we employ a monte carlo algorithm for the integrations, presented in the next section.

5.2.6 The monte carlo numerical integration

We employ here a monte carlo quadrature formula [9], that randomly selects pairs of interacting cubes, and satsifies the minimal possible complexity (due to the specific structure of the kernel), being of order $O(n_v^3 \log n_v^3)$, where n_v is the number of discretization points per velocity direction. This algorithm was first suggested in [1], as an improvement of Nanbu's scheme of the Boltzmann equation.
Nevertheless, this monte carlo solver introduces a new approximation that might affect the accuracy. We shall test the accuracy of the scheme against analytical solutions in the tests 1-4 of this chapter.

5.3 Numerical results for the full kinetic model

5.3.1 A 1D temperature gradient configuration

In the context of laser produced plasma, the heat conduction is the leading mechanism of energy transport between the laser energy absorption zone and the target ablation zone.
In such a system, the parameters of importance for the heat flux are

- the effective electron collision mean free path λ_e.
- the electron temperature gradient length λ_T.
- the magnetic field B and its orientation with respect to ∇T.

These parameters enable to distinguish different regimes of transport, according to the Knudsen and the Hall parameters.

On the one hand, the Knudsen number K_n is a mesure of the thermodynamic non-equilibrium of the system

$$K_n = \frac{\lambda_e}{\lambda_T}. \tag{5.24}$$

A regime characterized by $K_n \to 0$ refers to an hydrodynamic limit, whereas a regime characterized by $K_n \geq 1$ refers to a kinetic limit, where nonlocal phenomena occur. Let us note that typical parameters for ICF yield that $K_n \geq 0.1$, while the hydrodynamic regime (or local approach) fails at $K_n \geq 0.01$. This premature failure of the local approach in plasma is explained by a specific dependence of the electron mean free path on the electron energy. In our applications the energy is transported by the fastest electrons, which have a much longer mean free path.

On the other hand, the Hall parameter $\chi = \omega_c \tau$ quantifies the relative importance of magnetic and collisional effects. $\omega_c = eB/m_e$ is the electron cyclotron frequency and τ the mean electron-ion collision time

$$\tau = \frac{12\,\pi^2\,\epsilon_0^2\,\sqrt{m_e}\,T_e^{3/2}}{\sqrt{2\,\pi}\,n_i\,Z^2\,e^4\,\ln\Lambda}. \tag{5.25}$$

The aim of this section is to validate our solver in different regimes, in order to show its robustness with respect to the variations of the Knudsen and Hall parameters. Thus, we consider a simple gradient temperature configuration, shown in Figure 5.1, modelling a layer of homogeneous plasma. A laser deposits its energy on the hot temperature side and the absorbed energy is transported with electrons to the cold temperature side. A heat flux is created, contributing to preheating (with the fastest particles) of the region down the temperature gradient, and to smoothing of this temperature gradient. The charge separation induced by the movement of particles generates electric currents and electric fields. The heat flux and electric field are important in a preliminary transient phase. Latter in time they decrease and stabilize due to the collisional effect and the return current of cold particles. These quantities may be inhibited in the direction of the temperature gradient if the magnetic field, constant in the domain, is present. In that case, heat fluxes and electric fields are created also in the direction perpendicular to the temperature gradient. A Knudsen boundary layer is observed, having the extension of several collision mean free paths. It is due to the zero boundary current condition, where the populations that leave and enter the computational domain have different temperatures. However, since the boundaries are far enough from the temperature gradient, this boundary layer does not influence the heat flux propagation in the region of the temperature gradient. We observed that the presence of a strong magnetic field enforces the variation of the fluxes inside this boundary layer.

5.3.2 Test 1 : Electron transport in the local regime

Here, we consisider configurations that present small Knuden parameters: $Kn \ll 1$. In order to validate the numerical scheme in the local regime, we compare the heat flux $\mathbf{Q_{FP}}$ and electric field $\mathbf{E_{FP}}$ computed from the numerical solution of (6.18), with those analytically computed from an hydrodynamic model [5, 15].

Hydrodynamic model. Let us define the average over velocity of a function $A(\mathbf{v})$

$$\langle A \rangle = \frac{1}{n_e} \int_{\mathbb{R}^3} A(\mathbf{v})\, f(\mathbf{v})\, \mathbf{dv}, \tag{5.26}$$

where $n_e(t, \mathbf{x}) = \int_{\mathbb{R}^3} f(t, \mathbf{x}, \mathbf{v}) \mathbf{dv}$ is the density of electrons.

Following [5, 15], we introduce the macroscopic quantities

$$\begin{cases} \mathbf{j} = q_e\, n_e\, \langle \mathbf{v} \rangle, \\[2ex] \mathbf{q} = \dfrac{1}{2}\, m_e\, n_e \langle\, (\,\mathbf{v} \cdot \mathbf{v})\, \mathbf{v}\, \rangle, \\[2ex] \mathbf{R} = \displaystyle\int_{\mathbb{R}^3} m_e\, \mathbf{v}\, C_{e,i}(f_e)\, \mathbf{dv}, \end{cases} \tag{5.27}$$

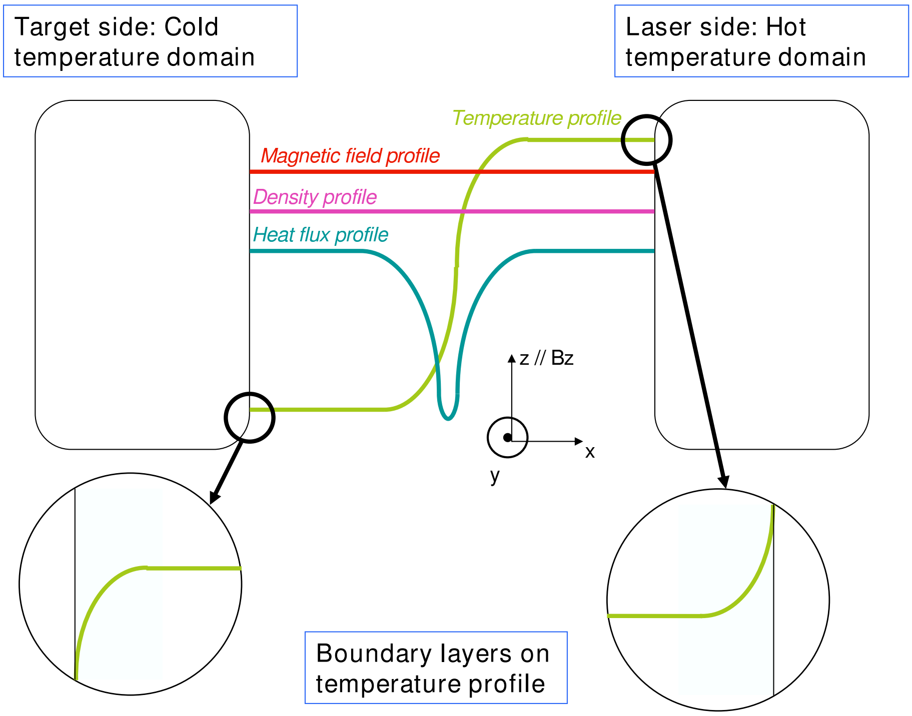

Figure 5.1: *Configuration of the temperature gradient test 1: a temperature profile is considered between two domains of plasma with particles at a thermal equilibrium. Zero current boundary conditions enable to maintain the mass conservation. A heat flux is generated wherever there is a nonzero temperature gradient. Knudsen boundary layers appear on the heat flux, temperature, and electromagnetic profiles. This boundary layer, located in a very narrow zone, close to the hydrodynamical discontinuity (where the zero curent boundary conditions are applied), is the signature of a stabilization of the distribution function at the thermal equilibrium. The boundaries are maintained far enough from the temperature gradient, so that no boundary effect should interfere with its evolution.*

and

$$\left\{\begin{aligned} p \;&=\; n_e\,T_e \;=\; \frac{1}{3}\,m_e\,n_e\langle\,(\mathbf{v} - \langle\mathbf{v}\rangle\,)\,\cdot\,(\mathbf{v} - \langle\,\mathbf{v}\,\rangle\,)\,\rangle, \\ \mathbf{\Pi} \;&=\; \frac{1}{3}\,m_e\,n_e\,\langle\,(\mathbf{v} - \langle\mathbf{v}\rangle\,)\otimes(\,\mathbf{v} - \langle\mathbf{v}\rangle\,)\,\rangle \;-\; p\,\mathbf{I}, \\ \mathbf{q_{loc}} \;&=\; \frac{1}{2}\,m_e\,n_e\langle\,[\,(\,\mathbf{v} - \langle\mathbf{v}\rangle\,)\,\cdot\,(\mathbf{v} - \langle\mathbf{v}\rangle)\,]\,(\,\mathbf{v} - \langle\mathbf{v}\rangle\,)\,\rangle, \end{aligned}\right. \tag{5.28}$$

where **j** is the electric current, **q** the total heat flow, **R** the friction force accounting for the transfer of momentum from ions to electrons in collisions, T_e is the temperature, p is the scalar intrinsic pressure, $\mathbf{\Pi}$ is the stress tensor, $\mathbf{q_{loc}}$ is the intrinsic heat flow and **I** the unit diagonal tensor.
Quantities p, $\mathbf{\Pi}$ and $\mathbf{q_{loc}}$ are defined in the local reference frame of the electrons, whereas **j**, **q** and **R** are defined relative to the ion center of mass frame. Ions are supposed to be at rest. We have the relation

$$\mathbf{q_{loc}} \;=\; \mathbf{q} + \mathbf{j}\,\cdot\,\frac{5\,p\,\mathbf{I} \;+\; 2\,\mathbf{\Pi}}{2\,n_e\,e} \;+\; \mathbf{j}\,\frac{m_e\,n_e\langle\mathbf{v}\rangle^2}{2\,n_e\,e}. \tag{5.29}$$

The validation of our Fokker-Planck-Landau solver in the domain close to the hydrodynamic regime (local regime) requires knowledge of the transport coefficients. Following the formalism of Braginskii [5] for the transport relations, the transport coefficients in the hydrodynamic regime have been calculated by Epperlein in [15]. These coefficients $\alpha_{\mathbf{ep}}$, $\beta_{\mathbf{ep}}$, $\kappa_{\mathbf{ep}}$, are the electrical resistivity, thermoelectric and thermal conductivity tensors, respectively. From these quantities, we are able to compare the heat flux and the electric field issued from the Fokker-Planck solver to those calculated analytically in [15], in the local regime.

The classical derivation procedure to obtain the transport coefficients involves the linearization of the Fokker-Planck-Landau equation, assuming the plasma to be close to the thermal equilibrium. The distribution function is approximated using a truncated Cartesian tensor expansion

$$f(t,\mathbf{x},\mathbf{v}) \;=\; f^{(0)}(||\mathbf{v}||^2) \;+\; \frac{\mathbf{v}}{||\mathbf{v}||}\cdot\mathbf{f^{(1)}}(t,\mathbf{x},||\mathbf{v}||).$$

Following [15], $\mathbf{\Pi}$ and $m_e\,n_e\langle\mathbf{v}\rangle^2$ are neglected and we consider appropriate velocity moments of $\mathbf{f^{(1)}}$, electric fields and heat fluxes are expressed as a function of thermodynamical variables. The coefficients of proportionality, in the obtained relations, are defined as the transport coefficients. Several notations can be used, depending on the chosen thermodynamical variables. Adopting the Braginskii notations, we obtain

$$\left\{\begin{aligned} \mathbf{R} \;&=\; \nabla p \;+\; e\,n_e\,\mathbf{E} \;-\; \mathbf{j}\times\mathbf{B} \;=\; \frac{\alpha_{\mathbf{ep}}\cdot\mathbf{j}}{n_e e} \;-\; \beta_{\mathbf{ep}}\cdot\nabla T_e, \\ \mathbf{q} \;&=\; -\frac{5}{2}\,\frac{\mathbf{j}}{e}\,T_e \;-\; \kappa_{\mathbf{ep}}\cdot\nabla T_e \;-\; \beta_{\mathbf{ep}}\cdot\mathbf{j}\,\frac{\mathbf{T_e}}{e}. \end{aligned}\right. \tag{5.30}$$

We want to compare of the results of the solver with the analytical electric fields and heat fluxes in the local regime. For that purpose, we use the values of coefficients, for $Z = 1$, that are tabulated in [15].

As for the components of these tensors, we make use of the standard notations $\|$, $\perp$, and $\wedge$. Directions denoted with $\|$ and $\perp$ are respectively parallel and perpendicular to the magnetic field. Consequently, the parallel and perpendicular components of a vector $\mathbf{u}$ are respectively $u_{\|} = \mathbf{b}\,(\mathbf{u}\cdot\mathbf{b})$ and $u_{\perp} = \mathbf{b}\times(\mathbf{u}\times\mathbf{b})$, where $\mathbf{b}$ is the unit vector in the direction of the magnetic field. The direction defined by the third direction in a direct orthogonal frame is denoted by $\wedge$. In the system (5.30), the relation between any transport coefficient tensor φ and vector $\mathbf{u}$ is defined by

$$\varphi\cdot\mathbf{u} \;=\; \varphi_{\|}\,\mathbf{b}\,(\mathbf{b}\cdot\mathbf{u}) \;+\; \varphi_{\perp}\,\mathbf{b}\,\times\,(\mathbf{u}\times\mathbf{b}) \;\pm\; \varphi_{\wedge}\,\mathbf{b}\times\mathbf{u}\,, \tag{5.31}$$

where the negative sign applies only in the case $\varphi = \alpha_{\mathbf{ep}}$.

These coefficients can be expressed in dimensionless form

$$\left\{\begin{aligned} \alpha^{\mathbf{c}}_{\mathbf{ep}} &= \alpha_{\mathbf{ep}}\,\frac{\tau}{m_e\,n_e},\\ \beta^{\mathbf{c}}_{\mathbf{ep}} &= \beta_{\mathbf{ep}},\\ \kappa^{\mathbf{c}}_{\mathbf{ep}} &= \kappa_{\mathbf{ep}}\,\frac{m_e}{n_e\,\tau\,T_e}. \end{aligned}\right. \tag{5.32}$$

The dimensionless transport coefficients $\alpha^{\mathbf{c}}_{\mathbf{ep}}, \beta^{\mathbf{c}}_{\mathbf{ep}}, \kappa^{\mathbf{c}}_{\mathbf{ep}}$ are functions of Z and the Hall parameter $\chi = \omega_c\tau$ only.
The heat flux and the electric field in (5.30) can then be rewritten in terms of dimensionless quantities, for the particular 1D geometry of our temperature gradient configuration. In that case, the scaling using a collision frequency (5.41)-(6.17) is used.

$$\left\{\begin{aligned} q_1 &= -\frac{5}{2}\,T_e\,n_e^{-1}\,j_1 - \chi\,T_e\,B_3^{-1}\nabla_{x_1}T_e\,\kappa^{\mathbf{c}}_{\mathbf{ep},\perp} - T_e\left(\beta^{\mathbf{c}}_{\mathbf{ep},\perp}\,j_1 - \beta^{\mathbf{c}}_{\mathbf{ep},\wedge}\,j_2\right),\\ q_2 &= -\frac{5}{2}\,T_e\,n_e^{-1}\,j_2 - \chi\,T_e B_3^{-1}\nabla_{x_1}T_e\,\kappa^{\mathbf{c}}_{\mathbf{ep},\wedge} - T_e\left(\beta^{\mathbf{c}}_{\mathbf{ep},\perp}\,j_2 + \beta^{\mathbf{c}}_{\mathbf{ep},\wedge}\,j_1\right),\\ E_1 &= n_e{}^{-1}\,j_2\,B_3 - n_e^{-1}\,\nabla_{x_1}\,p - \nabla_{x_1}T_e\beta^{\mathbf{c}}_{\mathbf{ep},\perp} + n_e{}^{-1}\,B_3\chi^{-1}\,(\alpha^{\mathbf{c}}_{\mathbf{ep},\perp}\,j_1 + \alpha^{\mathbf{c}}_{\mathbf{ep},\wedge}\,j_2),\\ E_2 &= -n_e{}^{-1}\,j_1\,B_3 - \nabla_{x_1}T_e\beta^{\mathbf{c}}_{\mathbf{ep},\wedge} + n_e{}^{-1}\,B_3\chi^{-1}\,(\alpha^{\mathbf{c}}_{\mathbf{ep},\perp}\,j_2 - \alpha^{\mathbf{c}}_{\mathbf{ep},\wedge}\,j_1). \end{aligned}\right. \tag{5.33}$$

The Hall parameter χ is expressed in terms of the dimensionless quantities B_3 and T_e:

$$\chi \;=\; \frac{3\,\sqrt{\pi}}{2\,\sqrt{2}}\,\frac{B_3\,T_e^{3/2}}{Z}. \tag{5.34}$$

We denote by $\mathbf{Q_{BR}}$ the heat flux and by $\mathbf{E_{BR}}$ the electric field computed from the system (5.33). The transport coefficients $\alpha_{\mathbf{ep}}, \beta_{\mathbf{ep}}, \kappa_{\mathbf{ep}}$ have been tabulated in [15] and will be compared with those obtained by our numerical solution approaching the kinetic FPL equation (6.18).

Let us note that in this configuration source terms can be considered stiff; the discretization of the collision operator is then of crucial importance and its accuracy can be tested. Moreover we provide, in this local regime, with validation results for a wide range of Hall parameters corresponding to ICF

applications.
The initial temperature gradient $T_e(x_1)$ has the form of a step

$$T_e(x_1) = \begin{cases} T_e^R(x_1) & \text{if} \quad x_1 > x_1^m \,, \\ \\ T_e^L(x_1) & \text{else} \,, \end{cases} \tag{5.35}$$

where T_e^R and T_e^L are third order polynomials in $x_1 - x_1^m$, x_1 standing for the space coordinate and x_1^m for the mid-point of the 1D domain. The coefficients of these polynomials are chosen such as they verify the following conditions at x_1^m

$$\begin{cases} \dfrac{\partial T_e^L}{\partial x_1}(x_1^m) = \dfrac{\partial T_e^R}{\partial x_1}(x_1^m) = \dfrac{T_R - T_L}{(x_1^R - x_1^L)/\lambda}, \\ \\ T_e^L(x_1^m) = T_e^R(x_1^m) = \dfrac{T_R + T_L}{2}, \end{cases} \tag{5.36}$$

and at the boundaries

$$\begin{cases} T_e^L(x_1^L) = T_L, \\ \\ T_e^R(x_1^R) = T_R, \\ \\ \dfrac{\partial T_e^L}{\partial x_1}(x_1^L) = \dfrac{\partial T_e^R}{\partial x_1}(x_1^R) = 0, \end{cases} \tag{5.37}$$

where T_L (resp. T_R) is the initial temperature of the leftmost (resp. rightmost) point x_1^L (resp. x_1^R) of the domain. Here, λ is a parameter that determines the initial stiffness of the temperature gradient.

The simulations are performed with the following parameters: the size of the dimensionless domain $L = x_1^R - x_1^L = 5400$, $2 \times v_{max} = 12$, the ion charge $Z = 1$, the frequency ratio $\nu_{e,i}/\omega_{pe} = 0.01$, the electron thermal velocity such as $v_{th}/c = 0.05$. The magnetic field is found from the Maxwell equations; the initial values are $B_3(t = 0, x_1) = 0.001, 0.01, 0.1$, or 1. In the test cases in the local regime, any variation to this initial value proved to be negligible. The initial electric field is zero over the domain: $E_1(t = 0, x_1) = E_2(t = 0, x_1) = 0$. The initial distribution function is a Maxwellian function depending on the local temperature, with a density that is constant over the domain. The initial temperature profile is chosen such as $T_L = 0.8$, $T_R = 1.2$ and $\lambda = 10$. This set of parameters enables us to consider the local regime, close to the hydrodynamic limit (the Knudsen number is about $1/500$). The second order scheme is used for the transport terms in the x_1, v_1, v_2 and v_3 directions. The dimensionless time step and mesh size are $\Delta t = 1/500$, $\Delta x_1 = L/126$, $\Delta v = 2v_{max}/32$ respectively. The grid has 126 points in space and 32^3 points in velocity; 42 processors were used for each simulation (CEA-CCRT-platine facility). The domain decomposition on the space domain allows each processor to deal only with 3 points in space. The fourth order scheme is used for the space and velocity transport terms. The zero current boundary condition is written explicitly in Section 3.3.4. The boundary conditions for fields are chosen with ghost points at their initial value (zero for the electric field and $0.001, 0.01, 0.1$, or 1 for the magnetic field. The results are presented in Figures 5.2-5.4. The typical run time is 24 hours for 40 collision times, with that set of parameters. The maximum difference between the numerical and the analytical solution is less than 10% for longitudinal macroscopic quantities (heat flux and electric field); 20% for transverse ones. Transverse quantities have only been considered for simulations presented in Figures 5.3 and 5.4 where the magnetic field was strong enough so that

- The transverse heat flux can attain its asymptotic value during the simulation time.
- transverse quantities have the value comparableto the longitudinal ones.

These conditions are fulfilled for $B_3 = 0.1, 1$.
In Figures 5.2-5.4, the results for simulations with $B_3 = 0.001$, $B_3 = 0.1$, $B_3 = 1$ are shown, respectively. The simulation with $B_3 = 0.01$ proved to show no significant differences with those with $B_3 = 0.001$.

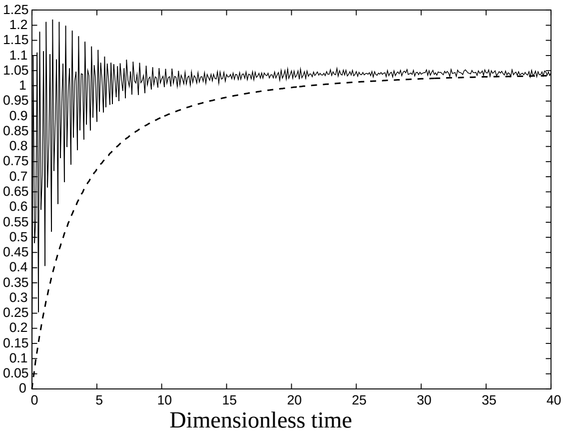

Figure 5.2: *The longitudinal (along the temperature gradient) heat flux ratio* $\frac{\max_{x_1}(Q_{FP})}{\max_{x_1}(Q_{BR})}$ *(dashed curve) and electric field ratio* $\frac{\max_{x_1}(E_{FP})}{\max_{x_1}(E_{BR})}$ *(oscillating curve) are shown against the dimensionless time. The dimensionless magnetic field is* $B_3 = 0.001$. *Asymptotic behavior, where the flux is well established, shows good agreement (less than* 5% *error) with analytical solution (Braginskii formalism), denoted by subscript BR.*

The numerical results are shown Figures 5.2-5.4 : a transient phase is observed before attaining a stationary regime. The oscillations are enforced by the magnetic field as it is observed in Figure 5.4, whereas the oscillations of electric fields are the signature of the plasma waves excited by the initial conditions. Then, these oscillations are damped in a few electron-ion collision times. These plasma oscillations are smoothed out by the large time steps we used in simulations, permitted by the implicit treatment of the Maxwell equations. However, these oscillations have a little importance on the asymptotic values and a little importance for accuracy. With a larger magnetic field, Figure 5.4, we observe frequency modulations at $\omega_c = \nu_{e,i}$ (corresponding to $B_3 = 1$), both in electric fields and heat fluxes. The total energy is conserved with a 0.1% accuracy in the case $B_3 = 0.001$, and with a 1% accuracy with $B_3 = 1$. The total density is conserved with accuracy of 0.01%.

In order to investigate Larmor rotation effects for simulations presented in Figures 5.3 and 5.4, we refined the space grid below the dimensionless Larmor radius $r_L = B_3^{-1}$. Thus the simulation presented in Figure 5.3 was repeated with the same parameters on the same time period: we have refined the grid

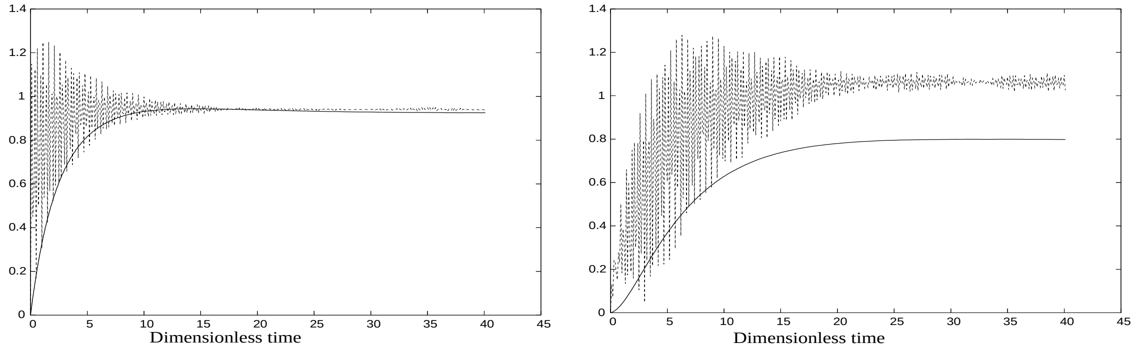

(a) Longitudinal (b) Transverse

Figure 5.3: *Longitudinal (a) and tranverse (b) heat flux* $\frac{\max_{x_1}(Q_{FP})}{\max_{x_1}(Q_{BR})}$ *(curve in bold) and electric field* $\frac{\max_{x_1}(E_{FP})}{\max_{x_1}(E_{BR})}$ *(dashed curve) are shown against the dimensionless time. Longitudinal quantities (along the temperature gradient) agree with the theoritical values with about* 10% *accuracy in the asymptotics. Transverse quantities agree with the theory with about* 20% *accuracy in the asymptotics. The dimensionless magnetic field is* $B_3 = 0.1$.

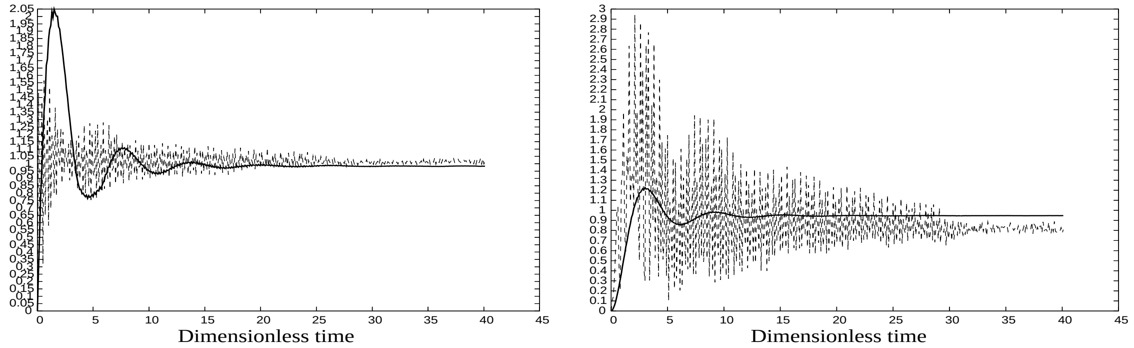

(a) Longitudinal (b) Transverse

Figure 5.4: *Longitudinal (a) and transverse (b) heat flux* $\frac{\max_{x_1}(Q_{FP})}{\max_{x_1}(Q_{BR})}$ *(curve in bold) and electric field* $\frac{\max_{x_1}(E_{FP})}{\max_{x_1}(E_{BR})}$ *(dashed curve) are shown against the dimensionless time. Longitudinal quantities (along the temperature gradient) agree with the theoritical values with about* 5% *accuracy in the asymptotics. Transverse quantities agree with the theory with about* 20% *accuracy in the asymptotics. The dimensionless magnetic field is* $B_3 = 1$.

to 1260 points in space (420 processors). In the same manner, the simulation presented in Figure 5.4 has been repeated with 6300 grid points in space (2100 processors) and $\Delta t = 1/1000$ (according to the CFL condition), during the same time period. The results prove to be similar to those with coarse space grids, both for macroscopic quantities and for the distribution functions. Thus no dependence on the Larmor radius is found. We recall here that the cyclotron period is always resolved, as the time steps are constrained by the CFL condition on the collision operators. The positivity property is always maintained.

5.3.3 Test 2 : Electron transport in the nonlocal regime without magnetic fields

Here, we consider configurations that present Knudsen parameters up to $Kn \simeq 1$. Therefore, we observe the behavior of the transport coefficients far from the hydrodynamic regime. These coefficients are normalized with the coefficients in the Spitzer-Härm regime, denoted by the subscript SH. The Spitzer-Härm regime is the hydrodynamic regime, with a zero magnetic field. Then it is possible to evaluate directly the ratio of effective thermal conductivity to the Spitzer-Härm conductivity, κ/κ_{SH}, by the relation:

$$\frac{\kappa}{\kappa_{SH}} = \frac{q_1}{q_{SH}}, \tag{5.38}$$

where q_1 is the heat flux in the x_1 direction. It is calculated from the numerical solution and q_{SH} from (5.33) in the Spitzer-Härm limit.

Transport coefficients are extracted from the domain where the flux and temperature gradient attain their maximum values. The effective Knudsen number, characterized by the wavelength of the temperature perturbation $k\lambda_{e,i}$ in the Fourier space, is computed from the gradient temperature profile. This enables us to evaluate a range for $k\lambda_{e,i}$ (due to an uncertainty for the estimation of $k\lambda_{e,i}$ in the $1D_{\mathbf{x}}$ space), corresponding to this temperature gradient. The results are compared with the analytical formula from [16]

$$\frac{\kappa}{\kappa_{SH}} = \frac{1}{1 + (30\, k\, \lambda_{e,i}\, \beta)^{4/3}}, \tag{5.39}$$

$$\beta = \left(\frac{3\pi}{128} \frac{3.2(0.24 + Z)}{(1 + 0.24\, Z)} \right)^{1/2} \frac{Z^{1/2}}{2}. \tag{5.40}$$

This formula has been obtained by a fit of data issued from the Fokker-Planck solver SPARK [16]. While considering the comparison between the numerical results and the analytical solution shown in Table 5.1, one should keep in mind that the test procedure involves a large domain of uncertainty. Three runs have been performed with the same precision for the temperature gradient. The CFL conditions are respected, maintaining the positivity of the distribution function.

5.3.4 Test 3: Electron transport in the nonlocal regime perpendicularly to the magnetic field

The objective of this section is to illustrate a competition between the nonlocal and magnetic effects on the distribution function. More precisely, we consider a situation where the Knudsen number $Kn \simeq 1/10$.

Table 5.1: Comparison between the numerical results and the analytical solution.

Parameters	RUN1	RUN2	RUN3
Size of the domain	5400	540	540
Stiffness parameter λ	10	10	100
Number of points along the Gradient	126	126	1260
Number of processors	42	42	420
Results			
$k\lambda_{e,i}$	10^{-3}	0.05 ± 0.03	0.2 ± 0.1
Analytical κ/κ_{SH}	0.998	[0.93 – 0.67]	[0.60 – 0.26]
Numerical κ/κ_{SH}	1.03	0.675	0.395

This corresponds to a situation with a stiffness parameter $\lambda = 100$. The $1D$ domain goes from 0 to $L = 540$, the grid has 1260 points in space, 420 processors were used for each simulation (10 collision times), during 6 hours. Other parameters are kept identical to those in the test cases in the local regime. Two cases are distinguished, respectively with weak magnetic fields effects, $\omega_c/\nu_{ei} = 10^{-2}$ (see Figures 5.6 and 5.7(a)), and strong magnetic fields effecs, $\omega_c/\nu_{ei} = 1$ (see Figures 5.5(b) and 5.7(b)). The magnetic field is calculated from the Maxwell equations; no more than 0.1% departure from their initial value is encountered after 10 collision times. The positivity of the distribution function is maintained, and the CFL conditions are satisfied. In Figures 5.5 and 5.6, the averaged distribution function is shown in the region of the temperature gradient

$$\sum_{j_2,j_3} f_e(t, x_1, v_{j_1}, v_{j_2}, v_{j_3}) \ ,$$

The initial distribution function, Figure 5.5(a), is a Maxwellian function with a temperature that depends on the space variable x_1. It is symmetric in the v_1 direction. After 10 collision times, for the simulation with $\omega_c/\nu_{ei} = 10^{-2}$, Figure 5.6, the distribution function keeps the same structure for the bulk electrons. Only the structure for the fastest electrons is modified. The fast electron population with positive velocities is depleted in the hot side of the temperature gradient, whereas the fast electron population with negative velocities is enforced, contributing to smoothing of the temperature gradient and heating of the bulk. These nonlocal effects are important, because the main contribution to the heat flux comes from the fastest particles.

The same distribution fonction is shown in Figure 5.5(b), at the same time, but for a simulation with a strong magnetic field $\omega_c/\nu_{ei} = 1$. The distribution fonction is here stronger localized. This means that the magnetic field tends to inhibit the electron transport, while forcing the Larmor rotation of electrons.

In order to gain more insight in the processes at stake, we show in Figure 5.7 the quantity

$$\sum_{j_2,j_3} \left[f_e(t, x_1, v_{j_1}, v_{j_2}, v_{j_3}) - f_e(t, x_1, -v_{j_1}, v_{j_2}, v_{j_3}) \right] \ ,$$

which is odd in the variable v_{j_1}. It accounts for the asymmetries between the positive and negative velocities, along the direction v_1, and contributes to the heat flux and the current. We observe that the fast population contributes to the total current with a negative sign, whereas the bulk population contributes to the return current, with a positive sign. Comparing Figures 5.7(a) and 5.7(b), we observe that the assymetries are strongly re-localized in the region of the temperature gradient, with a strong magnetic field.

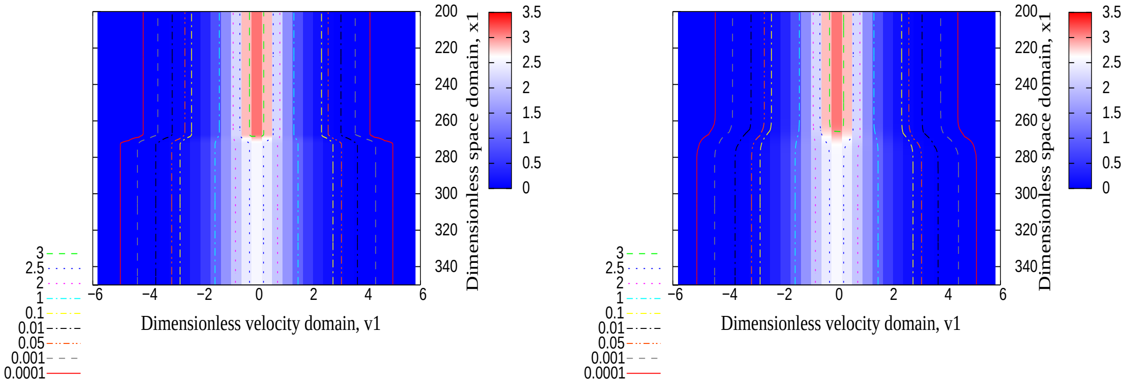

(a) $t\nu_{ei} = 0$ (b) $t\nu_{ei} = 10$, $\omega_c/\nu_{ei} = 1$

Figure 5.5: *Averaged distribution function in the* v_2 *and* v_3 *directions, in the region of the temperature gradient, at initial time (a), and at* $t\nu_{ei} = 10$ *(b), for a simulation with* $\omega_c/\nu_{ei} = 1$.

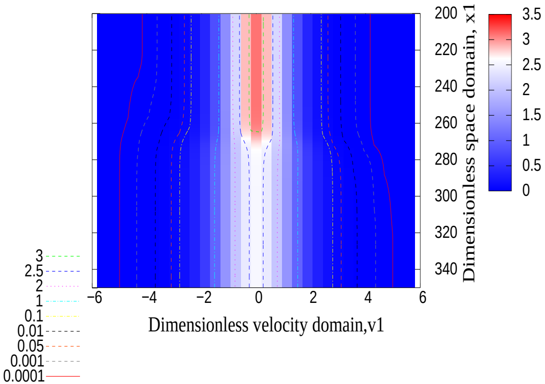

$t\nu_{ei} = 10$, $\omega_c/\nu_{ei} = 10^{-2}$

Figure 5.6: *Averaged distribution function in the* v_2 *and* v_3 *directions, in the region of the temperature gradient, at* $t\nu_{ei} = 10$*, for a simulation with* $\omega_c/\nu_{ei} = 10^{-2}$.

5.3.5 Test 4: 2D nonlocal magnetic field generation

We present here results on the nonlocal magnetic field generation in the relaxation of cylindrical laser hot spots, having a periodic structure, in a plasma with an initial constant density. This stands as a first step to prove the $2D_{\mathbf{x}}$ capabilities of the solver, and also as a comparison in the nonlocal regime with a model from the literature [6]. The extension of the present numerical schemes is straightforward on a $2D_{\mathbf{x}}$ grid. The fourth order scheme is used for the transport terms in the x_1, x_2, v_1, v_2 and v_3 directions.

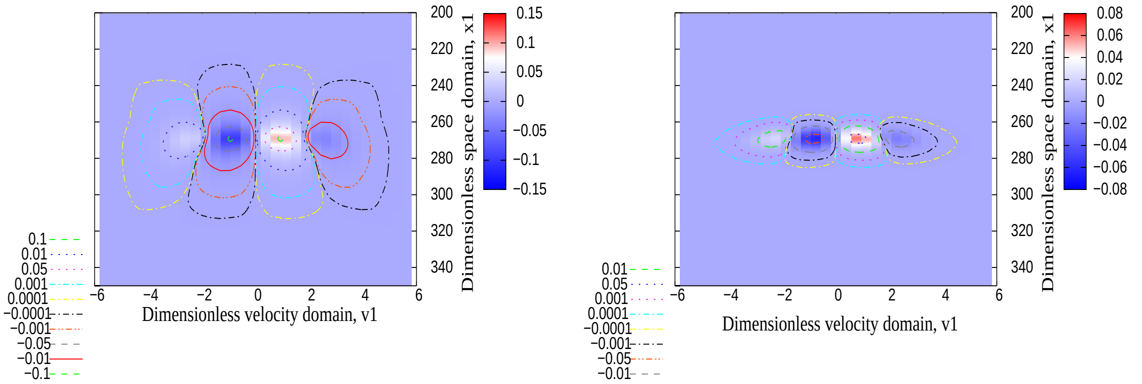

(a) $t\,\nu_{ei} \;=\; 10,\, \omega_c/\nu_{ei} = 10^{-2}$ (b) $t\,\nu_{ei} \;=\; 10,\, \omega_c/\nu_{ei} = 1$

Figure 5.7: *The quantity* $\sum_{j_2,j_3}\left[f_e(t,x_1,v_{j_1},v_{j_2},v_{j_3}) - f_e(t,x_1,-v_{j_1},v_{j_2},v_{j_3})\right]$ *is shown, in the region of the temperature gradient, at the same time* $t\,\nu_{ei} \;=\; 10$*, for* $\omega_c/\nu_{ei} = 10^{-2}$ *in panel (a), and* $\omega_c/\nu_{ei} = 1$ *in panel (b). It corresponds to the odd part of the distribution function.*

We consider a planar geometry with periodic boundary conditions for the distribution function and fields. For this application, the scaling using a collision frequency (5.41)-(6.17) is used. The initial dimensionless temperature profile is

$$T_e(\mathbf{x}, t = 0) \;=\; 1 \;+\; 0.12\, \exp\left(-\frac{\mathbf{x}^2}{R^2}\right),$$

with $R \;=\; 5.6$. We used the following parameters for the simulation: the frequency ratio is $\nu_{e,i}/\omega_{pe} \;=\; 0.003$, the ion charge is $Z = 5$. We do not consider here the electron-electron collision operator, because the electron-ion collisions dominate. Then the relaxation only acts with electron-ion collisions on the anisotropic part of the distribution function. The electron thermal velocity is such as $v_{th}/c \;=\; 0.05$. These parameters are close to those used in [28]. The size of the simulation domain is $L \;=\; 70$ for one space direction, $2 \times v_{max} \;=\; 12$ for one velocity direction. The initial electric and magnetic fields are zero over the domain. The initial distribution function is a Maxwellian function depending on the local temperature, the initial density being constant over the domain. The dimensionless time step and mesh size are $\Delta t = 1/500$, $\Delta x = \Delta y = L/100$, $\Delta v = 2v_{max}/32$, respectively. The grid has 100^2 points in space and 32^3 points in velocity; 625 processors are used for this simulation. With these parameters, the CFL conditions are satisfied and the distribution function remains positive. The simulation time is 24 hours.

First order process of temperature relaxation

The dominant process that is at play in this test case is the temperature relaxation of the hot spot. In this case the ratio *size of a hot spot / distance between hot spots* is small enough, allowing to consider, at first order, that each hot spot relaxes independently without interaction with neighbors. Therefore we employ the $1D_x$ non-magnetized nonlocal heat transport model [6], to validate this process. This model is designed to take into account nonstationary effects, which account for the dependance of the transport coefficients on time. Two characteristic relaxation regimes are identified in [6], respectively at the hydrodynamic and collisionless kinetic time scale.

Both electron-electron and electron-ion collisions are considered in [6]. Owing the fact that we have chosen $Z = 5$, the electron-electron collisions can be considered negligible in the model [6], for this particular set of parameters.

Figure 5.8 presents the evolution of the maximum of the temperature, obtained from the $2D_{\mathbf{x}} \times 3D_{\mathbf{v}}$ Maxwell-Fokker-Planck-Landau solver and from the model; it shows good agreement. The total mass is exactly preserved and the total energy is preserved with a 0.01% accuracy.

Several theoritical publications [7], [18], [25], [3], consider configurations where magnetic field effects are important.

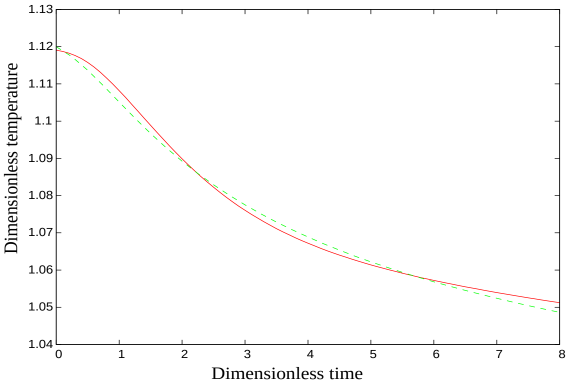

Figure 5.8: Evolution of the maximum of dimensionless temperature. Comparison between the Maxwell-Fokker-Planck-Landau solver (bold, red curve) and the model from [6] (dash, green curve).

Second order process of nonlocal interaction between hot spots

The interaction between hot spots become important if the ratio *size of a hot spot* / *distance between hot spots* is large enough, at a given temperature perturbation. The signature of this interaction is the magnetic field generation, due to the non-azimuthal symmetry, even if the density gradient is zero. This source of magnetic field cannot be described by hydrodynamic models. It is identified in [21] using a nonlocal kinetic description. A nonlocal Ohm's law that is proposed in [21] describes the magnetic field generation in plasma, at a constant density, with an isotropic pressure. A nonlocal source of magnetic field is proportional to the angle between the gradients of the third and fifth moments of the electron distribution function (see Figure 5.9(b)):

$$\frac{\partial \mathbf{B}}{\partial t} \propto \nabla_{\mathbf{x}} \left(\int_{\mathbb{R}^3} f_e ||\mathbf{v}||^3 \mathbf{dv} \right) \times \nabla_{\mathbf{x}} \left(\int_{\mathbb{R}^3} f_e ||\mathbf{v}||^5 \mathbf{dv} \right)$$

Here the lower order term $\nabla_{\mathbf{x}} n_e \times \nabla_{\mathbf{x}} T_e$, standing as a classical source of magnetic field generation, is discarded because of the constant density.

The magnetic field and the cross gradients of high order moments are shown in Figure 5.9, demonstrating a clear similarity. This test case demonstrates that our numerical method provides sufficiently high accuracy and low noise, allowing to recover the second order effects at the level better than 0.01%.

Having in view the scaling law for this mechanism with respect to the temperature perturbation [21]: $\omega_c/\nu_{ei} \propto (\delta T/T)^2$, we conclude that this magnetic field can influence the energy transport, if the temperature perturbation δT is large enough. Therefore, the accurate capture of high order moments by the numerical scheme is crucial for the energy transport.

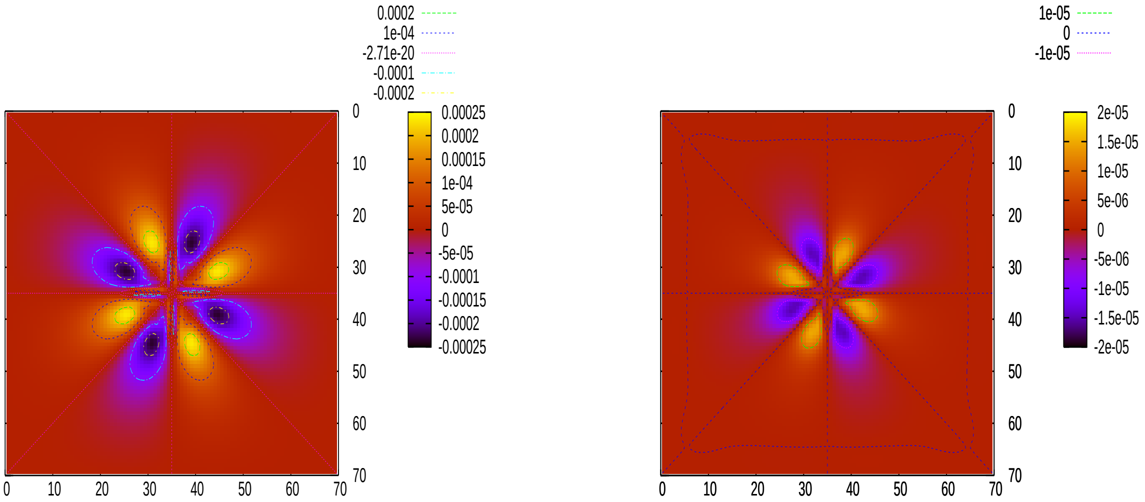

(a) Magnetic field

(b) Cross gradients of high order moments

Figure 5.9: *Dimensionless magnetic field and cross gradients of high order moments (third and fifth) at* $t\nu_{e,i} = 8$.

5.4 Perspectives

As a conclusion for this section, we propose several imporvements that could serve as a research direction line.

First, practically, the average of the discrete electron-ion collision operator in eight uncentrered collision operators, though computationally costly, is more robust than the decomposition in two, forward and backwards, operators [11, 14]. In order to reduce the computational cost, we could derive, for the electron-ion collision operator, a decomposition similar to the one used for the electron-electron collision operator, that is splitted in a centered operator and a viscosity operator.

Second, as far as an implicit treatment is desirable to reach demanding regimes [4, 17, 27, 23, 24] of low temperature/high density regimes faced to large phase space resolution volumes, the issue of positivity is essential. The relevence of implicit schemes in that context is still under debate. Also, if implicit schemes are considered, a multigrid preconditioning relying on frequential decomposition could be interesting.

Finally, automatic coding of implicit schemes should be considered: techniques such as Automatic Differentiation (AD) emerge and become standard . We mention the widely used Tapenade AD code from INRIA.
Third, having in view multi-physics contexts, the implementation of the collision/radiation operators must let free this extension, and, as far as possible, use unsplit techniques. Indeed, if two collision/radiative kernels (Bremsstrahlung, Compton, double Compton, etc) are computed at the same moment, there is a possibility to parallelize these tasks with a “fork and join” technique (OpenMP or MPI-2).
Finally, a sharper validation strategy might be considered that could rely on dimension independant, fully multi-scale techniques, such as the “echography” of codes [19].

Bibliography

[1] Babovski H., *A convergence proof for Nanbu's Boltzmann simulation scheme*, Eur. J. Mech. B/Fluids 8(1), 41, (1989).

[2] Balescu R., *Transport processes in plasmas vol.1 classical transport theory*, (1988).

[3] Bennaceur-Doumaz D., Bendib A., *Nonlocal electron transport in magnetized plasmas with arbitrary atomic number*, Physics of Plasmas, 13, 092308, (2006).

[4] Botchorishvili R., *Implicit Kinetic Schemes for Scalar Conservation Laws*, Rapport de recherche INRIA n3972, M3N project.

[5] Braginskii S. I., *Reviews of plasma physics*, Consultants Bureau, New York, Vol.1, p.205, (1965).

[6] Brantov A. V., Bychenkov V Yu., and Rozmus W., *Relaxation of a Thermal Perturbation in a Collisional Plasma*, Plasma Physics Reports, Vol 32, No 4, pp. 337-343, (2006).

[7] Brantov A. V., Bychenkov V. Yu. et al., *Linear theory of nonlocal transport in a magnetized plasma Plasma Physics Reports* , Physics of Plasmas, Vol.10, Issue 12, pp. 4633-4644, 2003.

[8] Buet C., Cordier S., *Numerical analysis of conservative and entropy schemes for the Fokker-Planck-Landau equation* , Numer. Anal. 36, 953-97, (1999).

[9] Buet C., Cordier S., Degong P., Lemou M., *Fast algorithm for numerical, conservative and entropy approximation of the Fokker-Planck-Landau equation* , J. Comput. Physics 133 310-322, (1997).

[10] Buet C., Cordier S., Filbet F., *Comparison of numerical scheme for Fokker-Planck-Landau equation* , ESAIM Proc. 10 161-181, (1999).

[11] Crouseilles N., Filbet F., *Numerical approximation of collisional plasmas by high order methods*, Journal of Computational Physics, 201, 546-572, (2004).

[12] Decoster A., Markowich P. A., Perthame B., *Modeling of collisions*, Research in applied mathematics, Masson, Paris, (1997).

[13] Degond P., Lucquin-Desreux B., *An entropy scheme for the Fokker-Planck collision operator of plasma kinetic theory*, Numer. Math. 68, 239-262 (1994).

[14] Duclous R., Dubroca B., Filbet F., Tikhonchuk V., High order resolution of the Maxwell-Fokker-Planck-Landau model intended for ICF application , *Journal Comp. Phys.* 228, 14, 5072-5100, (2009).

[15] Epperlein E. M., Haines M. G., *Plasma transport coefficients in a magnetic field by direct numerical solution of the Fokker-Planck equation*, Phys. Fluids 29 (4), (1986).

[16] Epperlein E. M., *Kinetic theory of laser filamentation in plasmas*, Phys. Rev. Letter 65, 2145, (1990).

[17] Epperlein E. M., *Implicit and Conservative Difference Scheme for the Fokker-Planck Equation*, Journal of Computational physics, 112, 291-297 (1994).

[18] Frolov B., Krasheninnikov S. I., Kingham R. J. and Edwards J., *Heat flux calculation in the semi-collisionless regime for substantial temperature variations including magnetic field*, New J. Phys. 8 56, (2006).

[19] Galeotti L., Califano F., Pegoraro F. *Echography of vlasov codes*, Physics Letter A, 355, 4-5, 381-385, 2006.

[20] Greengard L., Rokhlin V., *A fast algorithm for a particle simulation*, J. Comput. Phys., 73, 325, (1987).

[21] Kingham R. J., Bell A. R., *Nonlocal Magnetic-Field Generation in Plasmas without Density Gradients*, Phys. Rev. Letter, 88, 045004, (2002).

[22] Lemou M. *Multipole expansions for the Fokker-Planck-Landau operator*, Numer. Math., 78, 597-618, (1998).

[23] Lemou M., Mieussens L. *Implicit schemes for the Fokker-Planck-Landau equation*, SIAM J. S. C., 27, 3, 809-830, (2004).

[24] Mousseau V. A., Knoll D. A. *Fully Implicit Kinetic Solution of Collisional Plasmas*, Journal of Computational Physics, 136, 308-323, (1997).

[25] Nicolaï Ph. D., Feugeas J.-L., G. P. Schurtz *A practical nonlocal model for heat transport in magnetized laser*, Phys. Plasma, 13, 032701, (2006).

[26] L. Pareshi, G. Russo, G. Toscani, *Fast spectral method for Fokker-Planck-Landau collision operator* , J. Comput. Physics, 165, 216-236, (2000).

[27] Ridgers C. P., Kingham R. J., *Nanosecond time-scale Vlasov-Fokker-Planck laser-plasma simulation in a moving ion background*, High Power Laser Science, Theory and Computation, Central Laser Facility Annual Report, (2005-2006).

[28] V.K. Senecha, A.V. Brantov, V. Yu Bychenkov, V.T. Tikhonchuk *Temperature relaxation in hot spots in a laser-produced plasma*, Phys. Review E, 47, 1, 1998.

5.5 Appendix: Scaling with an electron-ion frequency

For the analysis of collisional processes, a new scaling is introduced here, that allows time steps to be of the order of the electron-ion collision time. In order to take into account transport phenomena occurring at the collision time scale, several parameters are required: the electron-ion collision frequency $\nu_{e,i}$, the associated mean free path $\lambda_{e,i}$, the thermal velocity v_{th}, and the cyclotron frequency ω_{ce}

$$\nu_{e,i} = \frac{Z\, n_0\, e^4\, \ln\Lambda}{8\,\pi\,\epsilon_0^2\, m_e^2\, v_{th}^3}\,, \quad \lambda_{e,i} = \frac{v_{th}}{\nu_{e,i}}\,, \quad v_{th} = \sqrt{\frac{\kappa_B T_0}{m_e}}\,, \quad \omega_{ce} = \frac{eB}{m_e}\,, \tag{5.41}$$

These parameters enable us to define the dimensionless parameters marked with a tilde.

- Dimensionless time, space and velocity, respectively

$$\tilde{t} = \nu_{e,i} t, \quad \tilde{x} = x/\lambda_{e,i}, \quad \tilde{v} = v/v_{th}. \tag{5.42}$$

- Dimensionless electric field, magnetic field, and distribution function, respectively

$$\tilde{E} = \frac{eE}{m_e v_{th} \nu_{e,i}}, \quad \tilde{B} = \frac{eB}{m_e \nu_{e,i}} = \frac{\omega_{ce}}{\nu_{e,i}}, \quad \tilde{f}_e = f_e \frac{v_{th}^3}{n_0}. \tag{5.43}$$

This leads to the following dimensionless equations

$$\begin{cases} \dfrac{\partial f_e}{\partial t} + \nabla_{\mathbf{x}} \cdot (\mathbf{v} f_e) - \nabla_{\mathbf{v}} \cdot ((\mathbf{E} + \mathbf{v} \times \mathbf{B}) f_e) = \dfrac{1}{Z} C_{e,e}(f_e, f_e) + C_{e,i}(f_e), \\ \dfrac{\partial \mathbf{E}}{\partial t} - \dfrac{1}{\beta^2} \nabla_{\mathbf{x}} \times \mathbf{B} = \dfrac{1}{\alpha^2} n\mathbf{u}, \\ \dfrac{\partial \mathbf{B}}{\partial t} + \nabla_{\mathbf{x}} \times \mathbf{E} = 0, \\ \nabla_{\mathbf{x}} \cdot \mathbf{E} = \dfrac{1}{\alpha^2}(1 - n), \\ \nabla_{\mathbf{x}} \cdot \mathbf{B} = 0, \end{cases} \tag{5.44}$$

where $\alpha = \nu_{e,i}/\omega_{pe}$ and $\beta = v_{th}/c$. The collision terms $C_{e,e}(f_e, f_e)$ and $C_{e,i}(f_e)$ are given in (6.19).

Chapter 6

From code validation to realistic simulations: kinetic transport for shock ignition

6.1 Introduction

The general framework of this chapter is the theoretical investigation of the electron energy transport in Inertial Fusion targets, for the shock ignition regime. This program is part of the European project HiPER which aims at demonstrating the feasablity of an Inertial Fusion reactor. This project, if successful, will have a very large societal and economical impact. A new approach to inertial fusion related to the fast ignition of compressed fuel is now being pursued by european scientists, allowing high target gains using moderate laser energies and powers. This approach, known as shock ignition, is still under discussion, and a major, and up to now unsolved issue of this scheme is the conversion of the laser energy into a very high pressure converging shock wave. The efficiency of this conversion mainly relies on the properties of the electron energy transport in plasmas. An important issue is the ability of electron diffusion to smooth out any departure from symmetry of the laser irradiation. Though this subject has been extensively studied in the past decades, it is not perfectly understood, nor acurately modelled in the target design codes. Moreover, the regimes of temperatures and densities specifically encountered in the shock ignition scheme have never been explored so far.

Detailed calculations of electron heat transport require the solution of the Vlasov-Fokker-Planck-Landau equations. The temporal scale of this model is the electron-electron collision frequency, whereas the spatial scale relates to the collision mean free path. These scales are very small as compared to the hydrodynamic time and spatial scale lenghts of an ICF target, so such complete simulations of target implosions where up to now considered as out of reach of state of the art computers and codes.

We propose here to calculate the electron transport on realistic spatial dimensions and physical time by using the recently developped Fokker-Planck codes on high performance computing (HPC) platforms from the GENCI organism. The proposed computational model is representative of shock ignition physics. This work is achieved within the frame of the HiPER project, and benefits from a collaboration between CELIA, Oxford University(UK), and Imperial College(UK). The analysis of the calculations will contribute to our physical understanding and cross calibration of codes from CELIA, Imperial College, and Oxford University. It will help validating reduced models implemented in the design codes.

This chapter sums up the developments that have been performed onto the Vlasov-Fokker-Planck-Landau solver, to reach the regimes of shock ignition. Several representative test for code cross-calibration are also proposed in appendix.

6.2 Specific developments in the reference deterministic solver

To achieve realistic numerical simulation of the electon transport for the shock ignition regime, we have develop several new features of the Vlasov-Fokker-Planck-Landau code. These concern, first the implementation of the laser collisional absorption at low intensity, second the extension of the numerical scheme to non-uniform meshes. These development were required by the configuration of the numerical simulations we have proposed in Appendix 6.8. Finally we mention a technique that could be appropriate to handle with large density gradients, such as those in the shock ignition regime (ranging from $0.1n_c$ to more than $100n_c$). This method relies on a rescaling technique.

6.2.1 $3D_\mathbf{v}$ Langdon IB heating operator derivation

The collisional conversion of the laser energy in the plasma, *via* electron-ion collisions, is called the inverse bremsstrahlung process. It is described by Langdon [22], and is approriate for relatively low intensities, up to 10^{14}-$10^{16}\mathrm{Wcm}^{-2}$. These are typically the laser intensities relevant in the shock ignition regime, at the spike launch.

Weak equivalence relation

We show here an isotropic extension of the Langdon operator to arbitrary distribution functions of the $3D_v$ space, together with a numerical finite volume scheme for its implementation in the deterministic reference code. We finally present some validation tests that show, on the one hand, the accuracy of the implementation, and on the other hand some new interesting features related to this operator.

Proposition 8. *The Langdon Inverse Bremsstrahlung (IB) heating operator [22]*

$$\frac{\partial f_0}{\partial t}(t,v) = \frac{Av_0^2}{3}\frac{1}{v^2}\frac{\partial}{\partial v}\left(\frac{g}{v}\frac{\partial f_0}{\partial v}(t,v)\right) , \tag{6.1}$$

and the $3D_\mathbf{v}$ *operator*

$$\frac{\partial f}{\partial t}(t,\mathbf{v}) = \frac{Av_0^2}{3}\nabla_\mathbf{v}\cdot\left[\frac{g}{v^5}\left[\mathbf{v}\otimes\mathbf{v}\right]\nabla_\mathbf{v} f(t,\mathbf{v})\right] , \tag{6.2}$$

are equivalent, in a weak sense.

Proof. Let us consider the approximation $g(v) = 1$, and the space homogeneous operators having the general form

$$\frac{\partial f}{\partial t}(t,\mathbf{v}) = \alpha\nabla_\mathbf{v}\cdot\left[\Gamma(v)\left[\mathbf{v}\otimes\mathbf{v}\right]\nabla_\mathbf{v} f(t,\mathbf{v})\right] , \tag{6.3}$$

where $\alpha \in \mathbb{R}$, and f has a compact support in the phase space.
Let $\varphi(v)$ be a smooth test function, that must belong in a regular enough space, which will be precised latter on.
The weak form of equation (6.3) can be writen as

$$\int_{\mathbb{R}^3}\frac{\partial f}{\partial t}(t,\mathbf{v})\varphi(v)d^3v = \alpha\int_{\mathbb{R}^3}\left[\beta'(v) + \beta(v)\frac{2}{v}\right] f(t,\mathbf{v})d^3v , \tag{6.4}$$

where $\beta(v) = \Gamma(v)\varphi'(v)v^2$.
Using the isotropic distribution function definition

$$f_0(t, v) \equiv \int_{S^2} f(t, \mathbf{v})d\Omega \ ,$$

a straightforward integration leads to

$$\int_0^\infty \frac{\partial f_0}{\partial t}(t, v)\varphi(v)dv = \alpha \int_0^\infty \left[\beta'(v) + \beta(v)\frac{2}{v}\right] f_0(t, v)v^2 dv \ , \tag{6.5}$$

Finally, the development of equation (6.5) with appropriate defined integrations by parts gives, $\forall\varphi \in \left\{\varphi \in \mathcal{D}(]0, \infty[) \ \big/ \beta'(v)v^2 \in L^1_{loc}(]0, \infty[) \ , \ \Gamma(v)\varphi'(v)v^3 \in L^1_{loc}(]0, \infty[), \right\}$

$$\int_0^\infty \frac{\partial f_0}{\partial t}(t, v)\varphi(v)v^2 dv = \alpha \int_0^\infty \frac{\partial}{\partial v}\left(\Gamma(v)v^4 \frac{\partial f_0}{\partial v}(t, v)\right)\varphi(v)dv \tag{6.6}$$

Finally we obtain the equivalence in the dual space, between the operators (6.3) and (6.7)

$$\frac{\partial f_0}{\partial t}(t, v) = \alpha \frac{1}{v^2}\frac{\partial}{\partial v}\left(\Gamma(v)v^4 \frac{\partial f_0}{\partial v}(t, v)\right) \ . \tag{6.7}$$

This proof applies in the particular case of Inverse Bremsstrahlung, where $\alpha = Av_0^2/3$ and $\Gamma(v) = 1/v^5$.

□

The operator (6.2) can be seen as the $3D_\mathbf{v}$ isotropic extension of the operator (6.1).
Here v_0 is the electron quiver velocity in the laser field, ω is the laser frequency, $\tau_{ei}^{-1} \equiv 2A/v^3$ is the electron-ion scattering rate, v_ω is defined by the relation $\omega\tau_{ei}(v_\omega) = 1$, and $g(v) = \left(1 + \omega^{-2}\tau_{ei}^{-2}(v)\right)^{-2} = \left(1 + v_\omega^6/v^6\right)^{-2}$. Let us consider that the collisions only act as a perturbation on the oscillation of the entire distribution, *i.e.* $\omega\tau_{ei} \gg 1$, then $g = 1$.
This approximation will be used for the numerical evaluation of g.

Finite Volume numerical scheme

Let us consider a uniform, cell-centered, cartesian grid $\left\{\mathbf{v_j} = \left(v_{j_1}, v_{j_2}, v_{j_3}\right)\right\}_{\mathbf{j}\in\mathbb{Z}^3}$ of the velocity space $\mathbb{R}^3$, , such as the point $\mathbf{v} = \mathbf{0}$ is located at a mesh interface. We define $\mathbf{j} = (j_1, j_2, j_3) \in \mathbb{Z}^3$, $\mathbf{e}_k$ the unit vector in the direction k, and $f_\mathbf{j}$ as an approximation of the distribution function $f(\mathbf{v_j})$. The operator (6.2) is rewritten using a conservative formulation

$$\begin{aligned} \frac{\partial f}{\partial t}(t, \mathbf{v}) &= \frac{Av_0^2}{3}\nabla_\mathbf{v} \cdot \mathcal{F} \ , \\ \mathcal{F} &= \left[\frac{g}{v^5}\left[\mathbf{v} \otimes \mathbf{v}\right] \nabla_\mathbf{v} f(t, \mathbf{v})\right] \ . \end{aligned}$$

We use a centered discretization in velocity, together with a forward Euler scheme

$$\frac{f_\mathbf{j}^{n+1} - f_\mathbf{j}^n}{\Delta t} = \frac{Av_0^2}{3} D^c \mathcal{F}_\mathbf{j}^n \ , \tag{6.8}$$

where

$$D^c \mathcal{F}^n_{\mathbf{j}} = \sum_{k=1}^{3} \frac{\mathcal{F}^n_{\mathbf{j+e_k/2}} - \mathcal{F}^n_{\mathbf{j-e_k/2}}}{\Delta v_k} ,$$

$$\mathcal{F}^n_{\mathbf{j+e_k/2}} = \left[\frac{g}{\tilde{v}^5_{\mathbf{j}+\mathbf{e}_k/2}} \left[\mathbf{v}_{\mathbf{j}+\mathbf{e}_k/2} \otimes \mathbf{v}_{\mathbf{j}+\mathbf{e}_k/2} \right] D^c f^n_{\mathbf{j+e_k/2}} \right] ,$$

$$D^c f^n_{\mathbf{j+e_k/2}} \cdot \mathbf{e}_l = \frac{1}{2} \left(\frac{f^n_{\mathbf{j}+\mathbf{e}_k+\mathbf{e}_l} - f^n_{\mathbf{j}+\mathbf{e}_k-\mathbf{e}_l}}{2\Delta v_l} + \frac{f^n_{\mathbf{j}+\mathbf{e}_l} - f^n_{\mathbf{j}-\mathbf{e}_l}}{2\Delta v_l} \right) ,$$

$$\mathbf{v}_{\mathbf{j}+\mathbf{e}_k/2} = \frac{1}{2} \left(\mathbf{v}_{\mathbf{j}+\mathbf{e}_k} + \mathbf{v}_{\mathbf{j}} \right) ,$$

$$\tilde{v}^5_{\mathbf{j}+\mathbf{e}_k/2} = \frac{1}{2} \left(\tilde{v}^5_{\mathbf{j}+\mathbf{e}_k} + \tilde{v}^5_{\mathbf{j}} \right) .$$

N.B. *The IB operator could have also been discretized using the log formulation.*

6.2.2 Validation with self-similar solutions

The numerical scheme is tested against a self-similar solution, presented in [22], such as

$$\begin{aligned} f(t \to \infty, \mathbf{v} = \mathbf{0}) &\propto t^{-3/5} , && (6.9) \\ f(t \to \infty, \mathbf{v}) &= \kappa_1(t) \exp(-\kappa_2(t) v^5) , && (6.10) \end{aligned}$$

where the coefficients $\kappa_i(t), i = 1, 2$ do not depend on the velocity variable.
The self-similar behaviour (6.9) should be accurately described, since $f(t, \mathbf{v} = \mathbf{0})$ controls the Inverse Bremsstrahlung absorption of the laser energy [22]. On the other hand, the super-gaussian velocity dependance (6.10) of the self-similar solution should also be tested.

Isotropic situation: quantitative check

The isotropic behaviour of equation (6.2) is tested with a space homogeneous configuration, that explores the relaxation of a Maxwellian distribution function

$$\mathcal{M}_{n_e,T_e,\mathbf{v}_e} = \frac{n_e}{(2\pi T_e)^{3/2}} e^{-(\mathbf{v}-\mathbf{v}_e)^2/(2T_e)} ,$$

towards a supergaussian state. The Maxwellian has initially a temperature $T_e = 1$, density $n_e = 1$, and drift velocity $\mathbf{v}_e = \mathbf{0}$. 32 velocity points per direction are used, with a truncation of the domain velocity at $v_{max} = \pm 8$. The time steps are chosen such as $\Delta t = 1/100$. The quiver velocity of the electrons is $v_0 = 1$, where the frequency parameter is $A = 1$.
In Figures 6.1-6.2, the self-similar behaviour (6.9)-(6.10) is recovered with high accuracy, as well as the isotropic geometry.

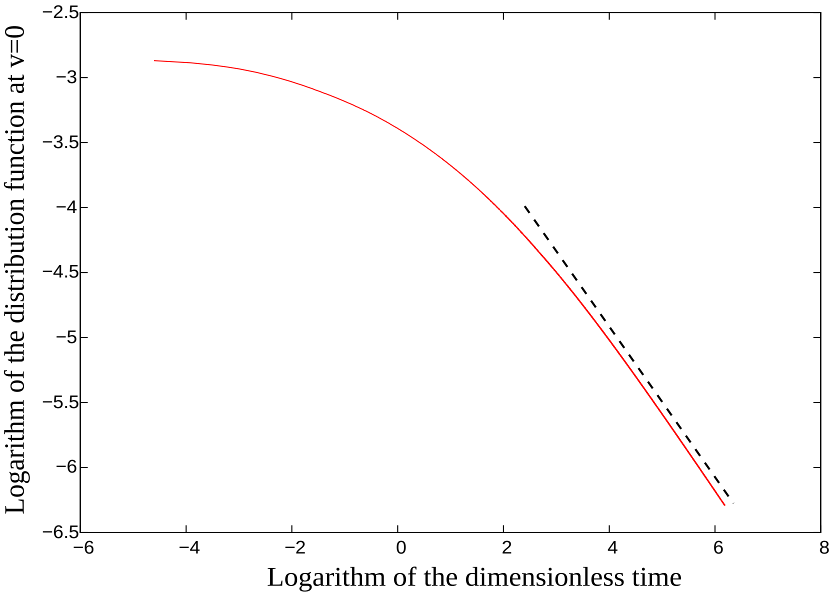

Figure 6.1: *Evolution of* $f(t, \mathbf{v} = \mathbf{0})$*. The dotted black line indicates the* $t^{-3/5}$ *recovered analytic self-similar behaviour, with less than 0.08 % error.*

Anisotropic situation: qualitative check

Let us now introduce a drift velocity $\mathbf{v}_e \propto \mathbf{e}_x$, where $\mathbf{e}_x$ is the unit vector in the x direction.
The other simulation parameters are the same as for the isotropic case. Figure 6.3 demonstrates a correct behaviour of the electronic population having a non-zero drift velocity, and heated *via* Inverse Bremsstrahlung. The fast electron population takes indeed more time to be heated than the slower population.

6.2.3 Extension of the Finite Volume transport scheme to non-uniform cartesian meshes

We present here the basics for an extension of the Finite Volume transport scheme to non-uniform cartesian spatial meshes. This is required by the observed large variations of mean-free-path in the transport region. The main steps for the discretization procedure are listed below.

The conservative discretization of free-transport terms

$$f_i^{n+1} = f_i^n - v\frac{\Delta t}{\Delta x_i}\left(f_{i+1/2}^n - f_{i-1/2}^n\right)$$

The choice for the stencil

The stencil is chosen $\{x_{i-1/2}, x_{i+1/2}, x_{i+3/2}\}$ for positive velocity v, and $\{x_{i-3/2}, x_{i-1/2}, x_{i+1/2}\}$ for negative velocity v [8].

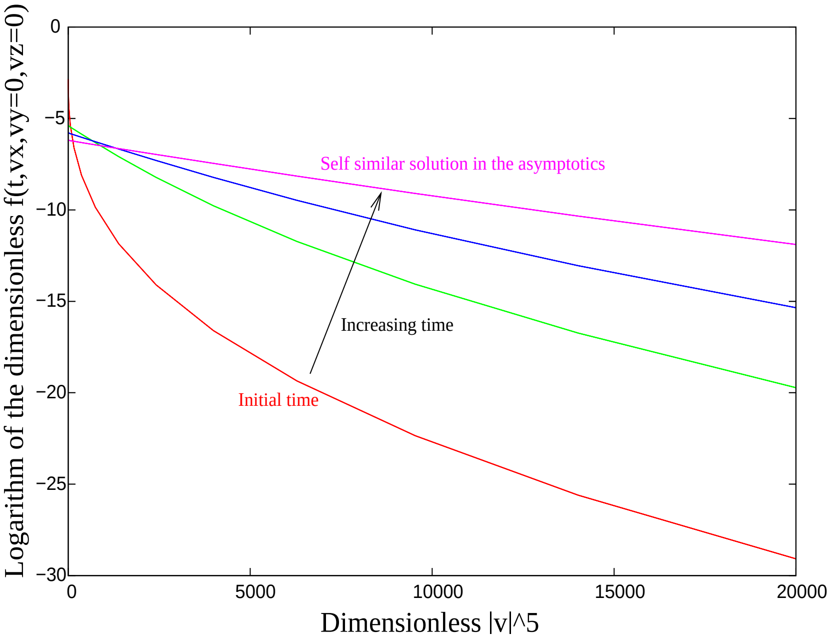

Figure 6.2: *Dimensionless* $f(t, v_x, v_y = 0, v_z = 0)$ *at different times. The final straight line denotes a super-gaussian dependance on the velocity dimension. Negative and positive velocities are surimposed, which shows the perfect conservation of the isotropic geometry at any time.*

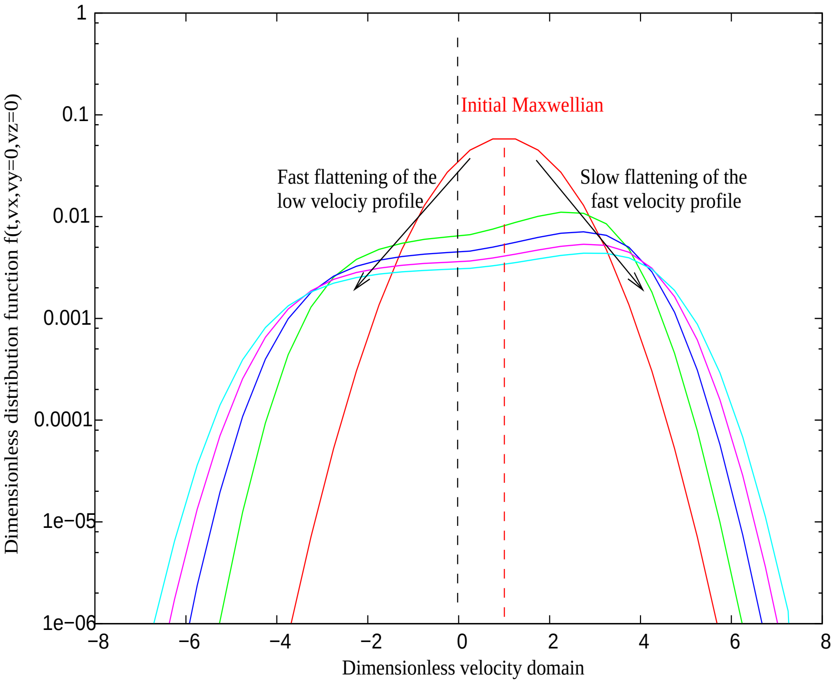

Figure 6.3: *A cut of the distribution function at* $v_y = 0$ *and* $v_z = 0$ *is shown for the anisotropic IB heating of an initial Maxwellian distribution function with non-zero drift velocity.*

The second order flux reconstruction technique "by primitive"

Here we only focus on the case of positive velocity v; the negative velocity case can be deduced by symmety arguments.
The average value in the cell is defined as

$$f_i^n = \frac{1}{\Delta x_i} \int_{x_{i-1/2}}^{x_{i+1/2}} f(t^n, x, v) dx \, .$$

The primitive function F_h should satisfy, on the required stencil,

$$F_h(x_{i+1/2}, v) - F_h(x_{i-1/2}, v) = \Delta x_i f_i^n \, ,$$

$$F_h(x_{i+3/2}, v) - F_h(x_{i+1/2}, v) = \Delta x_{i+1} f_{i+1}^n \, ,$$

$$F_h(x_{i+3/2}, v) = F_h(x_{i-1/2}, v) + \Delta x_i f_i^n + \Delta x_{i+1} f_{i+1}^n \, .$$

These conditions give

$$F_h(x, v) = F_h(x_{i-1/2}, v) + (x - x_{i-1/2}) f_i^n(v) + \frac{(x - x_{i-1/2})(x - x_{i+1/2})}{\Delta x_i + \Delta x_{i+1}} (f_{i+1}^n - f_i^n)$$

and finally the high order reconstruction

$$f_h(x, v) \equiv \frac{\partial F_h}{\partial x}(x, v) = f_i^n + \frac{2x(f_{i+1}^n - f_i^n)}{\Delta x_i + \Delta x_{i+1}} - \frac{x_{i+1/2} + x_{i-1/2}}{\Delta x_i + \Delta x_{i+1}} (f_{i+1}^n - f_i^n) \, .$$

Finally, the standard limiting procedure in Finite Volume MUSCL schemes consists in limiting the slope with a parameter $\nu_i^+ \in [0, 1]$

$$f_h(x, v) = f_i^n + \nu_i^+(v) \frac{(x - x_i)}{0.5(\Delta x_i + \Delta x_{i+1})} (f_{i+1}^n - f_i^n)$$

The limitation procedure

In the case of positive velocity v the slope limiter can be written as

$$\nu_i^+(v) = \begin{cases} 0 \quad \text{if} \quad (f_{i+1}^n - f_i^n)(f_i^n - f_{i-1}^n) < 0 \, , \\ \min\left(1, \dfrac{f_i^n}{f_{i+1}^n - f_i^n} \dfrac{\Delta x_i + \Delta x_{i+1}}{\Delta x_i}\right) \quad \text{elseif} \quad (f_{i+1}^n - f_i^n) > 0 \, , \\ \min\left(1, \dfrac{\left(f_{max}^n - f_i^n\right)}{-(f_{i+1}^n - f_i^n)} \dfrac{\Delta x_i + \Delta x_{i+1}}{\Delta x_i}\right) \quad \text{else} \, . \end{cases}$$

6.3 Arbitrary density/temperature: the rescaling velocity method

In this section, we mention a technique that could be suited to the extreme variations of hydrodynamical quantities in the transport region, and especially for the shock ignition regime. As such, an attractive perspective for handling with arbitrary densities and temperatures is described in [16]. It is based on a rescaling of the distribution function

$$g_e(t,\xi) = {T_e}^{3/2} f_e(t, \mathbf{u}_e + \xi \sqrt{T_e}) \,,$$

where the novel velocity space is rescaled in the electron moving frame $\xi = \dfrac{\mathbf{v} - \mathbf{u}_e}{\sqrt{T_e}}$. T_e is the temperature, $\mathbf{u}_e$ is the mean velocity, and n_e is the density.

This technique permits to preserve, at the discrete level, the collision invariants (mass, momentum and energy), the equilibrium states, of the original discretization of the collision operators, while avoiding the *vacuum problem*, at high density and low temperature, using an adpatative scaling to treat strong variations of the density, velocity, and temperature in space.

This method potentially permits to treat the large density/temperature gradients encountered in the Shock Ignition.

Therefore, with the prescribed variable change, the discretization of the homegeneous equation for electron-electron collisions

$$\frac{\partial f_e}{\partial t} = Q(f_e, f_e) \,, \ \mathbf{v} \in \mathbb{R}^3 \,,$$

is replaced by the discrete resolution of the system:

$$\begin{aligned}
\frac{\partial g_e}{\partial t} - \nabla_\xi \left(T_e^{-1/2} \left((\mathbf{u}_e)' + \left(\sqrt{T_e} \right)' \xi \right) g_e \right) &= {T_e}^{3/2} \tilde{Q}(g_e, g_e) \,, && (6.11)\\
(n_e \mathbf{u}_e)' = \frac{\mathrm{d}\,(n_e \mathbf{u}_e)}{\mathrm{d}t} &= {T_e}^2 \left(\int_{\mathbb{R}^3} \tilde{Q}(g_e, g_e) \xi d^3\xi \right) \,, && (6.12)\\
\left(\sqrt{T_e} \right)' = \frac{\mathrm{d}\sqrt{T_e}}{\mathrm{d}t} &= \frac{{T_e}^{3/2}}{2 \times 3 n_e} \left(\int_{\mathbb{R}^3} \tilde{Q}(g_e, g_e) \xi^2 d^3\xi \right) \,, && (6.13)\\
\tilde{Q}(g_e, g_e) &= Q(f_e, f_e) \,. && (6.14)
\end{aligned}$$

This techniques involves the computation of the collisions in the electron frame, not in the ion frame. Therefore, it is well-suited for the treatment of like particules, but not for electron-ion collisions, because these latter present desirable symmetry properties in the ion rest frame. Similarly, the technique is well-suited only for like electron populations, if a multiscale decomposition between fast and thermal electrons should be considered.

Also, in the particular regimes where self-similar solutions are valid, an analytic decoupling between the ODEs (6.12)-(6.13) and the PDE (6.11) is possible, and would permit a simpler resolution [16].

6.4 Conclusion

In this chapter, we have attempted to adress the issues related to the full scale simulation for transport in the shock ignition regime, with our reference Fokker-Planck-Landau code. We have brougth these elements together, as it could serve for the future transport simulation campaigns. Having this in view, data issued from PIC simulations of collisionless absorbtion of the laser light in the underdense region could be used as input for the transport code. Such data is provided in [21], in the regime of shock ignition.

Despite their accuracy, and owing to their computational cost, the reference calculation need to be completed by longer time scale simulations relying on reduced, faster models. On the other hand reduced model needs to know precisely what are their own limits, which is not trivial. In the next chapter, we step toward this direction.

Bibliography

[1] Bell A. R. and Kingham R. J. , PRL 91 035003, (2003).

[2] Bell A. R., Robinson A.P.L., Sherlock M., Kingham R. J. and Rozmus W. *Fast electron transport in laser-produced plasmas and the KALOS code for solution of the Vlasov-Fokker-Planck equation*, Plasma Physics and controlled fusion, 48, R37-R57, (2006).

[3] Betti R., Zhou C. D., Anderson K. S., Perkins L. J., Theobald W. and Solodov A. A., *Shock ignition of thermonuclear Fuel with High Areal Density*, Physical Review Letter, 98, 155001, (2007).

[4] Betti R., Zhou C. D., Anderson K. S., McKenty P. W., Skupsky S., Shvarts D., Goncharov V. N., Delettrez J. A., Radha P. B., Sangster T. C., Stoeckl C. and Meyerhofer D. D., *Shock ignition of thermonuclear Fuel with High Areal Density*, The fifth International Conference on Inertial Fusion Sciences and Applications (IFSA2007), Journal of Physics: Conference Series 112, 022024, (2008).

[5] Blanchot N., Bignon E., Coïc H., Cotel A., Couturier E., Deschaseaux G. and Forget N., *Multi-petawatt high-energy laser project on the LIL facility in Aquitaine*, Topical Problems of Nonlinear Wave Physics, Proc. SPIE, Vol. 5975, 59750C, (2006).

[6] Brysk H., P. Campbell P. M., Hammerling P., *Thermal conduction in laser fusion* Plasma Phys., 17, 473-484, (1975).

[7] Buet C., Cordier S., Degong P., Lemou M., *Fast algorithm for numerical, conservative and entropy approximation of the Fokker-Planck-Landau equation* , J. Comput. Physics 133, 310-322, (1997).

[8] Crouseilles N., Filbet F., *Numerical approximation of collisional plasmas by high order methods*, Journal of Computational Physics, 201, 546-572, (2004).

[9] Degond P., Lucquin-Desreux B., *An entropy scheme for the Fokker-Planck collision operator of plasma kinetic theory*, Numer. Math. 68, 239-262, (1994).

[10] Delettrez J. A. *et al*, Plasma Phys. Control. Fusion, 47, B791, (2005).

[11] Duclous R., Filbet F., Dubroca B., Tikhonchuck V. T., *High order resolution of the Maxwell-Fokker-Planck-Landau model intended for ICF applications*, 228, 14, pp 5072-5100, (2009).

[12] Duclous R., Filbet F., Dubroca B., *Analysis of a high-order Finite Volume Scheme for the Vlasov-Poisson System*, Submitted, preprint available on Francis Filbet home page (Lyon university).

[13] Dunne M. , Nature, 2, 2, 2006.

[14] Epperlein E. M., Haines M. G., *Plasma transport coefficients in a magnetic field by direct numerical solution of the Fokker-Planck equation*, Phys. Fluids 29 (4), (1986)

[15] Eserkipov, *Private communication*.

[16] Filbet F., Russo G., A rescaling velocity method for kinetic equations: the homogeneous case. *Proceedings Modelling and Numerics of Kinetic Dissipative Systems*, Lipari, Italy, Nova-Science, (2004).

[17] Miyanaga N. *et al.*, Inertial Fusion Sciences and Applications, ed B. Hammel, D. D. Meyerhofe, J. Meyer-ter-Vehn, and H. Azechi, p507, (2003).

[18] Johzaki *Private communication, ILE Osaka*.

[19] Kingham R. J., Bell A. R. *An implicit Vlasov-Fokker-Planck code to model non-local electron transport in 2-D with magnetic fields* Journal of Computational Physics, 194, 1-34, (2004).

[20] Kingham R. J., Bell A. R., *Nonlocal Magnetic-Field Generation in Plasmas without Density Gradients*, Phys. Rew. Letter, 88, 045004, (2002).

[21] Klimo O., Weber S., Tiknonchuk V. T., Limpouch J., *Particle in Cell Simulations of Laser Plasma Interaction in the Shock Ignition Scenario*, submitted to Plasma Phys. Control. Fusion.

[22] Langdon A. B., Nonlinear Inverse Bremsstrahlung and Heated-Electron Distributions, *Phys. Rev. Lett.* 44, 9, (1980).

[23] Lifshitz E. M. and Pitaevskii L. P., Chap 4., Physical Kinetics, Pergamon Press, Oxford, (1981).

[24] Nanbu K. and Yonemura S., J. Comput. Phys. 145, 639, (1998).

[25] Otsuka F., Omura Y., Verkhoglyadova O., Energetic particle parallel diffusion in a cascading wave turbulence in the foreshock region, Nonlin. Processes Geophys., 14, 587-601, (2007).

[26] Ridgers C. P., Thomas A. G. R. and Kingham R. J., Phys. Rev. Lett. **100**, 075003, (2008).

[27] Robinson et al, PRL 100 025002, (2008).

[28] Robinson et al., PPCF 48 1063, 2006

[29] Sangam A., Morreeuw J.-P. , Tikhonchuck V. T. *Anisotropic instability in a laser heated plasma*, Physics of Plasmas 14, 0531111, (2007).

[30] Sentoku Y. et al., J. Phys. IV France 133, 425-427, (2006).

[31] Sentoku Y., Kemp A., *Numerical methods for particle simulations at extreme densities and temperatures: weighted particles, relativistic collisions and reduced currents*, J. Comput. Phys. 227, n^o 14, 6846-6861, (2008).

[32] Takizuka T. and Abe H., J. Comput. Phys. 25, 205, (1977).

6.5 Appendix: Hydrodynamic profiles from CHIC at the spike pulse launch

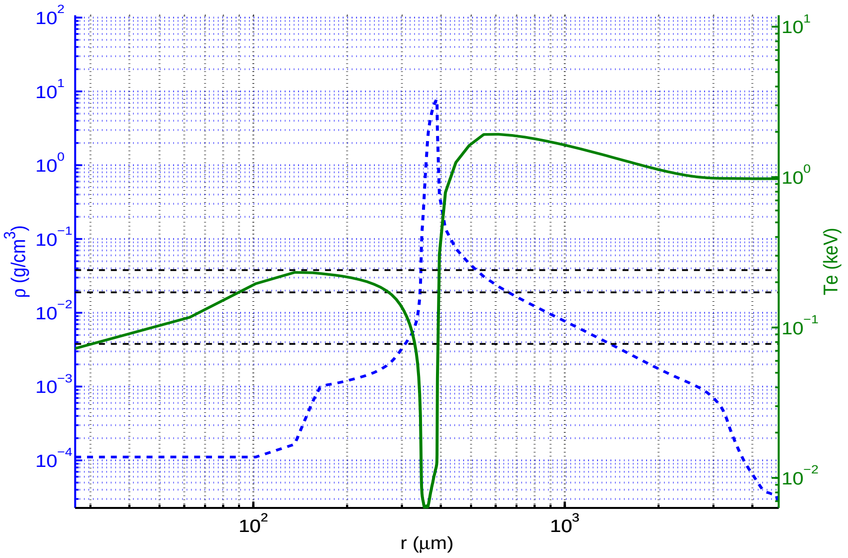

Figure 6.4: *Electronic Density and temperature from hydrodynamic data, over the 1D domain.*

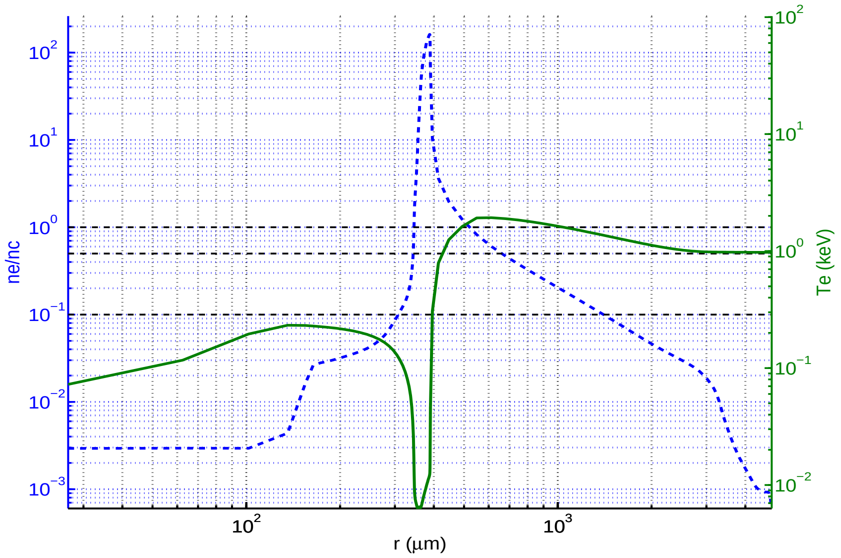

Figure 6.5: *Electronic Density in critical Density units and Temperature from hydrodynamic data, over the 1D domain.*

6.6 Appendix: Profiles fitted from $2D$-ALE hydrodynamic CHIC simulations

Potentially large electric fields may be generated at density discontinuities. Therefore a smooth density profile is required to avoid such an effect, especially if the ion density profile is kept constant, which is the case in our simulations. We choose a C^1 smooth fitting for temperature and density issued from CHIC $2D$ -ALE simulations. With such choice, the electric field can itself present discontinuities, because the fitting does not reach a C^2 smoothness.

Realistic fitted density and temperature profiles are presented at the time when the spike pulse is launched. They are issued from CHIC data, with the convention $n(x = 0) = n_c$. The fitted density profile is

$$n(x) = [0.0008 \times (x + x1)/(0.0029 \times (x + x1 - 7.6))^2]n_c \ ,$$

where $x1 = 2(600 \times \sqrt{36655}) + 115979)/4205$ μm, x is the position in micrometers, $n(x = 10 - x1) \simeq 165n_c$ is the leftmost boundary of the profile, $n(x = 1000 - x1) \simeq 0.0966n_c$ is the rightmost boundary of the profile.

The smooth - in the first dervative- fitted temperature profile (in keV) is

$$\begin{aligned} T_e^{left}(x) &= 0.00005 \times (200 - (x + x1 - 200)^2) + 2 \ , \qquad \text{if } 10 - x1 < x < x2 \ , \\ T_e^{right}(x) &= -0.00072 \times (x - x2) + T_e^{left}(x2) \ , \qquad \text{if } x2 < x < 1000 - x1 \ , \end{aligned}$$

where $x2 = 200 - x1 + 0.00072/(2 \times 0.00005)$ μm.

One may want to cut the density and temperature profiles, or broaden the space domain, while maintaining smooth profiles. To this aim we introduce an arbitrary cut-off position x_{cut} (in micrometers) such as $10 - x_1 \leq x_{cut} < 1000 - x_1$. This defines a cut-off density $n_{cut} = n|_{x_{cut}}$ and temperature $T_{cut} = T|_{x_{cut}}$. We introduce also the arbitrary distance L (in micrometers) as $L = x_{cut} - x_{min}$ and the density jump $\Delta n = n|_{(x_{cut}-L)} - n_{cut}$, where x_{min} is the position (in micrometers) of the leftmost domain boundary, at a prescribed temperature $T_{min} \leq T_{cut}$. We obtain for the corrected density and temperature profiles for $x_{min} \leq x \leq x_{cut}$

$$\begin{aligned} n(x) &= \frac{1}{L^2}\left(\left.\frac{\mathrm{d}n}{\mathrm{d}x}\right|_{x_{cut}} + \frac{2\Delta n}{L}\right)(x - (x_{cut} - L))^3 \\ &- \frac{1}{L}\left(\left.\frac{\mathrm{d}n}{\mathrm{d}x}\right|_{x_{cut}} + \frac{3\Delta n}{L}\right)(x - (x_{cut} - L))^2 + n_{cut} + \Delta n \ , \qquad \text{if } x_{min} \leq x \leq x_{cut} \ , \\ T(x) &= \frac{1}{L}\left[\left.\frac{\mathrm{d}T}{\mathrm{d}x}\right|_{x_{cut}} - \frac{1}{L}(T_{cut} - T_{min})\right](x - (x_{cut} - L))^2 \\ &+ \left[\frac{2}{L}(T_{cut} - T_{min}) - \left.\frac{\mathrm{d}T}{\mathrm{d}x}\right|_{x_{cut}}\right](x - (x_{cut} - L)) + T_{min} \ , \qquad \text{if } x_{min} \leq x \leq x_{cut} \ , \ . \end{aligned}$$

$$\begin{aligned} \left.\frac{\mathrm{d}n}{\mathrm{d}x}\right|_{x_{cut}} &= \frac{0.0008n_c}{(0.0029 \times (x_{cut} + x_1 - 7.6))^2}\left[1 - \frac{2(x_{cut} + x_1)}{(x_{cut} + x_1 - 7.6)}\right] \ . \\ \left.\frac{\mathrm{d}T}{\mathrm{d}x}\right|_{x_{cut}} &= -2 \times 0.00005 \times (x_{cut} + x_1 - 200) \ . \end{aligned}$$

6.7 Appendix: Scaling of the equations

The initial set of equations are, in S.I. Units,

$$\begin{cases} \dfrac{\partial f_e}{\partial t} + \nabla_{\mathbf{x}} \cdot (\mathbf{v} f_e) + \dfrac{q_e}{m_e} \nabla_{\mathbf{v}} \cdot ((\mathbf{E} + \mathbf{v} \times \mathbf{B}) f_e) = C_{e,e}(f_e, f_e) + C_{e,i}(f_e) + C_{\text{brem}}(f_e), \\[2ex] \dfrac{\partial \mathbf{E}}{\partial t} - c^2 \nabla_{\mathbf{x}} \times \mathbf{B} = -\dfrac{\mathbf{j}}{\epsilon_0} \\[2ex] \dfrac{\partial \mathbf{B}}{\partial t} + \nabla_{\mathbf{x}} \times \mathbf{E} = 0, \\[2ex] \nabla_{\mathbf{x}} \cdot \mathbf{E} = q_e(n_e - Z n_i), \\[2ex] \nabla_{\mathbf{x}} \cdot \mathbf{B} = 0, \end{cases} \tag{6.15}$$

where the Fokker-Planck-Landau collision terms $C_{e,e}(f_e, f_e)$ and $C_{e,i}(f_e)$ are given by

$$\begin{cases} C_{e,e}(f_e, f_e) \ = \ \dfrac{e^4 \ln \Lambda(t, \mathbf{x})}{8\pi\epsilon_0^2 m_e^2} \nabla_{\mathbf{v}} \cdot \left(\displaystyle\int_{\mathbb{R}^3} \Phi(\mathbf{v} - \mathbf{v}') \left[f_e(\mathbf{v}') \nabla_{\mathbf{v}} f_e(\mathbf{v}) - f_e(\mathbf{v}) \nabla_{\mathbf{v}'} f_e(\mathbf{v}') \right] \mathbf{dv}' \right), \\[2ex] C_{e,i}(f_e) \ = \ \dfrac{Z^2 n_i(t, \mathbf{x}) e^4 \ln \Lambda(t, \mathbf{x})}{8\pi\epsilon_0^2 m_e^2} \nabla_{\mathbf{v}} \cdot \left[\Phi(\mathbf{v}) \nabla_{\mathbf{v}} f_e(\mathbf{v}) \right], \\[2ex] \Phi(\mathbf{u}) = \dfrac{||\mathbf{u}||^2 \, \mathrm{Id} \ - \ \mathbf{u} \otimes \mathbf{u}}{||\mathbf{u}||^3}. \\[2ex] C_{\text{brem}}(f_e) = \dfrac{A v_0^2(x)}{3} \nabla_{\mathbf{v}} \cdot \left[\dfrac{g}{v^5} \left[\mathbf{v} \otimes \mathbf{v} \right] \nabla_{\mathbf{v}} f(t, \mathbf{v}) \right] \end{cases}$$

For the analysis of collisional processes, a scaling is introduced here, that is appropriate with respect to large time steps, of the order of the electron-ion collision time. In order to account for transport phenomena occuring at the collision time scale, several reference parameters are required: an electron-ion collision frequency $\nu_{e,i}\big|_{n_c}$, an electron-ion collision mean free path $\lambda_{e,i}\big|_{n_c}$, a plasma frequency $\omega_{pe}\big|_{n_c}$, a thermal velocity $v_{th}|_{n_c}$, and a cyclotron frequency ω_{ce}

$$\nu_{e,i}\big|_{n_c} = \sqrt{\frac{2}{9\pi}} \frac{Z \, n_c \, e^4 \, \ln \Lambda_c}{8 \, \pi \, \epsilon_0^2 \, m_e^2 \, v_{th}^3}, \quad \lambda_{e,i}\big|_{n_c} = \frac{v_{th}}{\nu_{e,i}}, \quad \omega_{pe}\big|_{n_c} = \sqrt{\frac{n_c e^2}{\epsilon_0 m_e}},$$

$$\lambda_D|_{n_c} = \sqrt{\frac{\epsilon_0 \kappa_B T_c}{n_c e^2}}, \quad v_{th}|_{n_c} = \sqrt{\frac{\kappa_B T_c}{m_e}}, \quad \omega_{ce} = \frac{eB}{m_e},$$

where $n_c = 9.10^{27}$ m^{-3} is the critical density, T_c is the initial temperature at the critical density point $x_c = 0$. The Coulomb logarithm [6] at that point is

$$\ln \Lambda_c = \max\left(2, \frac{1}{2} \ln\left(1 + \max\left(1, \frac{b_{max}^2}{b_{min}^2}\right)\right)\right),$$

$\ln \Lambda_0 \neq 2$, where $b_{max} = \max\left(\lambda'_D, r_i\right)$, $b_{min} = \max\left(b_{90}, \frac{1}{2}\lambda_{ei-Broglie}\right)$, $b_{90} = \frac{Ze^2}{4\pi\epsilon_0 3k_B T_c}$, $\lambda_{ei-Broglie} = \frac{\hbar}{\sqrt{3}m_e v_{th}}$, $\frac{4\pi}{3}r_i^3 n_i = 1$, $\lambda'_D = \sqrt{\frac{\epsilon_0 \kappa_B \sqrt{T_c^2 + T_{fermi}^2}}{n_c e^2}}$, T_{fermi} is defined from the Fermi energy $E_{fermi} = \frac{\hbar^2}{2m_e}\left(3\pi^2 n_c\right)^{2/3} = \frac{3}{2}k_B T_{fermi}$.
These parameters enable us to define the dimensionless parameters with tilde.

- Dimensionless time, space and velocity, respectively

$$\tilde{t} = \nu_{e,i} t, \quad \tilde{x} = x/\lambda_{e,i}, \quad \tilde{v} = v/v_{th}. \tag{6.16}$$

- Dimensionless electric field, magnetic field, and distribution function, respectively

$$\tilde{E} = \frac{eE}{m_e \, v_{th}|_{n_c} \, \nu_{e,i}\big|_{n_c}}, \quad \tilde{B} = \frac{eB}{m_e \, \nu_{e,i}\big|_{n_c}} = \frac{\omega_{ce}}{\nu_{e,i}\big|_{n_c}}, \quad \tilde{f}_e = f_e \frac{v_{th}|_{n_c}^3}{n_c}. \tag{6.17}$$

This leads to the following dimensionless equations

$$\begin{cases} \dfrac{\partial f_e}{\partial t} + \nabla_{\mathbf{x}} \cdot (\mathbf{v} f_e) - \nabla_{\mathbf{v}} \cdot ((\mathbf{E} + \mathbf{v} \times \mathbf{B}) f_e) = \omega_{ee} C_{e,e}(f_e, f_e) + \omega_{ei} C_{e,i}(f_e) + \omega_{\text{brem}} C_{\text{brem}}(f_e), \\ \dfrac{\partial \mathbf{E}}{\partial t} - \dfrac{1}{\beta^2} \nabla_{\mathbf{x}} \times \mathbf{B} = \dfrac{1}{\alpha^2} n\mathbf{u}, \\ \dfrac{\partial \mathbf{B}}{\partial t} + \nabla_{\mathbf{x}} \times \mathbf{E} = 0, \\ \nabla_{\mathbf{x}} \cdot \mathbf{E} = \dfrac{1}{\alpha^2}(1 - n), \\ \nabla_{\mathbf{x}} \cdot \mathbf{B} = 0, \end{cases} \tag{6.18}$$

where $\omega_{ee} = \sqrt{\frac{9\pi}{2}}\frac{1}{Z}\left[\frac{\ln \Lambda(t, \mathbf{x})}{\ln \Lambda_c}\right]$, $\omega_{ei} = \sqrt{\frac{9\pi}{2}}\left[\frac{\ln \Lambda(t, \mathbf{x})}{\ln \Lambda_c}\right]\left[\frac{n_i(\mathbf{x})}{Zn_c}\right]$, $\omega_{\text{brem}} = \frac{1}{6}\sqrt{\frac{9\pi}{2}}\left(\frac{v_0(x)}{v_{th}|_{n_c}}\right)^2$, $\alpha = \nu_{e,i}\big|_{n_c} / \omega_{pe}\big|_{n_c}$ and $\beta = v_{th}|_{n_c} \big/ c$. $n_i(\mathbf{x})$ is the ionic density. The Fokker-Planck-Landau collision terms $C_{e,e}(f_e, f_e)$ and $C_{e,i}(f_e)$ are given in (6.19)

$$\begin{cases} C_{e,e}(f_e, f_e) = \nabla_{\mathbf{v}} \cdot \left(\displaystyle\int_{\mathbb{R}^3} \Phi(\mathbf{v} - \mathbf{v}') \left[f_e(\mathbf{v}') \nabla_{\mathbf{v}} f_e(\mathbf{v}) - f_e(\mathbf{v}) \nabla_{\mathbf{v}'} f_e(\mathbf{v}') \right] \mathbf{dv}' \right), \\ C_{e,i}(f_e) = \nabla_{\mathbf{v}} \cdot \left[\Phi(\mathbf{v}) \nabla_{\mathbf{v}} f_e(\mathbf{v}) \right], \\ \Phi(\mathbf{u}) = \dfrac{||\mathbf{u}||^2 \, \mathrm{Id} - \mathbf{u} \otimes \mathbf{u}}{||\mathbf{u}||^3}. \\ C_{\text{brem}}(f_e) = \nabla_{\mathbf{v}} \cdot \left[\dfrac{g}{v^5} \left[\mathbf{v} \otimes \mathbf{v} \right] \nabla_{\mathbf{v}} f(t, \mathbf{v}) \right] \end{cases} \tag{6.19}$$

For the sake of simplicity for comparaison between the different solvers, the Coulomb logarithm could be approximated homogeneously as

$$\ln \Lambda(t, \mathbf{x}) \simeq \ln \Lambda_c \ ,$$

without affecting the realism of the simulations (due to the $1/\ln \Lambda$ dependence of the higher order terms in the Fokker Planck developments).

6.8 Appendix: configuration to test and compare the transport codes

In this section, we try to provide simple and realistic test cases, suitable for the shock ignition regime, on which to compare the different transport codes.

6.8.1 Academic test for the transport, with simplified configuration

We propose periodic (or reflective) boundary conditions.
The critical density is $n_c = 9 \times 10^{27}\mathrm{m}^{-3}$. The temperature $T_c = 1\mathrm{keV}$ is homogeneous over the domain. We approximate $\ln\Lambda(t,x) \simeq \ln\Lambda_c$, and choose a laser absorption source such as $\left(v_0(x)/v_{th}|_{n_c}\right)^2 = 0.1\ , \forall x \Big/ \frac{n_e}{n_c}(t,x) < 1$. The initial electric field and initial hydrodynamic profiles, are

$$\frac{n_e}{n_c}(t=0,x) = \frac{Zn_i(x)}{n_c} = \left[1+\sin\left(\frac{2\pi}{L}x\right)\right]\frac{n_{ref}}{n_c}\ , \tag{6.20}$$

$$\frac{T_e}{T_c}(t=0,x) = 1\ , \tag{6.21}$$

$$E_x(t=0,x) = 0\ . \tag{6.22}$$

These profiles are represented in figure 6.6.

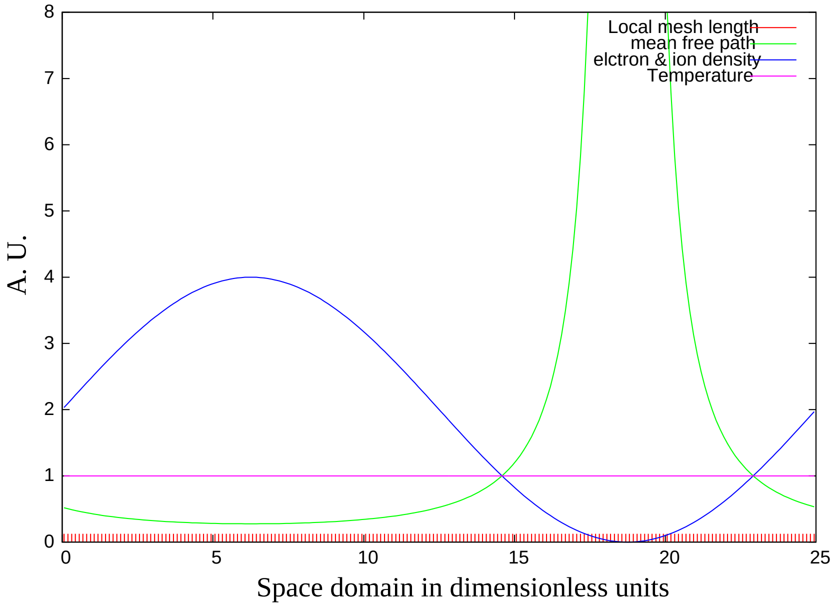

Figure 6.6: *Initial profiles for electron and ion densities, electron temperature. The discretization if uniform in space and velocity. The discretization in space resolves the mean free path. For this particular configuration,* $\frac{n_{ref}}{n_c} = 2$, $Z = 1$, $n_x = 200$, $n_{v_x} = n_{v_y} = n_{v_z} = 32$, $v_{max} = 6$, $L = 25$

6.8.2 Realistic test for the transport up to 12 n_c

For this simulation set-up, we perform a smooth fit of the 2D-ALE CHIC hydrodynamic profiles (in appendix 6.6), at the spike launching time, where we fix the parameters of appendix 6.6 as: $x_{cut} = -15.7$, $\Delta n = 0.1$, $L = (x_{cut} - x_{min})\ \lambda_{ei}|_{n_c} \times 10^6$, $T_{min} = 0.8 T_{cut}$, and $n_c = 9 \times 10^{27} \mathrm{m}^{-3}$.
Also the inverse bremsstrahlung heating zone is chosen as

$$\left(v_0(x)/v_{th}|_{n_c} \right)^2 = 0.1 \,, \forall x \Big/ \Big[0 < x/\ \lambda_{ei}|_{n_c} < 50 \times 10^{-6} /\ \lambda_{ei}|_{n_c} \Big]$$

. The figure 6.7 shows the resulting profiles of the dimensionless temperature, density, mean-free-path, together with the set-up of the non-uniform mesh below the mean-free-path.

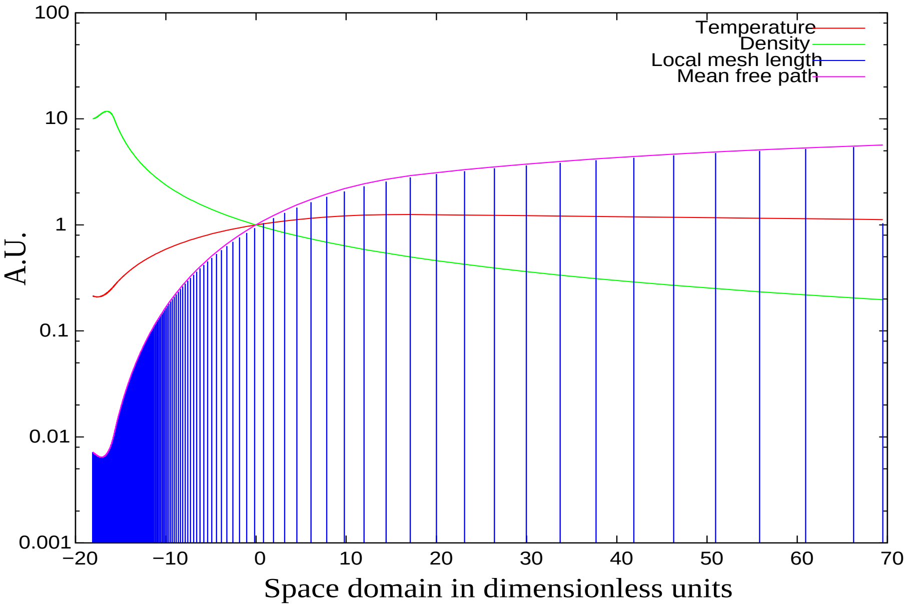

Figure 6.7: *Fitted hydrodynamic profiles from 2D-ALE CHIC simulations. The mesh geometry is set according to the mean free path. All quantities are scaled at the critical density, located at $x = 0$, according to appendix 6.7.*

Chapter 7

From kinetic to mesoscopic: a first validation of reduced description for electron transport. Application in both radiotherapy and ICF

7.1 Introduction

In this chapter, we wish to introduce a reduced model for electron transport, that relies on an angular moment closure, and validate the numerical implementation of this scheme in different regimes.

We shall first focus on the electron radiotherapy applications, which involves only collision processes very similar to those at play in ICF electron transport. After the problem formulation in section 7.2.1, we derive the approximation in section 7.2.2. This approximation consists of a system of nonlinear hyperbolic partial differential equations, whose properties we briefly discuss. Due to the possibility of shock solutions, hyperbolic PDEs have to be solved with great care. In section 7.2.4, we introduce a scheme which is adapted to the problem at hand. Numerical results for tests from the medical physics literature are presented in section 7.2.5.

As a second step, in section 7.3, we investigate the behaviour of such angular oment model faced with the collective effects of the Vlasov-Ampère system, that complete the collisional effects in electron ICF transport. The angular moment model proves to be accurate for the Landau damping as well as for the two-stream instability collective regimes.

Finally, in section 7.4, we put forward the analogy between electron radiotherapy and ICF electron transport with respect to the processes at play, and suggest that large angle collisions for ICF electron transport should be important as well.

7.2 The angular moment reduced model in the collisional regime of electron radiotherapy

The use of ionizing radiation is one of the main tools in the therapy of cancer. The aim of radiation treatment is to deposit enough energy in cancer cells so that they are destroyed. On the other hand, healthy tissue around the cancer cells should be harmed as little as possible. Furthermore, some regions at risk, like the spinal chord, should receive almost no radiation at all.

Most dose calculation algorithms in clinical use rely on the Fermi–Eyges theory of radiation which is insufficient at inhomogenities, *e.g.* void-like spaces like the lung. This work, on the other hand, starts with a Boltzmann transport model for the radiation which accurately describes all physical interactions.

Until recently, dose calculation using a Boltzmann transport equation has not attracted much attention in the medical physics community. This access is based on deterministic transport equations of radiative transfer. Similar to Monte Carlo simulations it relies on a rigorous model of the physical interactions in human tissue that can in principle be solved exactly. Monte Carlo simulations are widely used, but it has been argued that a grid-based Boltzmann solution should have the same computational complexity [19]. Electron and combined photon and electron radiation were studied in the context of inverse therapy planning *cf.* [148, 147] and most recently [149]. A consistent model of combined photon and electron radiation was developed [65] that includes the most important physical interactions. Furthermore, several neutral particle codes have been applied to the dose calculation problem, see [58] for a review.

7.2.1 A deterministic model for dose calculation

A ray of high energy electrons that interacts with human tissue is subject to elastic scattering processes and inelastic ones. It is this latter process that leads to energy deposition in the tissue *i.e.* to absorbed dose.

To formulate a transport equation for electrons we study their fluence in phase space. Let $\psi(r, \epsilon, \Omega) \cos \Theta dA d\Omega d\epsilon dt$ be the number of electrons at position r that move in time dt through area dA into the element of solid angle $d\Omega$ around Ω with an energy in the interval $(\epsilon, \epsilon + d\epsilon)$. The angle between direction Ω and the outer normal of dA is denoted by Θ. The kinetic energy ϵ of the electrons is the relativistic kinetic energy.

Boltzmann transport equation

The transport equation can generally be formulated as [41]

$$\begin{aligned} \Omega \cdot \nabla\psi(r, \epsilon, \Omega) &= \rho_{\text{in}}(r) \int\limits_{\epsilon}^{\infty} \int\limits_{\mathcal{S}^2} \sigma_{\text{in}}(\epsilon', \epsilon, \Omega' \cdot \Omega)\psi(r, \epsilon', \Omega')d\Omega' d\epsilon' \\ &+ \rho_{\text{el}}(r) \int\limits_{\mathcal{S}^2} \sigma_{\text{el}}(r, \epsilon, \Omega' \cdot \Omega)\psi(r, \epsilon, \Omega')d\Omega' \\ &- \rho_{\text{in}}(r)\sigma_{\text{in}}^{\text{tot}}(\epsilon)\psi(r, \epsilon, \Omega) \\ &- \rho_{\text{el}}(r)\sigma_{\text{el}}^{\text{tot}}(r, \epsilon)\psi(r, \epsilon, \Omega), \end{aligned} \tag{7.1}$$

with σ_{in} being the differential scattering cross section for inelastic scattering, and σ_{el} the differential cross section for elastic scattering; $\sigma_{\text{in}}^{\text{tot}} = \int_{S^2} \sigma_{\text{in}} d\Omega$ and $\sigma_{\text{el}}^{\text{tot}} = \int_{S^2} \sigma_{\text{el}} d\Omega$ are the total cross sections for inelastic and elastic scattering, respectively; ρ_{in} and ρ_{el} are the densities of the respective scattering centers.

Explicit formulas for the cross sections that we used in this model can be found in section 7.2.1. They are based on the model developed in [65]. The energy integration is performed over (ϵ, ∞) since the electrons lose energy in every scattering event. Also, we consider only electron radiation. Equation (7.1) could also be used to model electrons which are generated by the interactions of photons with matter, as in [65]. In this case we would have an additional source term on the right hand side for the generated electrons.

Besides the transport equation one needs an equation for the absorbed dose. It was derived in [65] as an asymptotic limit of a model with a finite lower energy bound $\epsilon_s > 0$. The formula is exact if one chooses the lower energy limit $\epsilon_s = 0$, as we do here.

$$D(r) = \frac{T}{\rho(r)} \int_0^{\infty} S(r, \epsilon')\psi^{(0)}(r, \epsilon')d\epsilon' \tag{7.2}$$

with

$$\psi^{(0)}(r, \epsilon) := \int\limits_{S^2} \psi(r, \epsilon, \Omega')d\Omega',$$

T being the duration of the irradiation of the patient and ρ the mass density of the irradiated tissue. If all quantities are calculated in SI units, equation (7.2) leads to SI units J/kg or Gray (Gy) for the dose.

S is the stopping power related to the inelastic cross section. It is defined as

$$S(r, \epsilon) = \rho_{\text{in}}(r) \int\limits_0^{\epsilon} \epsilon' \sigma_{\text{in}}(\epsilon, \epsilon')d\epsilon'.$$

Continuous slowing-down approximation

Electron transport in tissue has very distinctive properties. The soft collision differential scattering cross sections have a pronounced maximum for small scattering angles and small energy loss. This allows for a simplification of the scattering terms in the Boltzmann equation. The Fokker-Planck equation is the result of an asymptotic analysis for both small energy loss and small deflections. It has been rigorously derived in [117] and has been applied to the above Boltzmann model in [65]. However, some electrons will also experience hard collisions with large changes in direction and energy losses which have to be described by Boltzmann integral terms. Thus we only use an asymptotic analysis to describe energy loss, called continuous slowing-down approximation. This approximation has a greater domain of validity than the Fokker-Planck approximation. The Boltzmann equation in continuous slowing-down approximation (BCSD) is [91]

$$\begin{aligned}
\Omega \cdot \nabla\psi(r,\epsilon,\Omega) &= \rho_{\text{in}}(r) \int_{S^2} \sigma_{\text{in}}^{\text{CSD}}(\epsilon, \Omega' \cdot \Omega)\psi(r,\epsilon,\Omega')d\Omega' \\
&+ \rho_{\text{el}}(r) \int_{S^2} \sigma_{\text{el}}(r,\epsilon,\Omega' \cdot \Omega)\psi(r,\epsilon,\Omega')d\Omega' \\
&- \rho_{\text{in}}(r)\sigma_{\text{in,tot}}(\epsilon)\psi(r,\epsilon,\Omega) \\
&- \rho_{\text{el}}(r)\sigma_{\text{el,tot}}(r,\epsilon)\psi(r,\epsilon,\Omega) \\
&+ \frac{\partial}{\partial\epsilon}(S(r,\epsilon)\psi(r,\epsilon,\Omega))
\end{aligned} \tag{7.3}$$

with

$$\sigma_{\text{in}}^{\text{CSD}} = \int_0^\infty \sigma_{\text{in}}(\epsilon,\epsilon',\mu)d\epsilon'.$$

A truncation in the energy space is introduced, that does not allow particles with arbitrary high energy,

$$\lim_{\epsilon\to\infty} \psi(r,\epsilon,\Omega) = 0. \tag{7.4}$$

In the numerical simulations, we use a sufficiently large cutoff energy. Furthermore, we prescribe the ingoing radiation at the spatial boundary,

$$\psi(r,\epsilon,\Omega) = \psi_b(r,\epsilon,\Omega) \quad \text{for} \quad n \cdot \Omega < 0, \tag{7.5}$$

where n is the unit outward normal vector.

Modeling of Scattering Cross Sections

Henyey-Greenstein Scattering Theory The detailed interactions of electrons with atoms give rise to complicated explicit formulas for the scattering coefficients. Because of this, many studies use the simplified Henyey-Greenstein scattering kernel for elastic scattering [11],

$$\sigma_{HG}(\mu, g) = \frac{1-g^2}{4\pi(1+g^2-2g\mu)^{3/2}}. \tag{7.6}$$

The parameter g, which can depend on r, is the average cosine of the scattering angle and is a measure for the anisotropy of the scattering.

Mott and Møller Scattering A more realistic model for elastic and inelastic scattering of electrons in tissue has been developed in [65]. This model introduces material parameters (namely densities ρ_e and ρ_c, ionization energy ϵ_B and effective atomic charge Z). The energy integration for inelastic scattering is cut-off at ϵ_B.

The model uses the Mott scattering formula for elastic scattering [139, 138]

$$\sigma_{\text{Mott}}(r,\epsilon,\Omega'\cdot\Omega)=\frac{Z^2(r)r_{\text{e}}^2(1+\epsilon)^2}{4[\epsilon(\epsilon+2)]^2(1+2\eta(r,\epsilon)-\cos\vartheta)^2}\left[1-\frac{\epsilon(\epsilon+2)}{(1+\epsilon)^2}\sin^2\frac{\vartheta}{2}\right],$$

with $\vartheta=\arccos(\Omega'\cdot\Omega)$. Here, $\alpha\approx 1/137$ is the fine structure constant, Z is the atomic number of the irradiated medium, r_{e} is the classical electron radius. Z depends on r to account for heterogeneous media. To avoid an otherwise occurring singularity at $\vartheta=0$ a screening parameter

$$\eta(r,\epsilon)=\frac{\pi^2\alpha^2Z^{2/3}(r)}{\epsilon(\epsilon+2)},$$

can be introduced [159] that models the screening effect of the electrons of the atomic shell.

The dominant inelastic scattering process is Møller (electron-electron) scattering. Due to kinematical reasons of the scattering processes the range of solid angles in Møller scattering is restricted. The electron, which has the higher energy after the collision is called primary electron, the other electron secondary. Here, an incoming electron with energy ϵ' hits an electron at rest. After the collision, the angle between the directions of the electrons is at most $\pi/2$. Electrons are indistinguishable. For an angle in $[0,\pi/4]$, the electron with energy ϵ is the primary electron, for an angle in $[\pi/4,\pi/2]$, it is the secondary electron. Therefore the Møller cross section can be written as

$$\sigma_M=\tilde{\sigma}_M\chi_{\{0<\Omega\cdot\Omega'<\sqrt{2}/2\}}+\tilde{\sigma}_{M,\delta}\chi_{\{\sqrt{2}/2<\Omega\cdot\Omega'<1\}},$$

where χ denotes the characteristic function of a set,

$$\tilde{\sigma}_{\text{M}}(\epsilon',\epsilon,\Omega'\cdot\Omega)=\sigma_{\text{M}}(\epsilon',\epsilon)\delta_M(\mu,\mu_p)\frac{1}{2\pi},\quad \mu=\Omega'\cdot\Omega,$$

is the Møller differential cross section of primary electrons and

$$\tilde{\sigma}_{\text{M},\delta}(\epsilon',\epsilon,\Omega'\cdot\Omega)=\sigma_{\text{M}}(\epsilon',\epsilon)\delta_{\text{M},\delta}(\mu,\mu_\delta)\frac{1}{2\pi},\quad \mu=\Omega'\cdot\Omega,$$

is the Møller differential cross section of secondary electrons. Here,

$$\sigma_{\text{M}}(\epsilon',\epsilon)=\frac{2\pi r_{\text{e}}^2(\epsilon'+1)^2}{\epsilon'(\epsilon'+2)}\left[\frac{1}{\epsilon^2}+\frac{1}{(\epsilon'-\epsilon)^2}+\frac{1}{(\epsilon'+1)^2}-\frac{2\epsilon'+1}{(\epsilon'+1)^2\epsilon(\epsilon'-\epsilon)}\right],$$

and

$$\delta_M(\mu_{\text{e}},\mu_p)=\delta\left(\mu_{\text{e}}-\sqrt{\frac{\epsilon}{\epsilon'}\frac{\epsilon'+2}{\epsilon+2}}\right),\ \text{for } \epsilon>\frac{(\epsilon'-\epsilon_{\text{B}})}{2},$$

$$\delta_{\text{M},\delta}(\mu_{\text{e}},\mu_\delta)=\delta\left(\mu_{\text{e}}-\sqrt{\frac{\epsilon}{\epsilon'}\frac{\epsilon'+2}{\epsilon+2}}\right),\quad \epsilon<\frac{(\epsilon'-\epsilon_{\text{B}})}{2}.$$

Møller scattering does not take into account distant collisions. In the simulations the model parameters ρ_{el}, ρ_{in}, ϵ_B and Z are fitted to tabulated values taken from the database of the Penelope Monte Carlo code [125].

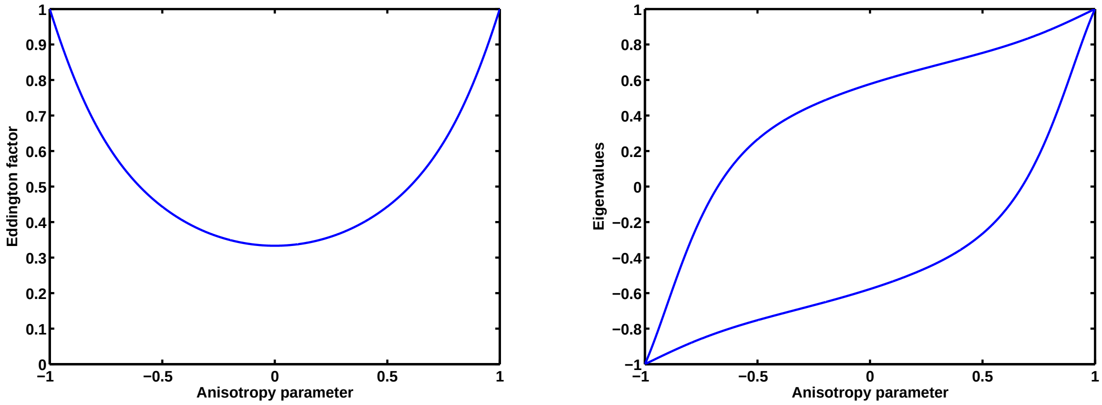

(a) Eddington factor.

(b) Eigenvalues.

Figure 7.1: Eddington factor χ and system eigenvalues versus anisotropy parameter $|\alpha|$.

7.2.2 Partial Differential Equation Model

We will try to reduce the cost of solving system (7.1) by assuming a minimum entropy principle for the angle distribution of particles. This principle has been first proposed by Jaynes [72] as a method to select the most likely state of a thermodynamical system having only incomplete information. It has subsequently been developed in [107], [95], [10] and [45], among others, and has become the main concept of rational extended thermodynamics [113]. A full account and an exhaustive list of references on the historical development can be found in [64].

We define the first three moments in angle:

$$\psi^{(0)}(r,\epsilon) = \int_{S^2} \psi(r,\epsilon,\Omega)d\Omega, \tag{7.7}$$

$$\psi^{(1)}(r,\epsilon) = \int_{S^2} \Omega\psi(r,\epsilon,\Omega)d\Omega, \tag{7.8}$$

$$\psi^{(2)}(r,\epsilon) = \int_{S^2} (\Omega\otimes\Omega)\psi(r,\epsilon,\Omega)d\Omega, \tag{7.9}$$

where we note that $\psi^{(0)}$ is a scalar, $\psi^{(1)}$ is a vector and $\psi^{(2)}$ is a tensor.

If we integrate the system (7.3) over Ω, we can derive the following equations,

$$\nabla_x\psi^{(1)} = \frac{\partial}{\partial\epsilon}(S\psi^{(0)}), \tag{7.10a}$$

$$\nabla_x\psi^{(2)} = -(T_M + T_{\mathrm{Mott}})\psi^{(1)} + \frac{\partial}{\partial\epsilon}(S\psi^{(1)}). \tag{7.10b}$$

We have introduced the transport coefficients

$$T_{\mathrm{in}}(r,\epsilon) = \pi\rho_{\mathrm{in}}(r)\int_{\epsilon_B}^{(\epsilon-\epsilon_B)/2}\int_{-1}^{1}(1-\mu)\sigma_{\mathrm{in}}(\epsilon,\epsilon',\mu)d\mu d\epsilon', \tag{7.11}$$

$$T_{\mathrm{el}}(r,\epsilon) = \pi\rho_{\mathrm{el}}(r)\int_{-1}^{1}(1-\mu)\sigma_{\mathrm{el}}(\epsilon,\mu)d\mu. \tag{7.12}$$

These coefficients and the stopping power can be computed for both Henyey-Greenstein and Mott/Møller scattering. Explicit expressions can be found in [65, 53].

The problem remains open for the computation of moment $\psi^{(2)}$ as a function of $\psi^{(0)}$ and $\psi^{(1)}$. The Minimum Entropy $M1$ closure for electrons [26] can be derived in the following way. To close the system we determine a distribution function ψ_{ME} that minimizes the entropy of the electrons,

$$H_R^*(\psi) = -\int_{S^2} \psi \log \psi d\Omega, \tag{7.13}$$

under the constraint that it reproduces the lower order moments,

$$\int_{S^2} \psi_{ME} d\Omega = \psi^{(0)} \quad \text{and} \quad \int_{S^2} \Omega \psi_{ME} d\Omega = \psi^{(1)}. \tag{7.14}$$

By using this entropy, we have implicitly assumed that the electrons obey classical Maxwell-Boltzmann statistics. This is justified, since here quantum effects can be neglected.

Analogous to the calculations in [95] we can show that the entropy minimizer has the following form,

$$\psi_{ME} = a_0 \exp(-\Omega \cdot a_1), \tag{7.15}$$

where a_0 is a non-negative scalar, and a_1 is a three component real valued vector. This is a Maxwell-Boltzmann type distribution and a_0, a_1 are (scaled) Lagrange multipliers enforcing the constraints. An important parameter is the anisotropy parameter α,

$$\alpha = \frac{\psi^{(1)}}{\psi^{(0)}},$$

whose norm is by construction less than or equal to one. If we compute the different moments of the distribution function given by (8.42) we obtain,

$$\psi^{(0)} = 4\pi a_0 \frac{\sinh(|a_1|)}{|a_1|}, \ \psi^{(1)} = 4\pi a_0 \frac{\sinh(|a_1|)(1 - |a_1| \coth(|a_1|))}{|a_1|^3}\, a_1. \tag{7.16}$$

In fact, these relations can be combined to give,

$$\alpha = \frac{1 - |a_1| \coth(|a_1|)}{|a_1|^2}\, a_1, \tag{7.17}$$

or by taking the modulus,

$$|\alpha| = \frac{|a_1| \coth(|a_1|) - 1}{|a_1|}. \tag{7.18}$$

The relation (7.18) cannot be inverted explicitly by hand, *i.e.* we cannot express $|a_1|$ as a function of α in a closed form. However, this relation determines a unique solution which can in principle be computed. If we assume that we know a_1, $\psi^{(2)}$ can be computed as

$$\psi^{(2)} = \psi^{(0)} \left(\frac{1 - \chi(\alpha)}{2} I + \frac{3\chi(\alpha) - 1}{2} \alpha \otimes \alpha \right), \tag{7.19}$$

where

$$\chi = \frac{|a_1|^2 - 2|a_1|\coth(|a_1|) + 2}{|a_1|^2} \tag{7.20}$$

is a function of α by means of (7.18).

For its efficient numerical evaluation, the Eddington factor has to be approximated. Several possibilities exist:

- One could solve the closure relation (7.18) for $|a_1|$ *e.g.* by a Newton iteration in each step during the simulation.
- One could precompute a table that gives the Eddington factor χ as a function of α.
- One could approximate $\chi(\alpha)$ by a suitable special function.

The second approach has been followed in [53]. It is advantageous only if the space in which one interpolates is low-dimensional. For more moments, this approach becomes infeasible, and the first approach has to be used.

In some cases, an *ansatz* for χ can provide a good approximation. This is the approach we are following here. The Eddington factor χ can be approximated by a very simple rational function,

$$\chi(\alpha) \approx \frac{a_6\,\alpha^6 + a_4\,\alpha^4 + a_2\,\alpha^2 + a_0}{\alpha^4 + b_2\,\alpha^2 + b_0.} \tag{7.21}$$

This approximation is very accurate (the difference with exact curve is about 10^{-15}). The coefficients are given by

$$\begin{aligned} a_0 &= 0.762066949972264, & b_0 &= 2.28620084991677,\\ a_2 &= 0.219172080193380, & b_2 &= -2.10758208969840,\\ a_4 &= -0.259725400168378, & &\\ a_6 &= 0.457105130221120. & & \end{aligned} \tag{7.22}$$

7.2.3 Properties of the System

In the literature, the system that has been thoroughly investigated (both analytically and numerically) is system (7.10) restricted to its conservative terms, without external sources, but with time-dependence.

In the present work, we adapt a pseudo-time technique. We focus on the spatial discretization and use a standard discretization for the terms on the right-hand side. Thus we consider

$$\frac{\partial}{\partial t}\psi^{(0)} + \nabla_x\psi^{(1)} = 0, \tag{7.23a}$$

$$\frac{\partial}{\partial t}\psi^{(1)} + \nabla_x\psi^{(2)}\left(\psi^{(0)}, \psi^{(1)}\right) = 0, \tag{7.23b}$$

with the closure (7.18).

The Eddington factor χ is shown in Figure 7.1. Furthermore, we show the system eigenvalues in two dimensions. In the isotropic regime (anisotropy parameter zero), they coincide with the P1 eigenvalues. On the other hand, in the case of free-streaming ($|\alpha| = 1$), they coincide and have absolute value one.

Thus the system (7.10) is hyperbolic and the speed of propagation is limited by one. Moreover the system is hyperbolic symmetrisable [45].

System (7.23) closed by the relation (7.19) has been analyzed thoroughly in [38]. There, solutions to Riemann problems are constructed and invariant regions are computed. Since the reconstruction (8.42) of the kinetic distribution ψ is always positive, it can be expected that system (7.23), (7.19) must admit a positive solution $\psi^{(0)}$ and a limited flux $\|\alpha\| < 1$. To our knowledge, however, there exists no proof of this fact. The invariant regions computed in [38] only cover a subset of all admissible values. For a related model [54], bounds were proved, but only in 1D and steady state. Nevertheless, we construct a scheme which preserves exactly the positivity of $\psi^{(0)}$ and the flux limitation, *i.e.* the convex set of the admissible states of the system (7.23) is [17]

$$\mathcal{A} = \left\{ \left(\psi^{(0)}, \psi^{(1)} \right) : \ \psi^{(0)} \geq 0, \ |\psi^{(1)}| \leq \psi^{(0)} \right\}.$$

In the absence of sources or boundaries, the total mass, momentum and energy are conserved.

In addition, the minimum entropy system recovers the equilibrium diffusion regime as a relaxation limit for large absorption coefficients [37].

In a two-dimensional geometry, we have in addition [17]: Let n be the unit normal vector to an interface; then the system exhibits two acoustic waves, with velocities $\lambda_L(n)$ and $\lambda_R(n)$, supplemented by a contact wave with velocity $\beta(n)$. The quantity $\beta \cdot n$ satisfies the following inequality $\lambda_L(n) \leq \beta(n) \cdot n \leq \lambda_R(n)$. The Riemann invariants associated with the contact wave are $\{\beta, \Pi\}$. They are defined by the relations

$$\psi_1 = (\Pi + \psi_0)\beta, \tag{7.24a}$$

$$\psi_2 = (\psi_0 + \Pi)\beta \otimes \beta + \Pi Id \ . \tag{7.24b}$$

7.2.4 Numerical Method

The properties of the continuous model should be reproduced by the numerical scheme. In particular the positivity and flux limitation constraints are fundamental. An HLL scheme [63] can be constructed [12, 28, 17], that satisfies the required properties. However such an approach cannot capture the contact discontinuity. To prevent this failure, an HLLC scheme [12] has been derived, that resolves the contact discontinuity and satisfies the physical constraints.

To complete this presentation of the numerical approximation, we mention that a suitable high order extension that preserves both the positivity and the flux limitation can be derived, relying on an appropriate limitation procedure.

An HLL scheme for the free transport $M1$ angular moment system

In this section, we derive a Finite Volume method, issued from the HLL method [63] to discretize the free transport equation contained in the system (7.23). Put in other words, we omit the source terms and we consider the one dimensional generic conservative system

$$\frac{\partial}{\partial t}\mathcal{U} + \frac{\partial}{\partial x}\left[\mathcal{F}\left(\mathcal{U}\right)\right] = 0 \ , \tag{7.25}$$

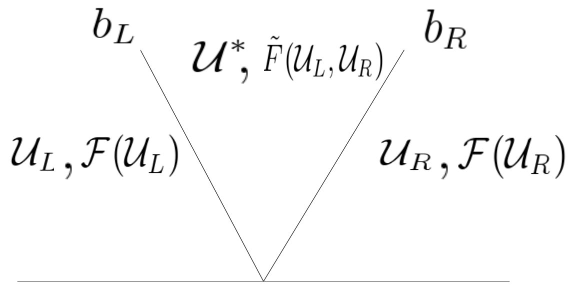

Figure 7.2: Structure of the approximate HLL Riemann Solver

where

$$\mathcal{U} = \begin{pmatrix} \psi_0 \\ \psi_1 \end{pmatrix}$$

and $\mathcal{F}$ stands for the flux of the $M1$ system in the x space direction.
We consider a structured mesh of size Δx_i, defined by the cells $I_i = [x_{i-1/2}, x_{i+1/2})$, where we have set $x_{i+1/2} = x_i + \Delta x/2$, $i \in \mathbb{Z}$, at time t^n. As usual, we consider known a piecewise contant approximation $U^h(x,t^n)$, defined by $U^h(x,t^n) = U_i^n, x \in I_i$, $\forall i \in \mathbb{Z}$.

At initial time $t = 0$, we impose

$$U_i^0 = \int_{x_{i-1/2}}^{x_{i+1/2}} U_0(x)dx,$$

where U_0 is the initial data. This approximation evolves in time, involving a suitable approximate Riemann solver. In the HLL approach, the exact Riemann solver solution is substituted by a single approximate state (see Figure 7.2). Here b_L and b_R are relevant approximations of λ_L and λ_R, respectively. Let us introduce the proposed approximate solution:

$$\mathcal{U}_{HLL}(x,t) \equiv \begin{pmatrix} \psi_0(x,t) \\ \psi_1(x,t) \end{pmatrix}_{HLL} = \begin{cases} \mathcal{U}_L & \text{if } \frac{x}{t} < b_L \,, \\ \mathcal{U}^* & \text{if } b_L \leq \frac{x}{t} \leq b_R \,, \\ \mathcal{U}_R & \text{if } b_R < \frac{x}{t} \,. \end{cases} \tag{7.26}$$

Moreover, the search of weak solutions leads to the Rankine-Hugoniot jump conditions

$$-b_L\,[\mathcal{U}^* - \mathcal{U}_L] + \left[\tilde{F} - \mathcal{F}(\mathcal{U}_L)\right] = 0, \tag{7.27a}$$

$$-b_R\,[\mathcal{U}_R - \mathcal{U}^*] + \left[\mathcal{F}(\mathcal{U}_R) - \tilde{F}\right] = 0. \tag{7.27b}$$

These relations provide us with an explicit expression for the intermediate state and flux of the numerical scheme

$$\mathcal{U}^* = \frac{b_R\mathcal{U}_R - b_L\mathcal{U}_L - (\mathcal{F}(\mathcal{U}_R) - \mathcal{F}(\mathcal{U}_L))}{b_R - b_L}\,, \tag{7.28a}$$

$$\tilde{F}(\mathcal{U}_L,\mathcal{U}_R) = \frac{b_R\mathcal{F}(\mathcal{U}_L) - b_L\mathcal{F}(\mathcal{U}_R) - b_Lb_R(\mathcal{U}_R - \mathcal{U}_L)}{b_R - b_L}\,, \tag{7.28b}$$

At each interface $x_{i+1/2}$, we impose the above HLL approximate Riemann solver, assuming the CFL like condition (7.29) ensuring that the Riemann solvers do not interact in the case where $b_{L,i+1/2} < 0$ and

$b_{R,i-1/2} > 0$:

$$\frac{\Delta t}{\Delta x} \leq \frac{b_{L,i+1/2} b_{R,i-1/2}}{b_{L,i+1/2} - b_{R,i-1/2}} . \tag{7.29}$$

We set $\mathcal{U}^h(x, t + \Delta t)$, at time $t^n + \Delta t$, the superposition of the non-interacting Riemann solutions. We define the updated approximation at time t^{n+1} by

$$\mathcal{U}_i^{n+1} = \frac{1}{\Delta x} \int_{x_{i-1/2}}^{x_{i+1/2}} \mathcal{U}^h(x, t^n + \Delta t).$$

An easy computation gives

$$\mathcal{U}_i^{n+1} = \mathcal{U}_i^n - \frac{\Delta t}{\Delta x}(F_{i+1/2}^n - F_{i-1/2}^n) , \tag{7.30}$$

where

$$F_{i+1/2}^n(\mathcal{U}_i^n, \mathcal{U}_{i+1}^n) = \begin{cases} \mathcal{F}\left(\mathcal{U}_i^n\right) & \text{if } 0 < b_{L,i+1/2} \\ \tilde{F}_{i+1/2}\left(\mathcal{U}_i^n, \mathcal{U}_{i+1}^n\right) & \text{if } b_{L,i+1/2} \leq 0 \leq b_{R,i+1/2} \\ \mathcal{F}\left(\mathcal{U}_{i+1}^n\right) & \text{if } b_{R,i+1/2} < 0 \end{cases}$$

The robustness of the scheme, namely the positivity, the flux limitation, the total mass preservation, has been established for the HLL scheme (see [17] for further details).
Finally, concerning the high order extension, we adopt a van Leer MUSCL technique [157], supplemented by a suitable slope limitation preserving these expected physical properties [16].

An accurate HLLC scheme

The HLL scheme has proved to be robust, however, its 2D extension fails when approximating contact waves. Several works [12, 17] introduce a more accurate scheme, the HLLC scheme, based on a two state approximation, denoted by U_L^* and U_R^*.

First, let us recall the relevant linearization that permits us to define an approximation with two intermediate states: on the one hand, the Rankine-Hugoniot conditions (7.27) are considered; on the other hand, they are supplemented by the continuity of the Riemann invariants accross the contact wave:

$$(\beta_x)_L^* = (\beta_x)_R^* = \beta_x^* \quad , \quad \Pi_L^* = \Pi_R^* = \Pi^* \ , \tag{7.31}$$

where β_x and Π are defined by the relation (7.24). The combination of both the Rankine-Hugoniot condition (7.27) and the relation (7.31) standing as the continuity of the Riemann invariants accross the contact wave, is sufficient to determine uniquely [12, 17] the two approximate states U_L^* and U_R^*, together with their associated fluxes $\tilde{F}_L$ and $\tilde{F}_R$. The proposed HLLC approximate solution can be written as

$$\mathcal{U}_{HLLC}(x, t) \equiv \begin{pmatrix} \psi_0(x, t) \\ \psi_1(x, t) \end{pmatrix}_{HLLC} = \begin{cases} \mathcal{U}_L & \text{if } \frac{x}{t} < b_L \ , \\ \mathcal{U}_L^* & \text{if } b_L \leq \frac{x}{t} \leq \beta_x^* \ , \\ \mathcal{U}_R^* & \text{if } \beta_x^* \leq \frac{x}{t} \leq b_R \ , \\ \mathcal{U}_R & \text{if } b_R < \frac{x}{t} \ . \end{cases} \tag{7.32}$$

Similar to the derivation of the HLL scheme, we integrate over a cell I_i the juxtaposition of the non-interacting HLLC Riemann approximate solvers at each interface (projection step), in order to obtain the updated quantity

$$\mathcal{U}_i^{n+1} = \frac{1}{\Delta x} \int_{x_{i-1/2}}^{x_{i+1/2}} \mathcal{U}^h(x, t^n + \Delta t).$$

This brief description of the HLLC scheme is now completed. It is able to capture exactly the contact wave, and satisfies the positivity, the flux limitation, and the total mass preservation.

7.2.5 Numerical Results

Central Void

The first test case is taken from the medical physics literature [11]. We consider only elastic scattering, which is modeled by the Henyey-Greenstein kernel. Thus $S = 0$ and $T_{\text{in}} = 0$. We compare the particle flux $\psi^{(0)}(x)$ obtained with the minimum entropy model (labeled M1) with a discrete ordinates solution of the transport equation (labeled SN) with sufficiently many angles (128). The method has been described in [47].

The test case consists of a one-dimensional geometry with three layers: optically thick, followed by optically thin followed again by optically thick. The layers have an equal depth of 40 mm. The scattering and absorption coefficients are $\sigma_s = 0.5$ mm^{-1}, $\sigma_a = 0.005$ mm^{-1} for the optically thick region, and $\sigma_s = 0.01$ mm^{-1}, $\sigma_a = 0.0001$ mm^{-1} for the optically thin region. Moreover, $g = 0$. Figure 7.3 shows the particle flux $\psi^{(0)}$ as a functon of space. Compared to the benchmark solution, the minimum entropy model slightly overestimates but nevertheless quite accurately describes the particle flux. In Figure 7.3 we also show the partice distribution function $\psi(x, \Omega)$, where $\Omega = (0, 0, \mu)$ in 1D. The main difference is that for M1, the forward-peak of the incoming particles reaches further into the medium.

Two-dimensional Void-like Layer

Our second test case, again taken from [11], is a two-dimensional quadratic domain which contains a void-like layer, shown in gray in Figure 7.4(a). Again, we consider only elastic scattering modeled by the Henyey-Greenstein kernel.

We take $\sigma_s = 0.5$ mm^{-1} and $\sigma_a = 0.005$ mm^{-1} inside the square, and $\sigma_s = 0.01$ mm^{-1} and $\sigma_a = 0.0001$ mm^{-1} in the void-like ring. In both regions, $g = 0$. An isotropic source of particles is placed on the left boundary. In a 2D contour plot (Figure 7.4), the fluxes ψ^0 from the discrete ordinate method and from the minimum entropy method are virtually indistinguishable. The propagation into the medium, as well as the void-like layer are equally well resolved. A difference between the models only becomes apparent in a logarithmic plot of a cut through the center of the square at $y = 50$ mm. Figure 7.4 shows the particle flux along this line. The difference between both solutions is again of the order of one percent.

Electrons on Water Phantom

As a first test case with energy loss, we consider a 10 MeV electron beam impinging onto a slab of water. In Figure 7.5 we compare the results computed with our code to the dose computed by the state-of-the-art Monte Carlo code PENELOPE [125]. This code has been extensively validated against experimental results.

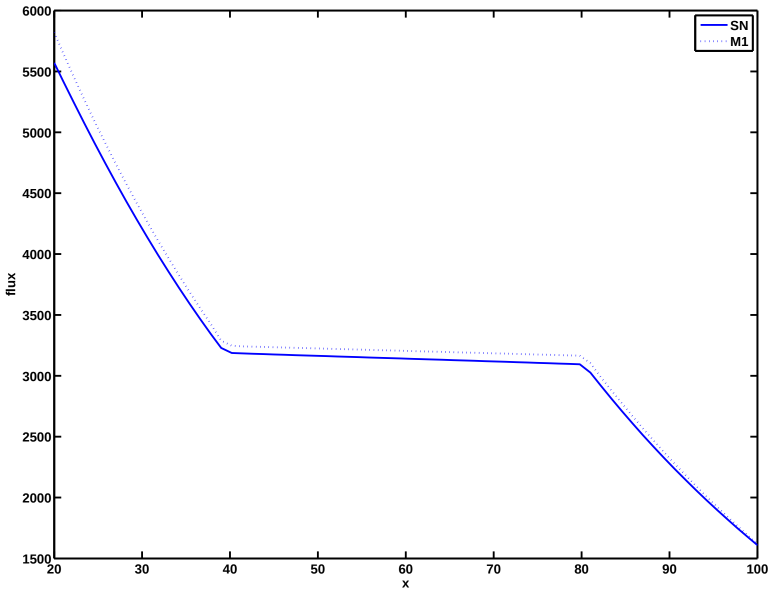

(a) Particle flux.

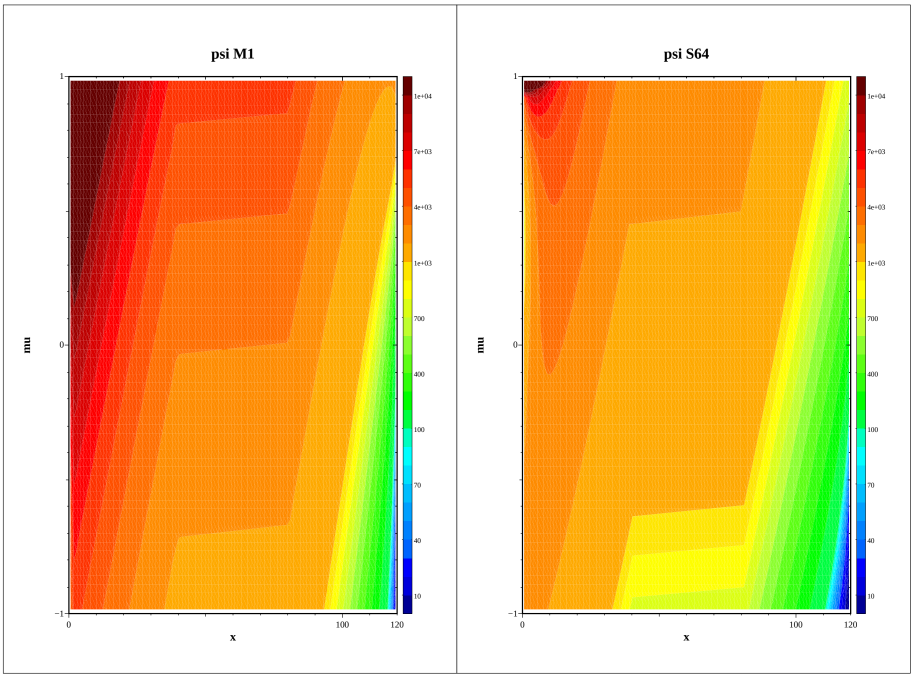

(b) Comparison of $M1$ and benchmark distribution functions. Logarithmic scale.

Figure 7.3: Geometry with central void.

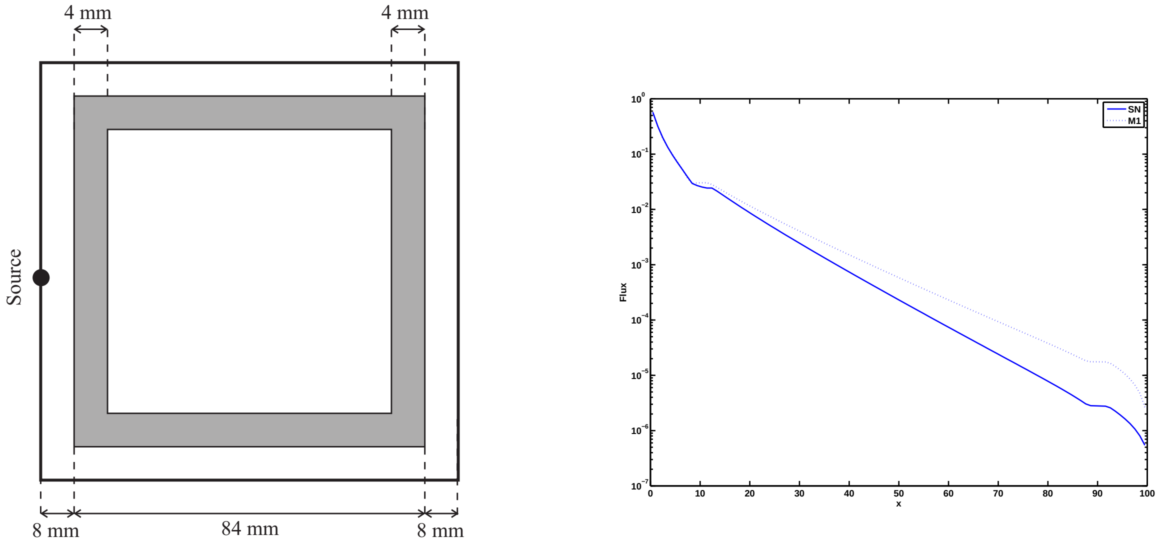

(a) Geometry containing void layer.

(b) Cut along $y = 50$ mm.

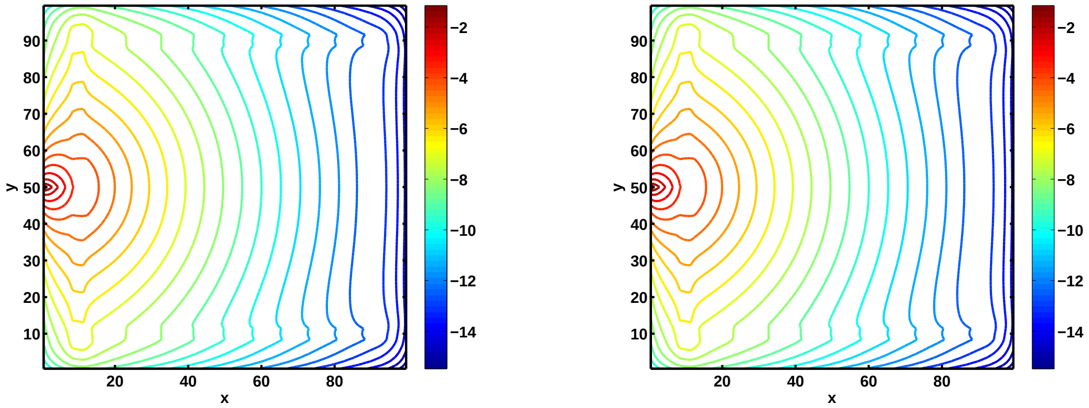

(c) Transport solution.

(d) Minimum entropy model.

Figure 7.4: Transport versus minimum entropy for void-like layer.

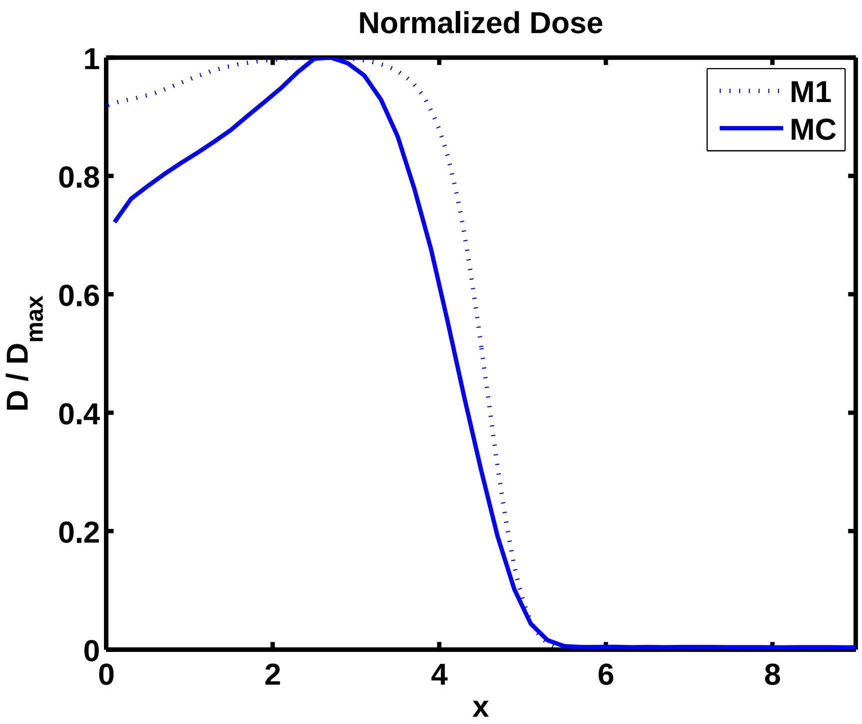

Figure 7.5: Dose for 10 MeV electron beam on water.

To obtain a good fit with the tabulated scattering data, we have fixed our model parameters for water as $\epsilon_B = 16.0$ eV, $Z = 9.40$, $\rho_{\text{el}} = 0.256 \times 10^{23}$ g/cm^3, $\rho_{\text{in}} = 6.21 \times 10^{23}$ g/cm^3. As boundary conditions, we have taken a very narrow Gaussian in energy, and a δ pulse in angle

$$\psi_b = \psi_0 \exp(-200 \times (\epsilon - \epsilon_{\text{beam}})^2)\delta(\mu - 1)$$

and computed the angular moments. PENELOPE was set up in a pseudo-1D setting with a large beam size perpendicular to the beam direction.

In order to compare the different formulations of the models, both depth-dose curves in Figure 7.5 have been normalized to dose maximum one. The penetration depth computed with the M1 model agrees very well with the Monte Carlo result. In fact this deviation is within the margin of differences between different Monte Carlo codes [132]. The only major difference occurs near the boundary, where the M1 model overestimates the dose. This might be due to the simplified physics (possibly neglection of Bremsstrahlung effects) or an oversimplification of the angular dependence of ψ in the M1 model. Both possibilities will be investigated further. However, we believe that this result can serve as a proof of concept of a PDE based modeling of dose computation.

7.2.6 CT Data

In our final test case, we compare our method with Monte Carlo results from PENELOPE using real patient CT data showing the hip bone. We took a two-dimensional slice of 6 × 6 cm from the three-dimensional CT data. A square region is split into 64×64 squares. In each of the squares, the material is

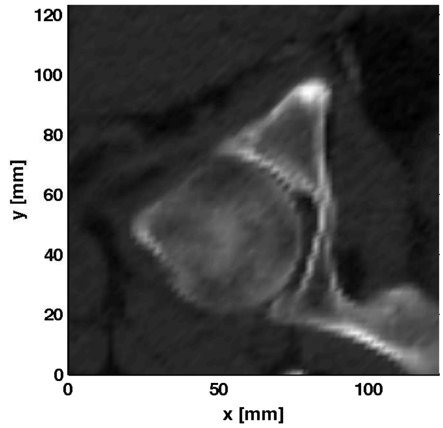

Figure 7.6: CT data of hip bone.

described by its Hounsfield grey value $\mathcal{G}(x,y)$. The grey values can be translated into physical parameters as follows,

$$\rho(x,y) = \left(\frac{\mathcal{G}(x,y)}{1000} + 1\right)\rho_{\mathrm{Water}},$$

i.e. the densities ρ_{el} and ρ_{in} for water are multiplied by a specified factor. The region shows the hip bone and the density varies between 86% and 226% of the value of water. The boundary conditions were set up similar to the previous case, with three beams of width 2 cm, each consisting of 10 MeV electrons, impinging from the centers of three sides of the domain. Contour plots of the dose distribution are shown in Figure 7.7. There, we also show two cuts through the dose distribution. looking at the 2D dose distribution, the contour lines agree very well. Note that, although we have used 3×10^{10} particles, there still is significant noise in the Monte Carlo results. The two cuts through the beam centers show that also quantitatively the independently computed dose distributions agree very well.

The computation time for the 3D Monte Carlo dose was 3×29 hours for 3×10^{10} particles on a 3GHz Pentium 4 with 1 GB RAM. In 1D, the minimum entropy model took about 1 second, in 2D 4 seconds. Thus we expect a computation time of several seconds in a full 3D dose computation.

Again, this result shows that if our model is developed further, it may serve as an alternative to existing dose computation methods.

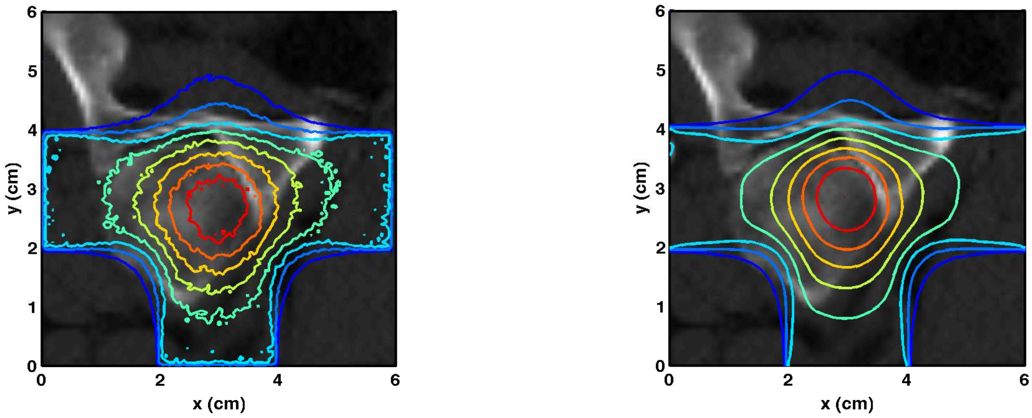

(a) Monte Carlo solution.

(b) Minimum entropy solution.

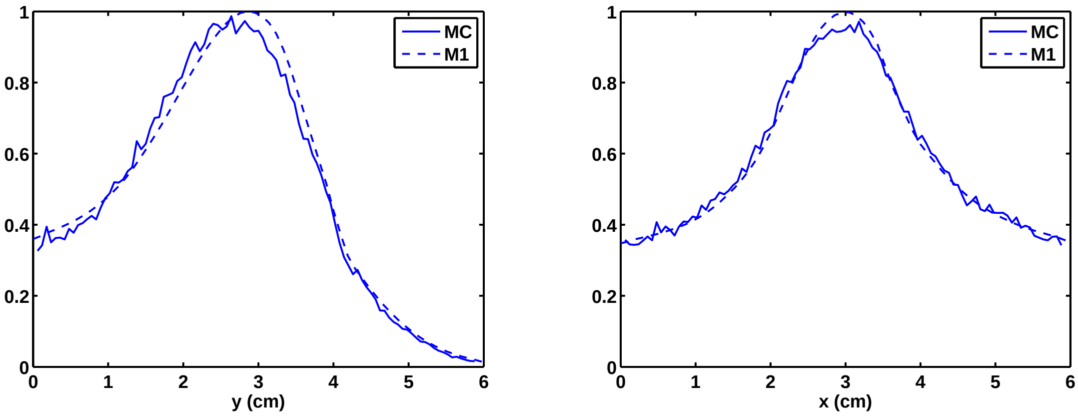

(c) Cut along $x = 3$ cm.

(d) Cut along $y = 3$ cm.

Figure 7.7: Dose distribution for three beams impinging on hip bone.

7.3 The angular moment reduced model in the collective regime of plasma physics

Having in view ICF applications, we have shown that the derived $M1$ reduced angular model is accurate with respect to the collisional processes. As a counterpart, in this section, we wish to explore the response of the model in the collective unmagnetized regime, which is still relevant for ICF plasma physics. We propose the linear Landau damping and Two-Stream Instability as first electrostatic $1D_x \times 1D_v$ validation tests.

7.3.1 Linear Landau damping

The Landau damping effect is triggered, in this section, with the following initial distribution function and electric field

$$\begin{aligned} f_e(t=0,x,v_x) &= [1 + A\cos(k_x x)]\, f_M(n_0,T_0,v_0)\,, & (7.33)\\ E_x(t=0,x) &= 0\,, & (7.34)\end{aligned}$$

where $L_x = 25$, $k_x = 2\pi/L_x$, f_M is the nonrelativistic Maxwellian with zero drift velocity $v_0 = 0$,arbitrary density n_0, and initial temperature $T_0 = 1$.

For the kinetic reference Vlasov model, we have chosen 64 discretization points in the space and velocity directions, and a truncation of the velocity domain at the dimensionless maximum velocity $|v_{max}| = 6$. We use, for the discretization of the $M1$ model, 128 points in velocity, with a truncation of the velocity domain at the dimensionless maximum velocity $v_{max} = 7$. We choose $dt = 1/100$ for both the $M1$ and reference simulations.

In Fig. 7.8, both $M1$ and reference kinetic (formal fourth order) simulations have the same analytical instability growth rates, in the linear (A=0.001) and nonlinear (A=0.1) Landau damping as well. The numerical schemes, in the linear phase of the instability, exhibit a very accurate agreement with the theory. The Fig. 7.8 shows, first, the correct behaviour of the reduced model in the collective electrostatic regime, and second, the accurate numerical treatment of the $M1$ reduced model by our numerical scheme. For $A = 0.1$, the nonlinear phase of the instability, some discrepancies apprear between the models. We may conclude that the mixing of the particles in the phase space needs to be more accurately described than the one-group $M1$ model.

7.3.2 Two-Stream Instability

The Two-Stream Instability is triggered, in this section, with the following initial distribution function and electric field

$$\begin{aligned} f_e(t=0,x,v_x) &= \left[\frac{1}{2} + A\cos(k_x x)\right] f_M(n_0,T_0,v_0) + \left[\frac{1}{2} - A\cos(k_x x)\right] f_M(n_0,T_0,-v_0)\,, & (7.35)\\ E_x(t=0,x) &= 0\,, & (7.36)\end{aligned}$$

where $L_x =$, $k_x = 2\pi/L_x$, f_M is the nonrelativistic Maxwellian with non-zero drift velocityies $|v_0| = 4$, arbitrary density n_0, and initial temperature $T_0 = 1$. For the kinetic reference Vlasov model, we have chosen 64 discretization points in the space and velocity directions, and a truncation of the velocity domain at the dimensionless maximum velocity $|v_{max}| = 12$. We use, for the discretization of the $M1$ model,

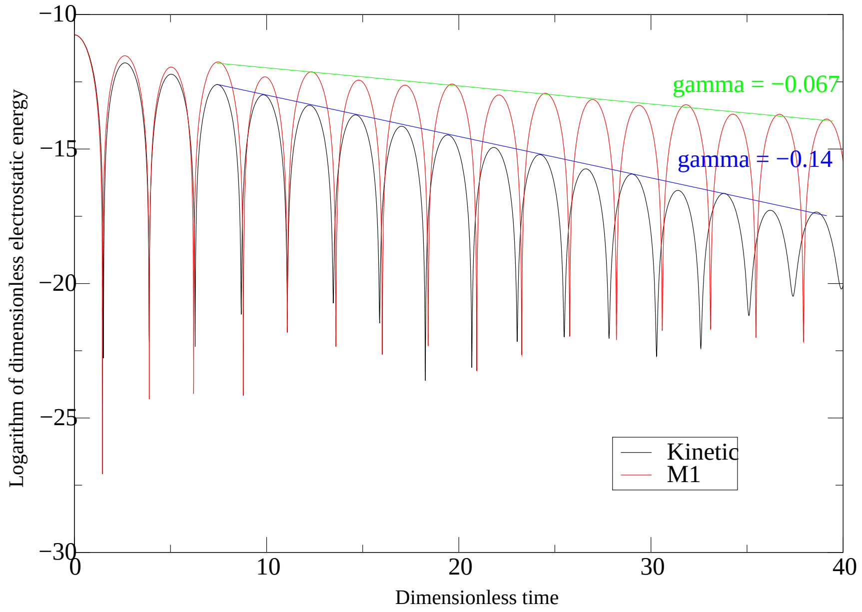

Figure 7.8: Comparison between the electronic $M1$ and reference kinetic solution

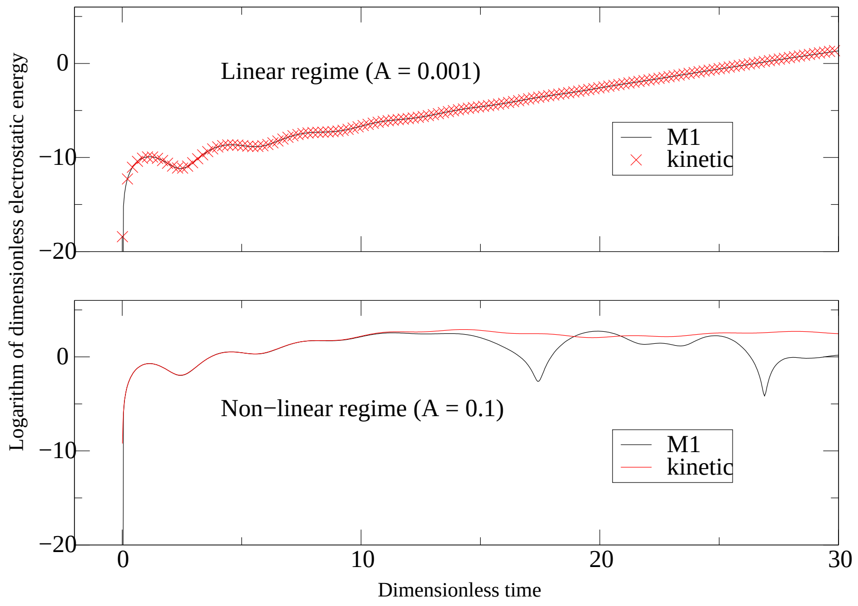

Figure 7.9: Comparison between the electronic $M1$ and reference kinetic solution

128 points in velocity, with a truncation of the velocity domain at the dimensionless maximum velocity $v_{max} = 7$. We choose $dt = 1/100$ for both the $M1$ and reference simulations.

In Fig. 7.9, both two-group $M1$ and reference kinetic (formal fourth order) simulations are consistent with respective analytical instability growth rates. The two groups are defined with positive and negative velocities, respectively. We have deliberately chosen a wavelenth number for which there exists a relatively large discrepancy between the analytical solutions issued from the dispersion relations of the reduced two-group $M1$ and reference Vlasov models. The Fig. 7.9 shows, first, the correct behaviour of the reduced model in the collective electrostatic regime, and second, the accurate numerical treatment of the $M1$ reduced model by our numerical scheme.

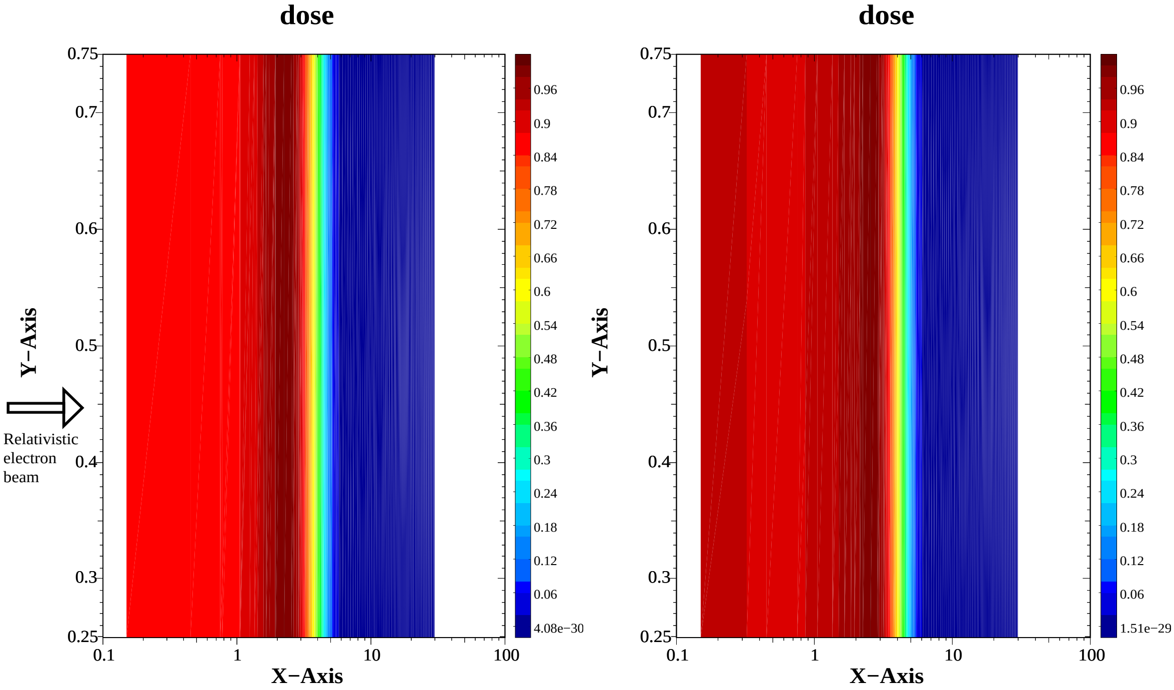

(a) Dose deposition with Møller scattering (b) Dose deposition without Møller scattering

Figure 7.10: The role of the relativistic electron inelastic collisions on dose deposition in water phantom

7.4 Standalone effects of ionization: the role of Møller inelastic scattering in radiotherapy and ICF

In this section, we investigate the effects of Møller inelastic scattering, related to large angle scattering, in water phantom, using the $M1$ model. The results show that the energy deposition is postponed in space (pushed forward with respect to the beam direction), and contributes to a non-diffuse localization of the energy deposition zone, for the stationnary solution. We finally present our results in relation with a Monte-Carlo simulation of electron transport in $D-T$, in the ICF context. Such simulation could be reproduced with less computational cost with the model present in Chapter 8.

7.4.1 The case of an electron beam propagation in water phantom for radiotherapy

The simulation parameters are the same as in the Sec. 7.2.5, except that the initial electron beam energy ϵ_{beam} is now valued 5 MeV. The Figures 7.10(a) and 7.10(b) suggest that the effect of the Møller scattering would be to push forward the dose deposition in the beam direction. As a consequence, the dose deposition is more peaked (less diffuse) than in the case where the Møller scattering is simply switched-off. We have shown here the importance of the large angle scattering, in a simple but representative $1D_x$ configuration.

7.4.2 The case of an electron beam propagation in $D-T$ for ICF

In this section, we present a Monte-Carlo simulation of relativistic electron propagation in $D-T$. This simulation is extracted from the HiPER technical report [68], and presented in relation of, first, the dose deposition of relativistic electron beam for radiotherapy, second, the model derived in the Chapter 8, that is able to describe the heating of a thermal plasma with collisions ranking from grazing to nongrazing (small to large angle), in a continuous manner.

The electron stopping power (7.37) and mean squared angular deflection (7.38) in $D-T$ is calculated using the Møller formula

$$\begin{aligned} \frac{\mathrm{d}E}{\mathrm{d}s} &= \frac{\mathrm{d}p}{\mathrm{d}t} = -\frac{4\pi n_e e^4}{m_e v^2}\left(\ln\frac{1.241\gamma(p) m_e v^2}{\hbar\omega_p\sqrt{\gamma(p)+1}} + \frac{0.409}{\gamma^2(p)} - \frac{0.818}{\gamma(p)}\right) \equiv \frac{D}{v^2(p)}\,, \qquad (7.37) \\ \frac{\mathrm{d}\left\langle\theta^2\right\rangle}{\mathrm{d}t} &= \frac{8\pi Z n_e e^4}{p^2 v(p)}\left[\ln\left(16.4\frac{\lambda_s}{\lambda_{Br}}\right) - 0.419\left(\frac{v(p)}{c}\right)^2\right], \qquad (7.38) \end{aligned}$$

where p, E, $v(p)$, $\gamma(p)$ are the momentum, energy, velocity and lorents factor of the fast electron. s is the distance along its path. λ_s is a screening length for the atoms or ions. λ_{Br} is the de Broglie wavelength of the fast electron. n_e and ω_{pe} are the electron density and plasma frequency of the $D-T$ medium.
If D is assumed constant, a simple solution can be obtained for the stopping distance s_{stop} and time t_{stop}

$$\begin{aligned} \mathrm{s_{stop}} &= \frac{E_0^2}{1.96E_0+1}\frac{1.56}{1-0.048\ln\rho} \quad \mathrm{g}\big/\mathrm{cm}^2 \qquad (7.39) \\ \mathrm{t_{stop}} &= \frac{m_e c^3}{D}\left(\frac{p_0}{m_e c} - \arctan\frac{p_0}{m_e c}\right), \qquad (7.40) \end{aligned}$$

where E_0 is the electron energy in MeV, ρ is the $D-T$ plasma density in $\mathrm{g}\big/\mathrm{cm}^2$.

An example of axial and radial energy deposition profiles for an MeV electron in 300 $\mathrm{g}\big/\mathrm{cm}^2$ $D-T$, calculated with a Monte-Carlo code using (7.37) and (7.38), is shown in Figure 7.11.

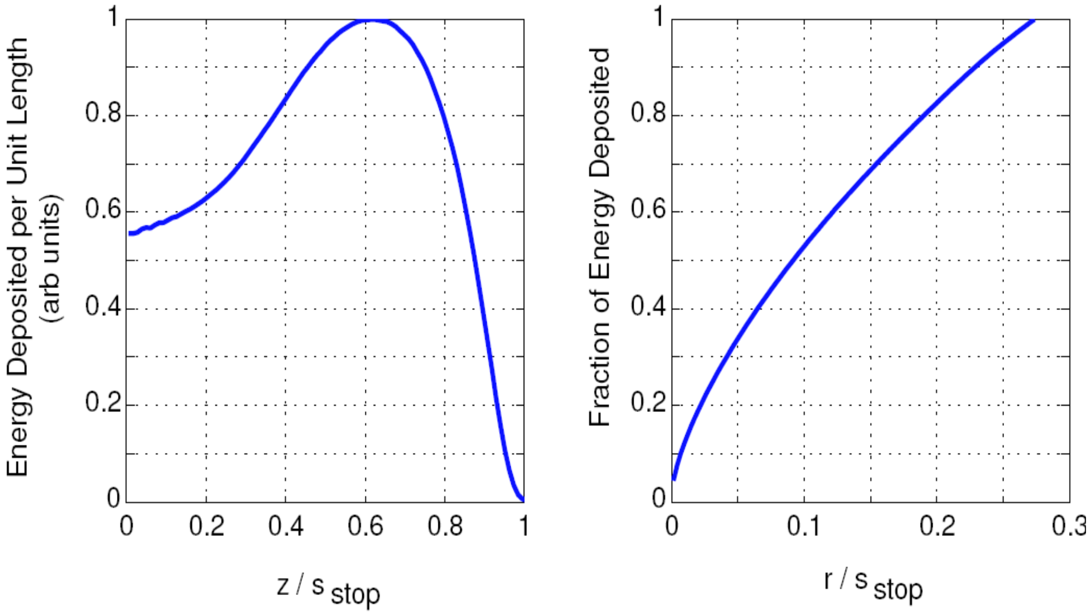

Figure 7.11: Average energy deposition profiles for an MeV electron in 300 $g\big/cm^2$ D-T. The z-axis is aligned along the initial direction of motion. These curves are exctracted from HiPER technical report [68]

The curve in Fig. 7.11 illustrates the similarity between the physics of electron transport in radiotherapy and the electron transport in ICF. Moreover it could stands as a reference simulation for the model we present in Chapter 8.

7.5 Conclusion

We have proposed in this chapter a reduced angular model, which is standard in terms of admissible states, and is appropriate for the description of the relativistic electron transport. It is valid in the collective or rarefied regimes, as well as in the collisional regime. Therefore its multi-group version should be well-suited for a multi-scale mesoscopic description of the electron transport in ICF plasma physics. A relevant HLLC scheme has been developped to account for the specific difficulties -in particular the flux limitation and contact discontinuities in $2D_{\mathbf{x}}$-, inherent to this $M1$-type system. We have proposed an analogy between electron transport in radiotherapy and ICF, and show the importance of collisions with large angle scattering in radiotherapy, then finally present a reference Monte-Carlo simulation for ICF (from the literature) that takes into account these effect, and could serve for a compararison with the model derived in the next Chapter 8.

Bibliography

[1] Agoshkov V., Boundary value problems for transport equations, *Birkhäuser, Boston* , (1998).

[2] Agoshkov V., On the existence of traces of functions in spaces used in transport theory problems, *Sov. Math. Dokl.* , 33, 628-632, (1986).

[3] Ahnesjö A. and Aspradakis M. M., Dose calculations for external photon beams in radiotherapy, *Phys. Med. Biol.* , 44, R99-R155, (1999).

[4] Ahnesjö A. and Saxner M. and Trepp A., A pencil beam model for photon dose calculation, *Med. Phys.*, 19, 263-273, (1992).

[5] Akcasu A. Z. and Holloway J. P., Fokker-Planck description of particle transport in finite media: Boundary conditions, *Phys. Rev. E* , 58, 4321-4331, (1998).

[6] Akcasu A. Z. and Larsen E. W., A statistical model for electron transport and dose calculations, *Ann. Nucl. Energy* , 23, 253-270, (1996).

[7] Alber M. and Nüsslin F., An objective function for radiation treatment optimization based on local biological measures, *Phys. Med. Biol.* , 44, 479-493, (1999).

[8] Alpen E. L., Radiation Biophysics, *Prentice Hall, Englewood Cliffs*, (1990).

[9] Andreo P., Monte Carlo techniques in medical radiation physics, *Phys. Med. Biol.* , 36, 861-920, (1991).

[10] Anile A. M. and Pennisi S. and Sammartino M., A thermodynamical approach to Eddington factors, *J. Math. Phys.* ,32, 544-550, (1991).

[11] Aydin E. D., Oliveira C. R. E., Goddard A. J. H., A comparison between transport and diffusion calculations using finite element-spherical harmonics radiation transport method, *Med. Phys.* ,29, 2013-2023, (2002).

[12] Batten P. and Clarke N. and Lambert C. and Causon D. M., *SIAM J. Sci. Comput.* , 18, 1553-1570, (1997).

[13] Bellomo N. and Maini P. K., Preface (special issue on cancer modelling), *Math. Mod. Math. Appl. Sci.* , 15, iii-viii, (2005).

[14] Bellomo N. and Maini P. K., Preface (special issue on cancer modelling), *Math. Mod. Math. Appl. Sci.* , 16, iii-vii, (2006).

[15] Bellomo N. and Maini P. K., Preface (special issue on cancer modelling), *Math. Mod. Math. Appl. Sci.* , 17, iii-vii, (2007).

[16] Berthon C., Stability of the MUSCL Schemes for the Euler Equations, *Comm. Math. Sci.* , 3, 133-157, (2005).

[17] Berthon C. and Charrier P. and Dubroca B., An HLLC Scheme to Solve the $M1$ Model of Radiative Transfer in Two Space Dimensions, *J. Sci. Comput.* , 31, 347-389, (2007).

[18] Börgers C., The radiation therapy planning problem, *IMA Volumes in Mathematics and its applications, Springer-Verlag*, 110, (1999).

[19] Börgers C., Complexity of Monte Carlo and Deterministic Dose-Calculation Methods *Phys. Med. Biol.* , 43, 517-528, (1998).

[20] Börgers C. and Larsen E. W.,Asymptotic Derivation of the Fermi Pencil-Beam Approximation, *Nucl. Sci. Eng.* , 123, 343-357, (1996).

[21] Bortfeld T.,Dosiskonformation in der Tumortherapie mit externer ionisierender Strahlung: Physikalische Möglichkeiten und Grenzen, *Habilitationsschrift der Ruprechts-Karls-Universität Heidelberg* ,

[22] Börgers C. and Larsen E. W.,On the accuracy of the Fokker-Planck and Fermi pencil-beam equations for charged particle transport , *Med. Phys.* , 23, 1749-175, (1996).

[23] Börgers C. and Larsen E. W.,Asymptotic derivation of the Fermi pencil-beam approximation , *Nucl. Sci. Eng.* ,2123, 343-357, (1996).

[24] Börgers C. and Larsen E. W.,The transversely integrated scalar flux of a narrowly focused particle beam , *SIAM J. Appl. Math.* , 55, 1-22, (1995).

[25] Bortfeld T. and Schlegel W.and Rhei B.,Decomposition of pencil beam kernels for fast dose calculations in three-dimensional treatment planning, *Med. Phys.* , 20, 311-318, (1993).

[26] Brunner T. A. and Holloway J. P., One-dimensional Riemann solvers and the maximum entropy closure, *J. Quant. Spectrosc. Radiat. Transfer* , 69, 543-566, (2001).

[27] Bucci K. K., Bevan A. and Roach M. III,Advances in radiation therapy: conventional to 3d, to IMRT, to 4D, and beyond, *CA Cancer J. Clin.* , 55, 117-134, (2005).

[28] Buet C. and Deprés B., Asymptotic preserving and positive schemes for radiation hydrodynamics, *J. Comput. Phys.*, 215, 717-740, (2006).

[29] Byun S.H. ,Advanced Radiation Physics, *Lecture Notes Med-Phys-775, McMaster University, http://www.science.mcmaster.ca/medphys/classes/graduate/MedPhys-775.php* , (2005).

[30] Calamai P.H. and Mor J. J., Projected gradient methods for linearly constrained problems , *Math. Program.*,39, 93, (1987).

[31] Case K. M. and Zweifel P. F., Linear Transport Theory, *Addison-Wesley* , (1967).

[32] Censor Y., Preface: Linear and nonlinear models and algorithms in Intensity-modulated radiation therapy (IMRT), *Lin. Alg. Appl.*, 428, 1203-1205, (2008).

[33] Cercignani C., The Boltzmann Equation and Its Applications, *Springer-Verlag, New York*, (1988).

[34] Chandrasekhar S.,Radiative Transfer , *Dover*, (1950).

[35] Cheng P., Dynamics of a radiating gas with applications to flow over a wavy wall, *AIAA Journal* ,4, 238-24 (1966).

[36] Clause P.-J. and Mareschal M., Heat Transfer in a gas between parallel plates: Moment method and molecular dynamics, *Phys. Rev. A* , 38, 4241-4252, (1988).

[37] Coulombel J.-F. and Golse F. and Goudon T., Diffusion approximation and entropy-based moment closure for kinetic equations, *Asymptotic Analysis*, 45, 1-39, (2005).

[38] Coulombel J.-F., Goudon T., Entropy-based moment closure for kinetic equations: Riemann problem and invariant regions, *J. Hyperbolic Diff. Eq.* , 3, 649-672, (2006).

[39] Dautray R. and Lions J. L., Mathematical Analysis and Numerical Methods for Science and Technology (v.6), *Springer, Paris* , (2007).

[40] Dautray R. and Lions J. L., Analyse mathematique et calcul numerique pour les sciences et les techniques (v.6), *Masson, S.A., Paris*, (1985).

[41] Davison B., Neutron transport theory, *Oxford: Oxford University Press*, (1957).

[42] Davisson C. M. and Evans R. D., Gamma-Ray Absorption Coefficients, *Rev. Mod. Phys.* , 24, 79, (1952).

[43] Dreye W., Maximisation of the entropy in non-equilibrium, *J. Phys. A* , 20, 6505-6517, (1987).

[44] Dubroca B., Habilitation à diriger des recherches, , (2000).

[45] Dubroca B. and Feugeas J.-L., Entropic Moment Closure Hierarchy for the Radiative Transfer Equation, *C. R. Acad. Sci. Paris Ser. I* , 329, 915-920, (1999).

[46] Dubroca B., Frank M., Klar A.and Thömmes G., Half space moment approximation to the radiative heat transfer equations, *ZAMM* , 83, 853-858, (2003).

[47] Dubroca B. and Frank M.,An Iterative Method for Transport Equations in Radiotherapy, *submitted to Proceedings of ECMI 08*, (2009).

[48] Dubroca B. and Klar A., Half moment closure for radiative transfer equations, *J. Comput. Phys.* , 180, 584-596, (2002).

[49] Eddington A., The Internal Constitution of the Stars, *Dover* , (1926).

[50] Eyges L., Multiple Scattering with energy loss, *Phys. Rev.* , 74, 1534-1535, (1948).

[51] Fasso A. and Goebel K. and Höfert M. and Ranft J. and Stevenson G., Shielding Against High Energy Radiation, *Landolt-Börnstein Numerical Data and Functional Relationships in Science and Technology, Springer-Verlag, Schopper H., New Series, Berlin, Heidelberg, New York, London, Paris, Tokyo, Hong Kong, Barcelona*, 11.

[52] Fischer A. E. and Marsden J. E., The Einstein Evolution Equations as a First-Order Quasi-Linear Hyperbolic System I, *Commun. Math. Phys.* , 26, 1-38, (1972).

[53] Frank M. and Hensel H. and Klar A., A fast and accurate moment method for dose calculation in electron radiotherapy, *SIAM J. Appl. Math.* , 67, 582-603, (2007).

[54] Frank M. and Pinnau R., Existence, Uniqueness and bounds for the half moment minimum entropy approximation to rediative heat transfer, *Appl. Math. Lett.* , 20, 189-193, (2007).

[55] Frank M. and Seaïd M., Janicka J., Klar A. and Pinnau R., A comparison of approximate models for radiation in gas turbines, *Progress in Computational Fluid Dynamics* , 4, 191-197, (2004).

[56] Gelbard E. M., Simplified spherical harmonics equations and their use in shielding problems, *Bettis Atomic Power Laboratory* , WAPD-T-118,j (1961).

[57] Gentile N. A., Implicit Monte Carlo Diffusion-An Acceleration Method for Monte Carlo Time-Dependent Radiative Transfer Simulations, *J. Comput. Phys.* , 172, 543-571, (2001).

[58] Gifford K. A., Horton J. L. Jr., Wareing T. A., Failla G. and Mourtada F., Comparison of a finite-element multigroup discrete-ordinates code with Monte Carlo for radiotherapy calculations, *Phys. Med. Biol.* , 51, 2253-2265, (2006).

[59] Golse F. and Perthame B., Generalized solution of the radiative transfer equations in a singular case, *Commun. Math. Phys.* , 106, 211-239, (1986).

[60] Gonzales-Rodriguez P. and Kim A. D., Light propagation in tissues with forward-peaked and large-angle scattering, *Appl. Opt.* , 47, 2599-2609, (2008).

[61] Gustafsson A., Development of a versatile algorithm for optimization of radiation therapy, *Department of Medical Radiation Physics, Stockholm* , (1996).

[62] Gustafsson A., Lind B. K. and Brahme A., A generalized pencil beam algorithm for optimization of radiation therapy, *Med. Phys.* , 21, 343-356, (1994).

[63] Harten A. and Lax P.D. and van Leer B., On Upstream Differencing and Godunov-Type Schemes for Hyperbolic Conservation Laws, *SIAM Rev.* , 25, 35-61, (1983).

[64] Hauck C. D., Levermore C. D. and Tits A. L., Convex Duality in Entropy-Based Moment Closures: Characterizing Degenerate Densities, *SIAM J. Control Optim.* , 47, 1977-2015, (2008).

[65] Hensel H.,Iza-Teran R. and Siedow N., Deterministic model for dose calculation in photon radiotherapy, *Phys. Med. Biol.* , 51, 675-693, (2006).

[66] Herty M., Pinnau R. and Seaid M. , Optimal Control in Radiative Transfer, *to appear in OMS* , (2007).

[67] Herty M., Pinnau R. and Thömmes G., Asymptotic and Discrete Concepts for Optimal Control in Radiative Transfer, *to appear in ZAMM* , (2007).

[68] HiPER technical report, Fusion Science case and design *Technical Background and Conceptual Design, version 1.0*.

[69] Hogstrom K. R., Mills M. D. and Almond P. R., Electron beam dose calculations, *Phys. Med. Biol.* , 26, 445-459, (1981).

[70] Huizenga H. and Storchi P. R. M., Numerical Calculation ofEnergy Deposition by Broad High-Energy Electron Beams, *Phys. Med. Biol.* , 34, 1371, (1989).

[71] Janssen J. J., Riedeman D.E.J, Morawska-Kaczynska M., Storchi P. R. M. and Huizenga H., Numerical Calculation ofEnergy Deposition by Broad High-Energy Electron Beams: III. Three-Dimensional Heterogeneous Media, *Phys. Med. Biol.* , 39, 1351, (1994).

[72] Jaynes E. T., Information theory and statistical mechanics, *Phys. Rev.* , 106, 620-630, (1957).

[73] Jeans J. H., The equations of radiative transfer of energy, *Monthly Notices Royal Astronomical Society* , 78, 28-36, (1917).

[74] Jette D., Electron dose calculations using multiple-scattering theory. A new theory of multiple scattering, *Med. Phys.* , 23, 459-477, (1996).

[75] Jette D., Electron dose calculations using multiple-scattering theory. A. Gaussian multiple-scattering theory, *Med. Phys.* , 15, 123-137, (1988).

[76] Johns H. E. J. and Cunningham J. R., The Physics of Radiology, *4th, Charles C. Thomas Publisher, Springfield*, (1983).

[77] Junk M., Maximum entropy for reduced moment problems, *Math. Meth. Mod. Appl. Sci.* , 10, 1001-1025, (2000).

[78] Junk M. and Unterreiter A., Maximum Entropy Moment Systems and Galilean Invariance, *Continuum Mech. Thermodyn.* , 14, 563-576, (2002).

[79] Kawrakow I. and Rogers D. W. O., The EGSnrc Code System, *NRCC, Report PIRS-701*, (2002).

[80] Kelley C.T., Iterative methods for optimization, *SIAM Frontiers in Applied Mathematics* , (1999).

[81] Kelley C.T., Existence and uniqueness of solutions of nonlinear systems of conductive radiative heat transfer equations, *Transp. Theory Stat. Phys.* , 25, 249-260, (1996).

[82] Koch R., Krebs W., Wittig S. and Viskanta R., The discrete ordinate quadrature schemes for multidimensional radiative transfer, *J. Quant. Spectrosc. Radiat. Transfer* , 53, 353-372, (1995).

[83] Korganoff V., Basic methods in transfer problems, *Dover* , (1963).

[84] Kremer G. M. and Müller I., Radiation Thermodynamics, *J. Math. Phys.* , 33, 2265-2268, (1992).

[85] Krook M., On the Solution of Equations of Transfer, *Astrophys. J.* , 122, 488, (1955).

[86] Kunisch K. and Rösch A., Primal–dual active set strategy for a general class of constrained optimization problems, *SIAM J. on Optimization* , 13, 321-334, (2002).

[87] Laitinen M. T. and Tiihonen T. , Conductive-Radiative Heat Transfer in Grey Materials, *Quart. Appl. Math.* , 59, 737-768, (2001).

[88] Laitinen M. T. and Tiihonen T., Integro-differential equation modelling heat transfer in conducting, radiating and semitransparent materials, *Math. Meth. Appl. Sci.* , 21, 375-392, (1998).

[89] Larsen E. W., Tutorial: The nature of transport calculations used in radiation oncology, *Transp. theory Stat. Phys.* , 26, 739, (1997).

[90] Larsen E. W.and Keller J. B., Asymptotic Solution of Neutron Transport Problems for Small Mean Free Path, *J. Math. Phys.* , 15, 75, (1974).

[91] Larsen E. W., Miften M. M., Fraass B. A. and Bruinvis I. A. D. , Electron dose calculations using the method of moments, *Med. Phys.* , 24, 111-125, (1997).

[92] Larsen E. W. and Thömmes G. and Klar A., New Frequency–Averaged Approximations to the Equations of Radiative Heat Transfer, *SIAM J. Appl. Math.* , 64, 565-582, (2003).

[93] Larsen E. W., Thömmes G., Klar A., Seaïd M. and Götz T., Simplified P_N Approximations to the Equations of Radiative Heat Transfer in Glass, *J. Comput. Phys.* , 183, 652–675, (2002).

[94] Levermore C. D., Moment Closure Hierarchies for Kinetic Theories, *J. Stat. Phys.* , 83, 1021-1065, (1996).

[95] Levermore C. D., Relating Eddington Factors to Flux Limiters, *J. Quant. Spectrosc. Radiat. Transfer* , 31, 149-160, (1984).

[96] Liu P., A new phase function approximation to Mie scattering for radiative transport equations, *Phys. Med. Biol.* , 39, 1025-1036, (1994).

[97] Lopez-Pouso 0., Trace theorem and existence in radiation, *Adv. Math. Sci. Appl.* , 10, 757-773, (2000).

[98] Luenberger, D. G., Optimization by vector space methods, *John Wiley&Sons, Inc., New York, London, Sydney, Toronto,* (1969).

[99] Mark J. C., The spherical harmonics method, Part II, *National Research Council of Canada* , MT 97, (1945).

[100] Mark J. C., The spherical harmonics method, Part I, *National Research Council of Canada* , MT 92, (1944).

[101] Marshak R. E., Note on the Spherical Harmonic Method as applied to the Milne problem for a sphere, *Phys. Rev.* , 71, 443-446, (1947).

[102] Mascali G., Romano V., Maximum entropy principle in relativistic radiation hydrodynamics, *Ann. Inst. Henri Poincaré* 67, 2, 123-144, (1997).

[103] Mascali G., Maximum entropy principle in relativistic radiation hydrodynamics II: Compton and double Compton scattering, *Continuum Mech. Thermodyn.* 14, 549-561, (2002).

[104] Mengüc M. P. and Iyer R. K., Modeling of Radiative Transfer Using Multiple Spherical Harmonics Approximations, *J. Quant. Spectrosc. Radiat. Transfer* , 39, 445-461, (1988).

[105] Mercier B., Application of accretive operators theory to the radiative transfer equations, *SIAM J. Math. Anal.* , 18, 393-408, (1987).

[106] Mihalas D. and Weibel-Mihalas B., Foundations of radiation hydrodynamics, *Dover* , (1999).

[107] Minerbo G. N., Maximum entropy Eddington factors, *J. Quant. Spectrosc. Radiat. Transfer* , 20, 541-545, (1978).

[108] Modest M. F., Radiative Heat Transfer, *2nd, Academic Press* , (1993).

[109] Morawska-Kaczynska M. and Huizenga H., Numerical Calculation of Energy Deposition by Broad High-Energy Electron Beams: II. Multi-Layered Geometry, *Phys. Med. Biol.* , 37, 2103, (1992).

[110] More J. J. and Toraldo G., Algorithms for bound constraint quadratic programming problems, *Numer. Math.* , 55, 377, (1989).

[111] Morel J. E. and McGhee J. M., A Three-Dimensional Time-Dependent Unstructured Tetrahedral-Mesh SP_N Method, *Nucl. Sci. Eng.* , 123, 319-327, (1996).

[112] Murray R. L., Nuclear Reactor Physics, *Prentice Hall*, (1957).

[113] Müller I. and Ruggeri T., Rational Extended Thermodynamic, *2nd, New York, Springer-Verlag* , (1993).

[114] Ore A., Entropy of radiation, *Phys. Rev.* , 98, 887, (1955).

[115] Pautz S. D. and Adams M. L., An asymptotic study of discretized transport equations in the Fokker-Planck limit, *Nucl. Sci. Eng.* , 140, 51-69, (2002).

[116] Pomraning G. C., Asymptotic and variational derivations of the Simplified P_N equations, *Ann. Nuclear Energy* , 20, 623, (1993).

[117] Pomraning G. C., The Fokker-Planck operator as an asymptotic limit, *Math. Mod. Meth. Appl. Sci.* , 2, 21-36, (1992).

[118] Pomraning G. C., The equations of radiation hydrodynamics, *Pergamon Press* , (1973).

[119] Porzio M. M. and Lopez-Pouso O., Application of accretive operators theory to evolutive combined conduction, convection and radiation, *Rev. Mat. Iberoam.* , 20, 257-275, (2004).

[120] Ripoll J.-F., An averaged formulation of the M1 radiation model with mean absorption coefficients and presumed probability density functions for turbulent flows, *J. Quant. Spectrosc. Radiat. Transfer* , 83, 493-517, (2004).

[121] Ripoll J.-F. and Wray A. A., A half-moment model for radiative transfer in a 3D gray medium and its reduction to a moment model for hot, opaque sources, *J. Quant. Spectrosc. Radiat. Transfer* , 93, 473-519, (2005).

[122] Rosen P., Entropy of Radiation, *Phys. Rev.*, 96, 555, (1954).

[123] Rosseland S., Theoretical Astrophysics: Atomic Theory and the Analysis of Stellar Atmospheres and Envelopes, *Clarendon Press* , (1936).

[124] Rossi B. and Greise K., Cosmic-ray theory , *Rev. Mod. Phys*, 13, 240-309, (1941).

[125] Salvat F. and Fernandez-Varea J. M. and Sempau J., PENELOPE-2008, A Code System for Monte Carlo Simulation of Electron and Photon Transport , ISBN 978-92-64-99066-1, OECD, (2008).

[126] Scherrer A., Küfer K.-h., Bortfeld Th.,Monz M. and Alonso F., IMRT planning on adaptive volume structures - a breakthrough in computational complexity, *Phys. Med. Biol.* , submitted.

[127] Schuster A., Radiation through a foggy atmosphere, *Astrophys. J.* , (1905).

[128] Schwarzschild K., Über das Gleichgewicht von Sonnenatmosphären, *Akad. Wiss. Göttingen, Math. Phys. Kl. Nachr.* , 195, 41-53, (1906).

[129] Schäfer M., Teilraum P_N-Modelle für Strahlungstransport, *TU Darmstadt* , (2004).

[130] Schäfer M., Frank M. and Pinnau R., A HIERARCHY OF APPROXIMATIONS TO THE RADIATIVE HEAT TRANSFER EQUATIONS: MODELLING, ANALYSIS AND SIMULATION, *Math. Meth. Mod. Appl. Sci.* , 15, 643-665, (2005).

[131] Seaïd M., Frank M., Klar A., Pinnau R. and G. Thömmes, Efficient numerical methods for radiation in gas turbines, *J. Comput. Appl. Math.* , 170, 217-239, (2004).

[132] Sempau J. and Wilderman S. J. and Bielajew A. F., DPM - a fast, accurate Monte Carlo code optimized for photon and electron radiotherapy treatment planning dose computations, *Phys. Med. Biol.*, 45, 2262-2291, (2000).

[133] Shepard D. M., Ferris M. C., Olivera G. H. and Mackie T. R, Optimizing the delivery of radiation therapy to cancer patients, *SIAM Rev.* , 41, 721-744, (1999).

[134] Sherman M. P., Moment Methods in Radiative Transfer Problems, *J. Quant. Spectrosc. Radiat. Transfer* , 7, 89-109, (1967).

[135] Spellucci P., Numerische Verfahren der nichtlinearen Optimierung, *Birkhäuser Verlag, Basel, Boston, Berlin* , (1993).

[136] Frank M., Klar. A., Larsen E.W. and Yasuda S.,Time-dependent Simplified PN Approximation to the Equations of Radiative Transfer, *J. Comput. Phys.* , 226, 2289-2305, (2007).

[137] Kuefer K.-H. *et al.*, Multicriteria optimization in intensity modulated radiotherapy planning, *Handbook of Optimization in Medicine, Pardalos P.M. and Romeijn H.E.* , (to appear).

[138] Lehmann C., Interaction of radiation with solids and elementary defect production, *North Holland* , (1977).

[139] Mott N. F. and Massey H. S. W., The theory of atomic collisions, *Clarendon Press* , (1965).

[140] Özisik M. N. and Menning J. and Hälg W., Half-Range Moment Method for Solution of the Transport Equation in a Spherical Symmetric Geometry, *J. Quant. Spectrosc. Radiat. Transfer* , 15, 1101-1106, (1975).

[141] Reich H. (Hrsg.), Dosimetrie ionisierender Strahlung, *Stuttgart, Teubner B. G.*, (1990).

[142] Storchi P.R.M. and Huizenga H., On a Numerical Approach of the Pencil Beam Model, *Phys. Med. Biol.*, 30, 467, (1985).

[143] Struchtrup H., Levermore Eddington Factor and Entropy Maximization, *unpublished* .

[144] Struchtrup H., On the Number of Moments in Radiative Transfer Problems, *Ann. Phys. (N.Y.)* , 266, 1-26, (1998).

[145] Struchtrup H., An Extended Moment Method in Radiative Transfer: The Matrices of Mean Absorption and Scattering Coefficients, *Ann. Phys. (N.Y.)* , 257, 111-135, (1997).

[146] Sykes J. B., Approximate Integration of the Equation of Transfer, *Monthly Notices of the Royal Astronomical Society* , 111, 377, (1951).

[147] Tervo J.and Kolmonen P., Inverse radiotherapy treatment planning model applying Boltzmann-transport equation, *Math. Models. Methods. Appl. Sci.* , 12, 109-141, (2002).

[148] Tervo J., Kolmonen P., Vauhkonen M., Heikkinen L. M. and Kaipio J. P., A finite-element model of electron transport in radiation therapy and related inverse problem, *problem*, 15, 1345-1361 , (1999).

[149] Tervo J. and Vauhkonen M. and Boman E., Optimal control model for radiation therapy inverse planning applying the Boltzmann transport equation, *Lin. Alg. Appl.*, 428, 1230-1249, (2008).

[150] Thömmes G., Radiative Heat Transfer Equations for Glass Cooling Problems: Analysis and Numerics, *TU Darmstadt* , (2002).

[151] Tröltzsch F., Optimale Steuerung partieller Differentialgleichungen - Theorie, Verfahren und Anwendungen, *Vieweg Verlag* , (2005).

[152] Turpault R., A consistent multigroup model for radiative transfer and its underlying mean opacities, *J. Quant. Spectrosc. Radiat. Transfer* , 94, 357-371, (2005).

[153] Turpault R., Modelisation, approximation numérique et applications du transfert radiatif en déséquilibre spectral couplé avec l'hydrodynamique, *Université Bordeaux I* , (2003).

[154] Turpault R., Construction d'une modèle M1-multigroupe pour les équations du transfert radiatif, *C. R. Acad. Sci. Paris Ser. I* , 334, 1-6, (2002).

[155] Turpault R., Frank M., Dubroca B. and Klar A. , Multigroup Half Space Moment Approximations to the radiative heat transfer equations, *J. Comput. Phys.* , 198, 363-371, (2004).

[156] Ulmer W. and Harder D., A Triple Gaussian Pencil beam Model for Photon beam Treatment Planning, *Z. Med. Phys.* , 5, 25-30, (1995).

[157] van Leer B., Towards the ultimate conservative difference scheme V: A second-order sequel to Godunov's method, *J. Comput. Phys.* , 32, 101-136, (1979).

[158] Williams M. M. R., The role of the Boltzmann transport equation in radiation damage calculations, *Prog. Nucl. Energy* , 3, 1-65, (1979).

[159] Zerby C. D. and Keller F. L., Electron transport theory, calculations and experiments, *Nucl. Sci. Eng.* , (1967).

7.6 Appendix: Explicit formulas for the cross sections

This appendix lists all scattering cross sections that are used in the Boltzmann model. All cross sections are calculated for the laboratory system where the scattering centers are at rest before scattering. Except for elastic Mott scattering, all differential scattering cross sections are differential in energy and in solid angle. They can be decomposed into a product of a cross section, that is only differential in solid angle or energy and a Dirac delta function, that guarantees energy and momentum conservation during the scattering event. The Mott cross section is only differential in solid angle. Total cross sections are calculated by integrating the double differential cross sections with respect to energy and solid angle. Because of the delta functions one integration is always trivial.

For all differential cross sections the following conventions are used: quantities with a prime belong to incoming particles, quantities without a prime to outgoing particles in a scattering event. The order of appearence in all differential cross sections is: energy of incoming (ϵ'), energy of outgoing (ϵ), direction of incoming (Ω'), direction of outgoing particles (Ω). To simplify notation and to keep the standard notation used in literature we use $\Omega' \cdot \Omega = \cos\vartheta \equiv \mu$, ϑ being the scattering angle in the laboratory system. Additionally we keep $\sin\vartheta$ and $\tan\vartheta$ in formulas, to maintain a handy notation. The relationship to $\cos\vartheta$ is evident. Furthermore it should be kept in mind that $\epsilon_\mathrm{B} = \epsilon_\mathrm{B}(r)$ which is not explicitly written to keep notation short. In all formulas the classical electron radius $r_\mathrm{e} = 2.8179 \cdot 10^{-15}$ m appears.

7.6.1 Differential cross section for Møller scattering

Due to kinematical reasons of the scattering processes the range of solid angles in Møller (electron-electron) scattering is restricted. The electron, which has the higher energy after the collision is called primary electron, the other electron secondary. Here, an incoming electron with energy ϵ' hits an electron at rest. After the collision, the angle between the directions of the electrons is at most $\pi/2$. Electrons are indistinguishable. For an angle in $[0, \pi/4]$, the electron with energy ϵ is the primary electron, for an angle in $[\pi/4, \pi/2]$, it is the secondary electron. Therefore the Møller cross section can be written as

$$\sigma_M = \tilde{\sigma}_M \chi_{0<\Omega\cdot\Omega'<\sqrt{2}/2} + \tilde{\sigma}_{M,\delta}\chi_{\sqrt{2}/2<\Omega\cdot\Omega'<1},$$

where χ denotes the characteristic function of a set, $\tilde{\sigma}_M$ is the Møller differential cross section of primary electrons and $\tilde{\sigma}_{M,\delta}$ is the Møller differential cross section of secondary electrons.

7.6.2 Differential cross section for Møller scattering of primary electrons, i.e. $\epsilon > (\epsilon' - \epsilon_{\mathrm{B}})/2$ [79]

$$\tilde{\sigma}_{\mathrm{M}}(\epsilon', \epsilon, \Omega' \cdot \Omega) = \sigma_{\mathrm{M}}(\epsilon', \epsilon)\delta_{M}(\mu_{\mathrm{e}}, \mu_{p})\frac{1}{2\pi}, \quad \mu_{\mathrm{e}} = \Omega' \cdot \Omega$$

with

$$\sigma_{\mathrm{M}}(\epsilon', \epsilon) = \frac{2\pi r_{\mathrm{e}}^{2}(\epsilon' + 1)^{2}}{\epsilon'(\epsilon' + 2)}\left[\frac{1}{\epsilon^{2}} + \frac{1}{(\epsilon' - \epsilon)^{2}} + \frac{1}{(\epsilon' + 1)^{2}} - \frac{2\epsilon' + 1}{(\epsilon' + 1)^{2}\epsilon(\epsilon' - \epsilon)}\right]$$

$$\delta_{M}(\mu_{\mathrm{e}}, \mu_{p}) = \delta\left(\mu_{\mathrm{e}} - \sqrt{\frac{\epsilon}{\epsilon'}\frac{\epsilon' + 2}{\epsilon + 2}}\right), \quad \epsilon > \frac{(\epsilon' - \epsilon_{\mathrm{B}})}{2}$$

7.6.3 Differential cross section for Møller scattering of secondary electrons, i.e. $\epsilon < (\epsilon' - \epsilon_{\mathrm{B}})/2$ [79]

$$\tilde{\sigma}_{\mathrm{M},\delta}(\epsilon', \epsilon, \Omega' \cdot \Omega) = \sigma_{\mathrm{M}}(\epsilon', \epsilon)\delta_{\mathrm{M},\delta}(\mu_{\mathrm{e}}, \mu_{\delta})\frac{1}{2\pi}, \quad \mu_{\mathrm{e}} = \Omega' \cdot \Omega$$

with

$$\begin{aligned} \sigma_{\mathrm{M}}(\epsilon', \epsilon) &= \frac{2\pi r_{\mathrm{e}}^{2}(\epsilon' + 1)^{2}}{\epsilon'(\epsilon' + 2)}\left[\frac{1}{\epsilon^{2}} + \frac{1}{(\epsilon' - \epsilon)^{2}} + \frac{1}{(\epsilon' + 1)^{2}} - \frac{2\epsilon' + 1}{(\epsilon' + 1)^{2}\epsilon(\epsilon' - \epsilon)}\right] \\ \delta_{\mathrm{M},\delta}(\mu_{\mathrm{e}}, \mu_{\delta}) &= \delta\left(\mu_{\mathrm{e}} - \sqrt{\frac{\epsilon}{\epsilon'}\frac{\epsilon' + 2}{\epsilon + 2}}\right), \quad \epsilon < \frac{(\epsilon' - \epsilon_{\mathrm{B}})}{2} \end{aligned}$$

7.6.4 Total cross section for Møller scattering of electrons [79]

$$\sigma_{\mathrm{M}}^{\mathrm{tot}}(\epsilon) = \int\limits_{\epsilon_{\mathrm{B}}}^{(\epsilon - \epsilon_{\mathrm{B}})/2} \sigma_{\mathrm{M}}(\epsilon, \epsilon')d\epsilon'$$

The lower limit of integration is due to the fact that the primary electron can only be scattered if at least the binding energy ϵ_{B} is transferred to the secondary electron (of a tissue molecule). Besides the evident motivation of this choice based on our model, this is a standard way to avoid singularities in calculating total cross sections (see *e.g.* [158]). The upper limit of integration is due to the fact that the primary electron has larger energy than the secondary electron and that the binding energy ϵ_{B} was introduced into the scattering processes (usually the upper limit is $\epsilon'/2$). One gets:

$$\begin{aligned} \sigma_{\mathrm{M}}^{\mathrm{tot}}(\epsilon) &= \frac{2\pi r_{\mathrm{e}}^{2}(\epsilon + 1)^{2}}{\epsilon(\epsilon + 2)} \\ &\times \left\{\frac{1}{\epsilon_{\mathrm{B}}} - \frac{3}{\epsilon - \epsilon_{\mathrm{B}}} + \frac{2}{\epsilon + \epsilon_{\mathrm{B}}} + \frac{\epsilon - 3\epsilon_{\mathrm{B}}}{2(\epsilon + 1)^{2}} + \frac{2\epsilon + 1}{\epsilon(\epsilon + 1)}g[\ln\frac{\epsilon + \epsilon_{\mathrm{B}}}{\epsilon - \epsilon_{\mathrm{B}}} - \ln\frac{\epsilon - \epsilon_{\mathrm{B}}}{\epsilon_{\mathrm{B}}}g]\right\} \end{aligned}$$

7.6.5 Differential cross section for Mott scattering of electrons [139, 138]

$\alpha \approx 1/137$ is the fine structure constant, Z is the atomic number of the irradiated medium. Z depends on r to account for heterogeneous media.

$$\begin{aligned}\sigma_{\mathrm{Mott}}(r,\epsilon,\Omega'\cdot\Omega) &= \frac{Z^2(r)r_{\mathrm{e}}^2(mc^2)^2}{4p^2c^2\beta^2\sin^4\frac{\vartheta_{\mathrm{e}}}{2}}\left[1-\beta^2\sin^2\frac{\vartheta_{\mathrm{e}}}{2}+Z\pi\alpha\beta\sin\frac{\vartheta_{\mathrm{e}}}{2}\left(1-\sin\frac{\vartheta_{\mathrm{e}}}{2})\right)\right]\\ &\approx \frac{Z^2(r)r_{\mathrm{e}}^2(mc^2)^2}{4p^2c^2\beta^2\sin^4\frac{\vartheta_{\mathrm{e}}}{2}}\left[1-\beta^2\sin^2\frac{\vartheta_{\mathrm{e}}}{2}\right],\end{aligned}$$

with $\beta^2 = \frac{\epsilon(\epsilon+2)}{(\epsilon+1)^2}$. The last approximation is justified, because in the energy range studied here and for typical low-Z media like water only small errors are made.

To avoid the singularity at $\vartheta_{\mathrm{e}} = 0$ a screening parameter η can be introduced [159] that models the screening effect of the electrons of the atomic shell:

$$\sigma_{\mathrm{Mott}}(r,\epsilon,\Omega'\cdot\Omega) = \frac{Z^2(r)r_{\mathrm{e}}^2(1+\epsilon)^2}{4[\epsilon(\epsilon+2)]^2(1+2\eta(r,\epsilon)-\cos\vartheta_{\mathrm{e}})^2}\left[1-\frac{\epsilon(\epsilon+2)}{(1+\epsilon)^2}\sin^2\frac{\vartheta_{\mathrm{e}}}{2}\right]$$

with

$$\eta(r,\epsilon) = \frac{\pi^2\alpha^2 Z^{\frac{2}{3}}(r)}{\epsilon(\epsilon+2)}$$

7.6.6 Total cross section for Mott scattering of electrons

$$\begin{aligned}\sigma_{\mathrm{Mott}}^{\mathrm{tot}}(r,\epsilon_{\mathrm{e}}) &= \frac{\pi(Z(r)r_{\mathrm{e}})^2}{\epsilon(\epsilon+2)}\\ &\times \left[\frac{(\epsilon+1)^2}{(\pi\alpha)^2Z^{2/3}(r)(1+\eta(r,\epsilon_{\mathrm{e}}))}+\frac{1}{1+\eta(r,\epsilon_{\mathrm{e}})}+\ln\eta(r,\epsilon_{\mathrm{e}})-\ln(1+\eta(r,\epsilon_{\mathrm{e}}))\right]\end{aligned}$$

Chapter 8

From classic to relativistic: extension of the model to high energy electrons, questioning grazing collisions.

8.1 Introduction

Large-scale, high intensity laser installations [6, 19, 12, 20, 41, 40] can achieve highly relativistic intensities and generate extremely high currents of relativistic electrons in interaction with solid targets. An accurate description of the transport of such high currents of relativistic electrons in dense matter is an important issue for many applications including the fast ignition of thermonuclear fusion targets, radiography of dense opaque objects, cancer therapy, lithography, etc. [7, 23, 38]. Recent proposed schemes for ignition also rely on pre-assembled overdense targets [28], and might face such regimes.

The complexity of this problem comes from the fact that the collective and collisional processes are operating in the same time and spatial scales and they require a kinetic description of particles in a very broad energy domain ranging from thermal electrons of a few tens or hundred eV of the main plasma to several tens of MeV of the beam electrons. The dominant physical processes include the collisions of beam electrons with the electrons and ions of plasma, the electron-ion and electron-electron collisions of plasma particles, production of secondary energetic electrons in head-on electron-electron collisions, generation of self-consistent electric and magnetic fields, return currents, and plasma heating. There is a necessity to describe correctly both the energy deposition of beam electrons and their transport from the injection to the energy deposition region.

A very large difference in energies and densities between the electron beam and the plasma electrons are revealed in the time and spatial scales of the collective and collisional processes, that makes it difficult to describe all physical processes within the same kinetic equation. It was suggested to separate the plasma and beam electrons and to consider them as two different populations. A theoretical approach that is currently implemented is based on the hybrid model where the plasma electrons are described in the fluid approximation, while the beam electrons are treated kinetically [3, 13, 15, 29]. While this approach has shown its capability to describe the major effects such as the collisional slowing down of beam electrons and the return current generation along with the self-consistent electric and magnetic fields, certain physical effects are left out of the frames of this model. In particular, the plasma electron distribution function is supposed to be close to the Maxwellian function and therefore the nonlocal effects in the plasma electric and thermal conductivities are neglected. Moreover, production of secondary fast electrons created in the head-on collisions of the beam and plasma electrons is discarded. A more advanced model of the fast electron transport would be necessary in order to evaluate the domain of validity of the hybrid model and to extend it to higher current densities, higher beam electron energies, and higher plasma densities.

The relativistic extension of the integro-differential Fokker-Planck-Landau kinetic equation [2] or simplified techniques [8, 43, 32, 4], have been proposed to incorporate the relativistic effects in the collisional process in the pitch-angle description. Several studies [44, 50] have been undertaken recently based on an electron kinetic code KALOS [4], to investigate issues related to the fast electron beam energy deposition in fusion targets. There the pitch-angle electron collisions and the self-consistent fields are described relativistically, however the effect of secondary electron production, including both relativistic effects and large momentum transfers, was neglected. The objective of this chapter is to consider in detail this latter process and to evaluate its importance, from a theoretical point of view and from the point of view of numerical treatment of the kinetic equation.

The problem of secondary electron production has been addressed in the publications [25, 27] that consider the effect of cosmic rays on the thunderstorm discharges in the Earth atmosphere. A kinetic modeling technique based on the relativistic Boltzmann equation, have been set up to describe large angle scattering processes and production of secondary electrons, that is often called *the ionization process*. Such specific models have been also derived for gas discharges, runaway breakdown [26], and Tokamak disruptions [22]. However, these models describe the background electrons as a cold [25] or a warm fluid [22] and consider them as a potential source of secondary electrons. The effect of the energy deposition in plasma was not considered there, whereas it is important issue for the transport problem. A non-Maxwellian distribution function of plasma electrons could be responsible for the modification of the electric conductivity, return current and other important effects [50].

The numerical realization of the relativistic collisional operator has been developed for the collisional particle-in-cell (PIC) or Monte Carlo (MC) codes [45, 47, 22]. However, independently of the domain of application, laser interaction with dense matter or a Tokamak plasma, the implementation cost of probabilistic methods into the kinetic models may be too high due to a large number of particles/macroparticles needed to maintain an acceptable low level of statistical fluctuations. Even PIC codes using weighted macroparticules [47] heavily rely on the small angle scattering to do so. This has lead authors [22] to derive a more specific model that incorporates specifically the production of secondary electrons.

The deterministic numerical methods [52] could be better suited for description of the large angle scattering effects, because they are by nature less dependent on the density and temperature conditions. As we will show in this chapter, the plasma heating process, which is due to small angle collisions, is of the same order, with a logarithmic accuracy, as the production of secondary electrons, due to large angle collisions. This rather general result will be illustrated here for simple distribution functions for the bulk and beam electrons.

A collisional interaction between the electrons in very different energy scales (from eV to MeV) justifies a need for two populations of electrons: the beam (fast) and the bulk (thermal) particles. However, a direct separation of two populations in the energy or momentum space cannot be efficient, since the bulk electron distribution function may have a long tail, and the fast particle distribution function may have an extension down to the fastest thermal particles. One has to allow for the particle to be transferred from one population to another. In this chapter we propose a model based on the electron kinetic equation, that separates the electrons in two populations operating in two different energy scales. The model is derived by using a procedure based on an operator decomposition technique, where the collision operators are interpreted in a systematic manner. This model respects the particle number, momentum and energy conservations, and introduces an artificial screening parameter in the cross sections, depending on the bulk electron temperature. A reasonable choice for this parameter is fundamental to maintain an acceptable number of particles in each population. Thus a numerical validation of the present model is necessary to find a compromise for this parameter and to gain confidence in the results.

The present chapter is structured as follows. In Sec. 8.2, the electron collision processes are described, a two population model is proposed and its design principles are discussed. In Sec. 8.3, the collision invariant preserving property of the procedure is highlighted. Then, basic properties of the model are illustrated on a simple beam-plasma configuration in Sec. 8.4. Finally, a reduced model suitable for numerical computations is presented in Sec. 8.5. A quantitative analysis is performed for the case of a mono-energetic electron beam propagation in a warm plasma. The importance of large angle scattering for the energy deposition and angular scattering of the beam is demonstrated.

8.2 Relativistic model of electron kinetics

8.2.1 Collision processes of importance for plasma physics

Let us consider a plasma made of electrons and immobile ions[1] of a charge Ze and a density n_i. The electrons are described by a relativistic kinetic equation

$$\frac{\mathrm{d}f_e}{\mathrm{d}t} \equiv \frac{\partial f_e}{\partial t} + \nabla_{\mathbf{x}} \cdot (\mathbf{v} f_e) + q_e \nabla_{\mathbf{p}} \cdot (\mathbf{E} + \mathbf{v} \times \mathbf{B}) f_e = C_{ee}(f_e, f_e) + C_{ei}(f_e). \tag{8.1}$$

Here, $q_e = -e$ is the charge of electron, the velocity and momentum $\mathbf{v} = \mathbf{p}/m_e\gamma$ are related by the relativistic factor $\gamma(\mathbf{p}) = \sqrt{1 + \mathbf{p}^2/m_e^2c^2}$, c is the speed of light, and m_e is the mass of electron. The electric and magnetic fields are described by the Maxwell's equations, where the electric charge and current densities, $\rho = e(Zn_i - n_e)$ and $\mathbf{j}$ are defined by the electron distribution function: $n_e(t, \mathbf{x}) = \int f_e(t, \mathbf{x}, \mathbf{p}) d\mathbf{p}$ and $\mathbf{j}(t, \mathbf{x}) = q_e \int f_e(t, \mathbf{x}, \mathbf{p}) \mathbf{v}\, d\mathbf{p}$. In what follows, we concentrate our discussion on the collisional effects leaving apart the convective terms in the left hand side of Eq. (8.1). Our main objective is to separate this kinetic equation into the fast and slow components and to describe the coupling between them.

The standard approach in the physics of Coulomb collisions consists in developing the collision integrals in series assuming a small momentum transfer in each collision. That reduces the general Boltzmann-like collision integral in the Landau-Fokker-Planck differential form containing the friction and diffusion terms in the phase space:

$$C_{e\alpha}[f_e] = \nabla_{\mathbf{p}} \cdot (\mathbf{F}_{D\alpha} f_e(\mathbf{p})) + \nabla_{\mathbf{p}} \cdot \Big(\mathbf{D}_\alpha \nabla_{\mathbf{p}} f_e(\mathbf{p})\Big). \tag{8.2}$$

In the non-relativistic limit and neglecting small ion mass corrections, $m_e/m_i \ll 1$, the electron-ion collision integral has only a diffusion term, $F_{Di} \simeq 0$, that is

$$\mathbf{D}_i = \frac{Z^2 n_i e^4 \ln \Lambda}{8\pi\epsilon_0^2} \Phi(\mathbf{v}) , \tag{8.3}$$

where $\Phi(\mathbf{u}) = (|\mathbf{u}|^2 \mathbf{I} - \mathbf{u} \otimes \mathbf{u})/|\mathbf{u}|^3$ is the tensor describing the pitch angle scattering, $\mathbf{u} = \mathbf{v} - \mathbf{v}'$ is the relative velocity, $\mathbf{I}$ is the unitary matrix, and $\ln \Lambda = \ln(\Delta p_{\max}/\Delta p_{\min})$ is the Coulomb logarithm, with $\Delta p_{\max} \sim p$ being the maximum momentum transfer in a collision between particles, $\Delta p_{\min} \simeq \hbar/\lambda_D$ is the minimum momentum transfer at the Debye cut-off, λ_D, and $\hbar$ is the Planck constant. The expressions for the electron-electron friction force and the diffusion coefficient, in the relativistic case, are as follows

$$\mathbf{F}_{De}[f_e] = \frac{e^4 \ln \Lambda}{4\pi\epsilon_0^2 m_e} \int \frac{\mathbf{v} - \mathbf{v}'}{|\mathbf{v} - \mathbf{v}'|^3} f_e(\mathbf{p}')\, d^3p', \tag{8.4}$$

$$\mathbf{D}_e[f_e] = \frac{e^4 \ln \Lambda}{8\pi\epsilon_0^2} \int \Phi(\mathbf{u}) f_e(\mathbf{p}')\, d^3p'. \tag{8.5}$$

In plasmas with highly charged ions, $Z \gg 1$, the electron-ion collisions dominate the diffusion, while the friction is related to the electron-electron collisions.

---

[1] The assumption of immobile ions makes the equations more readable. The ion motion can be included in the model with a marginal loss of accuracy.

A usual approximation of classical plasmas, where $\ln\Lambda \gg 1$, justifies the possibility to neglect the head-on collisions, which makes usually a small contribution of the order of $1/\ln\Lambda$. However, this statement of unimportance of large angle scattering events is not general, and there are conditions where the hard collisions could produce qualitatively new effects that do not exist in the Landau-Fokker-Planck approximation. One well-known example is the ionization of atoms or molecules by free electrons in partially-ionized plasmas. Another example is the electron-ion collisions in a strong laser field. The hard collisions dominate the electron heating rate if the electron quiver velocity is larger than the electron thermal velocity multiplied by the Coulomb logarithm [9].

In what follows we are considering a problem of an electron beam propagation through plasma. The characteristic beam electron energy, ϵ_b, is supposed to be much larger than the mean energy, $k_B T_e$, of the bulk electron population. In that case the hard collisions of the beam and bulk electrons, similarly as in the ionization process, produce energetic electrons and thus increase the fast electron population. Moreover, the collisions of beam and bulk electrons at small angles produce a fast electron tail in the bulk of electron distribution, which might affect the transport coefficients in such a plasma.

We develop a system of kinetic equations for the beam (fast) electrons described by the distribution function f_b, and the bulk (thermal) electrons described by the distribution function f_{th}, assuming that $\epsilon_b \gg k_B T_e$ and that that density of beam is small, $n_b \ll n_e$. We just suppose that the beam electrons could be relativistic, while the plasma electrons are non-relativistic, $k_B T_e \ll m_e c^2$.

8.2.2 Kinetic equations for two electron populations

The master equation that incorporates the hard collision processes is the relativistic Boltzmann equation [16, 48, 49]

$$\frac{\mathrm{d}}{\mathrm{d}t} f(\mathbf{p}) = \int_{\mathbb{R}^3} d^3q \int_{S^2} d\tilde{\boldsymbol{\Omega}}' \left[f(\mathbf{p}') f(\mathbf{q}') - f(\mathbf{p}) f(\mathbf{q}) \right] \tilde{u}\, \frac{\tilde{W}^2}{W_p W_q}\, Q(\tilde{p},\tilde{\mu})\,. \tag{8.6}$$

The notations for the momenta $\mathbf{p}$, $\mathbf{q}$ and energies W_p, W_q are applied to the outgoing particles, that is, after a collision event, whereas the momenta $\mathbf{p}'$, $\mathbf{q}'$ and energies $W_{p'}$, $W_{q'}$ refer to the ingoing particles, that is, before the same collision event. The conservation of the momentum and the energy in the collision implies that $\mathbf{p} + \mathbf{q} = \mathbf{p}' + \mathbf{q}'$ and $W_p + W_q = W_{p'} + W_{q'}$. The quantities marked with tilde (respectively without tilde) refer to quantities in the center of mass frame (respectively, in the laboratory frame) for a collision event, except for the scattering angle in the center of mass frame, denoted by θ. In particular, $\tilde{W}$ is the energy of colliding particles in the center of mass, $\tilde{\mu} = \cos\theta$ is the cosine of the interaction angle. $\tilde{u} = 2\tilde{p}c^2/\tilde{W}$ is the relative velocity. $v_M \equiv \tilde{u}\dfrac{\tilde{W}^2}{W_p W_q}$ is the Møller velocity, and Q is the total relativistic Rutherford cross section (8.7), that takes into account both relativistic and spin (including Pauli statistical principle) effects

$$\begin{aligned} Q(\tilde{p},\tilde{\mu}) &= Q_0 A(\tilde{p}) \left(\frac{1}{\sin^4(\theta/2)} + \frac{1}{\cos^4(\theta/2)} \right) \\ &+ Q_0 B(\tilde{p}) \left(\frac{1}{\sin^2(\theta/2)} + \frac{1}{\cos^2(\theta/2)} \right) + 2Q_0 C^2(\tilde{p})\,, \end{aligned} \tag{8.7}$$

where $Q_0 = (em_e c)^4/(16\pi\epsilon_0 \tilde{p}^2 \tilde{W})^2$ and the momentum-dependent functions are $A(\tilde{p}) = (1 + 2C(\tilde{p}))^2$, $B(\tilde{p}) = 1 + 4C(\tilde{p})$, $C(\tilde{p}) = \tilde{p}^2/m_e^2 c^2$.

The stiffness of the Boltmann operator is due to the long range Coulomb interaction. The complexity of its tensorial form, acting on the general distribution function f (gathering both thermal and fast particules), makes a numerical treatment very difficult. We develop a simplification procedure of the Boltzmann operator, that captures the essential processes and associated collision frequencies with a good accuracy. This procedure is relying on appropriate assumptions that respect the original collision invariants.

The first step is folding of the total cross section (8.7) $Q \to Q_f$. Owing the fact that electrons have to be considered identical, the cross section can be folded, that is, the electrons in the outgoing channel can be exchanged, and the singularities be concentrated at small angles. This step is necessary for development of the small angle scattering approach, and for derivation of the Landau type formulation presented in Eqs. (8.16) - (8.18).

As a second step, an intermediate -in momentum exchange- screening is introduced in the Rutherford cross-section, that makes it possible to discriminate between the smaller and larger angles (equivalently energy exchanges) for scattering, and thus to introduce a cut-off volume in the momentum space. This strategy is equivalent to the decomposition, at a finer level though, of the screened Coulomb potential $V(r)$ [**?**]

$$V(r) = \left[\frac{e^{-r/\lambda_D}}{r} - \mathbb{S}(r)\right]_{\text{“}smaller\ angles''} + \Big[\mathbb{S}(r)\Big]_{\text{“}larger\ angles''} ,$$

where $\mathbb{S} \geq 0$ is a smoothing function, which introduces an upper screening, and $\dfrac{e^{-r/\lambda_D}}{r} - \mathbb{S}(r) \geq 0$. This Debye-like screening procedure of the Coulomb singularity allows a re-interpretation of the above bracketed collisional processes. A rough, but sufficient condition, for such an interpretation to be safe, reads [25]

$$\frac{n_b}{n_{th}} \ll 1 \quad , \quad \frac{W_{th}}{W_b} \ll 1 ,$$

which reduces, for the model, the admissible configurations of the plasma. Here the subscripts $'b'$ and $'th'$ refer respectively to the beam and thermal plasma populations.

After a standard folding procedure of the cross-section of like particle collisions, it is decomposed, based on the intermediate screening, in two -or more than two- daughter cross sections. Each of these sub cross sections is interpreted as a specific collisional process -either the smaller or larger angle scattering-, which offers the possibility for a discrimination between two sets of particles, based on the momentum cut-off, and leads to the subsequent operators. Such a decomposition preserves a generality of the description, but is not unique. The positivity of the daughter cross sections is preserved during the decomposition. In the limit defined by the angle $\theta_a \to \theta_D \equiv 2\dfrac{\hbar}{\lambda_D \Delta p_{max}} \simeq 2\dfrac{\hbar}{\lambda_D \tilde{p}}$, the smaller angle scattering processes are selected. The larger angle ones shall be discarded by a Fokker-Planck-Landau procedure. On the other hand, the uppper cut-off $\theta_a > \theta_D$, above the Debye screening, defines the frontier between the smaller and larger scattering angles, and could be chosen such as to respect a robustness criteria, that is crucial for the numerical implementation of the model. The possiblity remains open to select an anisotropic cut-off in the momentum phase space.

The folded, screened cross section, reads $Q_f(\tilde{p}, \tilde{\mu}) = Q_f^{(sa)}(\tilde{p}, \tilde{\mu}) + Q_f^{(la)}(\tilde{p}, \tilde{\mu})$, where a possible choice for the daughter cross sections is as follows

$$\begin{aligned}
Q_f^{(sa)}(\tilde{p},\tilde{\mu}) &= \frac{2Q_0A(\tilde{p})}{\left(\sin^2(\theta/2)+\left[\frac{\theta_D}{2}\right]^2\right)^2} - \frac{2Q_0A(\tilde{p})}{\left(\sin^2(\theta/2)+\left[\frac{\theta_a}{2}\right]^2\right)^2}, && (8.8)\\
Q_f^{(la)}(\tilde{p},\tilde{\mu}) &= \frac{2Q_0A(\tilde{p})}{\left(\sin^2(\theta/2)+\left[\frac{\theta_a}{2}\right]^2\right)^2} - \frac{2Q_0B(\tilde{p})}{\sin^2(\theta/2)+\left[\frac{\theta_a}{2}\right]^2} + Q_0C(\tilde{p}). && (8.9)
\end{aligned}$$

Both functions are positively defined. The inclusion of screening terms in the nonlogarithmic terms is allowed because the relevent range for the parameter θ_a satisfies the multi-scale criteria $\theta_D \ll \theta_a \ll 1$, which involves $\cos^2\left(\frac{\theta_a}{2}\right) \simeq 1$. It does not affect the accuracy of the cross section, since the contributing, singular part remains physically screened. Rather than the decomposition (8.8)-(8.9), we prefer the screening and decomposition such as

$$\begin{aligned}
Q_f^{(sa)}(\tilde{p},\tilde{\mu}) &= \frac{2Q_0A(\tilde{p})}{\left(\sin^2(\theta/2)+\left[\frac{\theta_D}{2}\right]^2\right)^2} - \frac{2Q_0A(\tilde{p})\cos^2\left(\frac{\theta}{2}\right)}{\left(1+\left[\frac{\theta_a}{2}\right]^2\right)\left(\sin^2(\theta/2)+\left[\frac{\theta_a}{2}\right]^2\right)^2}, && (8.10)\\
Q_f^{(la)}(\tilde{p},\tilde{\mu}) &= \frac{2Q_0A(\tilde{p})\cos^2\left(\frac{\theta}{2}\right)}{\left(1+\left[\frac{\theta_a}{2}\right]^2\right)\left(\sin^2(\theta/2)+\left[\frac{\theta_a}{2}\right]^2\right)^2}\\
&\quad - \left[\frac{\cos^2\left(\frac{\theta_a}{2}\right)}{1+\left[\frac{\theta_a}{2}\right]^2}\right]\frac{2Q_0B(\tilde{p})}{\left(\sin^2(\theta/2)+\left[\frac{\theta_a}{2}\right]^2\right)} + Q_0C(\tilde{p})\,. && (8.11)
\end{aligned}$$

These daughter cross sections are positive. This form allows us to simplify forthcoming analytical computations and to postpone crucial hypothesis at the end of the computation.

The distinction between thermal $f_{th}^{\theta_a}$ and beam $f_b^{\theta_a}$ distribution functions is the consequence of the discrimination of the collisional processes. As a matter of fact, the two populations present two different resolutions for the phase-space discretization. In the remainder, we drop the superscripts θ_a on the distribution functions.

The processes associated with each of two energy scales are listed in Table 8.1. The two electron populations, thermal and fast, are allowed to share energy ranges, provided distinct energy exchange scales can be identified among the collision processes at stake. This leads to a simplification of the Bolzmann operator to a set of bilinear operators. The modeling choice for these operators and the attribution procedure to each of the populations, are also given in Table 8.1.

Concerning the thermal population, only pitch angle scattering between the thermal particles is taken into account (process $\mathrm{ST}^{(sa)}$). The large angle scattering of the thermal particle (process $\mathrm{ST}^{(la)}$) is neglected assuming $1/\ln\Lambda$ as a small parameter. The collisions of the thermal particles with the beam particles give raise to three processes. The small angle scattering (H) increases the energy of the thermal particle, while leaving it in its own population. The large angle scattering (IO) has two manifestations: the thermal particle gains energy and joins the beam population (IO^+) – this is the ionization term – and, at the same time, the thermal population looses this particle (IO^-).

Table 8.1: List of collisional processes considered for the beam and plasma electrons.

	Entering particle	Collisional process (sa)/(la) scattering	Target particle	Exiting particle	Collision model
Self Thermalisation: ST$^{(sa)}$	thermal	small angle scattering (sa)	thermal	thermal	Fokker-Planck-Landau
Self Thermalisation: ST$^{(la)}$	thermal	large angle scattering (la)	thermal	thermal	neglected
Heating: H	thermal	small angle scattering (sa)	beam	thermal	Fokker-Planck
Ionization gain: IO^{+}	thermal	large angle scattering (la)	beam	beam	Boltzmann gain term
Ionization loss: IO^{-}	thermal	large angle scattering (la)	beam	thermal	Boltzmann loss term
Slowing Down: SD$^{(sa)}$	beam	small angle scattering (sa)	thermal	beam	Fokker-Planck
Slowing Down: SD$^{(la)}$	beam	large angle scattering (la)	thermal	beam	Fokker-Planck
Self Thermalisation	beam	any scattering angle	beam	beam	neglected

Concerning the beam population, the process SD$^{(sa)}$ is identified as the small angle scattering on the thermal particles. It is the standard Fokker-Planck-Landau process producing the diffusion and friction of the beam in the phase space. The process SD$^{(la)}$ can be interpreted as large angle scattering of beam particles on the thermal particles, where particles of each population are maintained, in the outgoing channel (at the end of the collision process), in their original populations. This appears paradoxal, since the large angle scattering statement should be responsible for a thermal particle to become member of the beam population. We solve this by choosing a Fokker-Planck approach (see Sec. 8.3) for the process SD$^{(la)}$, that maintains the collision invariants of the bilinear Boltzmann form. Doing so, makes the large energy exchanges be discarded for thermal particles, as non-physical in this process. This is possible because we considered folded cross sections around small angles, and thus all scattering angles are gathered (considering the forward peakness of the Coulomb cross section) around zero. This Fokker-Planck treatment is valid for the beam particles as well, since the large energy exchanges can still be considered small with respect to the variation of the beam distribution function. Finally, all collisions between the beam particles are neglected because of a relatively small number of beam electrons.

The final model, that presents two energy exchange scales, reduces to

$$\frac{\mathrm{d}}{\mathrm{dt}} f_b(\mathbf{p}) = C_{IO^+}[f_{th}, f_b] + (C_{SD^{(sa)}}[f_b, f_{th}] + C_{SD^{(la)}}[f_b, f_{th}]) \,, \tag{8.12}$$

$$\frac{\mathrm{d}}{\mathrm{dt}} f_{th}(\mathbf{p}) = C_{IO^-}[f_{th}, f_b] + C_H[f_{th}, f_b] + C_{ST^{(sa)}}[f_{th}, f_{th}] \,, \tag{8.13}$$

where the explicit forms of the collision operators are presented in Eqs (8.14)-(8.18). In particular, the operators that describe hard collisions, where the two populations exchange particles, read

$$
\begin{aligned}
C_{IO^+}[f_{th}, f_b] &= \int_{\mathbb{R}^3} d^3q \int_{S^2} d\tilde{\mathbf{\Omega}}' \, f_{th}(\mathbf{p}') f_b(\mathbf{q}') \, \tilde{u} \, \frac{\tilde{W}^2}{W_p W_q} \, Q_f^{(la)}(\tilde{p}, \tilde{\mu}) \\
&= \int_{\mathbb{R}^3 \times \mathbb{R}^3} f_{th}(\mathbf{p}') f_b(\mathbf{q}') \, \frac{2c^4 \tilde{W}'^2}{W_p W_{p'} W_{q'}} \, \delta(\tilde{W}' - \tilde{W}) Q_f^{(la)}(\tilde{p}, \tilde{\mu}) d^3q' d^3p' \,, \qquad (8.14) \\
C_{IO^-}[f_{th}, f_b] &= -f_{th}(\mathbf{p}) \int_{\mathbb{R}^3} d^3q \int_{S^2} d\tilde{\mathbf{\Omega}}' \, f_b(\mathbf{q}) \, \tilde{u} \, \frac{\tilde{W}^2}{W_p W_q} \, Q_f^{(la)}(\tilde{p}, \tilde{\mu}) \\
&= -f_{th}(\mathbf{p}) \int_{\mathbb{R}^3 \times \mathbb{R}^3} f_b(\mathbf{q}) \, \frac{2c^4 \tilde{W}^2}{W_p W_q W_{p'}} \, \delta(\tilde{W}' - \tilde{W}) Q_f^{(la)}(\tilde{p}, \tilde{\mu}) d^3p' d^3q \\
&= -2\pi f_{th}(\mathbf{p}) \int_{\mathbb{R}^3} d^3q \, f_b(\mathbf{q}) \tilde{u} \, \frac{\tilde{W}^2}{W_p W_q} \int_{-1}^{1} Q_f^{(la)}(\tilde{p}, \tilde{\mu}) d\tilde{\mu} \,, \qquad (8.15)
\end{aligned}
$$

where the delta function accounts for the property of energy conservation for a collision between a fast and a thermal particle, in the center of mass frame. The last two forms in the right hand side of Eq. (8.12) are merged in $C_{SD}[f_b, f_{th}] = C_{SD^{(sa)}}[f_b, f_{th}] + C_{SD^{(la)}}[f_b, f_{th}]$.
The other processes can be described in the pitch angle limit

$$
\begin{aligned}
C_{SD}[f_b, f_{th}] &= \nabla_{\mathbf{p}} \cdot \Big(\underline{F_D}[f_{th}] f_b(\mathbf{p}) \Big) + \nabla_{\mathbf{p}} \cdot \Big(\underline{\mathbf{D}}[f_{th}] \nabla_{\mathbf{p}} f_b(\mathbf{p}) \Big) \,, \qquad (8.16) \\
C_H[f_{th}, f_b] &= \nabla_{\mathbf{p}} \cdot \Big(\underline{F_D}^{(sa)}[f_b] f_{th}(\mathbf{p}) \Big) + \nabla_{\mathbf{p}} \cdot \Big(\underline{\mathbf{D}}^{(sa)}[f_b] \nabla_{\mathbf{p}} f_{th}(\mathbf{p}) \Big) \,, \qquad (8.17) \\
C_{ST^{(sa)}}[f_{th}, f_{th}] &= \nabla_{\mathbf{p}} \cdot (F_{De}[f_{th}] f_{th}(\mathbf{p})) + \nabla_{\mathbf{p}} \cdot \Big(\mathbf{D}_e[f_{th}] \nabla_{\mathbf{p}} f_{th}(\mathbf{p}) \Big) \,. \qquad (8.18)
\end{aligned}
$$

The friction force F_{De} and diffusion coefficient $\mathbf{D}_e$ are given in Eqs. (8.4) and (8.5), because only small angle deviations in the non-relativistic regime are considered, with a logarithmic accuracy, for the scattering of thermal particles.
Finally, the bilinear forms $C_H[f_{th}, f_b]$ (Heating, with the cross section $Q_f^{(sa)}$), and $C_{SD}[f_b, f_{th}]$ (Slowing Down, with the cross section Q_f), of the Bethe type, are derived following the Landau method. The resulting expressions for the coefficients $\underline{F_D}[f]$ and $\underline{\mathbf{D}}[f]$ are given in Eqs. (8.20) - (8.21) and (8.27) - (8.29). They are respecting the collision invariants – the conservation of the total mass, momentum, and energy – for the complete distribution function $f_{th} + f_b$, for the model (8.12) - (8.13). The derivation presented in the next section is based on a decomposition of the collision operator in moments of the cross section. Compared to the original Landau derivation, the present approach differs only in non-logarithmic terms, but has the advantage of exactly preserving the collision invariants of the model, thus contributing to gain a confidence into it.

8.3 An invariant preserving Fokker-Planck procedure

We propose here a Fokker-Planck procedure of derivation of the model (8.12) - (8.13) from the original Boltzmann operator (8.7). Its particularity lies in the preservation of the collision invariants – total mass, momentum and energy –, for each process of the model, independently. The derivation of Fokker-Planck type operators starts from the weak form of the Boltzmann operator, operating on a arbitrary, forward-peaked folded cross section Q_f. Let us consider an arbitrary smooth test function $\mathcal{F}(\mathbf{p})$, and calculate the following integral

$$\left\langle \frac{\mathrm{d}}{\mathrm{dt}} f(\mathbf{p}), \mathcal{F} \right\rangle = \int_{S^2 \times \mathbb{R}^{3\times 2}} \mathcal{F}(\mathbf{p}) \left(f(\mathbf{p}') f(\mathbf{q}') - f(\mathbf{p}) f(\mathbf{q}) \right) \tilde{u} Q_f(\tilde{p}, \tilde{\mu}) \frac{\tilde{W}^2}{W_p W_q} \mathbf{d\tilde{\Omega}}' d^3q d^3p \, .$$

The right hand side of this equation can be rewritten, exchanging the incoming $\{\mathbf{p}', \mathbf{q}'\}$ and outgoing particles $\{\mathbf{p}, \mathbf{q}\}$, as

$$\frac{1}{2} \int_{S^2 \times \mathbb{R}^{3\times 2}} \left(\mathcal{F}(\mathbf{p}) - \mathcal{F}(\mathbf{p}') \right) \left(f(\mathbf{p}') f(\mathbf{q}') - f(\mathbf{p}) f(\mathbf{q}) \right) \tilde{u} Q_f(\tilde{p}, \tilde{\mu}) \frac{\tilde{W}^2}{W_p W_q} \mathbf{d\tilde{\Omega}}' d^3q d^3p \, .$$

Then a Taylor expansion is performed on the functions $\mathcal{F}$ and f, assuming small angle deviations, $\Delta p \ll p$ (small energy exchanges), and using the momentum conservation $\mathbf{p}' + \mathbf{q}' = \mathbf{p} + \mathbf{q}$

$$\begin{aligned}
\mathcal{F}(\mathbf{p}') &= \mathcal{F}(\mathbf{p}) - \Delta\mathbf{p} \cdot \frac{\partial \mathcal{F}}{\partial \mathbf{p}}(\mathbf{p}) + (-1)^n \frac{(\Delta p_i)^n}{n!} \frac{\partial^n \mathcal{F}}{\partial {p_i}^n}(\mathbf{p}) \qquad n > 1 \, , \\
f(\mathbf{p}') &= f(\mathbf{p}) - \Delta\mathbf{p} \cdot \frac{\partial f}{\partial \mathbf{p}}(\mathbf{p}) + (-1)^n \frac{(\Delta p_i)^n}{n!} \frac{\partial^n f}{\partial {p_i}^n}(\mathbf{p}) \qquad n > 1 \, , \\
f(\mathbf{q}') &= f(\mathbf{q}) + \Delta\mathbf{p} \cdot \frac{\partial f}{\partial \mathbf{q}}(\mathbf{q}) + \frac{(\Delta p_i)^n}{n!} \frac{\partial^n f}{\partial {q_i}^n}(\mathbf{q}) \qquad n > 1 \, , \\
\Delta\mathbf{p} &= \mathbf{p} - \mathbf{p}' \, ,
\end{aligned}$$

Only the terms being less than first order are retained, in these developments. Then we obtain the differential Landau form of the operator

$$C_L \left[f, f \right] = \nabla_{\mathbf{p}} \cdot \left(F_D[f] f(\mathbf{p}) \right) + \nabla_{\mathbf{p}} \cdot \left(\mathbf{D}[f] \nabla_{\mathbf{p}} f(\mathbf{p}) \right) \, , \tag{8.19}$$

where the drag force F_D and the matrix $\mathbf{D}$ are

$$\underline{F_D}[f] = \frac{1}{2} \int_{\mathbb{R}^3} \nabla_{\mathbf{q}} \cdot \langle \Delta\mathbf{p} \Delta\mathbf{p} \rangle \, f(\mathbf{q}) d^3q \, , \tag{8.20}$$

$$\underline{\mathbf{D}}[f] = \frac{1}{2} \int_{\mathbb{R}^3} \langle \Delta\mathbf{p} \Delta\mathbf{p} \rangle \, f(\mathbf{q}) d^3q \, . \tag{8.21}$$

These coefficients only depend on the matrix $\langle \Delta\mathbf{p} \Delta\mathbf{p} \rangle$, whose components are defined by

$$\left\langle \Delta p_i \Delta p_j \right\rangle \equiv \int_{S^2} \Delta p_i \Delta p_j \tilde{u} Q_f(\tilde{p}, \tilde{\mu}) \frac{\tilde{W}^2}{W_p W_q} d\tilde{\mu} d\tilde{\varphi} \, , \tag{8.22}$$

where the integration is conducted in the center of mass frame over the polar and azimuthal angles $\tilde{\mu}$ and $\tilde{\varphi}$. If two distinct populations, f_l and f_m are introduced (l and m referring either to the thermal or beam population), the following Boltzmann bilinear form is considered,

$$C_B \left[f_l, f_m \right] = \int_{\mathbb{R}^3} d^3q \int_{S^2} d\mathbf{\tilde{\Omega}}' \, \left[f_m(\mathbf{p}') f_l(\mathbf{q}') - f_m(\mathbf{p}) f_l(\mathbf{q}) \right] \tilde{u} \, \frac{\tilde{W}^2}{W_p W_q} \, Q_f(\tilde{p}, \tilde{\mu}) \, . \tag{8.23}$$

A first order Taylor expansion leads to the corresponding Landau bilinear form

$$C_L \left[f_l, f_m \right] = \nabla_{\mathbf{p}} \cdot \left(\underline{F_D}[f_m] f_l(\mathbf{p}) \right) + \nabla_{\mathbf{p}} \cdot \left(\underline{\mathbf{D}}[f_m] \nabla_{\mathbf{p}} f_l(\mathbf{p}) \right) \, . \tag{8.24}$$

The coefficients of this operator are written explicitly by using a decomposition with moments of the cross section. This avoids logarithmic approximations of this cross section Q_f, which remains the same for the Fokker-Planck and the Boltzmann operators. In the next section, we develop this procedure and justify formally that the Landau operator (8.19) (respectively the Landau bilinear form (8.24)) reproduces the conservation properties of the initial Boltzmann equation (8.6) (respectively the Boltzmann bilinear forms (8.23)).

8.3.1 A Fokker-Planck procedure based on moment decomposition

Let the cross section Q_f be arbitrary in this section, though forward-peaked. The analysis we propose here is based on the decomposition of the momentum exchange $\Delta\mathbf{p} = \Delta p_{\|}\mathbf{n} + \Delta\mathbf{p}_{\perp}$ in one parallel and two perpendicular components, with respect to the velocity $\mathbf{V} = V\mathbf{n}$ of the center of mass frame in the laboratory frame. If a Taylor expansion is performed on the weak form of Botzmann equation (8.6), with infinite order, the so-obtained operator $C\left[f, f\right](Q_f)$ involves the coefficients

$$\left\langle (\Delta p_{\|})^j\,(\Delta p_{\perp_1})^k\,(\Delta p_{\perp_2})^l \right\rangle\ ,$$

where the subscripts $\perp_1$ and $\perp_2$ refer to each perpendicular directions, and the brackets are defined by the expression (8.22).

The parallel component does not depend on the azimuthal angle $\tilde{\varphi}$. Then if $k+l$ is odd, the coefficient $\left\langle (\Delta p_{\|})^j\,(\Delta p_{\perp_1})^k\,(\Delta p_{\perp_2})^l \right\rangle$ is equal to zero, after integration in $\tilde{\varphi}$. In the case where $k+l$ is even, we obtain

$$\begin{aligned}\left\langle (\Delta p_{\|})^j\,(\Delta p_{\perp_1})^k\,(\Delta p_{\perp_2})^l \right\rangle &= \int_{-1}^{1}(1-\tilde{\mu})^j(1-\tilde{\mu}^2)^{\frac{l+k}{2}}K_{j,k,l}Q_f(\tilde{p},\tilde{\mu})d\tilde{\mu}\\ &\simeq 2^{\frac{l+k}{2}}\int_{-1}^{1}(1-\tilde{\mu})^{j+\frac{l+k}{2}}K_{j,k,l}Q_f(\tilde{p},\tilde{\mu})d\tilde{\mu}\ ,\end{aligned}$$

where the coefficients $K_{j,k,l}$ only depend on the variables $\tilde{p}$, $\mathbf{V}$, W_p, W_q, but not on the variable $\tilde{\mu}$. At this point we have made the logarithmic approximation $(1+\tilde{\mu})^{(l+k)/2} \simeq 2^{(l+k)/2}$ for the coefficient $\left\langle (\Delta p_{\|})^j\,(\Delta p_{\perp_1})^k\,(\Delta p_{\perp_2})^l \right\rangle$, in the case $k+l$ is even, assuming that the dominant contribution comes from the small angles, because of the divergence of the cross section. This allows to rearrange formally the operator as the infinite sum

$$\begin{aligned}C\left[f, f\right](Q_f) &= \sum_{m\in\mathbb{N}^*} C^{(m)}\left[f, f\right](Q_f)\ ,\\ C^{(m)}\left[f, f\right](Q_f) &\propto \int_{-1}^{1}(1-\tilde{\mu})^m Q_f(\tilde{p},\tilde{\mu})d\tilde{\mu}\ ,\end{aligned}$$

whatever the expression of the cross section is. In this decomposition, the contribution of the m^{th} moment of the cross section $\int_{-1}^{1}(1-\tilde{\mu})^m Q_f(\tilde{p},\tilde{\mu})d\tilde{\mu}$ is assigned to the formal operator $C^{(m)}(Q_f)$. Since this decomposition does not assume the explicit knowledge of the cross section, all the properties of the operator $C(Q_f)$ hold for each operator $C^{(m)}(Q_f)$. In particular , dropping terms with $m > 1$, the collision invariants are preserved for the operator $C^{(1)}(Q_f)$. This procedure remains valid when bilinear forms are considered for two distinct populations. Then we obtain the conservation properties on these bilinear forms

$$\int_{\mathbb{R}^3} C_L\left[f_l, f_m\right] \mathrm{d}^3p \;=\; \int_{\mathbb{R}^3} C_B\left[f_l, f_m\right] \mathrm{d}^3p = 0 \tag{8.25}$$

$$\int_{\mathbb{R}^3} \mathcal{F}(\mathbf{p}) C_L\left[f_l, f_m\right] \mathrm{d}^3p \;=\; \int_{\mathbb{R}^3} \mathcal{F}(\mathbf{p}) C_B\left[f_l, f_m\right] \mathrm{d}^3p = -\int_{\mathbb{R}^3} \mathcal{F}(\mathbf{p}) C_B\left[f_m, f_l\right] \mathrm{d}^3p\,, \tag{8.26}$$

where $\mathcal{F}(\mathbf{p})$ can be either $\mathbf{p}$, or W_p. Moreover the only equilibrium states of this operator are the Maxwellian distribution functions f_l and f_m whose temperature and mean velocity are the same. These conservation properties can be rigourously proved for the operators (8.16) - (8.17), with the explicit expressions of the Fokker-Planck components (8.27) - (8.29), given in the next section. The energy conservation will be illustrated in the case of a model issued from [25], that has been modified following this procedure, in the section 8.4.1.

This approach only differs from the original Landau-Fokker-Planck development in non-logarithmic terms. However, these additional non-logarithmic contribution prove to be essential to maintain the correct conservation properties (8.26) all through the model derivation.

8.3.2 Explicit expression of the Fokker-Planck coefficients

In this section, we choose the cross section Q_f, defined by the sum of expressions (8.10) and (8.11), and derive the Fokker-Planck coefficients from the above presented Fokker-Planck procedure. The cross section shows a singularity at $\tilde{\mu} \to 1$, that corresponds to small angle scattering. Then the operator $C^{(1)}(Q_f)$ contains both logarithmic and non-logarithmic terms; the non-logarithmic contribution being located inside the cross section. The other operators $C^{(m)}(Q_f)$, $m > 1$, only contain non-logarithmic terms, and are dropped in the following sections.

The coefficient $\langle\Delta\mathbf{p}\Delta\mathbf{p}\rangle$ is no more a pure diffusion matrix if the Landau derivation of Sec. 8.3.1 is applied. In this context, the quantities $\langle\Delta\mathbf{p}\Delta\mathbf{p}\rangle$ and $\nabla_{\mathbf{q}} \cdot \langle\Delta\mathbf{p}\Delta\mathbf{p}\rangle$ are written as

$$\langle\Delta\mathbf{p}\Delta\mathbf{p}\rangle = \mathbf{M}\tilde{u}2\pi\frac{\tilde{W}^2}{W_pW_q}\int_{-1}^{1}(1-\tilde{\mu})Q_f(\tilde{p},\tilde{\mu})d\tilde{\mu}\,, \tag{8.27}$$

where the matrix $\mathbf{M}$ is defined as

$$\mathbf{M} = \left(\mathbf{I}\tilde{p}^2 + \frac{\tilde{p}^2c^2}{4\tilde{W}^2}\left(\mathbf{p}+\mathbf{q}\right)\otimes\left(\mathbf{p}+\mathbf{q}\right) - \frac{1}{4}\left(\mathbf{p}-\mathbf{q}\right)\otimes\left(\mathbf{p}-\mathbf{q}\right)\right)\,, \tag{8.28}$$

and thus

$$\nabla_{\mathbf{q}} \cdot \langle\Delta\mathbf{p}\Delta\mathbf{p}\rangle = \tilde{u}\pi\frac{\mathbf{p}(W_pW_q - \mathbf{p}\cdot\mathbf{q}c^2) - \mathbf{q}m_e^2c^4}{W_pW_q}\int_{-1}^{1}(1-\tilde{\mu})Q_f(\tilde{p},\tilde{\mu})d\tilde{\mu}\,. \tag{8.29}$$

With this approximation, the coefficients satisfy the relation $-\nabla_{\mathbf{q}} \cdot \langle\Delta\mathbf{p}\Delta\mathbf{p}\rangle = 2\langle\Delta\mathbf{p}\rangle - \nabla_{\mathbf{p}} \cdot \langle\Delta\mathbf{p}\Delta\mathbf{p}\rangle$. Therefore we obtain the equivalence between the Landau operator of Eq. (8.19) and the Fokker-Planck form

$$C_L\left[f,f\right] = -\nabla_{\mathbf{p}} \cdot \left(f(\mathbf{p})\int_{\mathbb{R}^3} f(\mathbf{q})\langle\Delta\mathbf{p}\rangle\, d^3q\right) + \frac{1}{2}\nabla^2_{\mathbf{p}} \cdot \left(f(\mathbf{p})\int_{\mathbb{R}^3} f(\mathbf{q})\langle\Delta\mathbf{p}\Delta\mathbf{p}\rangle\, d^3q\right).$$

The equivalence between the Landau and Fokker-Planck forms remains true for the bilinear operators.

8.3.3 Coulomb logarithms and cross sections

The collision integral C_{SD} describes the scattering of beam on plasma electrons. Its Coulomb logarithm is defined with the Debye cut-off parameter θ_D. It is contained in the coefficient $\int_{-1}^{1}(1-\tilde{\mu})Q_f(\tilde{p},\tilde{\mu})d\tilde{\mu}$. The contribution of the collisions between beam electrons and ions can be directly incorporated, substituting $Z \to Z+1$.

The plasma heating (process H in Table 8.1) is defined by the energy deposition of fast particles, while they are scattered on small angles on the plasma electrons. The Coulomb logarithm is contained in the coefficient $\int_{-1}^{1}(1-\tilde{\mu})Q_f^{(sa)}(\tilde{p},\tilde{\mu})d\tilde{\mu}$.

The Boltzmann operators that exchange particles(processes $IO^{\pm}$ in Table 8.1), have an integral form that presents a logarithmic singularity. The analogy with the Coulomb logarithm will be illustrated in the case of a beam electron population in Sec. 8.4.

8.4 Energy exchange of beam electrons in a cold plasma

8.4.1 Kinetic equation for beam electrons

Relativistic electron-ion and electron-electron collision operators for a low density electron beam propagating through a cold and dense plasma were derived in [25]. It was shown that under the conditions $n_b \ll n_e$ and $\epsilon_b \gg k_B T_e$, they can be presented as a sum of three terms. First two terms correspond to the small angle collisions (process E in Table 8.1), and they have a Fokker-Planck differential form (8.2):

$$C_t[f_b(\mathbf{p})] = \nabla_{\mathbf{p}} \cdot \left(F_D \frac{\mathbf{p}}{p} f_b(\mathbf{p})\right) + \nabla_{\mathbf{p}} \cdot \left[D\left(I_d - \frac{\mathbf{p}\otimes\mathbf{p}}{p^2}\right)\nabla_{\mathbf{p}} f_b(\mathbf{p})\right]. \tag{8.30}$$

The drag force F_D is due to the electron-electron collisions, while the diffusion term D describes the elastic scattering accounts for the electron-electron and electron-ion collisions. If only logarithmic terms are retained

$$F_D = \frac{Ze^4 n_i \ln\Lambda}{4\pi\epsilon_0^2 m_e v^2}, \quad D = F_D(Z+1)\frac{p}{2\gamma} . \tag{8.31}$$

These expressions are similar to Eqs. (8.4) and (8.5) in the non-relativistic case, with the same expression for the Coulomb logarithm. In addition, the large angle collisions (process F in Table 8.1) are responsible for production of secondary high energy electrons. This term, so-called, *ionization integral* [25], reads

$$C_I[f_b(\epsilon,\mu,\varphi)] = \alpha(\epsilon)\int_{\epsilon_{min}}^{+\infty}\int_{S^2} f_b(\epsilon',\mu',\varphi')\frac{(\epsilon'+m_ec^2)^2}{\epsilon(\epsilon+2m_ec^2)}K(\epsilon',\epsilon)\delta_E d\epsilon' \frac{d\Omega_{p'}}{2\pi} . \tag{8.32}$$

Here, the collision rate, α, the kernel, K, and the Delta function accounting for the energy conservation δ_E, are defined as

$$\alpha(\epsilon) = \frac{Zn_i e^4}{8\pi\epsilon_0^2 m_e c}\frac{\sqrt{\epsilon(\epsilon+2m_e c^2)}}{\epsilon+m_e c^2}\,, \tag{8.33}$$

$$K(\epsilon',\epsilon) = \left(\frac{1}{\epsilon^2}+\frac{1}{\epsilon'+m_e c^2}\right)\,, \tag{8.34}$$

$$\delta_E = \delta(\mathbf{\Omega_p}\cdot\mathbf{\Omega_{p'}} - \mu_0(\epsilon',\epsilon))\,, \tag{8.35}$$

$$\mu_0(\epsilon',\epsilon) = \sqrt{\frac{\epsilon(\epsilon'+2m_e c^2)}{\epsilon'(\epsilon+2m_e c^2)}}\,, \tag{8.36}$$

where $\epsilon' = m_e c^2(\gamma'-1)$ and $\epsilon = m_e c^2(\gamma-1)$ are the kinetic energies of the incoming and outgoing particles, associated to the Lorentz factors γ' and γ. The momentum $\mathbf{p}$ is written in spherical coordinates in terms of the variables (ϵ,μ,φ). Here the ionization integral (8.32) involves the cross section $Q_f^*(|\tilde{p}|,\tilde{\mu})$ folded around the large angles. It is defined as $Q_f(|\tilde{p}|,\tilde{\mu}) = Q_f^*(|\tilde{p}|,-\tilde{\mu})$.

The integral (8.32) does not contain the Coulomb logarithm, contrary to the friction and diffusion terms. However it contains a logarithmic dependence on the low energy limit, and that makes it of the same order as the diffusion and friction terms. This is illustrated in the next section for the case of a mono-energetic electron beam.

8.4.2 Energy losses of a mono-energetic electron beam on a cold plasma

Let us consider a mono-energetic electron beam with energy $\epsilon_b = m_e c^2(\gamma_b - 1)$ propagating in a direction defined by the polar axis z. The beam distribution function writes

$$f_b(\gamma,\mu) = \frac{n_b}{2\pi m_e^3 c^3}\,\frac{1}{\gamma_b\sqrt{\gamma_b^2-1}}\,\delta(\gamma-\gamma_b)\,\delta(\mu-1). \tag{8.37}$$

The beam energy loss is defined as

$$-\frac{\mathrm{dW}_b}{\mathrm{dt}} = -m_e c^2\frac{\mathrm{d}}{\mathrm{dt}}\int_{\mathbb{R}^3}(\gamma-1)\,f_b(\mathbf{p})d^3p.$$

The beam energy loss due to pitch-angle collisions with plasma electrons is described by the friction term in Eq. (8.30), which gives

$$-\frac{\mathrm{dW}_{bt}}{\mathrm{dt}} = n_b v_b F_D = \ln\left(\frac{p_b}{\hbar/\lambda_D}\right)\frac{Ze^4 n_i n_b}{4\pi\epsilon_0^2 m_e c}\,\frac{\gamma_b}{\sqrt{\gamma_b^2-1}}\,. \tag{8.38}$$

Here, for a background plasma of 0.1 keV, with a density of $10^{21}\mathrm{cm}^{-3}$, the minimum kinetic energy $\epsilon_{\min}$, related to the momentum $\hbar/\lambda_D$, is of the order of 10 meV.
The energy loss due to hard collisions with plasma electrons is obtained from the ionization integral in Eq. (8.32)

$$-\frac{\mathrm{dW}_{bi}}{\mathrm{dt}} = -n_b\int_{\gamma_{\min}}^{\gamma_b}\alpha(\gamma)\frac{\gamma_b\gamma}{(\gamma+1)}\left(\frac{1}{(\gamma-1)^2}+\frac{1}{\gamma_b^2}\right)\sqrt{\frac{\gamma^2-1}{\gamma_b^2-1}}d\gamma\,. \tag{8.39}$$

The integral over the energy has a logarithmic divergence at the lower limit $\gamma_{\min} \simeq 1$, corresponding to small angle collisions.

Further, turning to the Fokker-Planck procedure described in Sec. 8.3, we demonstrate an energy conservation property (8.40), similar to Eq. (8.26), in the model (with cold plasma) of [25]. This model is modified here in two aspects: first, the complete cross sections are retained, and second, the Fokker-Planck derivation procedure described in Sec. 8.3 is applied. These modifications lead to the following expression for the energy loss in Eq. (8.38)

$$-\frac{\mathrm{dW}_{bi}}{\mathrm{dt}} = -Zn_i n_b c^2 \pi m_e c \frac{(\gamma_b - 1)\sqrt{\gamma_b^2 - 1}}{\gamma_b} \int_{-1}^{1} (1-\tilde{\mu}) Q_f(\tilde{p}, \tilde{\mu}) d\tilde{\mu} = \frac{\mathrm{dW}_{bt}}{\mathrm{dt}} \; . \tag{8.40}$$

8.5 Reduced model for fast electron distribution functions

8.5.1 Assumptions concerning the electron distribution function

In order to simplify the ionization operator (IO), we assume that the thermal electron population, with the density n_{th}, has an isotropic energy distribution

$$f_{th}(\mathbf{p}) = \frac{n_{th}}{4\pi m_e^3 c^3} F_{th}(\gamma_p) \; , \tag{8.41}$$

with the normalization $\int_1^\infty \gamma(\gamma^2 - 1)^{1/2} F_{th}(\gamma)\, \mathrm{d}\gamma = 1$. Also, in order to simplify the calculations, we only retain the dominant part of the cross sections, that contains the Coulomb logarithm. The cross sections in the ionization operator (IO) can be further simplified, owing to the fact that all the quantities that do not contribute to the logarithmic divergence can be approximated with the assumption of weak dependence with respect to the temperature of the thermal population.

We describe the beam distribution function within the M1 model [5, 18, 53], that relies on the angular moment closure in the phase space. Its angular dependence is defined from the minimum entropy principle [36, 39]

$$f_b(\mathbf{p}) = \rho_0(\gamma_p) \exp(-\mathbf{\Omega_p} \cdot \mathbf{a_1}(\gamma_p)), \tag{8.42}$$

where $\mathbf{\Omega_p}$ is the unit vector in the $\mathbf{p}$ momentum direction, ρ_0 is a non negative scalar ($\rho_0 \geq 0$), and $\mathbf{a_1}$ is a three component real valued vector. The functions $\mathbf{a_1}$ and ρ_0 only depend on the fast electron energy. An important parameter is the anisotropy of beam distribution $\mathcal{A} = \mathbf{f}_1 / f_0$, where

$$f_0(p) = \int_{S_2} f(\mathbf{p})\, \mathrm{d}\mathbf{\Omega_p} \; , \quad \mathbf{f_1}(p) = \int_{S_2} \mathbf{\Omega_p} f(\mathbf{p})\, \mathrm{d}\mathbf{\Omega_p} \; , \quad \mathbf{f_2}(p) = \int_{S_2} \mathbf{\Omega_p} \otimes \mathbf{\Omega_p} f(\mathbf{p})\, \mathrm{d}\mathbf{\Omega_p} \; .$$

The anisotropy parameter is by construction less or equal than one ($\|\mathcal{A}\| \leq 1$). The *ansatz* (8.42) ensures the analytical computation of moment $\mathbf{f_2}$ as a function of f_0 and $\mathbf{f_1}$, based on a tabulated Eddington factor [17], which defines the relation between $\mathcal{A}$ and $\mathbf{a_1}$.

An important feature of the M1 model, consists of the fact that it reproduces *exactly* both beam-like and isotropic distribution functions. Moreover, the form (8.42) is convenient for the calculation of the ionization operator that presents a very narrow domain of integration over the angular variable.

Under the assumptions formulated above, the ionization (IO) operator takes the following form

$$\frac{\mathrm{d}}{\mathrm{d}t} f_{b,0}(p) = \nu_{io} \int_1^\infty \mathrm{d}\gamma_{q'} \int_1^\infty \mathrm{d}\gamma_{p'}\, F_{th}(\gamma_{p'})\, f_{b,0}(q')\, G_0(\gamma_{p'}, \gamma_{q'}, \gamma_p, \gamma_c)\, \mathbf{1}_{L_-<L_+}\,, \tag{8.43}$$

$$\frac{\mathrm{d}}{\mathrm{d}t} \mathbf{f_{b,1}}(p) = \nu_{io} \int_1^\infty \mathrm{d}\gamma_{q'} \int_1^\infty \mathrm{d}\gamma_{p'}\, F_{th}(\gamma_{p'})\, \mathbf{f_{b,1}}(q')\, G_1(\gamma_{p'}, \gamma_{q'}, \gamma_p, \gamma_c)\, \mathbf{1}_{L_-<L_+}\,, \tag{8.44}$$

where we have introduced an effective collision frequency $\nu_{io} \equiv e^4 n_{th}/4\pi\epsilon_0^2 m_e^2 c^3$, the dimensionless kernels G_0 and G_1, which are regular kernels, $\mathbf{1}_{L_-<L_+}$ is an indicative function, valued 1, if $L_- < L_+$, and 0 otherwise, with $L_\pm = O(\|\mathbf{p}'\|)$. This indicative function can be narrow, as the energies on the outgoing channel may present a very narrow divergence in angles. However, a fine energy discretization of the thermal population allows to capture this feature. This is an imporatnt aspect of the model. The integrals (8.43) and (8.44) depend on the parameter γ_c that separates the fast and slow electron populations.

8.5.2 Relaxation of a mono-energetic electron beam in a thermal Maxwellian plasma

Let us consider a mono-energetic beam with the distribution function (8.37) propagating through a homogeneous Maxwellian plasma with a non-relativistic temperature $\Theta_{th} = k_B T_{th}/m_e c^2 \ll 1$. The finite value of Θ_{th} is needed for the calculation of the ionization integral. However, it may be set to zero in the calculations of the slowing down operator (SD), as the particles affected by this process do not move from one population to another. This choice makes it appear an explicit logarithmic divergence of the singularity.

First, we analyse the value of the ionization integral by evaluating the ionization rate, that is, the evolution of the number of beam electrons with time. This provides also with a hint for choosing the separation parameter γ_c, as it should not lead to a significant leakage of the thermal population.

$$\begin{aligned}\frac{\mathrm{d}n_b}{\mathrm{d}t} &= \frac{\mathrm{d}}{\mathrm{d}t} \int_{\mathbb{R}^3} f_b(\mathbf{p})\mathrm{d}^3 p \\ &= n_b \nu_{io} \int_1^\infty \mathrm{d}\gamma_p \int_1^\infty \mathrm{d}\gamma_{p'} \frac{\gamma_p \left(\gamma_p^2 - 1\right)^{1/2}}{\gamma_b \left(\gamma_b^2 - 1\right)^{1/2}} F_{th}(\gamma_{p'})\, G_0(\gamma_{p'}, \gamma_{q'}, \gamma_p, \gamma_c) \mathbf{1}_{L_-<L_+}.\end{aligned}$$

The dependence of the secondary electron production rate on the beam electron energy and on the cut-off parameter is shown in Fig. 8.1 for the representative case of a 5 keV thermal plasma. The ionization rate presents a strong dependence with respect to γ_c if the cut-off energy is chosen very close to the thermal energy of plasma electrons. This dependence becomes weaker as soon as the cut-off energy goes far in the tail of the plasma distribution function. The production of secondary electrons increases also with the energy of fast electrons. Both these effects can be easily understood if one accounts for the fact that, even in the pitch angle scattering event, the secondary electron gains a significant energy. Indeed, assuming the scattering angle $\theta \ll 1$ and the large energy of the beam electrons, $\gamma_b \gg 1$, one finds from the energy and momentum conservation relations that the energy of secondary electron is

$$\epsilon' \simeq \frac{1}{2} m_e c^2 \gamma_b^2 \theta^2.$$

The secondary electron energy would be 700 keV if the 5 MeV is scattered to a small angle of 10°. Therefore too small energy cut-off corresponds to accounting for the pitch angle scattered electrons as

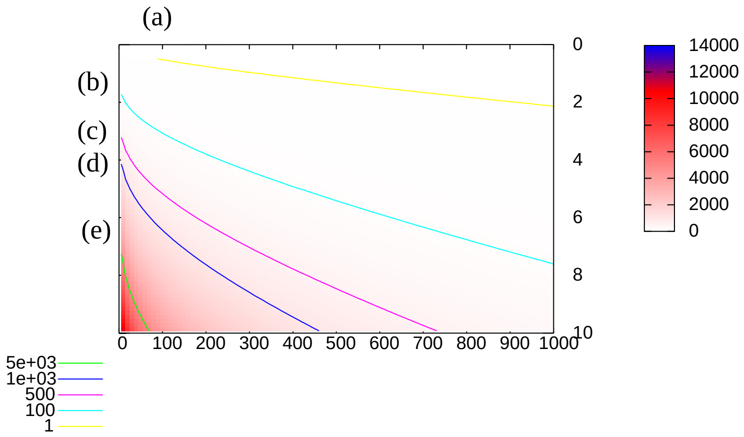

Figure 8.1: Production rate $(\nu_{io}n_b)^{-1}\mathrm{d}n_b/\mathrm{d}t$ of secondary electrons by a beam electrons propagating in a 5 keV Maxwellian thermal plasma as a function of the beam energy and the energy cut-off parameter. Isolines 1, 100, 500, 1000, 5000 for the production rates are labelled with respective letters (a)-(e).

the secondary beam electrons. For this reason the choice of the cut-off energy is problem dependent. It must be chosen in such a domain where the dependence of the secondary electron production with respect to the cut-off energy is weak. Figure 8.1 proves the existence of such a domain for the beam-plasma configuration. Moreover, this figure illustrates two more points: first, the model respects the positivity of G_0, second, the ionization rate profile is peaked for a low energy cut-off.

One can also analyse the relative contribution of the ionization and slowing down mechanisms to the total momentum. In the limit of low plasma temperature and retaining only the logarithmic terms, one finds the following expression for the slowing down rate of the fast electron momentum:

$$\begin{aligned} n_b \frac{\mathrm{d}\langle \mathbf{p}\rangle_t}{\mathrm{d}t}\cdot \mathbf{e_z} &\equiv \int_{\mathbb{R}^3} C_t[f_b]\,(\mathbf{p}\cdot\mathbf{e_z})\,\mathrm{d}^3p = \\ &-n_b\nu_{io}m_ec\ln\left(\frac{p_b}{\hbar/\lambda_D}\right)\frac{\gamma_b^2+(Z+1)\gamma_b}{\gamma_b^2-1}\,, \end{aligned} \tag{8.45}$$

where the Bethe operator (8.30), with friction and diffusion coefficients (8.31) was taken into account. The averaged contribution of this process to the total beam momentum is negative.

The contribution to the total beam momentum due to the ionization operator is

$$\begin{aligned} n_b \frac{\mathrm{d}\langle \mathbf{p}\rangle_{io}}{\mathrm{d}t}\cdot \mathbf{e_z} &\equiv \frac{\mathrm{d}}{\mathrm{d}t}\int_{\mathbb{R}^3} f_b(\mathbf{p})\,\mathbf{p}\cdot\mathbf{e_z}\,\mathrm{d}^3p = \\ m_ecn_b\nu_{io}\int_1^\infty \mathrm{d}\gamma_p &\int_1^\infty \mathrm{d}\gamma_{p'}\,\frac{\gamma_p\left(\gamma_p^2-1\right)^{1/2}}{\gamma_b\left(\gamma_b^2-1\right)^{1/2}}\,F_{th}(\gamma_{p'})\,G_1(\gamma_{p'},\gamma_b,\gamma_p,\gamma_c)\,\mathbf{1}_{L_-<L_+}\,. \end{aligned} \tag{8.46}$$

The ratio of the momentum evolution rates (8.46) over (8.45) is shown Fig. 8.2. The dependence with respect to the energy cut-off parameter is found to be strong as well, even if the momentum tends to weaken the singularity, compared to Fig 8.1. Moreover, this ratio exhibits a negative sign, which implies a positive contribution of the secondary electrons into the beam momentum. Large values of this ratio is the signature of the importance of the secondary electron production, under these conditions.

The conservation of the total momentum in the plasma-beam system implies that the fast electron beam cannot gain energy from plasma. This fact provides another hint for the choice of the cut-off parameter. We are now in position to prescribe a choice for the energy cut-off parameter, that could be defined at an apropriate isosurface in Fig. 8.2, that is, where we can ensure a weak dependence with respect to that parameter.

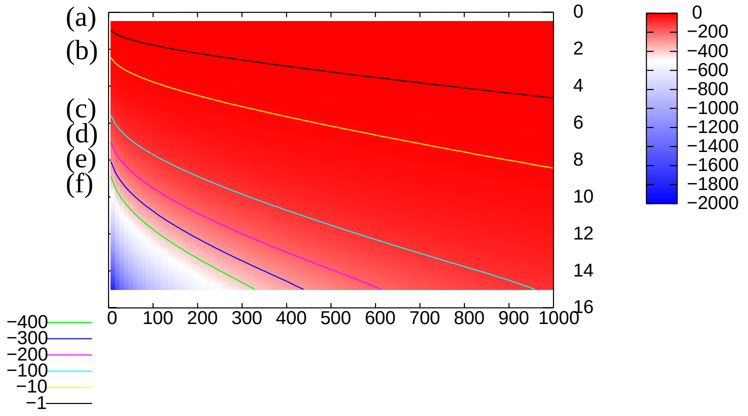

Figure 8.2: Relative contribution (large over small angle scattering) to the momentum transfer rate of beam particles in a 5 keV Maxwellian thermal plasma as a function of the beam energy and the energy cut-off parameter. Isolines -1, -10, -100, -200, -300, -400 for this ratio are labelled with respective letters (a)-(f).

8.5.3 Influence of the energy-scale cut-off parameter on the propagation of oscillations

In [1], the authors are proposing a sophisticated renormalization procedure upon the non-homogeneous, non-relativistic Boltzmann equation. They show that oscillations are immediately damped by a singular cross section. Conversely, the oscillations, if a cut-off is applied, propagate. The question that arises is: what is the effect of the energy exchange cut-off parameter on the propagation of these oscillations? For instance, one may expect a transfer of these oscillations, at fixed energy, from one population to another. This could be possible because the two populations are allowed to share energy ranges, and also because the Boltzmann gain and loss terms are split between the populations.

8.6 Conclusion

We have shown that the large angle scattering in electron-electron collisions [51], and resulting production of secondary fast electrons [25], is of great importance for the overall dynamics of the electron beam and plasma populations, at relativistic energies. We proposed a robust reduced model to deal with such a mechanism. This model is based on a decomposition of the relativistic Boltzmann collision operator, relying itself on a decomposition over the relativistic Rutherford cross section, instead of a partition of the phase-space between populations, as done usually. This model proposes a natural definition for the thermal and beam populations, according to the collision process they are issued from. The two populations are allowed to share energy ranges in the model. Further quantitative evaluation are foreseen to check the accuracy of the model and quantify the influence of the large angle scattering on the fast electron transport. This can be achieved using Monte-Carlo codes, such as *Geant* or *Penelope*. Such comparison could also be profitable contribution for specifications to the HiPER project [14]. Beyond $10-20$ MeV beam energies, Bremsstrahlung, density effects, photon production, and creation of electron-positron pairs, should complete this model [34, 35].

Bibliography

[1] Alexandre R. Villani C. (2002). *On the Boltzmann equation for long-range interactions*, Comm. Pure Appl. Math, 55, 30-70.

[2] Beliaev S. T. and Budker G. I. (1956). , Dokl. Akad. Nauk SSSR 107, 807 [Sov. Phys. Dokl. (1957) 1, 218].

[3] Bell A. R., Davies J. R., Guerin S., and Ruhl H. (1997). *Fast-electron transport in high-intensity short-pulse laser-solid experiments*, Plasma Phys. Control. Fusion, 39, 653.

[4] Bell A. R., Robinson A. P. L., Sherlock M., Kingham R. J. and Rozmus W. (2006). *Fast electron transport in laser-produced plasmas and the KALOS code for solution of the Vlasov-Fokker-Planck equation*, Plasma Phys. and Control. Fusion, 48, R37.

[5] Berthon C., Charrier P., Dubroca B. (2007). *An HLLC Scheme to Solve the M_1 Model of Radiative Transfer in Two Space Dimensions*, Journal of Scientific Computing, 31, 3.

[6] Blanchot N., Bignon E., Coïc H., Cotel A., Couturier E., Deschaseaux G. and Forget N. (2006). *Multi-petawatt high-energy laser project on the LIL facility in Aquitaine*, Topical Problems of Nonlinear Wave Physics, Proc. SPIE, Vol. 5975, 59750C.

[7] Borghesi M., Campbell D. H., Schiavi A., illi O., Galimberti M., Gizzi L. A., Mackinnon A. J., Snavely R. D., Patel P., Hatchett S., Key M. and Nazarov W. (2002). *Propagation issues and energetic particle production in laser-plasma interactions at intensities exceeding* $10^{19} Wcm^{-2}$, Laser and Particle Beams, 20, 31-38.

[8] Braams B. J. and Karney C. F. F. (1987). *Differential Form of the Collision Integral for a Relativistic Plasma*, Phys. Rev. Lett., 59, 16 .

[9] Brantov A., Rozmus W., Sydora R., Capjack C. E., Bychenkov V. Yu., and Tikhonchuk V. T. (2003). *Enhanced inverse bremsstrahlung heating rates in a strong laser field*, Phys. Plasmas 10, 3385.

[10] Bret A., Gremillet L., Bénisti D., and Lefebvre E. (2008). *Exact Relativistic Kinetic Theory of an Electron-Beam-Plasma System: Hierarchy of the Competing Modes in the System-Parameter Space*, Phys. Rev. Lett., 100, 205008.

[11] Cottrill L. A., Langdon A. B., Lasinski B. F., Lund S. M., Molvig K., Tabak M., Town R. P. J. and Williams E. A. (2008). *Kinetic and collisional effects on the linear evolution of fast ignition relevant beam instabilities*, Physics of plasmas, 15, 082108.

[12] Danson C. N. *et al.*, (2005). *Vulcan petawatt: Design, operation and interactions at 5X10(20) Wcm(-2)*, Las. Part. Beams, 23, 1, 87-93.

[13] Davies J. R., Bell A. R., Haines M. G., and Guerin S. M. (1997). *Short-pulse high-intensity laser-generated fast electron transport into thick solid targets*, Phys. Rev. E, 56, 7193.

[14] Davies J. R. (2009). *Fast Electron Transport Calculations for HiPER Benchmarking Collision Routines WP9.1.8*.

[15] Davies J. R. (2003). *Electric and magnetic field generation and target heating by laser-generated fast electrons*, Phys. Rev. E, 68, 056404.

[16] De Groot S.R., Van Leeuwen W. A., and Van Weert C. G. (1980). *Relativistic kinetic theory*, North Holland, Amsterdam.

[17] Duclous R., Dubroca B., Frank M. (2009). *Deterministic Partial Differential Equation Model for Dose Calculation in Electron Radiotherapy*, Submitted.

[18] Dubroca B. and Feugeas J.-L. (1998). *Hiérarchie de Modèles aux Moments pour le Transfert Radiatif*.

[19] Delettrez J. A. *et al* (2005). Plasma Phys. Control. Fusion, 47, B791.

[20] Dunne M. (2006). , Nature, 2, 2.

[21] Eriksson L.-G., Helander P., Andersson F., Anderson D., Lisak M. (2004). *Current Dynamics during Disruptions in Large Tokamaks*, Physical Review Letter, 92, 20.

[22] Eriksson L.-G. and Helander P. (2003). *Simulation of runaway electrons during tokamak disruptions*, Computer Physics communications, 154, 175.

[23] Glezos N., Raptis I. (1996). *A fast electron beam lithography simulator based on the Boltzmann transport equation*, Computer-Aided Design of Integrated Circuits and Systems, IEEE transactions on, 15, 1, 92-102.

[24] Gremillet L., Bonnaud G., and Amiranoff F. (2002). *Filamented transport of laser-generated relativistic electrons penetrating a solid target*, Phys. Plasmas, 9, 941.

[25] Gurevich A. V., Zybin K. P., and Roussel-Dupré R. (1998). *Kinetic equation for high energy electrons in gases*, Phys. Lett. , A 237, 240.

[26] Gurevich A. V. and Zybin K. P. (2001). *Runaway breakdown and electric discharges in thunderstorms*, Reviews of Topical Problems. Physics-Uspekhi, 44, 1119.

[27] Gurevich A. V., Lukyanov A. V., Zybin K. P., and Roussel-Dupré R. (1998). *Spherical symmetrical approach to the theory of runaway breakdown*, in Electron Kinetics and Application of Glow Discharges, Edited by U. Kortshagen and L.D. Tsendin, Plenum Press, New York.

[28] Holmlid *et al.,* (2009). *Ultrahigh-density deuterium of Rydberg matter clusters for inertial confinement fusion targets'*. Las. Part. Beams, 27, 3, 529-32.

[29] Honrubia J. J., Antonicci A., and Moreno D. (2004). *Hybrid simulations of fast electron transport in conducting media*, Las. Part. Beams, 22, 129.

[30] Honrubia J. J., Kaluza M., Schreiber J., Tsakiris G. D. , and Meyer-ter-Vehn J. (2005). *Laser driven fast electron transport in preheated foil targets*, Phys. Plasmas, 12, 052708.

[31] Jackson J. D., Classical Electrodynamics, *John Wiley and sons*, New York (1975).

[32] Karney C. F. F. and Fisch N. J. (1985). *Efficiency of current drive by fast waves*, Physics of Fluids, 28, 1.

[33] Lampe M. (1970). *Multiple scattering and Energy Loss of a Fast Test Electron Beam in a Plasma*, The physics of Fluid, 13, 10.

[34] Landau L. D. and Lifshitz E. M. (1973). *Relativistic Quantum Mechanics*, Pergamon, New York, 1973.

[35] Lefebvre E. (1996). *Electron and photon production from relativistic laser-plasma interactions*, Nuclear Fusion, 43, 629-633.

[36] Levermore D. (1996). *Moment Closure Hierarchies for Kinetic Theories*, J. Stat. Phys., Vol. 83.

[37] Lifshitz E., Pitayevski L. (1981). *Course of theoretical physics. Vol. 10. Physical Kinetics*, Translated from the Russian by J. B. Sykes and R. N. Franklin, Pergamon Press, Oxford Elmsford, N.Y. .

[38] Mangles S. P. D., *et al.,* (2006). *Table-top laser-plasma acceleration as an electron radiography source*, Las. Part. Beams, 24, 1, 185-90.

[39] Minerbo G. N. (1978). *Maximum entropy Eddington Factors*, J. Quant. Spectrosc. Radiat. Transfer, 20, 541.

[40] Neumayer P. *et al.,* (2005). *Status of PHELIX laser and first experiments*, Las. Part. Beams, 23, 3, 385-9.

[41] Miyanaga N. *et al.* (2003). Inertial Fusion Sciences and Applications, ed B. Hammel, D. D. Meyerhofe, J. Meyer-ter-Vehn, and H. Azechi, p. 507.

[42] Parks P. B., Cowan T. E., Runaway electron production during intense electron beam penetration in dense plasma, *Physics of Plasma*, 14, 013102, (2007).

[43] Robiche J. and Rax J. M. (2004). *Relativistic kinetic theory of pitch angle scattering, slowing down, and energy deposition in a plasma*. Physical Review E, 70, 046405.

[44] Robinson A. P. L., Kingham R. J., Ridgers C. P. and Sherlock M. (2008). *Effect of transverse density modulations on fast electron transport in dense plasma*. Plas. Phys. and Control. Fusion, 50, 065919.

[45] Rhul H. *Classical Particle Simulations with the PSC code. An introduction to the PSC code*. RUB, Bochum, Germany.

[46] Santos J.J *et al*, Fast electron propagation in high density plasmas created by shock wave compression *Plasma Physics and Controlled Fusion*, 51, 014005, (2009).

[47] Sentoku Y., Kemp A. J., Numerical methods for particule simulations at extreme densities and temperatures: Weighted particules, relativistic collisions and reduced currents, *Journal of Computational Physics*, 227, 6846-6861 (2008).

[48] Stewart J.M. (1971). *Non-Equilibrium Relativistic Kinetic theory*, Lecture Notes in Phys. 10, Springer-Verlag, Berlin.

[49] Synge J.L. (1957). *The relativistic gas*, North-Holland, Amsterdam.

[50] Sherlock M., Bell A. R. , Kingham R. J., Robinson A. P. L. and Bingham R. (2007). *Non-Spitzer return currents in intense laser-plasma interactions*, Phys. Plasmas, 14, 102708.

[51] Shoub E. C. (1987). *Failure of the Fokker-Planck approximation to the Boltzmann integral for (1/r) potentials*, Phys. Fluids, 30, 5.

[52] Symbalisty E. M. D., Roussel Dupré R. A., Yukhimuk V. A. (1998). *Finite Volume Solution of the Relativistic Boltzmann Equation for Electron Avalanche Studies*, IEEE Transactions on Plasma Science, 26, 5.

[53] Turpault R. (2002). *Construction of a multigroup M1 model for the radiative transfer equations*, Comptes Rendus Mathématique, 334, 4, 331-336.

8.7 Appendix: M1 Kernels of the ionization operator

$$
\begin{aligned}
G_0(\gamma_{p'},\gamma_{q'},\gamma_p,\gamma_c) &= \frac{M}{\pi(8(\tilde{\gamma}_l^2-1)\tilde{\gamma}_l)^2} \times \left[-S_- \frac{2(2N-D)L_-}{D\sqrt{D-2L_-^2}} + S_+ \frac{2(2N-D)L_+}{D\sqrt{D-2L_+^2}} \right. \\
&- \left. S_- \sqrt{2}\arctan\left(\frac{\sqrt{2}L_-}{\sqrt{D-2L_-^2}} \right) + S_+ \sqrt{2}\arctan\left(\frac{\sqrt{2}L_+}{\sqrt{D-2L_+^2}} \right) \right] , \\
G_1(\gamma_{p'},\gamma_{q'},\gamma_p,\gamma_c) &= \frac{H}{\pi(8(\tilde{\gamma}_l^2-1)\tilde{\gamma}_l)^2} \left[S_- \frac{D-N-L_-^2}{\sqrt{D-2L_-^2}} - S_+ \frac{D-N-L_+^2}{\sqrt{D-2L_+^2}} \right] \\
&+ \frac{(\gamma_p-\gamma_{p'})(\gamma_{p'}+\gamma_{q'})}{\sqrt{(\gamma_{q'}^2-1)(\gamma_p^2-1)}} G_0(\gamma_{p'},\gamma_{q'},\gamma_p,\gamma_c) ,
\end{aligned}
$$

where $G_0 > 0$ if $L_- < L_+$, and

$$
\begin{aligned}
\tilde{\gamma}_l^2 &= \frac{\gamma_{p'}\gamma_{q'}+1}{2} , \\
B &= (\gamma_q+\gamma_{p'})\gamma_{p'} > 0 , \\
D &= \left\{ \left[2(\gamma_c^2-1) + \left(\frac{\gamma_p-\gamma_{p'}}{\gamma_{p'}+\gamma_q} \right) B \right]^2 \right. \\
&+ \left. 2(\gamma_{p'}^2-1) + \left[2(\gamma_c^2-1)\frac{\gamma_p+\gamma_{q'}}{\gamma_{p'}+\gamma_q} + \left(\frac{\gamma_p-\gamma_{p'}}{\gamma_{p'}+\gamma_q} \right)^2 B \right] \right\} \\
&\times \left[(\gamma_p^2-1) + (\gamma_{q'}^2-1) + (\gamma_p-1)(\gamma_{p'}+\gamma_{q'}) \right] > 0 , \\
H &= \left(\frac{\gamma_p+\gamma_{q'}}{\gamma_{p'}+\gamma_q} \right) \frac{1}{\gamma_p\sqrt{\gamma_p^2-1}} 8\pi(2\tilde{\gamma}_l^2-1)^2(\tilde{\gamma}_l^2-1)^2\tilde{\gamma}_l^2 , \\
M &= \frac{8\pi}{\gamma_p}\sqrt{\gamma_{q'}^2-1}(2\tilde{\gamma}_l^2-1)^2(\tilde{\gamma}_l^2-1)^2\tilde{\gamma}_l^2 \times \left(\frac{\gamma_p+\gamma_{q'}}{\gamma_{p'}+\gamma_q} \right) , \\
N &= \left(\frac{\gamma_{p'}+\gamma_q}{\gamma_p+\gamma_{q'}} \right) \left[2(\gamma_c^2-1) + \left(\frac{\gamma_p-\gamma_{p'}}{\gamma_{p'}+\gamma_q} \right) B + \left(\frac{\gamma_p+\gamma_{q'}}{\gamma_{p'}+\gamma_q} \right) (\gamma_{p'}^2-1) \right] \\
&\times \left[(\gamma_p^2-1) + (\gamma_{q'}^2-1) + (\gamma_p-1)(\gamma_{p'}+\gamma_{q'}) \right] > 0 ,
\end{aligned}
$$

whith the small parameters $L_\pm$

$$\begin{aligned}
\Theta_1^\pm &= \pm\sqrt{(\gamma_{p'}^2-1)(\gamma_q^2-1)}\,,\\
\Theta_2^\pm &= \pm\sqrt{(\gamma_{p'}^2-1)}\sqrt{[(\gamma_p^2-1)+(\gamma_{q'}^2-1)+(\gamma_p-1)(\gamma_{p'}+\gamma_{q'})]}\,,\\
\Theta_3^\pm &= -(\gamma_p-\gamma_{p'})(\gamma_{p'}+\gamma_{q'})\pm\sqrt{(\gamma_{q'}^2-1)(\gamma_p^2-1)}\,,\\
L_+ &= \max\left(-\sqrt{\frac{D}{2}},\min\left(\Theta_1^+,\Theta_2^+,\Theta_3^+,\sqrt{\frac{D}{2}}\right)\right)=O\left(\frac{\|\mathbf{p}'\|}{m_e c}\right)\,,\\
L_- &= \min\left(\sqrt{\frac{D}{2}},\max\left(\Theta_1^-,\Theta_2^-,\Theta_3^-,-\sqrt{\frac{D}{2}}\right)\right)=O\left(\frac{\|\mathbf{p}'\|}{m_e c}\right)\,.
\end{aligned}$$

The parameters $L_\pm$ are issued from the integration boundaries over an angle variable. They remain small as the energy of the thermal population.

For the sake of completness of the model, we finally give the expression of the sign functions

$$\begin{aligned}
S_- &= \operatorname{sign}\left(N-L_-^2\right)\\
S_+ &= \operatorname{sign}\left(N-L_+^2\right)
\end{aligned} \tag{8.47}$$

8.8 Appendix: Scaling with an electron-ion frequency in the case of a beam population

There are two basic temporal scales in the kinetic equation (8.1). One is related to the collective electron motion and is characterized by the electron plasma frequency, $\omega_{pe}=\sqrt{Zn_ie^2/\epsilon_0 m_e}$, another is the time of electron collisions characterized by the electron ion collision frequency, ν_{ei}. As it depends on the electron velocity, we have a possibility to choose either the thermal velocity of plasma electrons, $v_{th}=\sqrt{\kappa_B T_e/m_e}$, or a characteristic velocity of beam electrons, which is close to c. Since we are interested in the beam electrons and on their effect on plasma, it is more appropriate to normalize the electron-ion collision frequency to its value related to the fast electrons,

$$\nu_{ei}=Z^2n_ie^4\ln\Lambda/8\pi\epsilon_0^2m_e^2c^3. \tag{8.48}$$

Consequently, the electron velocity is normalized by c, the electron momentum by $m_e c$, and the electron distribution function by $Zn_i/m_e^3c^3$. Then, our small parameters are the ratio of electron collision and plasma frequencies:

$$\nu=\frac{\nu_{ei}}{\omega_{pe}}=\frac{Z^{3/2}\sqrt{n_i}e^3\ln\Lambda}{8\pi\epsilon_0^{3/2}m_e^{3/2}c^3}\ll 1, \tag{8.49}$$

the ratio of the beam density to the plasma electron density $n=n_b/Zn_i\ll 1$ and the plasma temperature, $k_BT_e/m_ec^2\ll 1$.

Table 8.2: Cut-off parameters

$k_BT_e/(m_ec^2)$	$K_{min}/(m_ec^2)$	$K_{max}/(m_ec^2)$
0.1	0.02	1
1	0.3	10
10	1	100

For the problems where the collisional effects dominate, it is appropriate to choose the collision frequency for normalization of the time, $\nu_{ei}t \to t$. Then the space coordinate is normalized by the electron mean free path, $\mathbf{x}\nu_{ei}/c \to \mathbf{x}$, and the electric and magnetic fields are normalized by $m_ec\nu_{ei}/e$ and $m_e\nu_{ei}/e$, correspondingly.

8.9 Appendix: Fast electron Transport Calculations for HiPER Benchmarking Collision Routines WP9.1.8 (courtesy from J.R. Davies)

8.9.1 Fast electrons

The fast electrons should be set up at time zero with a number density

$$n_b \propto \cos^2\left(\frac{z\pi}{20\Delta z}\right), 0 \le z \le 10\Delta z\,, \tag{8.50}$$

where Δz is the grid spacing specified for the diagnostics, and a 3D, relativistic Maxwellian momentum distribution for: $k_BT_e/(m_ec^2) = 0.1\,,\ 1\,,\ 10$. Particle based codes should use 10^6 particles for the fast electrons. The cut-off between fast and background electrons (K_{min}) and the upper cut-off (K_{max} since a Maxwellian distribution extends to infinity) are given in Table 8.2. Electrons with an energy below K_{min} should be assumed to deposit their energy.
The probability density function for the Lorentz factor γ of a 3D, relativistic Maxwellian is

$$f(\gamma) = \frac{\beta}{K_2(\beta)}\gamma\sqrt{\gamma^2-1}\exp(-\gamma\beta)\,, \tag{8.51}$$

where $\beta = m_ec^2/(k_BT_e)$ and K_n is the modified Bessel function of the first kind, which comes from the normalization $\int_1^\infty f(\gamma)d\gamma = 1$. In terms of the magnitude of the momentum p this is

$$f(p) = \frac{\beta}{K_2(\beta)}\frac{p^2}{m_e^3c^3}\exp(-\gamma(p)\beta)\,, \tag{8.52}$$

where $\gamma(p) = \sqrt{1+p^2\big/(m_e^2c^2)}$. The probability density function for any given component of momentum p_i is

$$f(p_i) = \frac{1}{2m_ec}\frac{1+\gamma_i}{(1-\beta)K_1(\beta)+K_2(\beta)}\exp(-\gamma(p_i)\beta)\,, \tag{8.53}$$

Table 8.3: Grid spacing parameter for various temperatures

$k_B T_e/(m_e c^2)$	$\Delta z/(cT)$
0.1	0.05
1	0.1
10	1

8.9.2 Background

Static, uniform, infinite media with atomic numbers of $Z = 1$ (hydrogen), 13 (aluminium), 79 (gold). A fixed constant should be used for all the $\ln\Lambda$'s. If the distribution of the background particles has to be specified use a Maxwellian with a temperature of $K_{min}/10$ and a density 100 times greater than the maximum fast electron density. If possible, following the runs with a fixed $\ln\Lambda$ the Al and Au runs should be repeated with values of $\ln\Lambda$ for room temperature and pressure and the hydrogen run for a electron density of $7.2310^{31}/\mathrm{m}^3$ (300 g/cm^3 $D - T$) and a temperature ($k_B T_e/e$) of 1 keV.

8.9.3 Boundary Conditions

Reflective boundary at z = 0 and place the far z boundary far enough away that it has no effect.

8.9.4 Diagnostics

1. The fast electron energy as a function of time.
2. The time by which 90% of the fast electron energy has been lost.
3. The fast electron energy deposition (energy per unit length) on a uniform axial grid with points at $(k - 0.5)\Delta z$, where k is an integer greater than zero.
4. The depth within which 90% of the fast electron energy is lost.

The results should be expressed in the following units:
Length: cT ,
Time: T ,
Total Fast Electron Energy: 1 ,
where $T = (4\pi\epsilon_0^2 m_e^2 c^3)\Big/ n_e e^4 L$, n_e is the background electron density and L is the fixed value used for all of the $\ln\Lambda$'s or 1 for runs using variable $\ln\Lambda$. The grid spacing Δz is given by in Table 8.3. The grid should have 100 points or more. For runs using variable $\ln\Lambda$'s, appropriate values should be chosen and clearly specified. Appropriate values should be chosen for the spatial and temporal grids used by the codes. This is just a specification for the diagnostic that will be compared.

Chapter 9

Conclusion and perspectives

9.1 Main results and consequences of the present work

The present essay aimed at the development of a mathematical basis for crucial processes of ICF physics. It can be summarized in five points.

First, we have developed a $2D_{\mathbf{x}} \times 3D_{\mathbf{v}}$ parallel Maxwell-Fokker-Planck-Landau solver, which can serve as a reference simulation tool, because it can handle with highly anisotropic distribution functions. We have demonstrated the computational affordability of this approach, and shown the relevance of such a tool to capture high order moments of the distribution function, in particular when magnetic field and collision effects are coupled. We have then proposed an extension of the numerical schemes to the relativistic regime, where additional processes for electron acceleration and transport occur.

Second, we provide with a mathematical proof of convergence of a high order Finite Volume scheme, and comparison between simulation results, which shows good behaviour with respect to discontinuities in the phase space. This mathematical and numerical work is reaching the numerical requirements necessary to the treatment of high intensity regimes, such as wavebreaking, bubble regime, or high harmonic generation on plasma.

Third, we have developed angular reduced models, based on previous works on radiative transfer, that are able to describe the isotropic distribution functions (thermal, highly collisional, for example), as well as highly anisotropic distribution functions (of fast particles, for example), coupled with realistic collision/ionization/radiation kernels. We have demonstrated the accuracy and robustness of such electron $M1$ models, while performing academic and fundamental simulations for electron radiotherapy and ICF applications.

Fourth, we have proposed an accurate, fast and robust modelling, for long-range Coulomb interaction, of an arbitrary type of collision events, ranking from grazing and multiple, to hard and single, without artificial discrimination between collision events, the Coulomb force being indeed continuous by nature. This model is, in particular, able to describe the heating of a kinetic thermal population with Coulomb collision of arbitrary angle.

Finally, we turned our model, our numerical methods to realistic simulations, concerning the shock ignition scheme. In the ICF, this latter is currently one of most promising candidates among advanced inertial fusion projects. The 2009 KiTSI project (an acronym for Kinetics Transport for Shock Ignition) has recently been pointed out as a milestone on the critical path in the HiPER roadmap, as well as for the shock ignition design on the National Ignition Facility (Livermore, Ca). The reason is that realistic design for shock ignition relying only on experiments would be meaningless. A credible design, including realistic constraints and effects of random imperfections, will come from numerical modeling. So the achievement of a predictive, validated, integrated numerical model is a central issue. Of course, a shock ignition study includes partial experimental validation of the concept using medium scale laser facilities, integrated experiments using the Omega facility of the University of Rochester (NY-USA) and scale 1 ignition demonstration on the National Ignition Facility (Livermore, Ca).

Among the possible perspectives that emerge from this work, we would like to mention the quantification of the importance of hard collisions for regimes of interest, together with the issue of the implementation of this process in a PIC solver. We are now in position to explore and characterize new regimes of transport, that will serve for a better understanding of the electron transport, and may become fundamental processes upon which new schemes for ignition or particle acceleration could be constructed.

The model accounting for these hard collisions, presented in Chapter 8, proves to be rich in term of mathematical issues, such as rigorous mathematical derivation of the model, or conditional stability analysis [1].

Bibliography

[1] Alexandre , Villani C., *On the Boltzmann equation for long-range interactions*, Comunication on Pure and Applied Mathematics, 55, 1, 30-70, 2001.